Evolution géologique de l'avant-arc sud péruvien : apports des données géo-thermochronologiques

Melanie Noury

UNIVERSITÉ DE GRENOBLE

THÈSE

Pour obtenir le grade de

DOCTEUR DE L'UNIVERSITÉ DE GRENOBLE

Spécialité : **Sciences de la Terre, de l'Univers et de l'environnement**

Arrêté ministériel : 7 août 2006

Présentée par

Mélanie NOURY

Thèse dirigée par **Thierry SEMPERE**
codirigée par **Matthias BERNET**

préparée au sein du **Laboratoire ISTerre**
dans **l'École Doctorale Terre, Univers, Environnement**

Evolution géologique de l'avant-arc sud péruvien : apports des données géo-thermochronologiques

Thèse soutenue publiquement le **5 décembre 2014**,
devant le jury composé de :

Dr Etienne JAILLARD
DR1, IRD ISTerre, Université de Grenoble, France (Président)
Pr. Todd EHLERS
Professeur, Université de Tübingen, Allemagne (Rapporteur)
Pr. Massimiliano, ZATTIN
Professeur, Université de Padoue, Italie (Rapporteur)
Dr. Richard SPIKINGS
Adjoint Scientifique, Université de Genève, Suisse (Examinateur)
Dr. Xavier ROBERT
CR2, IRD ISTerre, Université de Grenoble, France (Invité)
Dr. Thierry SEMPERE
DR2, IRD ISTerre, Université de Grenoble, France (Directeur de thèse)
Dr. Matthias BERNET
MdC, Université de Grenoble, France (Co-directeur de thèse)

Université Joseph Fourier / Université Pierre Mendès France /
Université Stendhal / Université de Savoie / Grenoble INP

GEOLOGICAL EVOLUTION OF THE SOUTHERN PERUVIAN FOREARC:

Insights from geo-thermochronology

Mélanie NOURY

You're probably on the right track

if you feel like a sidewalk worm during a rainstorm

Larry Page, 2009

University of Michigan Commencement Address

Table of contents

Acknowledgments 7

Abstract 11
Résumé 13

Introduction 17

Chapter I – Geological context: The Andes of southern Peru 21

Chapter II – Methods 41

Chapter III – Early Paleogene crustal extensional collapse in response to Late Cretaceous arc growth and flare-up in the Arequipa belt of southern Peru, Central Andes 59

Chapter IV – Thermochronologic evidence for Eo-Oligocene orogen-parallel extension in the forearc of southern Peru. 121

Chapter V – Neogene crustal flow-driven subsidence of Altiplano edges defines two episodes of Andean crustal thickenning 157

Chapter VI – Summary and outlook 179

Résumé étendu 185

Appendix A: $^{40}Ar/^{39}Ar$ dating 207
Appendix B: Zircon (U-Th)/He dating 211
Appendix C: Apatite and zircon fission-track sample preparation 213
Appendix D: Zircon U-Pb Analyses (In-Situ) 217
Appendix E: Zircon U-Pb analyses (Detrital) 227
Appendix F: Zircon Fission-track analyses (Plutonic and Metamorphic rocks) 249
Appendix G: Apatite Fission-track analyses (Plutonic and Metamorphic rocks) 261
Appendix H: Zircon Fission-track analyses (Huanca basin) 281
Appendix I: Apatite Fission-track analyses (Huanca basin) 297
Appendix J: Zircon Fission-track analyses (Modern river sediments) 313
Appendix K: Apatite Fission-track analyses (Modern river sediments) 329

Acknowledgments

Soyons reconnaissants aux personnes qui nous donnent du bonheur ;
elles sont les charmants jardiniers par qui nos âmes sont fleuries…

Marcel Proust – Les Plaisirs et les Jours

This work greatly benefited from the advices and support of many people and I would like to thank all those who helped me since the beginning of my PhD. First, I would like to acknowledge here my two advisors: Thierry Sempere and Matthias Bernet, this work would not be what it is without their help. Thierry, thank you for giving me the opportunity to work on this project, for introducing me to the Peruvian geology and for all the discussions we had about various topics during the very good times I spent in Peru. Matthias, I am truly grateful to you for introducing me to the wonderful world of fission-track, for giving me the opportunity to teach undergraduate courses (especially in Buis-les Barronies) but also for sharing your passion for Colombia and overall for your endless support.

I would like to express also my gratitude to the members of the committee who accepted to review this work: Etienne Jaillard, Todd Ehlers, Massimiliano Zattin, Richard Spikings and Xavier Robert. Their numerous and pertinent comments greatly improved this manuscript.

Papers presented in this dissertation will be published in collaboration with different co-authors who deserve special thanks. Thibaud Simon-Labric and Taylor Schildgen who made respectively zircon (U-Th)/He and ^{40}Ar-^{39}Ar analyses and whose inputs and critical reviews really improved Chapter 4. Jean-Louis Paquette welcomed me warmly in his lab in Clermont-Ferrand and surely spent quite some time performing zircon U-Pb dating for this study, many thanks to him. I also thank Urs Schaltegger who permitted me to perform zircon U-Pb dating in Lausanne with Alexey Ulianov who kindly introduced me to laser ablation of zircons.

Because, everything would have been harder without the people who helped me in the field and in the lab, I would also like to thank warmly José Berrospi, Manuel Flores and Edwin Torres from Peru for their logistical support during the fieldwork; François Sénebier and Francis Coeur for mineral separations and their good mood; Elizabeth Hardwick and Mélanie

Balvay for their valuable help in the ISTerre fission-track laboratory and for sharing their office with me. I would also like to thank people from Peru and Colombia who made my different stays there unforgivable: Thierry of course but also Lucille and Carlos in Peru and Maria, Ana and Juliana in Colombia. ¡Muchísimas gracias!

Last but not least, I deeply thank all those who surrounded me during these three years with their love and friendship. They deserve a full section of greetings, in French.

Donc un immense merci à tous ceux que j'ai rencontré à ISTerre, en particulier Carole, Karim et Romain pour leur amitié et leur soutien quotidien et inconditionnel. Anne-Marie qui m'a accueillie chez elle au tout début de ma thèse et dans son chalet pour de magnifiques WE (dans le registre hébergement - merci aussi à Pam). Rachel pour avoir partagé mon bureau, ses meringues (et surtout ce qui va avec) mais aussi une Mustang rouge décapotable. La team café-croissant-du-matin/café-chocolat-du-midi avec Natalie, Jean, Catherine pour leur soutien même matinal et pour toutes les fois ou ils m'ont donnée une bonne excuse pour ne pas retourner travailler tout de suite. Bertrand, Audrey, Margaux et Cécile qui avaient toujours leur porte de bureau ouverte pour que je puisse venir me plaindre.

A ISTerre, j'aimerai aussi remercier Christine pour les heures de bavardage et son efficacité administrative à toute épreuve ; les membres de l'équipe TRB et en particulier Pascale qui a rempli mon planning d'enseignement, Christophe qui a accepté d'être mon tuteur du CIES (et qui fait un super génépi), Fabienne pour son sourire ; Julien, Jérôme et Stéphane pour l'ambiance, Xavier (encore) pour tous ses conseils, Laurent pour son écoute, mais aussi Alexandra pour avoir partagé quelques cours ainsi que Emilie pour son soutien et ses conseils très avisés ! Enfin je remercie l'ensemble des thésards du labo pour tous les bons moments passés sur la terrasse, à la cafèt' ou au bar : Gabi, Zakaria, Paul, Franz, Eric, Alexis, Baptiste, Benjamin, Gwen, Pierre, Jonathan, Charlotte, Marion, Lucie, Hélène et tous les autres que j'ai sûrement oubliés ; ainsi que les amies rencontrées à Chamonix Caro et Gwladys pour leur bonne humeur rafraichissante à 6 semaines de rendre le manuscrit. Et merci aussi à Abir pour toutes nos petites pauses qui m'ont bien manquées quand tu as dû partir. Je n'oublie pas tous les gens avec qui j'ai eu le plaisir de partager le bureau le plus éloigné de la porte d'entrée du labo : Elizabeth, Mélanie, Thierry Calmus, Arnaud, Maélianna, Amandine, Christophe, Sergio, Thibaud et aussi Julie et Anne. Je n'oublie pas non plus celui ou celle qui a volé mes bidons bleus et les échantillons qui étaient dedans.

Ma vie pendant ces trois ans aurait été bien plus fade sans tous les copains, donc merci aussi à Michel pour le bol d'air breton et tout ce qui vient avec, à Julie et Anne-So pour les discussions, les jeux et les rires ; à Julien pour les soirées saoulpape improvisées ; à JD pour les grands films et puis aussi à Emilie, Nicolas, Solène, Annette et tous les copains de la LaiTUE pour tous les bons moments passés ensemble, le soir, le WE et même parfois au petit-dèj. Une pensée spéciale pour Pierre (Peter) et nos petites discussions qui m'ont bien changé les idées pendant la rédaction (et après) ; ainsi que pour Estelle, Hervé, Céb, Stephen, Jan, Loraine, Jacqueline, Paul toujours prêts pour partager du bon temps quand on se revoit. Un grand merci à mes collocs Clément, Cola, Louis-Abel, Gentianne, Marie, Simon et Véro pour tous les instants partagés au 17 rue Beethoven et parcequ'ils m'ont supportée pendant au moins un an et se sont même montrés intéréssés par « ma science ».

Malgré la distance, j'ai aussi toujours pu compter sur l'écoute, le soutien, la franchise, l'humour et l'amitié de mes mentors Mélody et Justine, toujours prêtes à déconner et à taroter. Et puis je ne remercierai jamais assez mes amies de longue date Charlotte, Marion, Hyacinthe et Anne d'être simplement là, merci d'être juste vous.

Je voudrais aussi remercier ici tous les gens qui se sont déplacés pour assister à ma soutenance de thèse et en faire une journée mémorable, en particulier Yves et Catherine (grâce à qui je n'ai pas été complètement larguée sur les pistes grenobloises), Marcel pour sa bonne humeur, Albert car sa présence m'a beaucoup touchée ainsi que Anna et Martine pour avoir aidé à préparer le kig-ha-farz. Merci aussi aux fêtards d'à-côté pour cette soirée sensationnelle !

Enfin, les mots les plus simples étant souvent les plus forts, j'adresse toute mon affection à l'ensemble de ma grande famille et en particulier à mes sœurs Marie-Claire et Sophie. Peu de mots peuvent exprimer ce que je dois à mes parents Christine et Jacques. Votre confiance et votre amour me portent et me guident tous les jours. Merci d'avoir aiguisé ma curiosité, de m'avoir laissée libre, de m'avoir appris le respect, le partage, la liberté et d'avoir fait de moi ce que je suis. Je vous aime.

Abstract

The southern Peruvian margin has been located above a major ocean-continent subduction zone since at least the Early Paleozoic, resulting in the formation of one of the largest orogens in the world: the Central Andes, where crustal thickness is >60 km over a large area. This overthickening is currently thought to have occurred incrementally only during the last 30 Ma. To understand how and when crustal overthickening was acquired, most of the previous studies have focused on the magmatic arc evolution and on deformation, uplift and erosion history of the backarc. The tectono-thermal Cenozoic evolution of the forearc remains poorly known, whereas it is a zone prone to recording changes in subduction dynamics.

The objective of this dissertation is to address the thermal evolution and the coupling between magmatic, tectonic and sedimentary processes over the past 200 Ma in the present-day forearc of southern Peru where the crust thickens from ~30 km along the coastline to more than 60 km under the present-day volcanic arc. New geo- and thermochronological data coupled to a novel geological map illuminate the evolution of the south Peruvian margin since the Jurassic. Three key periods of the margin evolution are addressed in this dissertation: the onset of crustal thickening, the deformations associated in the forearc with the formation of the Bolivian Orocline and the Neogene crustal thickening of the Central Andean orogen.

We show that crustal thickening likely began between 90 and ~50 Ma after more than 200 My of lithospheric thinning during a three step evolution of the magmatic arc as follows: growth (90-74 Ma), flare-up (74-62 Ma), extensional collapse (62-50 Ma). Extension prevailed in the forearc since then and waned until ~30 Ma. In addition, we evidence important normal fault zones striking perpendicular to the southern Peruvian margin that delineate large northwestward tilted blocks. This deformation reveals orogen parallel extension in the forearc during the Paleogene likely due to the formation of the Bolivian Orocline by counterclockwise rotation of rigid blocks. Finally, geomorphic features in the coastal area of southern Peru reveal two periods of surface uplift (~23 to 10 Ma and since ~4.5 Ma), separated by a period of surface subsidence (from ~10 to ~4.5 Ma). The same chronology has been described on the Amazonian side of the Central Andean orogen. We thus propose that this evolution is due to large-scale crustal thickness variations; surface uplift being triggered by addition of mantle-derived magmas to the crust and subsidence by ductile flow away from the previously overthickened crust.

Résumé

La marge sud péruvienne est située au niveau d'une zone majeure de subduction ocean-continent depuis au moins le Paleozoique inférieur. C'est dans ce cadre que s'est formé l'un des plus importants orogènes du monde : les Andes Centrales. En effet, l'épaisseur crustale y est >60 km et ce sur une importante surface. Cependant, on considère actuellement que ce surépaississement a été acquis incrémentalement seulement depuis ~30 Ma. Dans le but de comprendre comment et quand ce surrépaississement est apparu, la majeure partie des études précédentes s'est focalisée sur l'évolution de l'arc magmatique et sur l'histoire de la déformation, du soulèvement et de l'érosion de la zone d'arrière arc. Cependant, l'évolution tectonique et thermique de l'avant arc reste mal connue bien que cette zone soit susceptible de bien enregistrer les changements liés à la dynamique de subduction.

Cette thèse à pour objectif de mieux contraindre l'évolution thermique et les couplages entre les processus magmatiques, tectoniques et sédimentaires depuis 200 Ma dans l'avant-arc actuel du sud du Pérou. De nouvelles données géo-thermochronologiques couplées à une nouvelle carte tecto-stratigraphique éclaircissent l'évolution de la marge péruvienne depuis le Jurassique. Trois périodes clefs sont analysées dans ce mémoire : le début de l'épaississement crustal, les déformations de l'avant-arc associées à la formation de l'Orocline bolivien et l'épaississement crustal de l'orogène des Andes Centrales pendant le Néogène.

Nous montrons que l'épaississement crustal a probablement commencé entre 90 et 50 Ma après plus de 200 Ma d'amincissement, et ce a la faveur d'une évolution en trois étapes : croissance initiale (90-74 Ma), « flare-up » (74-62 Ma) et effondrement extensionnel (62-50 Ma). L'extension a ensuite prédominé dans l'avant-arc tout en diminuant progressivement jusqu'à ~30 Ma. Par ailleurs, nous mettons en évidence d'importantes zones de failles normales orientées perpendiculairement à la marge sud-péruvienne et qui délimitent de grands blocs basculés vers le nord-ouest. Ces déformations révèlent une extension parallèle à l'orogène dans l'avant arc pendant le Paléogène, probablement due à la formation de l'Orocline bolivien par rotation antihoraire de blocs rigides. Enfin, les traits géomorphiques visibles dans la zone cotiere du sud du Pérou permettent de définir deux périodes de soulèvement de la surface (entre 23 et 10 Ma et depuis ~4.5 Ma), séparées par une période de subsidence (entre ~10 et ~4.5 Ma). La même chronologie ayant été décrite sur le versant Amazonien de l'orogène, nous proposons que cette évolution soit due à des variations à

grande échelle de l'épaisseur crustale ; le soulèvement de la surface étant provoqué par addition à la croûte de magma d'origine mantellique et la subsidence par un flux de matériel crustal ductile depuis les zones précédemment sur-épaissies.

Introduction

Geologic processes affect where and how we live. They cause the rise of mountain ranges, growth of volcanoes or land subsidence, and thus permit to sculpt landscapes, shape coastlines and influence the climate. Their study is thus of crucial importance in assessing natural risks as landslides, earthquakes, volcanic hazards and climate change. Obviously, their understanding is also essential for evaluating water, hydrocarbon and mineral resources.

All geologic processes are related directly or indirectly to plate tectonics and most of them take place at plate boundaries. It is considered that the main driving force of plate tectonics is subduction (Conrad and Lithgow-Bertelloni, 2002) (the process by which a plate converges and sinks into the mantle under another plate (Amstutz, 1951; White et al., 1970; Stern, 2002)). Moreover, subduction zones are the site of important and recurrent earthquakes, intense volcanism, mountain building and world-class ore deposits. The study of these processes is thus important for understanding the links between subduction, magmatism, genesis of ore deposits and topography.

The Pacific Ocean is surrounded by the world's longest subduction zone: the circum-Pacific belt. The eastern part of this belt is characterized by the world's longest mountain range, the Andes. The Andean cordillera contrasts with other major orogens such as the Alps or Himalayas because it does not follow from the collision of two continental plates but from the subduction of the Nazca oceanic plate under the South American continental plate. In the Central Andes, the crust is >60 km-thick over a large area: the Altiplano-Puna plateau (Assumpção et al., 2013; Chulick et al., 2013; van der Meijde et al., 2013). However, how and when this overthickness was acquired remains debated. Indeed, the subduction has been almost continuous under the Central Andean margin since at least ~215 Ma (Boekhout et al., 2012) but deformation that lead to the present-day Central Andes orogen are known to begin only in the Eocene (Sempere et al., 1990a; Horton, 2005). It has been proposed that thermal weakening of the crust due to long-lived magmatism above the subducting slab may have had an effect on the delay between the onset of subduction and formation of the Altiplano-Puna plateau (Isacks, 1988; James and Sacks, 1999).

Yet, most of the studies addressing the Central Andean orogeny have focused on the magmatic arc evolution and on deformation, uplift and erosion history of the backarc

(Mégard, 1984; Kono et al., 1989; Soler and Bonhomme, 1990; Allmendinger et al., 1997; Wörner et al., 2000; Kay et al., 2005; Oncken et al., 2006; Trumbull et al., 2006; Haschke et al., 2006; Garzione et al., 2008; Barnes and Ehlers, 2009; Mamani et al., 2010; Martinod et al., 2010; Charrier et al., 2013); however, the thermal history of the forearc, is still poorly known whereas this zone is prone to record the changes in subduction dynamics.

The objective of my dissertation was to address the thermal evolution and the coupling between magmatic, tectonic and sedimentary processes over the past 200 Ma in the present-day forearc of southern Peru. Therefore, my Ph.D. work was focused on the forearc of the Central Andes, where the crust thickens from ~30 km along the coastline to more than 60 km under the present-day volcanic arc. Whereas overthickening of continental crust is commonly viewed as the result of tectonic shortening, in this region the upper part of the crust exhibits little to no evidence of crustal shortening and in contrast many extensional features (James, 1971; Myers, 1975; Tosdal et al., 1984). Because crustal overthickening often results in extensional collapse and/or significant erosion, here I address this issue through a regional-scale study of exhumation using fission-track dating and tectono-sedimentary study of the Mesozoic to Cenozoic forearc deposits. I focus on the present-day forearc of southern Peru, because it provides extensive outcrops of basement, arc-related plutonic rocks as well as backarc sedimentary rocks of different ages that allow comparing the chronology of exhumation of deep-seated rocks with magmatic and sedimentary processes.

This manuscript is composed of six chapters. The first chapter presents succinctly the geological context of the Central Andes. The second chapter focuses on the methods I performed during this Ph-D work and used in the following three chapters. I address there the main aspects of thermochronological dating methods and more particularly the zircon and apatite fission-track dating techniques.

Chapters III to VI are designed as papers ready to be submitted. They present three aspects of the evolution of the present-day forearc of southern Peru I addressed during my Ph.-D. In chapter III, I firstly present in details the Mesozoic evolution of the present-day forearc and the novel geological map I propose for this region. This chapter later focuses on the Upper Cretaceous Paleogene evolution of the copper-rich Arequipa Belt. This region is interesting as it has been shown that after more than 200 Myr of lithospheric thinning, a magmatic flare-up occurred there between ~74 and ~62 Ma (Demouy et al., 2012) precisely

when the Central Andean margin switched to crustal thickening (Mamani et al., 2010). This chapter thus addresses the role of the different processes that were involved during the early Andean orogenic evolution.

Chapter IV assesses the Eocene history of deformation and exhumation in the forearc linked to the Bolivian Orocline formation. I focus on the coastal area of southern Peru where rigid block rotation is responsible for the present-day crescent-shape of the orogen are expected to have been the most important. Using thermochronology and studying deposits in the Eocene to early Miocene basin, I evidence Eo-Oligocene orogen-parallel extension in the southern Peruvian forearc.

Chapter V addresses the Neogene Andean crustal thickening history, still seen from the forearc side of the orogen. Dating geomorphic features and comparing the results with published data from the backarc reveals that the orogenic evolution is likely more complex than previously thought. Indeed, I show that crustal thickness was likely comparable to today's and that lower crustal flow may have redistributed crustal masses around ~10 Ma. Finally I present the main conclusions and perspectives of this work in chapter VI.

Chapter I – Geological context:

The Andes of southern Peru

I. 1 – Architecture of subduction zones

In the plate tectonic context, the strains provoked by plate subduction cause the biggest earthquakes, e.g. the Mw 9.5 Valdivia earthquake, which occurred in 1960 in Chile, is the most powerful earthquake ever recorded by mens. Subduction processes are also responsible for an intense magmatic activity, and they are also the sites where most of the present-day continental crust forms. Subduction is thus one of the major geological processes observed at the Earth's surface. I hereunder present the general architecture of a subduction zone to define the terms I will use latter in this manuscript.

Subduction zones present the same schematic architecture (Stern, 2002) (Fig. I.1): an oceanic plate (the "subducting plate" or "slab") sinks into the mantle under the «upper plate». At the border between the two plates it exists an oceanic "trench". 150 to 200 km away from this trench there is usually a volcanoes belt on the upper plate. This belt parallel to the trench is called the volcanic arc. The zone between the trench and the arc is named the « forearc » and is often affected by subsidence leading to the formation of a « forearc basin ». At the upper plate edge, sediments scraped off from the subducting plate and from erosion of the forearc potentially accumulate in an accretionary prism, the zone located on the other side of the arc is called « backarc » (Fig. I.1).

When the subducting plate sinks into the mantle, its temperature and pressure increase, these changes trigger the dehydration of the slab. This has for effect to hydrate the upper plate's mantle wedge whose melting point lowers, mantle material partially melts and mantle-derived magma is then able to spring and ascend in the upper plate to form the volcanic arc, parallel to the trench (Fig. I.1). The position of the volcanic arc is thus directly linked to the dip of the slab. When the slab is flat, the volcanic arc is located far away from the oceanic trench or even inexistent while it is close to the trench when the slap dip is important.

Therefore, in most cases, by adding magmatic material of mantellic origin to the crust, subduction processes trigger crustal thickening. However, collision of an exotic terrane, an island arc or of the accretionary prism with the upper plate can also trigger crustal thickening by thrusting. It has to be noted that subduction may also thin the crust, this process is called "tectonic erosion". It is believed to allow basal erosion of the forearc, tearing off crustal material in the subducting wedge (von Huene and Scholl, 1991). This process not only thins the continental crust, it also permits to recycle it driving it back to the mantle.

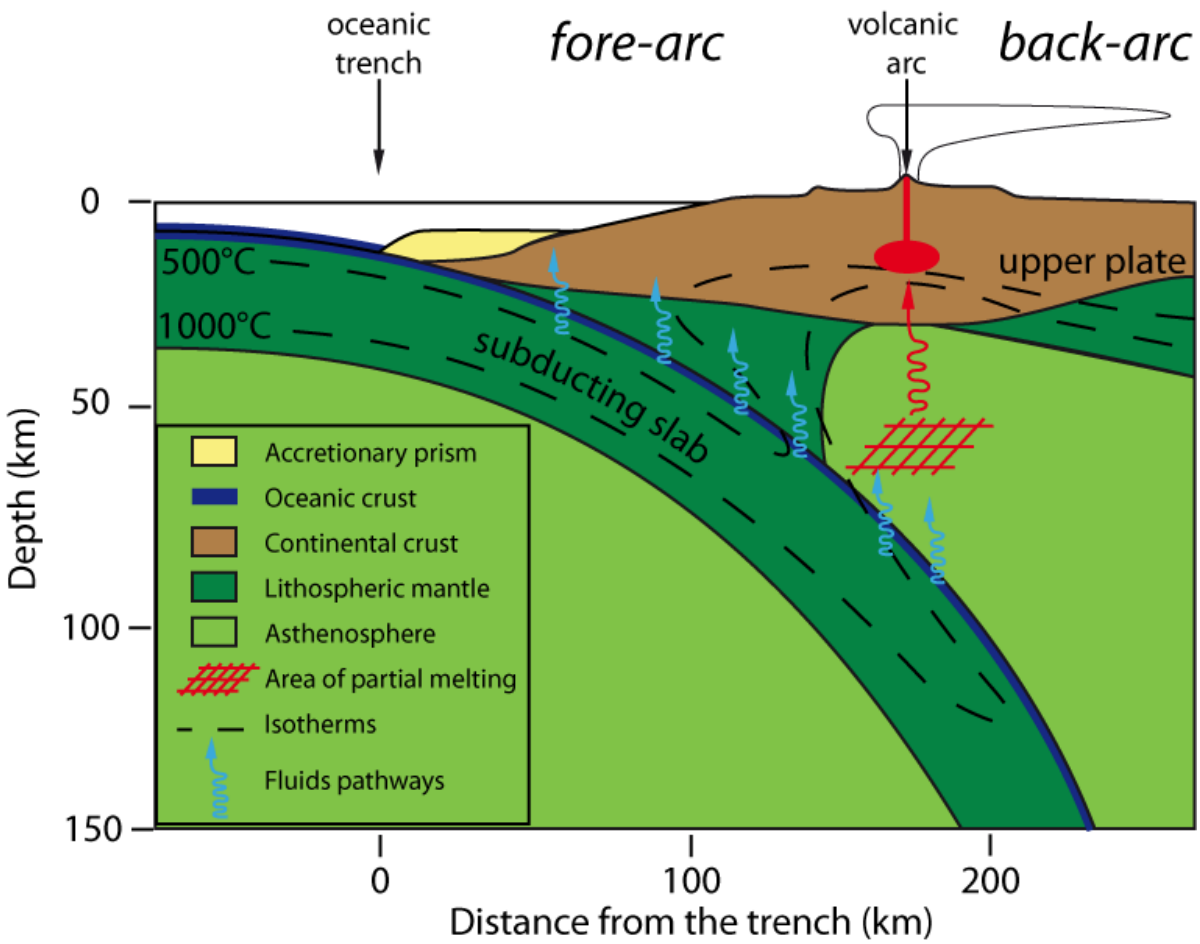

Figure I.1: Schematic architecture of a subduction zone, no vertical exaggeration

I. 2 – Basics of Andean geology

I. 2. A – The Andean Cordillera

The eastern Pacific subduction zone gave rise to the longest mountain belt in the world, the Andes. The "Andean Cordillera" strikes broadly N-S over ~8000 km, is submitted to different climates, has different inherited characteristics, and stands above different subduction settings (normal slab dip, flat-slab, or triple-junction); it is also the second largest place in the world where the crust is >60 km thick over a large area (Beck et al., 1996). For all these reasons the Andean Cordillera is an interesting geological object to study to investigate the causal links that may exist between these observations.

The Andean mountain range can be divided from north to south in three segments of distinct orientation: the Colombian-Ecuadorian segment, the Peruvian segment and the Chilean segment. Topographically, it can also be divided into three slightly different domains: the Northern, Central and Southern Andes (Fig. I.2). These domains correspond to different plate settings and hence building processes and present-day structure of the chain. In Fig. I.2, I present a model of plate boundaries as described by (Bird, 2003). This subdivision is mainly based on seismicity. However, areas of extreme structural complexity are not divided into different plates but instead are defined as "orogens" (Fig. I.2).

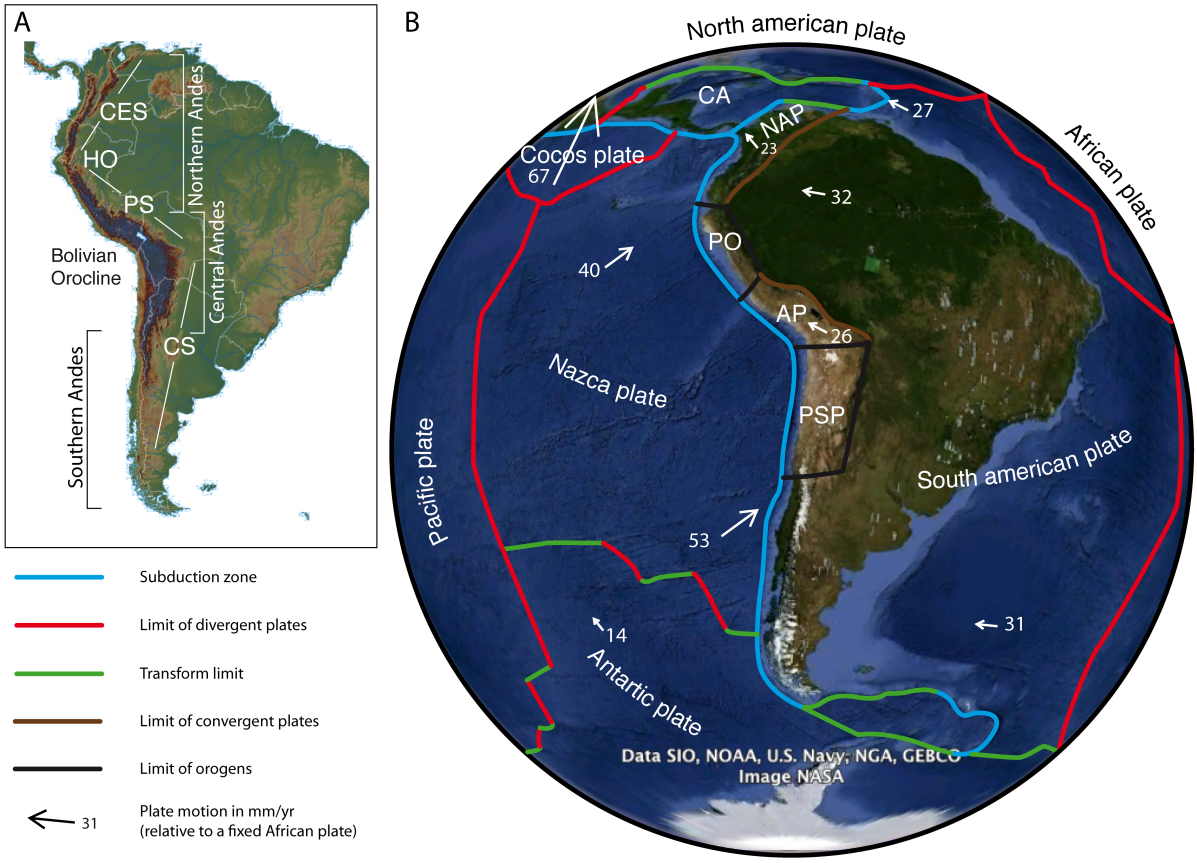

Figure I.2: The Andes in the South American context. A: elevation map of South America, the Andean Cordillera runs along the western border of the continent and is divided in three main segments: Colombian-Ecuadorian segment (CES), Peruvian segment (PS) and Chilean segment (CS) separated by the Huancabamba Orocline (HO) and the Bolivian Orocline. B: satellite view of South America (from Google Earth) and limits of lithospheric plates, color corresponding to the tectonic setting of these boundaries. CA: Central American plate; NAP: North Andean Plate; PO: Peru Orogen; AP: Altiplano Plate; PSP: Puna-Sierras Pampeanas orogen. Arrows show plate motion vectors relative to a fixed African Plate. (after Bird, 2003)

The Colombian-Ecuadorian segment (Fig. I.2), between 12°N and 3°S, trends NNE to SSW. It develops at the convergent boundary between North Andean and South America plates. According to Bird (2003), the motion of North Andean plate with respect to South America is 9 mm/yr toward N076°. The Peruvian segment between 3°S and 21°S follows a NW to SE trend. The Huancabamba Orocline separates it from the Colombian-Ecuadorian segment (Fig. I.2). The Peruvian segment is composed of the "Peru orogen" at north and of the Altiplano plate at south. The Peru orogen is located at the boundary between the Nazca and South American plates and coincides with a flat slab subduction zone. Together with the Colombian Ecuadorian segment, the Peru orogen forms the narrow Northern Andes. In turn, the Altiplano plate is sandwiched between the Nazca plate and the South American plate and is located above the eastern flank of the subducting Nazca ridge. This Altiplano block moves with respect to South America at 15 mm/yr toward N059°E (Fig. I.2).

The Chilean segment (Fig. I.2) stands between 21°S and 50°S, is oriented NS, and separated from the Peruvian segment by the Bolivian Orocline (Fig. I.2). It is composed of the "Puna–Sierras Pampeanas" orogen at north, which lies at the boundary between South America and Nazca plates. This orogen is also lying over a flat-slab subduction zone. Together with the Altiplano plate, the Puna–Sierras Pampeanas orogen forms the high and wide Central Andes. In turn, the southern part of the Chilean segment from 35°S to 55°S, where topography is much lower and where the mountain belt is narrow, is often called Southern Andes.

The Nazca plate is standing at west of the South American continent, and subducts under it. Motion of the Nazca plate with respect to South America plate reaches 80 mm/yr toward the east, south of the Puna–Pampean orogen and in front of the Bolivian Orocline and 69 mm/yr in front of the Huancabamba Orocline (Beck et al., 1996).

The Central Andes and the Southern Andes, in contrast with the Northern Andes, formed in a context of pure subduction. Indeed, no terrane accretion occurred since the initiation of the subduction in the Proterozoic (Loewy et al., 2004; Cawood, 2005). Central Andes are however the Andean part where the orogenic volume is the most important. There, the orogen is extremely wide (~800 km from the trench to the subandean thrusts in the backarc) and the crust reaches 70 km of thickness (Beck et al., 1996; Assumpção et al., 2013), sustaining the second high elevated plateau in the world: the Altiplano.

I. 2. B – The Central Andes

The Central Andes can be divided from east to west into four main domains: the Eastern Cordillera, the Altiplano, the Western Cordillera and the forearc (Fig. I.3) (Sébrier et al., 1988). The Eastern Cordillera is a typical fold and thrust belt, thus characterized by and important tectonic shortening. There, deformation began during the Late Oligocene (~30–~25 Ma), while the Bolivian Orocline began to develop. It resulted in the eastward Andean orogenic growth and formation of the present-day Eastern Cordillera fold and thrust belt (Sempere et al., 1990b; Uba et al., 2006).

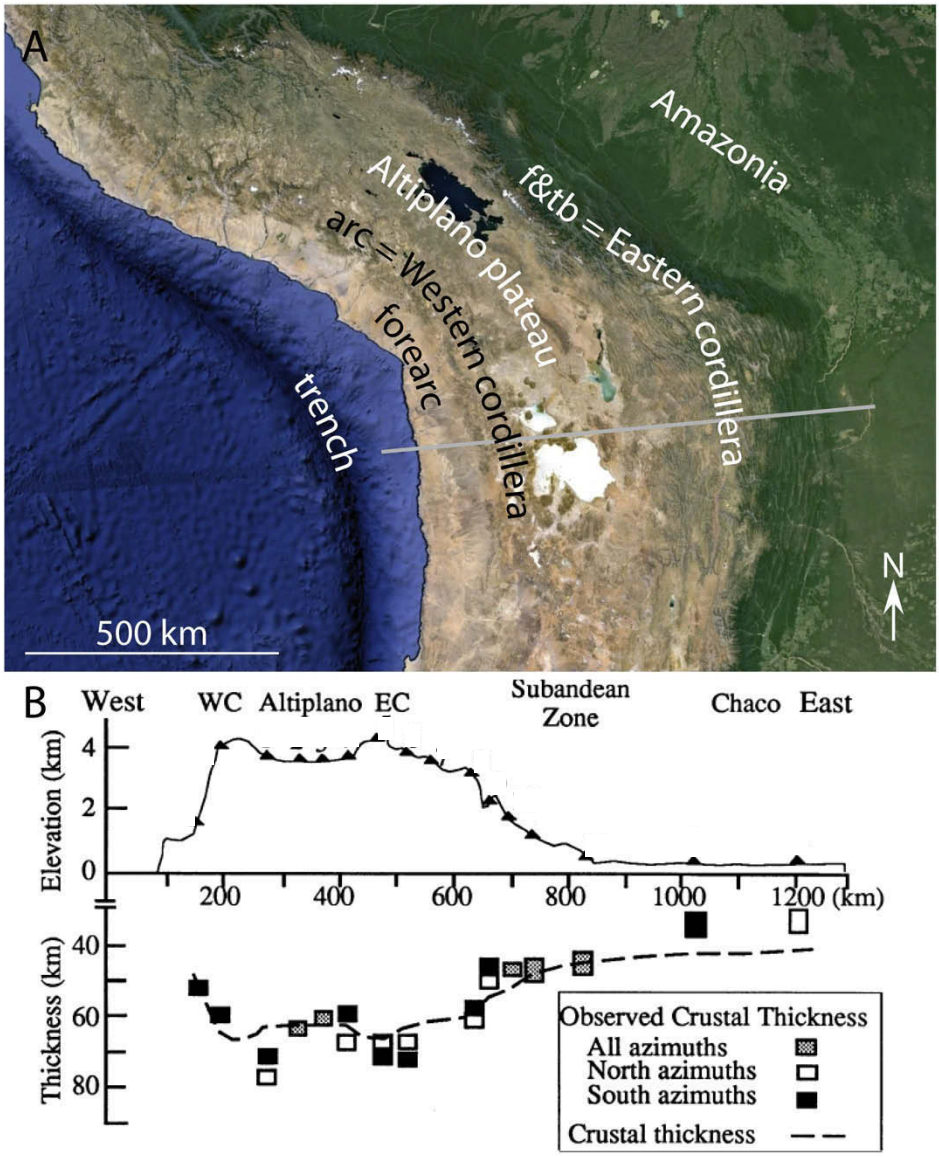

Figure I.3: The Central Andes. A: Landsat image and main geomorphic domains (f&tb = fold and thrust belt) after Sébrier et al., 1988. B: Cross section (along the grey line on A) showing topography (solid line) and observed (squares) and predicted (dotted line) crustal thickness based on the topography assuming an Airy-type behavior (after Beck, 1996).

West of the Eastern Cordillera stands the Altiplano, a high elevated plateau in average at 3800 m above sea level (Fig. I.3). In turn, the active volcanic arc, also called the Western Cordillera, forms the western border of the Altiplano endorrheic basin. The crust is very thick under the Western Cordillera, the Altiplano and the Eastern Cordillera. It reaches its greatest thickness under the active volcanic arc, on the western border of the orogen, whereas it is slightly thinner under the fold and thrust belt (Fig. I.3). An important topographic gradient affects the Pacific side of the Western Cordilera (the forearc), which is mainly devoid of compressional deformation (James, 1971; Kono et al., 1989; Beck et al., 1996); and crustal thickness rapidly thins toward the west under the forearc (Beck et al., 1996).

As stated above, no allochtonous terranes accreted on the margin since at least the Neoproterozoic (Cawood, 2005). However, the volcanic arc in the Central Andes developed since at least the Jurassic (Mamani et al., 2010; Demouy et al., 2012; Boekhout et al., 2012) and migration of the trench-forearc-arc-backarc system since ~200 Ma is recorded in the present-day forearc of southern Peru (Mamani et al., 2010) (Fig. I.4). The present-day forearc region is thus ideal to study an active continental margin over a long period of time.

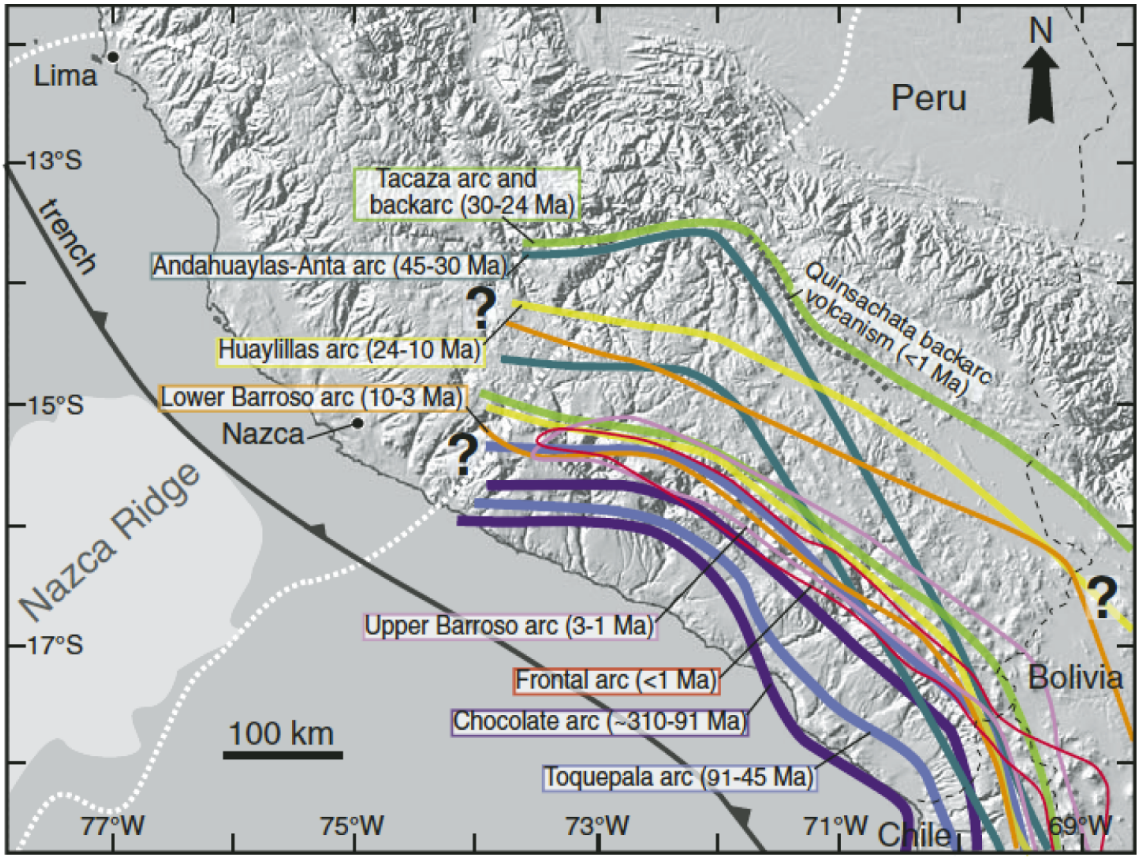

Fig. I.4: Location of the different magmatic arc and backarc areas in southern Peru since ~310 Ma (Mamani et al., 2010).

I. 3 – South Peruvian margin evolution

The forearc region of southern Peru can be divided in three areas, parallel to the trench from northeast to southwest: the coastal batholith (to which belongs the Arequipa belt) the Caravelí-Aplao Neogene basin and the Coastal belt (Fig. I.5). These different areas are reviewed in details in Chapters III to V but I present hereunder the overall evolution of the margin since the Paleozoic.

In Southern Peru, basement is composed of Proterozoic rocks that have a complex metamorphic history forming the "Arequipa Massif". In particular, between Camaná and Cocachacra a large metamorphic inlier of ~1.1 Ga ultra- high temperature granulites crops out (Martignole and Martelat, 2003; Loewy et al., 2004; Casquet et al., 2010). The Arequipa massif is however mainly composed of gneisses of Proterozoic age that are unconformably overlain in the San Juan area (Fig. I.5) by Neo-Proterozoic glaciogenic deposits (Chew et al., 2007; Chew and Kirkland, 2011).

According to different authors, the subduction as known as today emplaced on the western south American margin either at 650 Ma (Chew et al., 2008), ~570 Ma (Cawood, 2005) or >450 Ma (Collins, 2003). In southern Peru, the first plutons with a subduction-related geochemical signature intruded the Arequipa Massif during the Ordovician, between 473 and 440 Ma (Mukasa and Henry, 1990; Loewy et al., 2004; Mišković et al., 2009). From Late Permian to Middle Jurassic, southern Peru underwent rifting (Sempere et al., 2002). A marker of this intense extension can be observed in the Ocoña valley where a large detachment fault (the Ocoña detachment; Fig. I.5) separates gneisses of the Arequipa massif from Pensylvanian deposits (Fig. I.6) (Taipe, 2004).

During the ~215-90 Ma interval, a sinistral trantensional regime was prevailing in the Peruvian segment (Jaillard et al., 1990) and an important marine backarc basin developed. This type of basin has a typical sedimentary architecture: volcanic rocks are deposited on the arc-side slope of the basin and sedimentary facies evolve toward volcaniclastic sandstone, often of greenish color. Slumped deposits and shales fill the axis of the basin while well-sorted sandstones accumulate on the continental slope. Thus, sedimentary facies of backarc basin deposits permit to infer the position of the arc at the time of deposition and knowing the regional stratigraphy and age of the different plutons, it is possible to reconstruct the migration of the arc through time. I did this exercise for southern Peru using a literature

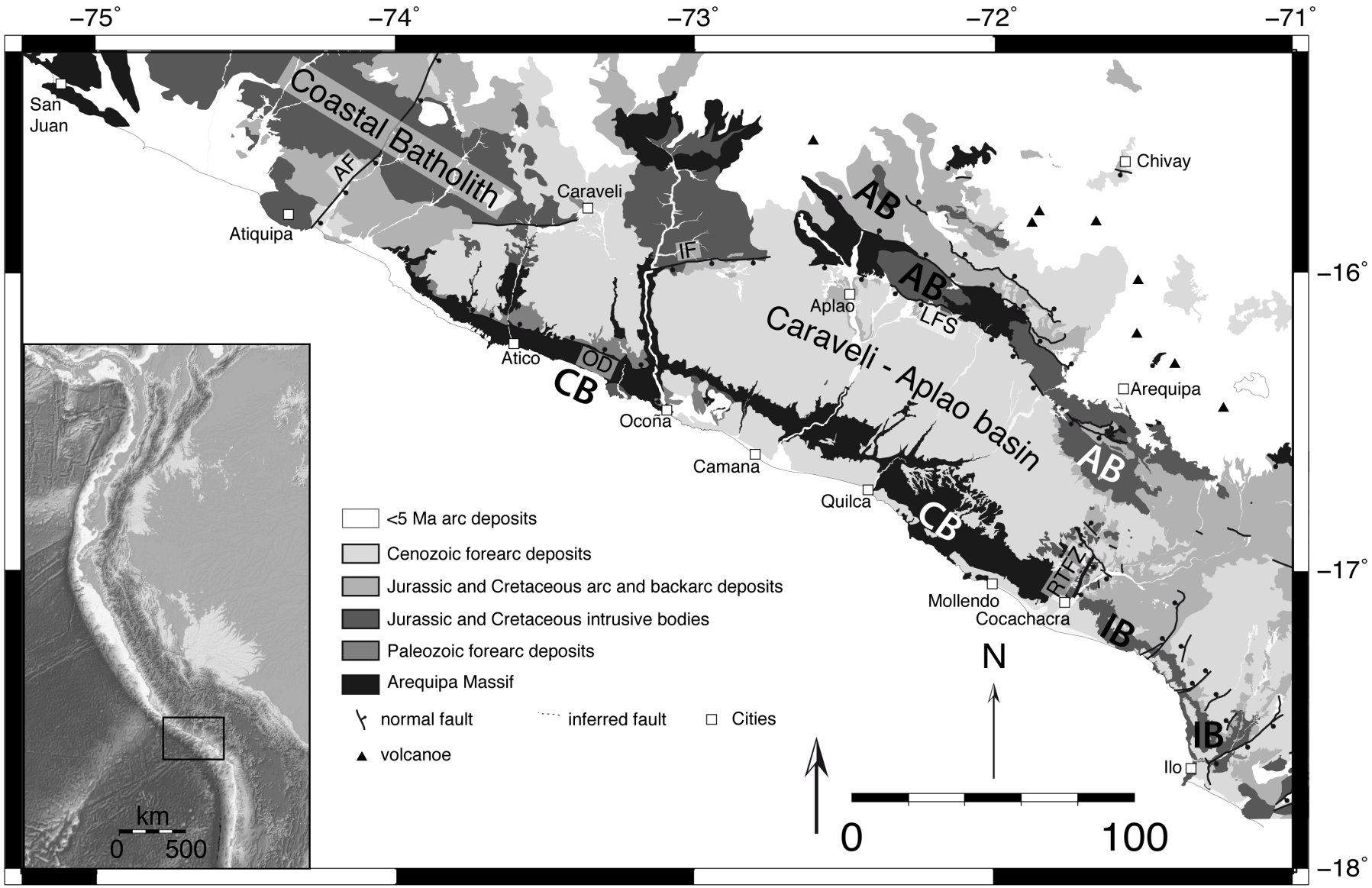

Figure I.5: Geological sketch map of the forearc of southern Peru, after INGEMMET and our own fieldwork, showing the different geological domains mentioned in the text. AB: Arequipa Belt; CB: Coastal Belt; IB: Ilo Batholith. AF: Atiquipa Fault; IF: Iquipi Fault; OD: Ocoña Detachment; RTFZ: Río Tambo Fault Zone.

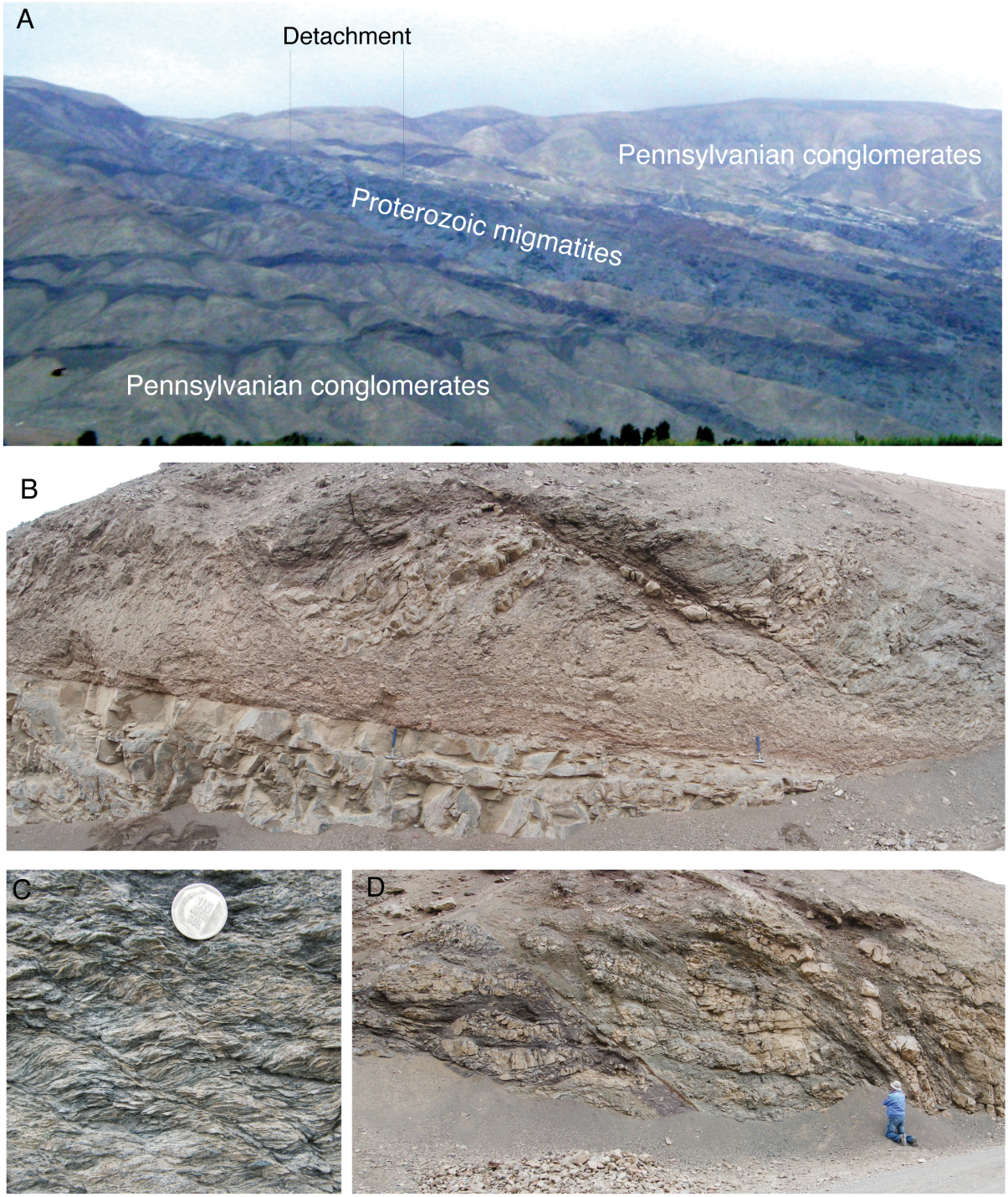

Figure I.6: Evidences of margin extension during the Paleozoic: the Ocoña detachment. A: The detachment fault creates a structural slab in the landscape, well expressed in the Ocoña valley. B: The Ocoña detachment fault zone (hammers for scale); C: C-S structures in the Proterozoic migmatites few meters under the detachment fault; D: Extensional deformation in the Pennsylvanian deposits.

compilation; results are shown in Fig. I.7 and in the following paragraphs

In southern Peru, the Jurassic to mid-Cretaceous backarc basin deposits (Fig. I.5) form the Chocolate and Yura Formations (Vicente, 1981). According to a recent geochronological study by Demouy et al. (2012), at 200 Ma, magmatic activity was located in the Arequipa area, it then migrated to the southwest (Fig. I.7) to build the Ilo batholith (Fig. I.4) in the coastal area between 175 and 152 Ma (Boekhout et al., 2012). In the Arequipa belt, the backarc basin deposits recorded this migration of the arc as sediments evolved gradually from lavas to volcaniclastic sandstones, shales and latter to sandstones deposited on the Amazonian slope of the back-arc basin (Fig. I.7).

At ~130 Ma, the arc was located in the present-day offshore but, the arc started to migrate back toward the continent (Fig. I.7). Between 110 and 106 Ma, the magmatic arc was back on the present-day coast and few plutons emplaced in the Ilo batholith (Boekhout et al., 2012). It is important to note that an important marine transgression affected the backarc basin at this time and that a carbonate platform formed in the backarc basin (Fig. I.7).

At ~90 Ma, the arc is back in the Arequipa belt (Fig. I.7) (Demouy et al., 2012) and the carbonate platform collapses in a giant mass wasting (Callot et al., 2008). The backarc basin experienced then a rapid fall of the base level, and sediments deposited in the backarc turned continental. These sediments were derived from the southwest, where the volcanic arc was located (Jaillard, 1994). The arc stayed in the Arequipa belt until ~60 Ma (Fig. I.7) (Demouy et al., 2012), during this period important volumes of magmas emplaced as well as important porphyry-copper deposits (Mukasa, 1986; Demouy et al., 2012; Quang et al., 2003).

At ~45 Ma, the arc is located in the present-day Altiplano (Fig. I.4) (emplacement of the Yauri batholith) and continental forearc deposits accumulated in the Caravelí-Aplao basin (Fig. I.5 and I.7). Around 30 Ma, first thrusts developed in the Eastern Cordillera (Sempere et al., 1990b; Uba et al., 2006), the Bolivian Orocline formed (Roperch et al., 2006) and the arc started to migrate back toward the southwest and its present-day location (Fig. I.4 and I.7) (Mamani et al., 2010). It has to be noted that there is no evidence of important upper-crustal tectonic shortening in the present-day forearc of southern Peru that, on the contrary, exhibits normal faulting (James, 1971; Sébrier et al., 1985, 1988; Sempere et al., 2008).

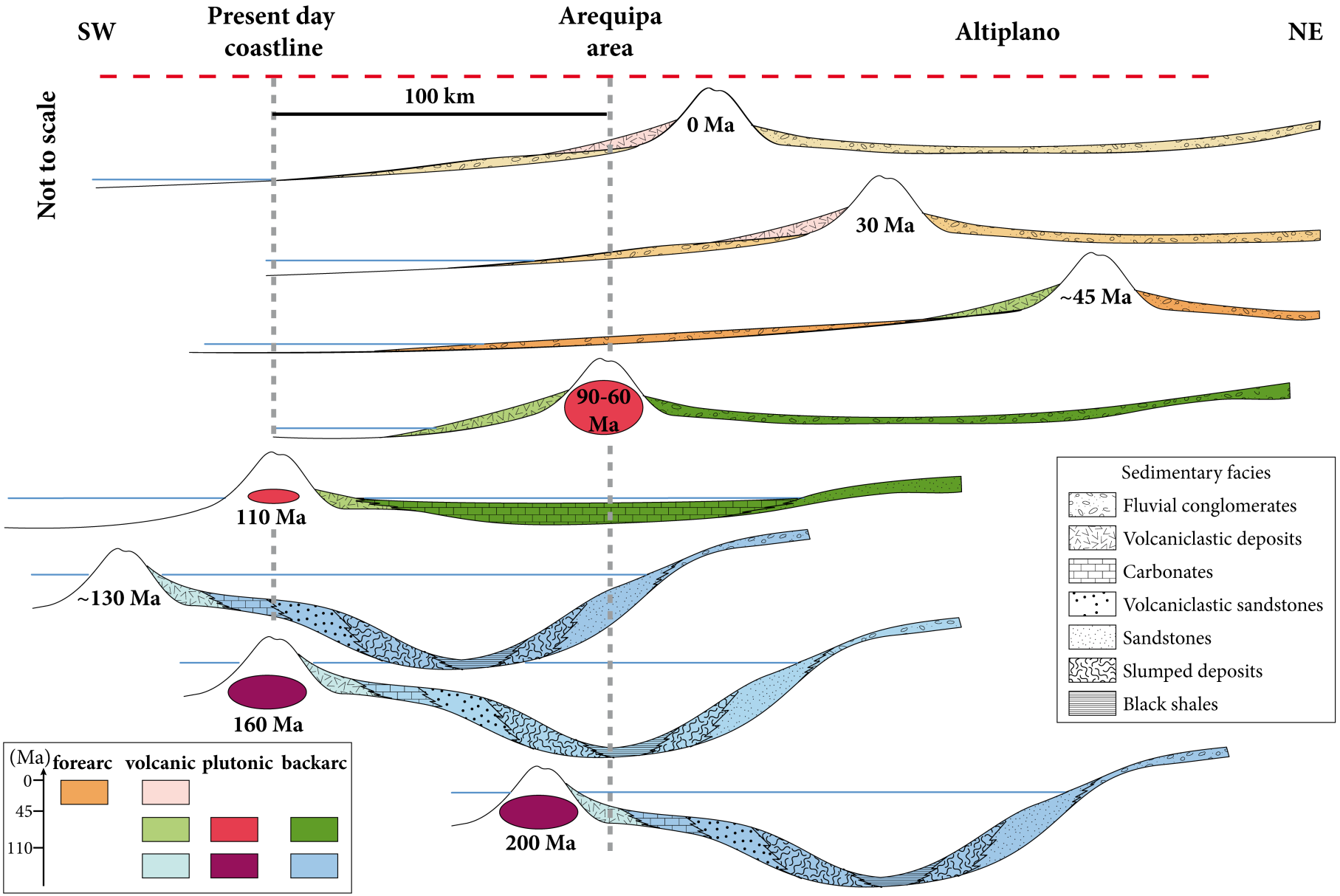

Fig. I.7: Schematic cross-sections of NE-SW orientation across the present-day forearc (see location of present-day coastline and Arequipa area) showing the lateral migration of the forearc–arc–backarc system and associated sedimentary facies through time after a literature compilation.

An important change thus occurred during the Middle Cretaceous when a carbonate platform developed in the backarc basin before to massively collapse at ~90 Ma (Callot et al., 2008). Just after this event, the backarc basin turned continental and sediments that were previously derived from the NE started to come from the southwestern border of the basin, where the volcanic arc was located. However, why the arc suddenly formed a relief at ~90 Ma is unclear. In addition, balanced structural cross-sections at the orogenic scale only explain 70 to 80% of the crustal thickening under the Altiplano plateau by the tectonic shortening observed in the Eastern Cordillera and the origin of a large amount of crustal mass (20 to 30 %) remains unknown (Allmendinger et al., 1997). Thus, processes leading to the anomalous crustal thickness in the Central Andes (Beck et al., 1996; Assumpção et al., 2013; van der Meijde et al., 2013) and in particular in its western area that does not exhibit upper crustal shortening (Sempere et al., 2008) remain enigmatic. Moreover, the subduction is usually held responsible for crustal thickening; it was, however, established for hundreds of million years (Mukasa and Henry, 1990; Collins, 2003; Loewy et al., 2004; Cawood, 2005; Chew et al., 2008; Casquet et al., 2010), whereas high topography (and thus anomalous crustal thickness) exists for less than 30 Ma (Sempere et al., 1990b; Garzione et al., 2008). It thus seems that crustal thickening and the related formation of topography (or surface uplift) are not related to the whole history of subduction but only to its recent past. The question then arises as which processes permit to thicken the crust in an ocean-continent subduction context.

One option to get new insights on this question is to compare the chronologies of different phenomena resulting from different processes. For example it is possible to compare magmatic phenomena as increased production of magma (linked to subduction), sedimentary records (linked to erosion and thus to formation of topography) and exhumation of deeper rocks as basement (linked to tectonics, erosion and formation of topography). In this study, I focus on the present-day forearc of southern Peru because it permits to study the margin evolution over a long period of time, and thus to characterize important turning points in the margin history. Moreover, it seems that inception of the Bolivian Orocline formation is associated with the beginning of the deformation in the Eastern Cordillera (Roperch et al., 2006; Arriagada et al., 2008) and because the forearc experienced the most important block rotations, it is prone to give insights on the beginning of the deformation. Finally, because the Pacific Ocean base level is close, forearc of the Central Andes is likely to have recorded surface uplift associated with crustal thickening. Together with a detailed knowledge of the regional

geology, I use in this study zircon U-Pb dating as well as thermochronology (apatite and zircon fission-track dating) to provide new insights on the Central Andes evolution.

References

Allmendinger, R.W., Jordan, T.E., Kay, S.M., and Isacks, B.L., 1997, The Evolution of the Altiplano-Puna Plateau of the Central Andes: Annual Review of Earth and Planetary Sciences, v. 25, p. 139–174, doi: 10.1146/annurev.earth.25.1.139.

Amstutz, A., 1951, Sur l'évolution des structures alpines: Archives Sci., v. 4, p. 323–329.

Arriagada, C., Roperch, P., Mpodozis, C., and Cobbold, P.R., 2008, Paleogene building of the Bolivian Orocline: Tectonic restoration of the central Andes in 2-D map view: Tectonics, v. 27, p. TC6014, doi: 10.1029/2008TC002269.

Assumpção, M., Feng, M., Tassara, A., and Julià, J., 2013, Models of crustal thickness for South America from seismic refraction, receiver functions and surface wave tomography: Tectonophysics, v. 609, p. 82–96, doi: 10.1016/j.tecto.2012.11.014.

Barnes, J.B., and Ehlers, T.A., 2009, End member models for Andean Plateau uplift: Earth-Science Reviews, v. 97, p. 105–132, doi: 10.1016/j.earscirev.2009.08.003.

Beck, S.L., Zandt, G., Myers, S.C., Wallace, T.C., Silver, P.G., and Drake, L., 1996, Crustal-thickness variations in the central Andes: Geology, v. 24, p. 407–410.

Bird, P., 2003, An updated digital model of plate boundaries: Geochem. Geophys. Geosyst., v. 4, doi: 10.1029/2001GC000252.

Boekhout, F., Spikings, R., Sempere, T., Chiaradia, M., Ulianov, A., and Schaltegger, U., 2012, Mesozoic arc magmatism along the southern Peruvian margin during Gondwana breakup and dispersal: Lithos, v. 146–147, p. 48–64, doi: 10.1016/j.lithos.2012.04.015.

Callot, P., Sempere, T., Odonne, F., and Robert, E., 2008, Giant submarine collapse of a carbonate platform at the Turonian–Coniacian transition: The Ayabacas Formation, southern Peru: Basin Research, v. 20, p. 333–357, doi: 10.1111/j.1365-2117.2008.00358.x.

Casquet, C., Fanning, C.M., Galindo Francisco, M. del C., Pankhurst, R.J., Rapela, C.W., and Torres, P., 2010, The Arequipa Massif of Peru: New SHRIMP and isotope constraints on a Paleoproterozoic inlier in the Grenvillian orogen: Journal of South American earth sciences, v. 29, p. 128–142.

Cawood, P.A., 2005, Terra Australis Orogen: Rodinia breakup and development of the Pacific and Iapetus margins of Gondwana during the Neoproterozoic and Paleozoic: Earth-Science Reviews, v. 69, p. 249–279, doi: 10.1016/j.earscirev.2004.09.001.

Charrier, R., Hérail, G., Pinto, L., García, M., Riquelme, R., Farías, M., and Muñoz, N., 2013, Cenozoic tectonic evolution in the Central Andes in northern Chile and west central Bolivia: implications for paleogeographic, magmatic and mountain building evolution: International Journal of Earth Sciences, v. 102, p. 235–264, doi: 10.1007/s00531-012-0801-4.

Chew, D., and Kirkland, C., 2011, The Chiquerío Formation, southern Peru: The Geological Record of Neoproterozoic Glaciations, p. 481–486.

Chew, D., Kirkland, C., Schaltegger, U., and Goodhue, R., 2007, Neoproterozoic glaciation in the Proto-Andes: Tectonic implications and global correlation: Geology, v. 35, p. 1095–1098, doi: 10.1130/G23768A.1.

Chew, D.M., Magna, T., Kirkland, C.L., Mi□kovi□, A., Cardona, A., Spikings, R., and Schaltegger, U., 2008, Detrital zircon fingerprint of the Proto-Andes: Evidence for a Neoproterozoic active margin? Precambrian Research, v. 167, p. 186–200, doi: 10.1016/j.precamres.2008.08.002.

Chulick, G.S., Detweiler, S., and Mooney, W.D., 2013, Seismic structure of the crust and uppermost mantle of South America and surrounding oceanic basins: Journal of South American Earth Sciences, v. 42, p. 260–276, doi: 10.1016/j.jsames.2012.06.002.

Collins, W.J., 2003, Slab pull, mantle convection, and Pangaean assembly and dispersal: Earth and Planetary Science Letters, v. 205, p. 225–237, doi: 10.1016/S0012-821X(02)01043-9.

Conrad, C.P., and Lithgow-Bertelloni, C., 2002, How Mantle Slabs Drive Plate Tectonics: Science, v. 298, p. 207–209, doi: 10.1126/science.1074161.

Demouy, S., Paquette, J.-L., de Saint Blanquat, M., Benoit, M., Belousova, E.A., O'Reilly, S.Y., García, F., Tejada, L.C., Gallegos, R., and Sempere, T., 2012, Spatial and temporal evolution of Liassic to Paleocene arc activity in southern Peru unraveled by zircon U–Pb and Hf in-situ data on plutonic rocks: Lithos, v. 155, p. 183–200, doi: 10.1016/j.lithos.2012.09.001.

Garzione, C.N., Hoke, G.D., Libarkin, J.C., Withers, S., MacFadden, B., Eiler, J., Ghosh, P., and Mulch, A., 2008, Rise of the Andes: Science, v. 320, p. 1304–1307, doi: 10.1126/science.1148615.

Haschke, M., Günther, A., Melnick, D., Echtler, H., Reutter, K.-J., Scheuber, E., and Oncken, O., 2006, Central and Southern Andean Tectonic Evolution Inferred from Arc Magmatism, *in* Oncken, O., Chong, G., Franz, G., Giese, P., Götze, H.-J., Ramos, V.A., Strecker, M.R., and Wigger, P. eds., The Andes, Frontiers in Earth Sciences, Springer Berlin Heidelberg, p. 337–353.

Horton, B.K., 2005, Revised deformation history of the central Andes: Inferences from Cenozoic foredeep and intermontane basins of the Eastern Cordillera, Bolivia: Tectonics, v. 24, p. TC3011, doi: 10.1029/2003TC001619.

Von Huene, R., and Scholl, D.W., 1991, Observations at convergent margins concerning sediment subduction, subduction erosion, and the growth of continental crust: Reviews of Geophysics, v. 29, p. 279–316, doi: 10.1029/91RG00969.

Isacks, B.L., 1988, Uplift of the Central Andean Plateau and Bending of the Bolivian Orocline: J. Geophys. Res., v. 93, p. 3211–3231, doi: 10.1029/JB093iB04p03211.

Jaillard, E., 1994, Kimmeridgian to Paleocene tectonic and geodynamic evolution of the Peruvian (and Ecuadorian) margin, *in* Cretaceous tectonics of the Andes, Earth Evolution Sciences, Braunschweig, Vieweg, p. 101–167.

Jaillard, E., Soler, P., Carlier, G., and Mourier, T., 1990, Geodynamic evolution of the northern and central Andes during early to middle Mesozoic times: a Tethyan model: Journal of the Geological Society, v. 147, p. 1009–1022, doi: 10.1144/gsjgs.147.6.1009.

James, D.E., 1971, Andean crustal and upper mantle structure: Journal of Geophysical Research, v. 76, p. 3246–3271, doi: 10.1029/JB076i014p03246.

James, D.E., and Sacks, I.S., 1999, Cenozoic formation of the Central Andes; a geophysical perspective, *in* Geology and ore deposits of the Central Andes, Special Publication, Skinner B. J., p. 1–25.

Kay, S.M., Godoy, E., and Kurtz, A., 2005, Episodic arc migration, crustal thickening, subduction erosion, and magmatism in the south-central Andes: Geological Society of America Bulletin, v. 117, p. 67–88, doi: 10.1130/B25431.1.

Kono, M., Fukao, Y., and Yamamoto, A., 1989, Mountain building in the central Andes: Journal of Geophysical Research: Solid Earth, v. 94, p. 3891–3905, doi: 10.1029/JB094iB04p03891.

Loewy, S.L., Connelly, J.N., and Dalziel, I.W.D., 2004, An orphaned basement block: The Arequipa-Antofalla Basement of the central Andean margin of South America: Geological Society of America Bulletin, v. 116, p. 171–187, doi: 10.1130/B25226.1.

Mamani, M., Wörner, G., and Sempere, T., 2010, Geochemical variations in igneous rocks of the Central Andean orocline (13°S to 18°S): Tracing crustal thickening and magma generation through time and space: Geological Society of America Bulletin, v. 122, p. 162–182.

Martignole, J., and Martelat, J.-E., 2003, Regional-scale Grenvillian-age UHT metamorphism in the Mollendo–Camana block (basement of the Peruvian Andes): Journal of Metamorphic Geology, v. 21, p. 99–120, doi: 10.1046/j.1525-1314.2003.00417.x.

Martinod, J., Husson, L., Roperch, P., Guillaume, B., and Espurt, N., 2010, Horizontal subduction zones, convergence velocity and the building of the Andes: Earth and Planetary Science Letters, v. 299, p. 299–309, doi: 10.1016/j.epsl.2010.09.010.

Mégard, F., 1984, The Andean orogenic period and its major structures in central and northern Peru: Journal of the Geological Society, v. 141, p. 893–900.

Van der Meijde, M., Julià, J., and Assumpção, M., 2013, Gravity derived Moho for South America: Tectonophysics, v. 609, p. 456–467, doi: 10.1016/j.tecto.2013.03.023.

Mi□kovi□, A., Spikings, R.A., Chew, D.M., Ko□er, J., Ulianov, A., and Schaltegger, U., 2009, Tectonomagmatic evolution of Western Amazonia: Geochemical characterization and zircon U-Pb geochronologic constraints from the Peruvian Eastern Cordilleran granitoids: Geological Society of America Bulletin, v. 121, p. 1298–1324, doi: 10.1130/B26488.1.

Mukasa, S.B., 1986, Zircon U-Pb ages of super-units in the Coastal batholith, Peru: Implications for magmatic and tectonic processes: Geological Society of America Bulletin, v. 97, p. 241–254.

Mukasa, S.B., and Henry, D.J., 1990, The San Nicolás batholith of coastal Peru: early Palaeozoic continental arc or continental rift magmatism? Journal of the Geological Society, v. 147, p. 27–39, doi: 10.1144/gsjgs.147.1.0027.

Myers, J.S., 1975, Vertical crustal movements of the Andes in Peru: Nature, v. 254, p. 672–674, doi: 10.1038/254672a0.

Oncken, O., Hindle, D., Kley, J., Elger, K., Victor, P., and Schemmann, K., 2006, Deformation of the Central Andean Upper Plate System — Facts, Fiction, and Constraints for Plateau Models, *in* Oncken, O., Chong, G., Franz, G., Giese, P., Götze, H.-J., Ramos, V.A., Strecker, M.R., and Wigger, P. eds., The Andes, Frontiers in Earth Sciences, Springer Berlin Heidelberg, p. 3–27.

Quang, C.X., Clark, A.H., Lee, J.K.W., and B, J.G., 2003, 40Ar-39Ar ages of hypogene and supergene mineralization in the Cerro Verde-Santa Rosa porphyry Cu-Mo cluster, Arequipa, Peru: Economic Geology, v. 98, p. 1683–1696.

Roperch, P., Sempere, T., Macedo, O., Arriagada, C., Fornari, M., Tapia, C., García, M., and Laj, C., 2006, Counterclockwise rotation of late Eocene–Oligocene fore-arc deposits in southern Peru and its significance for oroclinal bending in the central Andes: Tectonics, v. 25, p. TC3010, doi: 10.1029/2005TC001882.

Sébrier, M., Lavenu, A., Fornari, M., and Soulas, J.-P., 1988, Tectonics and uplift in Central Andes (Peru, Bolivia and Northern Chile) from Eocene to present: Géodynamique,.

Sébrier, M., Mercier, J.-L., Mégard, F., Laubacher, G., and Carey-Gailhardis, E., 1985, Quaternary normal and reverse faulting and the state of stress in the central Andes of south Peru: Tectonics, v. 4, p. 739–780, doi: 10.1029/TC004i007p00739.

Sempere, T., Carlier, G., Soler, P., Fornari, M., Carlotto, V., Jacay, J., Arispe, O., Néraudeau, D., Cárdenas, J., Rosas, S., and Jiménez, N., 2002, Late Permian–Middle Jurassic lithospheric thinning in Peru and Bolivia, and its bearing on Andean-age tectonics: Tectonophysics, v. 345, p. 153–181, doi: 10.1016/S0040-1951(01)00211-6.

Sempere, T., Folguera, A., and Gerbault, M., 2008, New insights into Andean evolution : an introduction to contributions from the 6th ISAG symposium (Barcelona, 2005): Tectonophysics, v. 459, p. 1–13, doi: 10.1016/j.tecto.2008.03.011.

Sempere, T., Hérail, G., Oller, J., and Bonhomme, M.G., 1990a, Late Oligocene-early Miocene major tectonic crisis and related basins in Bolivia: Geology, v. 18, p. 946–949, doi: 10.1130/0091-7613(1990)018<0946:LOEMMT>2.3.CO;2.

Sempere, T., Hérail, G., Oller, J., and Bonhomme, M.G., 1990b, Late Oligocene-earlyMiocene major tectonic crisis and related basins in Bolivia: Geology, v. 18, p. 946–949.

Soler, P., and Bonhomme, M.G., 1990, Relation of magmatic activity to plate dynamics in central Peru from Late Cretaceous to present: Geological Society of America Special Papers, v. 241, p. 173–192, doi: 10.1130/SPE241-p173.

Stern, R.J., 2002, Subduction Zones: Reviews of Geophysics, v. 40, p. 1012, doi: 10.1029/2001RG000108.

Taipe, E., 2004, Détachement en extension et sedimentation : Les bassins Pennsylvaniens d'Atico et Ocoña (Sud Pérou) (Mémoire de DEA) : Université Paul Sabatier, 38 p.

Tosdal, R.M., Clark, A.H., and Farrar, E., 1984, Cenozoic polyphase landscape and tectonic evolution of the Cordillera Occidental, southernmost Peru: Geological Society of America Bulletin, v. 95, p. 1318–1332.

Trumbull, R.B., Riller, U., Oncken, O., Scheuber, E., Munier, K., and Hongn, F., 2006, The Time-Space Distribution of Cenozoic Volcanism in the South-Central Andes: a New Data Compilation and Some Tectonic Implications, *in* Oncken, O., Chong, G., Franz, G., Giese, P., Götze, H.-J., Ramos, V.A., Strecker, M.R., and Wigger, P. eds., The Andes, Frontiers in Earth Sciences, Springer Berlin Heidelberg, p. 29–43.

Uba, C.E., Heubeck, C., and Hulka, C., 2006, Evolution of the late Cenozoic Chaco foreland basin, Southern Bolivia: Basin Research, v. 18, p. 145–170, doi: 10.1111/j.1365-2117.2006.00291.x.

Vicente, J.-C., 1981, Elementos de la estratigrafía mesozoica sur-peruana, *in* Cuencas sedimentarias del Jurásico y Cretácico de América del Sur, Buenos Aires, Volkheimer, W., Musacchio, E. A., p. 319–351.

White, D.A., Roeder, D.H., Nelson, T.H., and Crowell, J.C., 1970, Subduction: Geological Society of America Bulletin, v. 81, p. 3431–3432, doi: 10.1130/0016-7606(1970)81[3431:S]2.0.CO;2.

Wörner, G., Hammerschmidt, K., Henjes-Kunst, F., Lezaun, J., and Wilke, H., 2000, Geochronology (40Ar/39Ar, K-Ar and He-exposure ages) of Cenozoic magmatic rocks from Northern Chile (18-22°S): implications for magmatism and tectonic evolution of the central Andes: Revista geológica de Chile, v. 27, p. 205–240, doi: 10.4067/S0716-02082000000200004.

Chapter II – Methods

During my PhD, I performed apatite and zircon fission-track dating, as well as zircon U-Pb dating for analysis of different samples of crystalline, volcanic and sedimentary rocks. I hereunder describe briefly the methods and the underlying concepts for interpreting the results.

Note that I also discuss data provided by co-authors and obtained by other methods such as $^{40}Ar/^{39}Ar$ on micas and zircon (U-Th)/He analyses. Methods for collection of these data are presented in Appendices A and B respectively.

II. 1 – Introduction to geo-thermochronology

II. 1. A – Definition

Geo-thermochronology is a technique that uses the radioactive decay of for example ^{238}U and ^{235}U or the spontaneous fission of ^{238}U for obtaining apparent cooling ages. These dating methods are all based on a radioactive decay law that links the time *t* since the system closed to the amount of parent and daughter atoms (respectively N_p and N_d) through the following equation:

$$N_d = N_p\left(e^{\lambda t} - 1\right)$$

Which can be transformed in:

$$t = \frac{1}{\lambda}\ln\left[\frac{N_d}{N_p} + 1\right]$$

For the U-Pb, $^{40}Ar/^{39}Ar$ and (U-Th)/He methods this means that knowing the radioactive decay constant λ of the system used and the number of parent and daughter isotopes (N_p and N_d) remaining inside the mineralogical system, one is able to estimate the time *t* since when the analyzed mineral cooled under given temperature.

In case of the fission-track methods, for one million ^{238}U atoms that will decay by alpha decay (and several beta decay steps) to ^{206}Pb, one ^{238}U atom will decay by spontaneous fission, following the fission-decay constant of about $\approx 9\times10^{15}$ y^{-1}. By determining the track density and the U concentration on a given internal grain surface, an apparent cooling age can be determined, because the preservation of latent tracks in the crystal is mainly dependent on temperature, as discussed below.

II. 1. B – Principle concepts: closure temperature and the partial annealing/retention zone

a – The closure temperature concept.

The closure temperature (T_c) concept, as developed by Dodson (1973) is based on diffusion of daughter isotopes out of a crystal (in case of the (U-Th)/He and the $^{40}Ar/^{39}Ar$ dating systems) or the annealing of fission tracks in apatite or zircon. This concept states that at a given temperature, the closure temperature, the system changes from an open to a closed system. This means, at ambient temperatures higher than the closure temperature daughter isotopes quickly defuse out of the crystal, or latent fission-tracks are rapidly fully annealed and not retained or preserved in the crystal. On the contrary, at ambient temperatures lower than the closure temperature, the daughter isotopes or latent fission-tracks are retained inside the crystal, and the system is considered as "closed" (Fig. II.1).

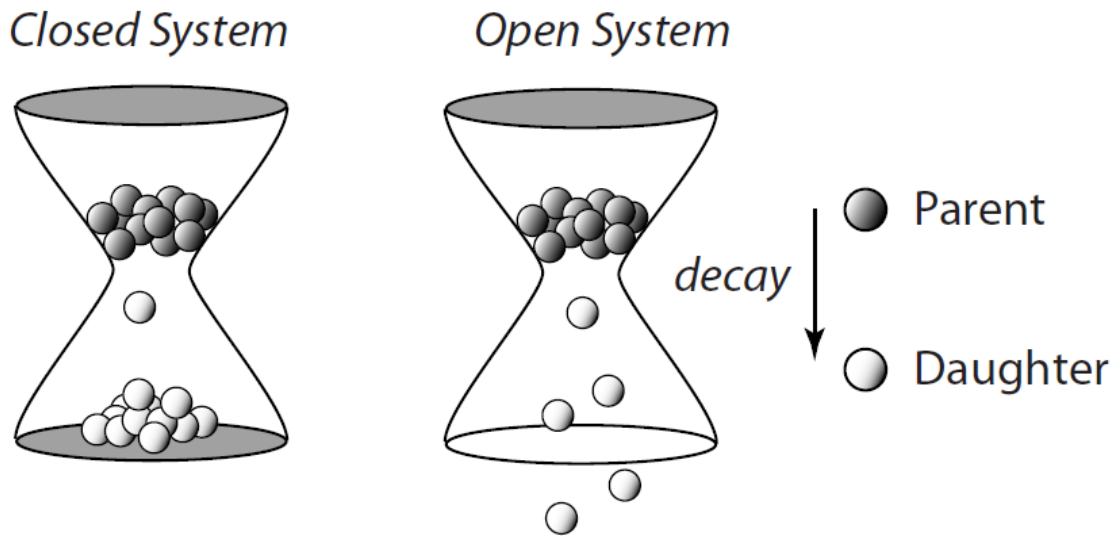

Figure II.1: Schematic illustration of a closed or open system with respect to the retention of radiogenic daughter products (Braun et al., 2006)

The T_c is different for each dating system and depends primarily on the cooling rate (Fig. II.2). The faster the cooling rate, the higher is the closure temperature of the system and vice versa. However, the T_c also depends on the chemical composition of the crystal, grain size (^{40}Ar-^{39}Ar, (U-Th)/He), and the amount of accumulated radiation damage (Green and Duddy,

1989; Corrigan, 1993; Braun et al., 2006).

The T_c concept has to be regarded as a simplifying concept that works well for minerals that experienced relatively fast monotonic cooling (>10°C/Myr). In this case the T_c for the apatite and zircon fission-track systems are about 120 °C and 240°C respectively. However, very slow cooling (<2°C/Myr) or re-heating because of volcanic activity, intrusions, circulation of hot fluids and/or burial) may cause partial retention (for $^{40}Ar/^{39}Ar$, (U-Th)/He systems) or annealing (for apatite and zircon fission-track systems).

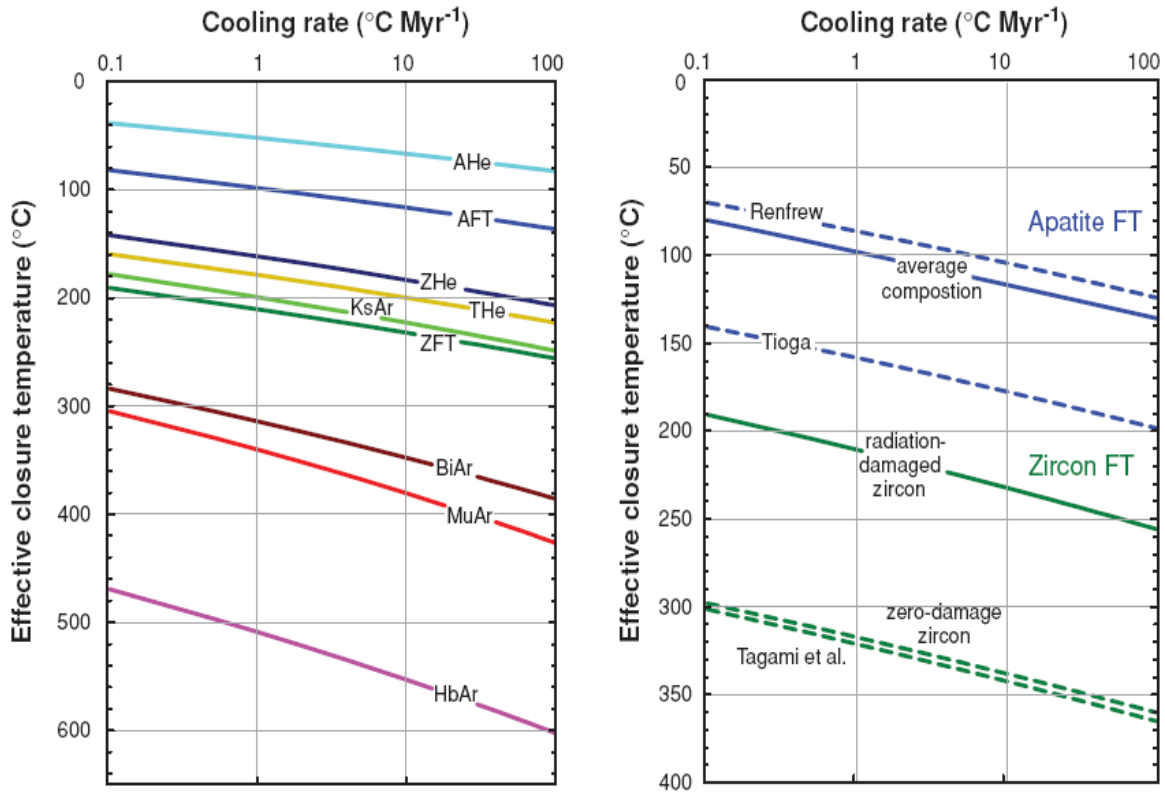

Figure II.2: Closure temperatures depending on cooling rates for different thermo-chronological systems (Reiners and Brandon, 2006). A: apatite; Z: zircon; T: titanite; Bi: biotite; Mu: muscovite; Hb: Hornblend; He: (U-Th)/He method; FISSION-TRACK: fission-track method; Ar: 40Ar-39Ar method. For example Ahe stand for "apatite (U-Th)/He method". Renfrew and Tioga are two types of apatites with different compositions, respectively nearly end-member fluoroapatite and fluor/hydroxylapatite considered to be the least and most retentive of the common naturally occurring in apatite (Carlson et al., 1999). The line labeled "Tagami et al." was obtained for natural zircons from a 21-Ma dacite tuff (Tagami et al., 1998).

b – Partial annealing and retention zone concepts

The partial annealing zone (PAZ) (Wagner, 1979) or partial retention zone (PRZ) (Wolf et al., 1996) concepts are based on the fact that annealing of fission-tracks or retention of He or ^{40}Ar is only partial over a given temperature range, depending on the dating system (Fig. II.3). The upper and lower limits of the PAZ and PRZ are defined respectively at the temperatures were 10% and 90% annealing of fission tracks or retention of He (or ^{40}Ar) occur in the crystal. The temperature limits of this range depend on the holding time of a crystal within the PAZ or PRZ, and therefore on the rate of cooling (Fig. II.3). If the cooling rate is slow the crystal passes the PAZ or PRZ slowly and significant resetting can occur. Similarly, in case of reheating, a crystal can reenter the temperature range of the PAZ or PRZ, resulting in the partial to full loss of information on the previous thermal history, especially because the rates of reheating are generally poorly known, if at all). For common orogenic cooling rates of 10-20°C/Myr the apatite and zircon fission-track PAZ are in general between about 60-110°C and 200-250°C respectively.

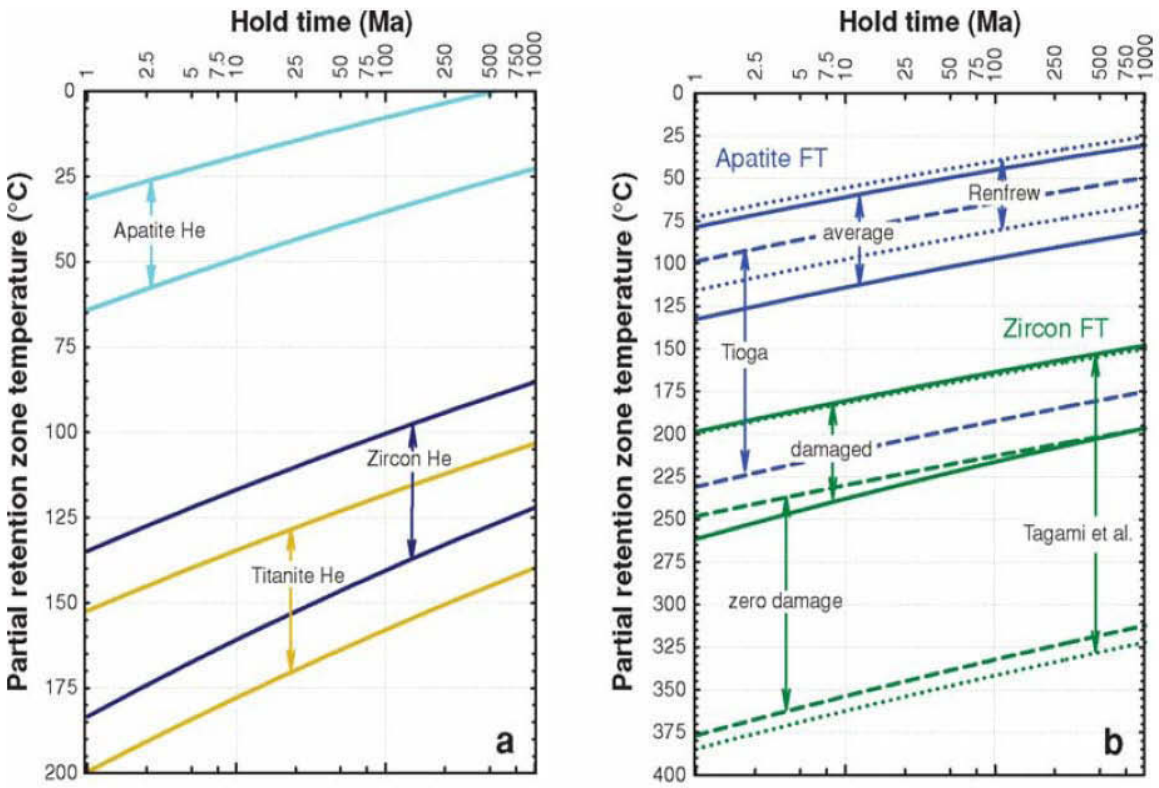

Figure II.3: Loss-only partial retention and annealing zones of different thermochronologic systems (Reiners and Brandon, 2006). Upper and lower boundaries correspond to 90% and 10% retention.

Thermochronologic data can be used for reconstructing the thermal history of upper crustal rocks by determining the timing and rates of cooling and/or modelling of exhumation rates. The thermal histories and exhumation rates can then be used for obtaining information on relief formation, sediment provenance analysis and in the conjunction with known geological constraints of the study area to determine the geologic evolution of this area and the processes that were responsible for this evolution.

II. 1. C – Choice of the thermochronometer

The choice of the thermochronometer will depend on the given geological problem to resolve available minerals (lithology) to analyze and of their closure temperature. Thus, systems with very high closure temperatures will be used to date crystallization and metamorphism events, e.g. zircon U-Pb dating. These techniques belong to the field called "geochronology", whereas systems with mid to lower closure temperatures will be preferred to study processes affecting the Earth's upper crust (Fig 4).

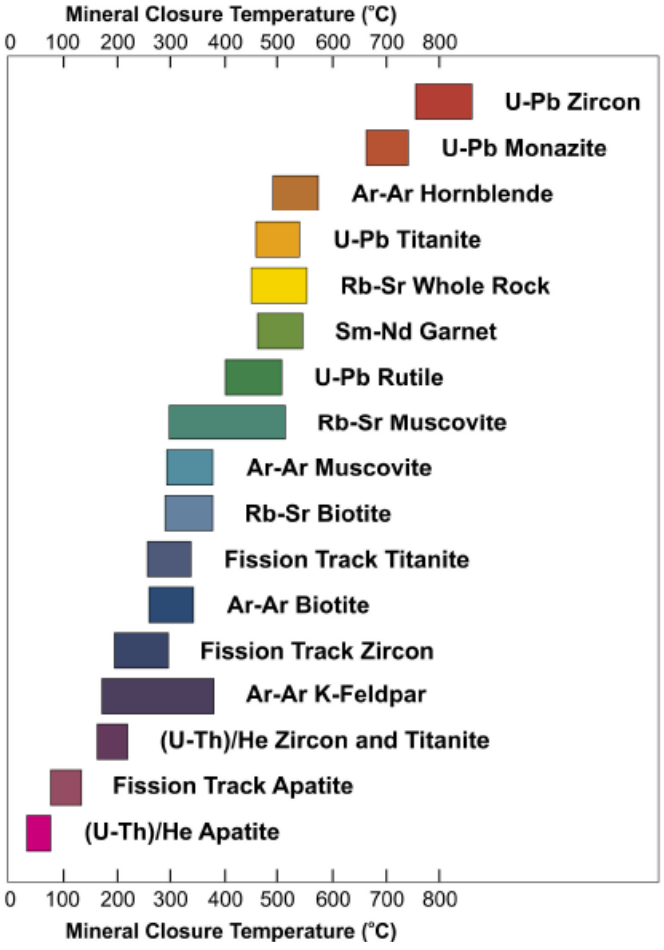

Figure II.4 : Closure temperature range of different geo- and thermochronologic dating techniques

II. 2 – U-Pb DATING

Zircon uranium-lead (U-Pb) dating method (Ko☒ler and Sylvester, 2003; Jackson et al., 2004) is commonly used for magmatic and metamorphic rock dating, provenance analysis and thus for geological reconstructions. Indeed, its closure temperature is very high (800 ± 50°C) (Lee et al., 1997). This method relies on two separate decay chain of the two naturally unstable isotopes of uranium (^{238}U and ^{235}U) to two stable isotopes of lead (^{206}Pb and ^{207}Pb, respectively). Ages t since when the system closed are given by the following equations:

$$\frac{^{206}Pb}{^{238}U} = e^{\lambda_{238}t} - 1$$

$$\frac{^{207}Pb}{^{235}U} = e^{\lambda_{235}t} - 1$$

Measuring respectively the ^{206}Pb/^{238}U and ^{207}Pb/^{235}U ratios, we can thus obtain two ages t for the same grain and plot these ages in the so-called Concordia diagram (Wetherill, 1956) drawn in a ^{206}Pb/^{238}U — ^{207}Pb/^{235}U space (Fig. II.5). In this space, the Concordia curve represents the place where ordinate and abscissa give the same age ("concordant ages"). Any analyzed zircon that plots on the Concordia gives the age of crystallization of this zircon. When ages obtained by the two methods are not concordant, the analyzed zircon plots away of the Concordia curve. This happens often and means that the system has been opened and that the Pb diffused out of the crystal lattice. If different zircons from the same sample were analyzed, they usually plot on a line defining the sample's Discordia. The upper intercept of the Discordia with the Concordia permits to obtain the age of closure of the system whereas the lower intercept gives the age of system opening (e.g. age of metamorphism).

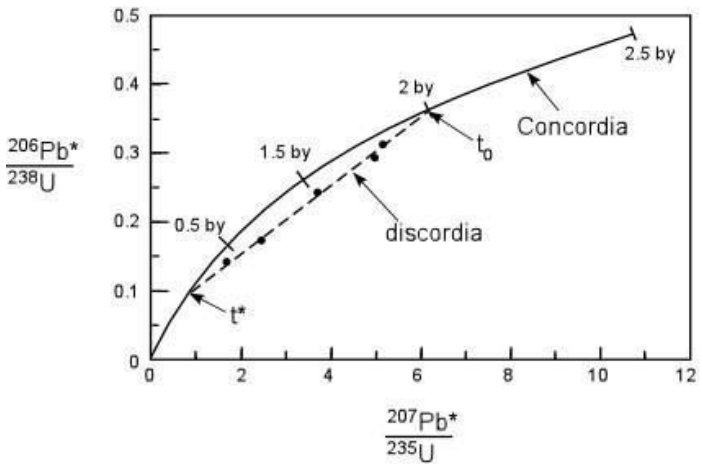

Figure II.5: Concordia diagram. Black curve corresponds to the *Concordia line* (Wetherill, 1956), age of crystallization of any zircon analyzed that plots on this curve are indicated by ticks. Discordia line is dotted. The upper intercept between *Discordia* and *Concordia* gives the crystallization age t_0 of the zircons analyzed (black dots) whereas lower intercept gives the age t* of Pb loss.

II. 3 – Fission-track dating

The spontaneous fission of ^{238}U produces two charged ions that recoil in opposite directions from each other. The two charged ions travel for a total distance of about 16 µm in apatite and 11 µm in zircon, causing ionization damage in the crystal structure by displacement of electrons and atoms. These damage zones are known as latent fission-track (Price and Walker, 1963; Fleischer et al., 1975). In principal fission tracks are randomly oriented in the crystal, but for apatite only crystals mounted parallel to the crystal c-axis should be analyzed to avoid anisotropy effects in track annealing (Donelick et al., 2005). Fission tracks are visible with an optical microscope only after chemical etching that makes the latent tracks wider.

II. 3. A – Sample preparation

Apatite and zircon are accessory minerals, more common in upper crustal felsic rocks and their metamorphic equivalents, and highly variable contents in clastic sedimentary rocks. It is thus necessary to sample 4 to 8 kg (or more) of rock, depending on lithology. After crushing, samples are sieved and the 100–200 µm fraction is conserved for apatite fission-track analysis and the 80–160 µm fraction for zircon fission-track. These grain sizes are suitable for microscopic observations and track counting. As apatite and zircon are heavy minerals with specific gravities of 3.1-3.2 for apatite and higher than 4.6 for zircon, mineral separation is done with a Gemini shaking table and with heavy liquids (LST and Methylene Iodide). The separated apatite and zircon grains are respectively mounted in epoxy resin and Teflon® sheets, and polished in order to expose an internal surfaces. Mounts are then etched: during 20 seconds at 21°C in 5.5M HNO_3 for apatite and during 5 to 100 hours at 228°C in NaOH+KOH melt for zircon (see paragraph II.2.B). Spontaneous fission tracks in contact with the mineral surface are being etched and become visible with an optical microscope (Fig. II.6).

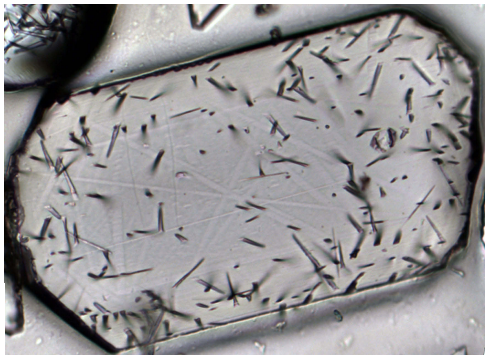

Figure II.6: Fission-tracks in a ~100 µm long apatite crystal (Picture by D. Chew).

II. 3. B – Etching theory

The geometry of etched tracks is controlled by two chemical attack factors: the general attack on the grain surface and the chemical dissolution along the track (Fleischer and Price, 1964). Etching rates depend on different factors as the crystallographic orientation of the grain or the degree of ionization of the mineral's lattice. But in any case, etching rate is higher for tracks than for surfaces.

After etching, most of the tracks that were intersecting the polished surface are thus visible, except those whose inclination under the surface is smaller than a critical angle (Fleischer and Price, 1964; Fleischer et al., 1975). This angle is very important for age calculation because observed track density has to be corrected from this effect. Note also that when etching time increases, the number of tracks revealed increases also because tracks that began under the original surface are progressively attained via the removal of the mineral surface while tracks etched at an early stage remains visible after long etched times.

A good determination of age is thus dependent on the closeness between the observed track density and the "real" latent track density. Thus, etching rate of the surface needs to be as small as possible. A good way to be sure that this is the case is to count only the grains with shallow and thin polishing scratches (Naeser et al., 1980). Moreover, etch time must be as short as possible to have very few new tracks added by removal of the original surface towards the center of the grain. For highly anisotropic minerals such as zircons, it is thus necessary to proceed by step-etching to determine the optimum etch time. This observation procedure needs a trained operator. On the other hand, for apatites that are almost isotropic, etch time is very slow and needs to be always the same (20 seconds) to be able to compare length data between laboratories.

II. 3. C – Individual grain age determination

a. *Principle*

Counting of visible fission tracks is equivalent to counting the number of fission events that happened above and below the analyzed grain surface since the mineral cooled below the closure temperature. As the fission-track annealing velocity varies with the crystallographic direction (Green and Durrani, 1978; Laslett et al., 1984), the number of fission track N_s is thus determined by convention on surfaces parallel to the c-axis of crystals where the rate is the slower.

However, the concentration of remaining ^{238}U isotopes in the grain remains unknown. To determine it, we use the fact that the ratio of $^{238}U/^{235}U$ is constant in nature (it equals 137.88; Steiger and Jäger, 1977), and that fission of ^{235}U can be induced by capture of a neutron during irradiation with thermal neutrons. It is thus possible to estimate the ^{238}U concentration indirectly knowing the density of induced fission-tracks from ^{235}U following irradiation (and neglecting the alpha decay of ^{235}U because ^{238}U and ^{235}U are in a secular equilibrium).

To do so, we use the external detector method (Fig. II.7) that consists of attaching a uranium free mica detector to the grain mount and irradiating the samples together with dosimeter glasses and age standards with thermal neutrons in a research reactor. The capture of a neutron by a ^{235}U will induce its fission and the formation of induced tracks inside the mineral lattice. Fission of ^{235}U atoms near the polished surface of the grain will also damage the external detector and leave induced tracks in the mica. After irradiation the mica is etched with 48% hydrofluoric acid (HF) for 18 minutes at 20°C to reveal the induced tracks. The intensity of the neutron flux is estimated with a U-doped dosimeter glass in which the concentration in ^{235}U is known (15 ppm IRMM540R for apatite fission-track analysis and 39.8 ppm CN1 for zircon fission-track analysis). For this study, all samples were irradiated at the FRM II reactor in Munich, Germany. Apatite fission-track samples were submitted to a flux around $4.5x10^{15}$ neutrons/cm^2 during 6.5 to 7 minutes, whereas zircon (containing much more uranium) were irradiated under a flux of ~$0.55x10^{15}$ neutrons/cm^2 during 55 to 60 seconds.

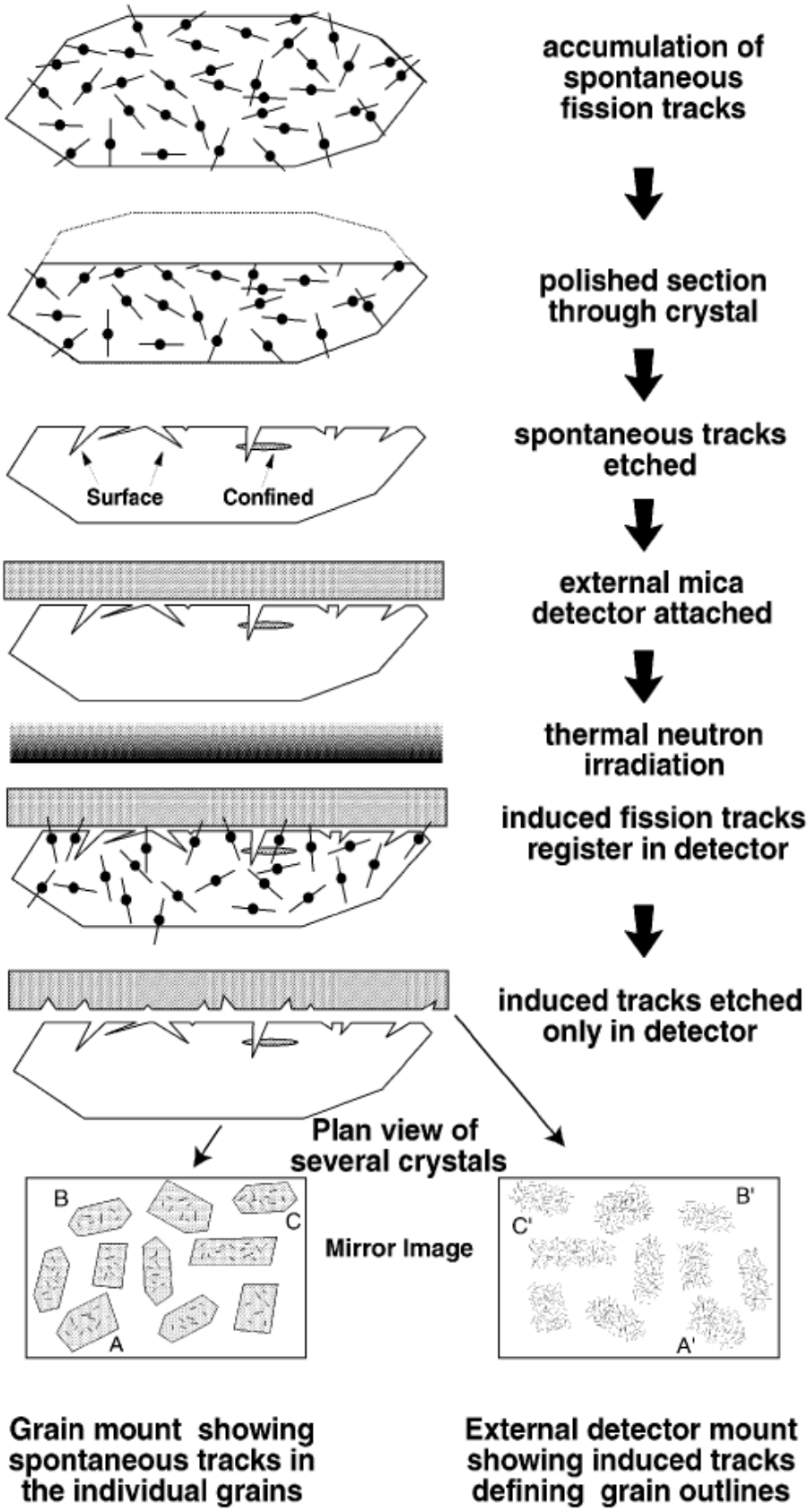

Figure II.7: Schematic outline of the external detector method (Gallagher et al., 1998)

a – Age determination

The external detector method (Fig. II.7) permits dating individual apatite or zircon grains and the fission-track age is calculated with the following equation:

$$FTage = \frac{1}{\lambda_d} \ln[1 + g\lambda_d \xi \rho_d \frac{N_s}{N_i}]$$

Where $FTage$ is the fission-track age of the apatite or zircon grain, λ_d is the total decay constant of ^{238}U (1.55×10^{-4} Ma^{-1}), g a geometrical factor (0.5), ξ the "zeta calibration factor" (see paragraph III.2.C.c), ρ_d the induced track density of the dosimeter glass depending on the neutron flux, N_s the number of spontaneous tracks (counted in the grain), and N_i the number of induced tracks (counted in the external mica detector).

b – Zeta factor determination

The eye of the operator gets trained whereas its visual acuity may change. Moreover, the "counting style" of each operator may be different. For example, one would count a track when it touches the reticule while someone else (like myself) will only consider tracks whose etch pit is touching the reticule. Thus, each operator induces a different bias in the age determination. To correct it, we determine a "zeta factor" using age standards whose fission-track age is precisely known (Hurford and Green, 1983; Hurford, 1990). The value is calculated from the deviation between the age obtained by the operator and the real age of the standard. As the zeta factor evolves with time for each operator, it needs to be determined quite often. Ideally, we should determine zeta factors with standards spanning a large age interval to have a good calibration for any age obtained. In this study we used three different age standards: Fish Canyon and Durango tuffs for apatite, and Buluk and Fish Canyon tuffs for zircon fission-track analyses.

c – Factor of errors

We have seen above that the external detector method allows calculating an age and the associated error for each individual grain. However, the ages within the same sample may vary a lot. These "extra-Poissonian" variations are due to experimental and geological factors such as under-etching of spontaneous tracks, bad contact between the grain mount and the mica detector, presence of grains originating from different sources and/or differential annealing between grains because of their different chemistry (Burchart, 1981; Green, 1981).

First of all, one should test if the distribution of single grain ages is normal or not. This is easily done by the statistical method of the χ^2 test (Galbraith, 1981) (Galbraith, 1981): if $\chi^2 >$ 5%, then the distribution tested is considered to contain only one population ("normal" distribution). In this case, different ages can be calculated from the age distribution of single grains (Galbraith and Laslett, 1993):

- The "mean age" is the arithmetic mean of the distribution. It depends on the ratio of spontaneous and induced track counts but does not take into account the precision of each single age. It represents only the minimum age of the last cooling below the 120°C isotherm.

- The "pooled age" is the age calculated from the sum of spontaneous and induced tracks. This method assumes that all grains have the very same age and does not take into account the variability of the individual grain ages.

- The "central age" is the mean of the logarithmic distribution of the ages pondered by the uncertainty on each individual grain age (Galbraith and Laslett, 1993; Gallagher, 1995). It is thus less sensible than the others to "extra-Poissonian" variations. In this study, for all samples that passed the χ^2 test, we used the central age.

A sample may contain grains with a wide range of ages that statistically belong to more than one age population. For example, in detrital sediments each grain may have recorded a different thermal history and therefore more than one population may be detected ($\chi^2 <$ 5%). In general, for bedrock samples with simple cooling histories about 20–30 individual grains to determine the apparent cooling age. For samples from detrital sediments and non-reset sedimentary rocks up to 100 grains if possible should be analyzed for better capturing.

d – Parameters of fission-track annealing

As we have seen above, fission tracks are not stable and fade away under certain temperature conditions (concept of thermal annealing; Fleischer et al., 1975). This ability of the mineral lattice to return from a disordered partially amorphous state (accumulated fission-track and alpha damages) to an ordered crystalline structure (no damage) is likely due to diffusion of interstitial atoms to their original position because of thermal activation due to heating (Paul and Fitzgerald, 1992; Paul, 1993). Various authors have studied the behavior of fission tracks under controlled temperature and pressure conditions and time (Yamada et al., 1995; Barbarand et al., 2003) as well as in different natural settings such as deep boreholes (Naeser and Forbes, 1976), contact metamorphic aureoles (Naeser and Faul, 1969), monotonous cooling of plutonic rocks (Harrison et al., 1979). Results of annealing experimental studies shows that as well as for etching, the track-annealing rate depends upon different factors, the main important ones are listed below:

- Crystallographic orientation of the tracks (annealing parallel to the c-axis is slower) (e.g. Green et al., 1986; Tagami et al., 1990),

- Chemical composition of the mineral: Cl-rich apatites anneal more slowly than fluoroapatites (Green et al., 1986). A positive correlation between the Cl-content and the D_{par} value of apatite (a measurement of the size of the etch pit parallel to the crystal c-axis) has been observed (see summary in (Donelick et al., 2005). Apatite with D_{par} values < 1.75 μm are considered as fast annealing and with values > 1.75 μm as slow annealing. D_{par} is.

- Accumulation of radiation damage in the considered crystal (mostly for zircons and sphenes). Older zircons (with a greater damage accumulation) see their tracks anneal more slowly than younger zircons),

- Pressure seems to play a role in apatites but not at the geological scale (Wendt et al., 2002) and has almost no influence on annealing rate in zircons.

References

Barbarand, J., Carter, A., Wood, I., and Hurford, T., 2003, Compositional and structural control of fission-track annealing in apatite: Chemical Geology, v. 198, p. 107–137, doi: 10.1016/S0009-2541(02)00424-2.

Braun, J., Beek, P. van der, and Batt, G., 2006, Quantitative Thermochronology: Numerical Methods for the Interpretation of Thermochronological Data: Cambridge University Press, 273 p.

Burchart, J., 1981, Evaluation of uncertainties in fission-track dating: Some statistical and geochemical problems: Nuclear Tracks, v. 5, p. 87–92, doi: 10.1016/0191-278X(81)90030-5.

Carlson, W.D., Donelick, R.A., and Ketcham, R.A., 1999, Variability of apatite fission-track annealing kinetics: I. Experimental results: American Mineralogist, v. 84, p. 1213–1223.

Corrigan, J.D., 1993, Apatite fission-track analysis of Oligocene strata in South Texas, U.S.A.; testing annealing models: Chemical Geology, v. 104, p. 227–229.

Dodson, M.H., 1973, Closure temperature in cooling geochronological and petrological systems: Contributions to Mineralogy and Petrology, v. 40, p. 259–274, doi: 10.1007/BF00373790.

Donelick, R.A., O'Sullivan, P.B., and Ketcham, R.A., 2005, Apatite Fission-Track Analysis: Reviews in Mineralogy and Geochemistry, v. 58, p. 49–94, doi: 10.2138/rmg.2005.58.3.

Fleischer, R.L., and Price, P.B., 1964, Techniques for geological dating of minerals by chemical etching of fission fragment tracks: Geochimica et Cosmochimica Acta, v. 28, p. 1705–1714, doi: 10.1016/0016-7037(64)90017-1.

Fleischer, R.L., Price, P.B., and Walker, R.M., 1975, Nuclear Tracks in Solids: Principles and Applications: University of California Press, 636 p.

Galbraith, R.F., 1981, On statistical models for fission track counts: Journal of the International Association for Mathematical Geology, v. 13, p. 471–478, doi: 10.1007/BF01034498.

Galbraith, R.F., and Laslett, G.M., 1993, Statistical models for mixed fission track ages: Nuclear Tracks and Radiation Measurements, v. 21, p. 459–470, doi: 10.1016/1359-0189(93)90185-C.

Gallagher, K., 1995, Evolving temperature histories from apatite fission-track data: Earth and Planetary Science Letters, v. 136, p. 421–435, doi: 10.1016/0012-821X(95)00197-K.

Gallagher, K., Brown, R., and Johnson, C., 1998, Fission Track Analysis and Its Applications to Geological Problems: Annual Review of Earth and Planetary Sciences, v. 26, p. 519–572, doi: 10.1146/annurev.earth.26.1.519.

Green, P.F., 1981, “Track-in-track” length measurements in annealed apatites: Nuclear Tracks, v. 5, p. 121–128, doi: 10.1016/0191-278X(81)90034-2.

Green, P.F., and Duddy, I.R., 1989, Some comments on paleotemperature estimation from apatite fission-track analysis.: Journal of Petrol. Geol., v. 12, p. 111–114.

Green, P.F., Duddy, I.R., Gleadow, A.J.W., Tingate, P.R., and Laslett, G.M., 1986, Thermal annealing of fission tracks in apatite: 1. A qualitative description: Chemical Geology: Isotope Geoscience section, v. 59, p. 237–253, doi: 10.1016/0168-9622(86)90074-6.

Green, P.F., and Durrani, S.A., 1978, A quantitative assessment of geometry factors for use in fission track studies: Nuclear Track Detection, v. 2, p. 207–213, doi: 10.1016/0145-224X(78)90025-X.

Harrison, T.M., Armstrong, R.L., Naeser, C.W., and Harakal, J.E., 1979, Geochronology and thermal history of the Coast Plutonic Complex, near Prince Rupert, British Columbia: Canadian Journal of Earth Sciences, v. 16, p. 400–410, doi: 10.1139/e79-038.

Hurford, A.J., 1990, Standardization of fission track dating calibration: Recommendation by the Fission Track Working Group of the I.U.G.S. Subcommission on Geochronology: Chemical Geology: Isotope Geoscience section, v. 80, p. 171–178, doi: 10.1016/0168-9622(90)90025-8.

Hurford, A.J., and Green, P.F., 1983, The zeta age calibration of fission-track dating: Chemical Geology, v. 41, p. 285–317, doi: 10.1016/S0009-2541(83)80026-6.

Jackson, S.E., Pearson, N.J., Griffin, W.L., and Belousova, E.A., 2004, The application of laser ablation-inductively coupled plasma-mass spectrometry to in situ U–Pb zircon geochronology: Chemical Geology, v. 211, p. 47–69, doi: 10.1016/j.chemgeo.2004.06.017.

Ko□ler, J., and Sylvester, P.J., 2003, Present Trends and the Future of Zircon in Geochronology: Laser Ablation ICPMS: Reviews in Mineralogy and Geochemistry, v. 53, p. 243–275, doi: 10.2113/0530243.

Laslett, G.M., Gleadow, A.J.W., and Duddy, I.R., 1984, The relationship between fission track length and track density in apatite: Nuclear Tracks and Radiation Measurements (1982), v. 9, p. 29–38, doi: 10.1016/0735-245X(84)90019-X.

Lee, J.K.W., Williams, I.S., and Ellis, D.J., 1997, Pb, U and Th diffusion in natural zircon: Nature, v. 390, p. 159–162, doi: 10.1038/36554.

Naeser, C.W., and Faul, H., 1969, Fission track annealing in apatite and sphene: Journal of Geophysical Research, v. 74, p. 705–710, doi: 10.1029/JB074i002p00705.

Naeser, C.W., and Forbes, R.B., 1976, Variation of fission track ages with depth in two deep drill holes.: EOS (Alerican Geophysical Union Transactions), v. 57, p. 353.

Naeser, C.W., Izett, G.A., and Obradovitch, J.D., 1980, Fission track and K-Ar ages of natural glasses: U.S. Geological Survey Bulletin, v. 1489, p. 1–31.

Paul, T.A., 1993, Transmission electron microscopy investigation of unetched fission tracks in fluorapatite—physical process of annealing: Nuclear Tracks and Radiation Measurements, v. 21, p. 507–511, doi: 10.1016/1359-0189(93)90190-K.

Paul, T.A., and Fitzgerald, P., 1992, Transmission electron microscope investigation of fission tracks in apatite: American Mineralogist, v. 77, p. 336–344.

Price, P.B., and Walker, R.M., 1963, Fossil tracks of charged particles in mica and the age of minerals: Journal of Geophysical Research, v. 68, p. 4847–4862, doi: 10.1029/JZ068i016p04847.

Reiners, P.W., and Brandon, M.T., 2006, Using Thermochronology to Understand Orogenic Erosion: Annual Review of Earth and Planetary Sciences, v. 34, p. 419–466, doi: 10.1146/annurev.earth.34.031405.125202.

Steiger, R.H., and Jäger, E., 1977, Subcommission on geochronology: Convention on the use of decay constants in geo- and cosmochronology: Earth and Planetary Science Letters, v. 36, p. 359–362, doi: 10.1016/0012-821X(77)90060-7.

Tagami, T., Galbraith, R.F., Yamada, R., and Laslett, G.M., 1998, Revised Annealing Kinetics of Fission Tracks in Zircon and Geological Implications, *in* Haute, P. van den and Corte, F. de eds., Advances in Fission-Track Geochronology, Solid Earth Sciences Library 10, Springer Netherlands, p. 99–112.

Tagami, T., Ito, H., and Nishimura, S., 1990, Thermal annealing characteristics of spontaneous fission tracks in zircon: Chemical Geology: Isotope Geoscience section, v. 80, p. 159–169, doi: 10.1016/0168-9622(90)90024-7.

Wagner, G.A., 1979, Correction and Interpretation of Fission Track Ages, *in* Jäger, P.D.E. and Hunziker, P.D.D.J.C. eds., Lectures in Isotope Geology, Springer Berlin Heidelberg, p. 170–177.

Wendt, A.S., Vidal, O., and Chadderton, L.T., 2002, Experimental evidence for the pressure dependence of fission track annealing in apatite: Earth and Planetary Science Letters, v. 201, p. 593–607, doi: 10.1016/S0012-821X(02)00727-6.

Wetherill, G.W., 1956, Discordant Uranium-Lead Ages: Transactions, American Geophysical Union, v. 37, p. 320.

Wolf, R.A., Farley, K.A., and Silver, L.T., 1996, Helium diffusion and low-temperature thermochronometry of apatite: Geochimica et Cosmochimica Acta, v. 60, p. 4231–4240, doi: 10.1016/S0016-7037(96)00192-5.

Yamada, R., Tagami, T., Nishimura, S., and Ito, H., 1995, Annealing kinetics of fission tracks in zircon: an experimental study: Chemical Geology, v. 122, p. 249–258, doi: 10.1016/0009-2541(95)00006-8.

Chapter III – Early Paleogene crustal extensional collapse in response to Late Cretaceous arc growth and flare-up in the Arequipa belt of southern Peru, Central Andes

This chapter is similar to a paper that will be submitted to the *Geological Society of America Bulletin* in collaboration with Thierry Sempere, Matthias Bernet, Alexey Ulianov and Jean-Louis Paquette (zircon U-Pb analyses).

New geo- and thermochronogical data coupled to a new tectono-stratigraphic map illuminate the Late Cretaceous–Paleogene evolution of the copper-rich Arequipa belt of southern Peru. During the Lower Cretaceous, the Andean subduction arc migrated from the coastline towards the Arequipa region where it established between ~90 and ~52 Ma. This ~38 Myr long evolution comprised three stages: initial growth (~90–74 Ma), flare-up (~74–62 Ma), and gravitational collapse (~62–52 Ma). Between ~84 and ~76 Ma, the arc was developed significantly enough to destabilize its stratigraphic cover and trigger large-scale mass-wastings, at least on its backarc slope. During initial growth of the arc, the backarc basin was also rapidly evolving toward continental conditions. Arc growth persisted and resulted in magmatic flare-up from ~74 to ~62 Ma. In-situ and detrital apatite and zircon fission-track data and geological relationships indicate that extensional exhumation by regional-scale normal faulting and block tilting started at ~62–60 Ma. We interpret this Late Cretaceous to Early Paleocene evolution as reflecting an extensional collapse of the arc due to important addition of mantle-derived magmas in the crust. As a result, the Arequipa belt now appears as a well-preserved taphrogen of Early Paleogene age where extensional conditions lasted through the Eocene and waned until ~30 Ma.

III. 1 – INTRODUCTION

The Central Andes illustrate an extreme case of orogenic growth related to an ocean-continent subduction. Across the terrestrial forearc (the western side of the orogen), the current crustal thickness rapidly increases from ~30 km along the coastline to >60 km beneath the magmatic arc, where maximum thickness is generally recorded (James, 1971; Kono et al., 1989; Beck et al., 1996; Beck and Zandt, 2002). Given the subduction context, this crustal overthickening results likely from tectonic and magmatic processes that interacted in a complex way (Sempere et al., 2008).

However, the currently dominant paradigm in the Central Andes postulates that crustal thickening mostly resulted from contractional tectonics, which is believed to have propagated from west to east (Isacks, 1988; Suárez et al., 1983). Nevertheless, the upper crust in the forearc of southwestern Peru exhibits little to no evidence of tectonic shortening but, in contrast, many extensional features (James, 1971; Myers, 1975; Tosdal et al., 1984; Kono et al., 1989; James and Sacks, 1999; Sempere and Jacay, 2008). Moreover, it has been shown that the Central Andean margin, which had undergone significant lithospheric thinning over >200 Myr, switched to crustal thickening at ~90 Ma (Mamani et al., 2010). Both these observations question the importance of magmatic addition and/or underplating in the crustal overthickening of the arc region and invites to investigate in detail the 'early' geological evolution of the orogen through an integrated study of the Late Cretaceous to Paleogene magmatic, sedimentary, tectonic, and exhumation records.

In this chapter, we focus on the Arequipa belt of southern Peru (Fig. III.1) because it was recently shown to have been the locus of a magmatic flare-up during the latest Cretaceous and earliest Paleocene (Demouy et al., 2012). This area thus provides an ideal location to test the role of arc magmatism during the early Andean crustal thickening. Moreover, because overthickening of the crust generally results in its collapse and/or significant erosion, which both lead to exhumation of rocks, we have addressed this issue using fission-track and zircon U-Pb dating. We propose a new tectono-stratigraphic chart and map, combine it with new thermochronological and geochronogical data, and our current knowledge of the regional stratigraphy and magmatism in order to produce a refined picture of the geological evolution of the region during the Late Cretaceous and Paleogene. Our conclusions shed light on the processes that were involved during the early stage of the Central Andean orogeny.

III. 2 – GEOLOGY OF THE AREQUIPA REGION

III. 2. A – Geological architecture of the forearc

Peru has been located above a major ocean-continent subduction zone since at least the Early Paleozoic, and possibly since ~650 Ma (Chew et al., 2008). This margin has therefore maintained a magmatic arc during most of its evolution, with a forearc basin extending between the arc and the subduction trench, and a backarc basin extending between the arc and the South American mainland. The study area is located in the present-day terrestrial forearc of southern Peru, it is bounded by the Pacific coastline and the present-day volcanic arc, which is commonly referred to as the Western Cordillera (Fig. III.1). In this region the main structural features are parallel to the subduction trench, which trends NW-SE at these latitudes (Fig. III.1). The study area presents two belts, namely the coastal and Arequipa belts, which are separated by the ~1 km-high Clemesí elevated surface. A few valleys have incised this surface (Fig. III.1) providing continuous outcrops showing that no marked geological boundaries separate the two belts.

The coastal belt is characterized by a ~1 km-high escarpment, which is often referred to as the "Coastal Cordillera". This escarpment mostly exposes crystalline basement consisting of Proterozoic metamorphic rocks and Ordovician plutons that crop out northwest of the Río Tambo fault zone (RTFZ – Fig. III.2; Roperch et al., 2006). Southeast of the RTFZ, mainly plutonic rocks of Jurassic and mid-Cretaceous age, and a ~3 km-thick succession of Late Paleozoic to Jurassic volcano-sedimentary strata outcrop (Boekhout et al., 2013). In this work we use "coastal escarpment" instead of "Coastal Cordillera" because in general no relief exists along its northeastern side.

The Arequipa belt, where the study area is located, is dominantly structured by regional-scale normal faults (Fig. III.1; Sébrier et al., 1985; Demouy et al., 2012), and exposes a variety of rocks that range from Proterozoic to Cenozoic in age (Fig. III.2). The abundance of plutonic and volcanic rocks of Late Cretaceous to earliest Eocene age indicates that the coeval subduction arc was located along the Arequipa belt (Fig. I.7 and III.2.C), and especially along the La Caldera Horst (LCH) (Fig. III.1).

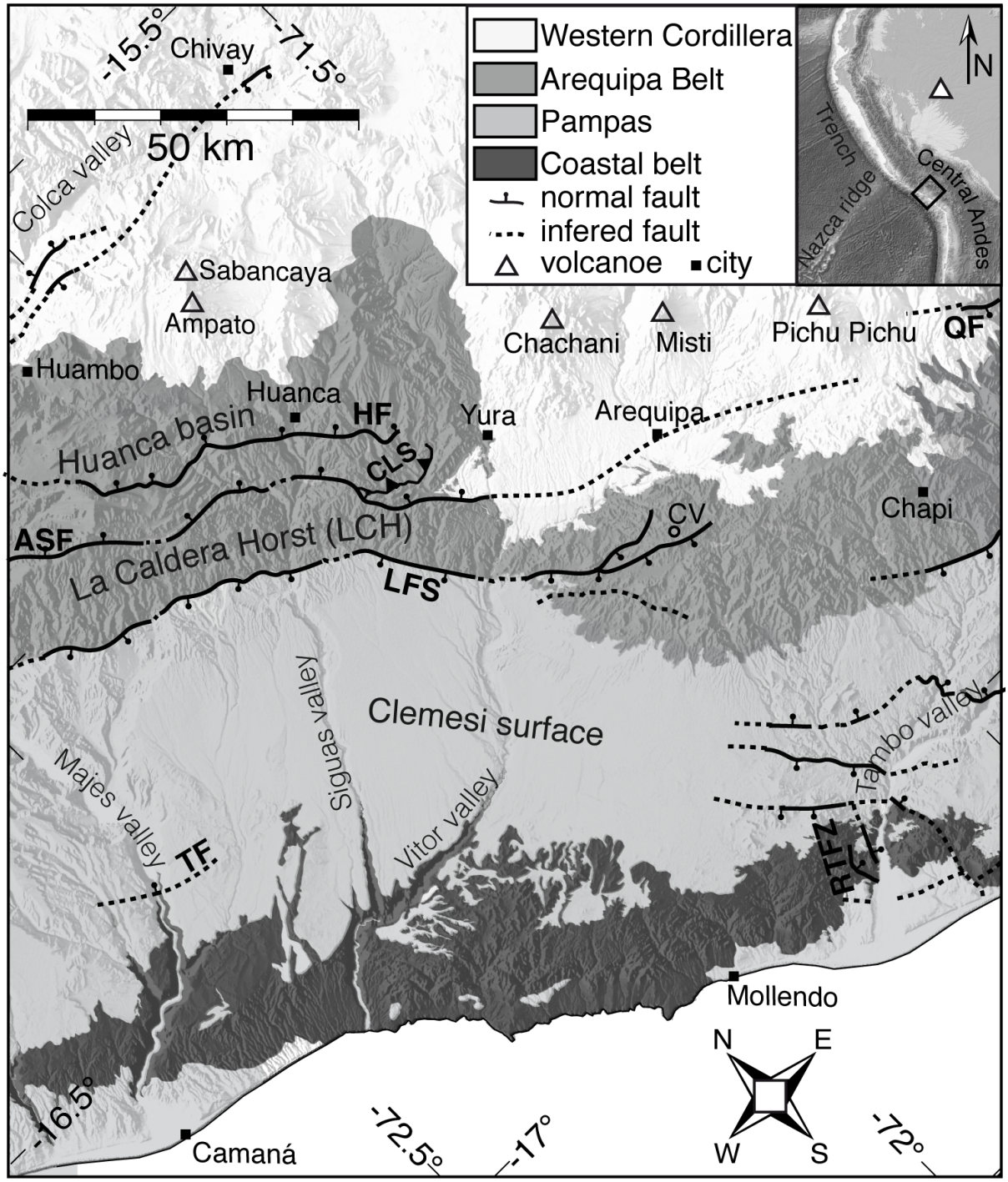

Figure III.1: Main geomorphic and tectonic features of southern Peru. Inset: location of the study area in the northeastern south American framework. ASF: Agua Salada fault; CF: Cenicienta Fault; CLS: Cincha-Lluta slump; CV: Cerro Verde porphyry copper deposit; HF: Huanca fault; LFS: Luclla fault; RTFZ: Río Tambo fault zone; TF: Toran fault; QF: Quinistacas fault.

The geological record indicates that coastal southern Peru has been submitted to an arid to hyper-arid climate since at least the mid-Cretaceous (Hartley et al., 2005), which has largely contributed to preserve quite ancient geomorphic and geologic features (Dunai et al., 2005). Among them, the hyper-arid elevated Clemesí surface (Fig. III.1), gently dipping towards the ocean, extends between the Arequipa belt and the coastal escarpment. It represents the abandonment surface of a Late Neogene sedimentary system that covered older rocks bridging the coastal and Arequipa belts. The Majes, Siguas, Vítor and Tambo valleys incise the Clemesí surface (Fig. III.1).

III. 2. B – First order stratigraphy

Because specific rocks and paleogeographies characterize each of the belts described in the section III. 2 A, it has been possible to reconstruct the positions of the trench-forearc-arc-backarc system in southern Peru for a number of time intervals. Our compilation of these reconstructions (Vicente, 1981 and 1982; James and Sacks, 1999; Mamani et al., 2010; Boekhout et al., 2012; Demouy et al. 2012) and our own ongoing work show that the trench-forearc-arc-backarc system in southern Peru has considerably migrated across time since the Carboniferous (Fig. I.7 and Fig. III.2).

In the study area, the crystalline basement is dominantly exposed along the coastal region (Fig. III.3) where its rocks form most of the coastal escarpment between 71.7° and 74.0°W. Basement rocks consist of ~1.2–0.9 Ga-old ultra-high-temperature (UHT) migmatites and subordinate Ordovician granitoids (Casquet et al., 2010; Martignole and Martelat, 2003).

The basement is overlain by a >5 km-thick stratigraphic succession of Late Paleozoic to mid-Cretaceous age where forearc, arc, and backarc sedimentary facies deposits are piled-up in this order (Sempere et al., 2002 and 2012), reflecting the migration of the system toward the southwest (Fig. I.7 & III.2). During this period, arc and locally backarc plutons of Late Paleozoic to mid-Cretaceous age emplaced, forming the so-called 'Coastal Batholith' (Boekhout et al., 2012; Demouy et al., 2012).

Whereas a carbonate platform began to develop in the backarc basin ~110 Ma ago (Arcurquina limestones), a major change occurred starting at ~90 Ma (Fig. I.7; Mamani et al.,

2010). This change included the re-establishment of the arc in the Arequipa belt, major gravitational collapses of the upper sedimentary basin fill (Callot et al., 2008; Demouy et al., 2012) and the continentalization of the backarc basin. Numerous intrusions spanning the ~90-62 Ma interval occurred specifically along the Arequipa belt, which also includes paleovolcanic systems as young as ~52 Ma (Clark et al., 1990; Bidgood, 2000; Simmons et al., 2013). In particular, the arc apparently underwent a magmatic flare-up during the ~70-62 Ma interval, at least in the Cerro Verde area (Demouy et al., 2012). Volcanic and volcaniclastic strata reflecting the same evolution accumulated during the ~90-55 Ma interval, overlying unconformably older sedimentary units but apparently with no angularity.

Between ~52 and ~45 Ma, at about the longitudes of Arequipa (~71.3° – 74.2° W), the arc migrated ~100-150 km northwards (James and Sacks, 1999). During this period, in the study area, subhorizontal forearc red beds dated ~50-30 Ma uncomformably deposited over the previously described sedimentary pile. Since 30 Ma, the arc is migrating back towards the southwest and its present-day position. Oligocene to present sedimentary and volcanic accumulations variably overlie the rocks previously deposited in the present-day forearc.

In order to reflect these migrations of the trench-forearc-arc-backarc system in the study area, we propose a new tectonostratigraphic chart (Fig. III.2) and its associated map (Fig. III.3) in which we combine units that had previously been mapped separately. Apart from the basement and the Carboniferous forearc deposits of the "Yamayo Formation", we choose to differenciate three periods of time: ~200–110 Ma, 110–45 Ma and 45–0 Ma. For each of these periods, we distinguish rocks formed in plutonic, forearc, volcanic arc and backarc contexts (Fig. III.2 and III.3). To map the study area (Fig. III.3), we used the existing geological maps at the 1:100,000 scale published by the INGEMMET, our own field observations, satellite pictures available under *Google Earth* and SRTM data.

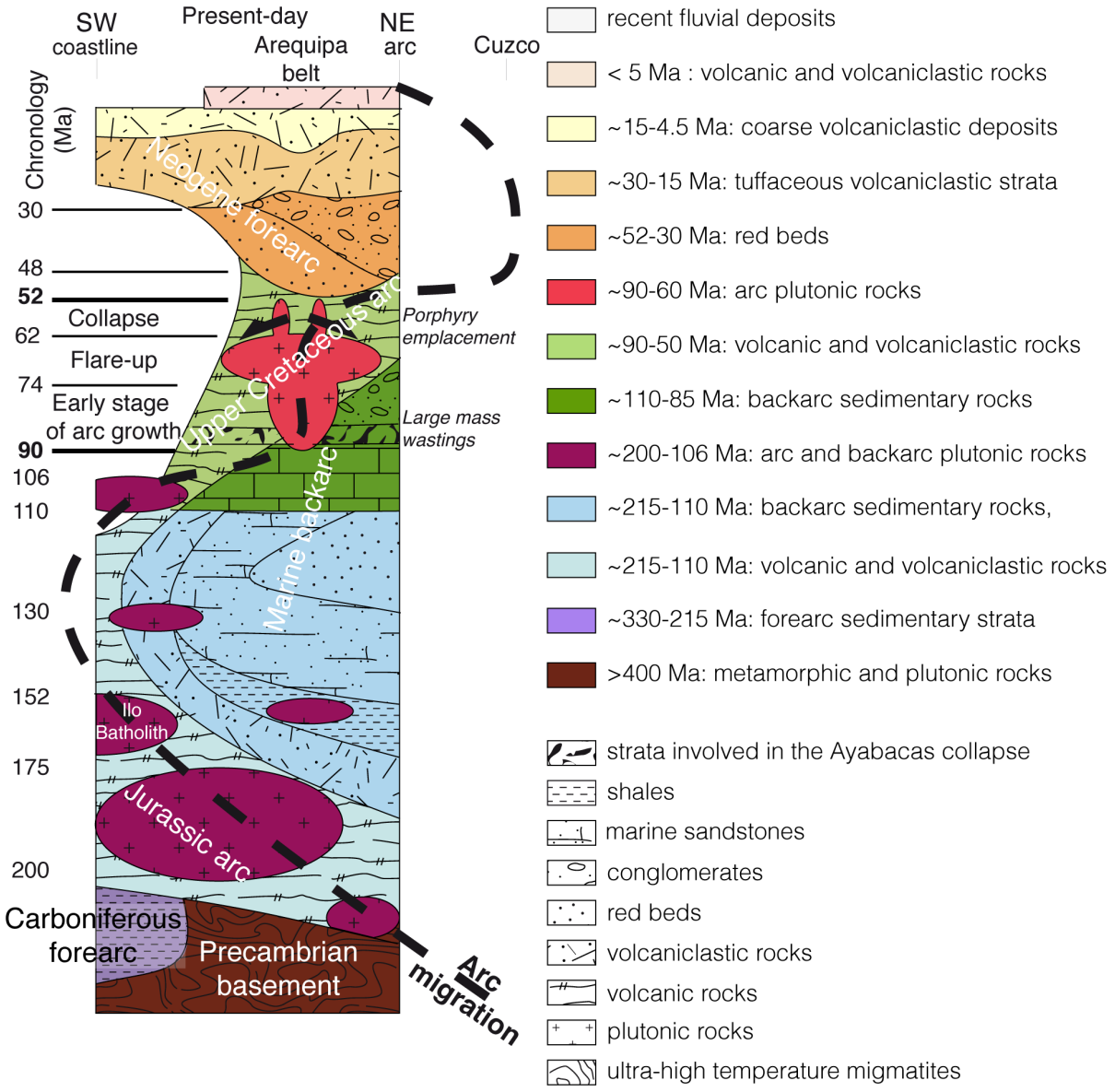

Figure III.2: Tectonostratigraphic chart for southern Peru; left vertical corresponds to the approximate stratigraphy on the coastline SE of Mollendo, right vertical to the supposed stratigraphy under the present-day volcanic arc as exposed in Huambo area. Note the migration of the forearc, arc (black dotted line), backarc system overtime. Arc deposits are colored in light and backarc deposits in darker tones.

(next page) Figure III.3: A. Tectonostratigraphic map of the study area revised from the geological mapping by INGEMMET. B. Cross-section along the transect "ab" and perpendicular to the main structural features. AS: Ayabacas Sole (basal decolement of the Cincha Llutlla slump deposit); ASF: Agua Salada Fault System; CF: Cenicienta Fault; LFS: Lluclla Faut System; HF: Huanc Fault; QF: Quinistacas Fault; RTFZ: Río Tambo Fault Zone; TF: Toran Fault. Colors are the same than in Fig. III.2. Grey hatched area corresponds to the Cincha-Lluta slump deposit. Colors are the same than in Fig. III.2.

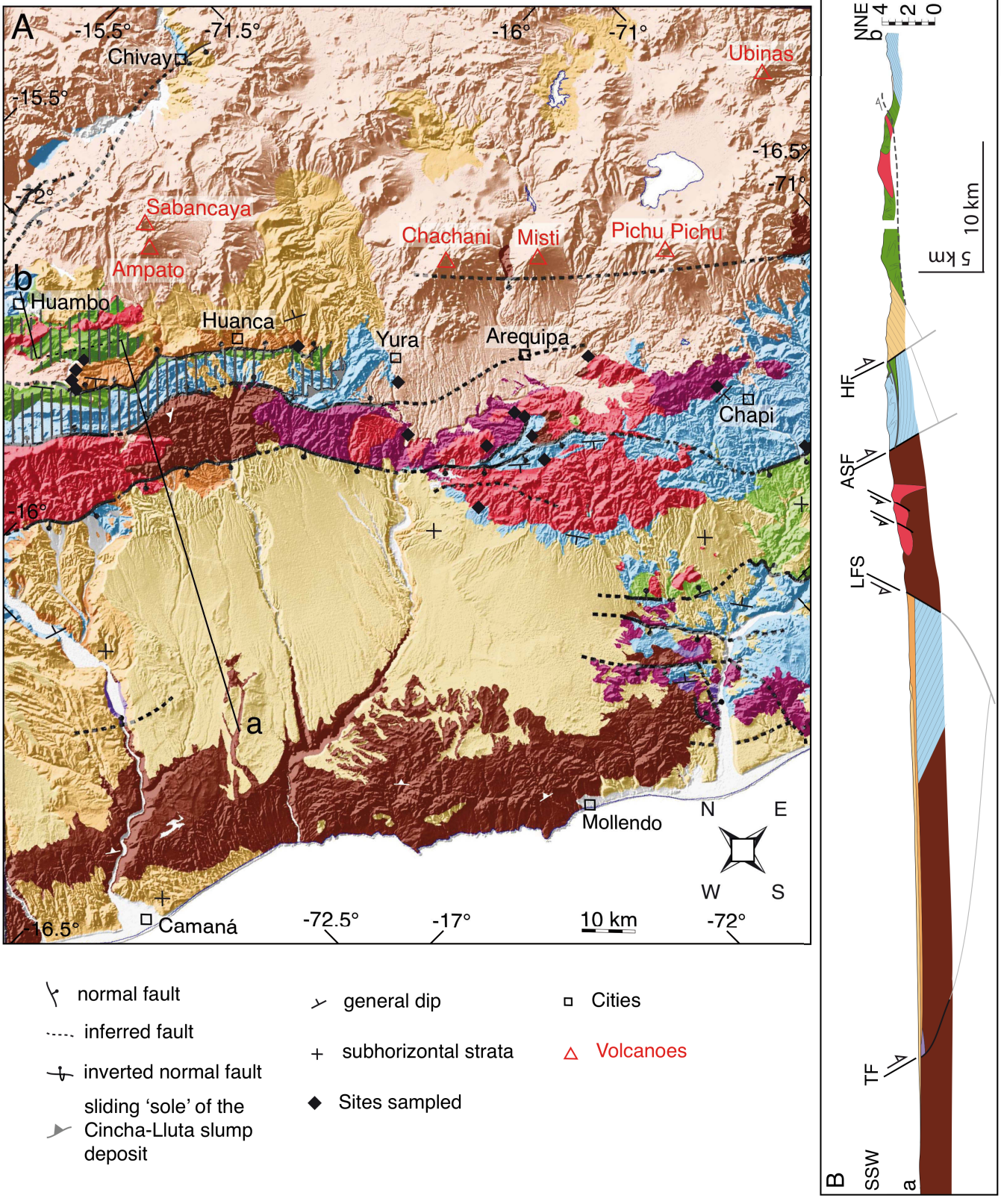
A
-15.5°
-71.5°
-16°
-71°
Chivay
Ubinas
-15.5°
-16.5°
-72°
-71°
Sabancaya
Ampato
Chachani
Misti
Pichu Pichu
b
Huambo
Huanca
Yura
Arequipa
Chapi
-16°
a
Mollendo
N
E
W
S
-16.5°
Camaná
-72.5°
-17°
10 km
-72°
normal fault
inferred fault
inverted normal fault
sliding 'sole' of the Cincha-Lluta slump deposit
general dip
subhorizontal strata
Sites sampled
Cities
Volcanoes
Elevation (km)
NNE
b
4
2
0
10 km
5 km
HF
ASF
LFS
TF
B
SSW
a

III. 2. C – Structural style and major faults

The overall Arequipa region has been structured by large-scale extensional deformation (Fig. III.3). The contact between the basement and the overlying succession is locally stratigraphic but more generally an extensional detachment (Sempere et al., 2012; Boekhout et al., 2013). In the northwestern part of the Arequipa belt, the Agua Salada and Lluclla normal faults bound the LCH, where mostly Proterozoic metamorphic rocks and Mesozoic–Paleocene plutons crop out (Fig. III.3). About, 2.6 km WSW of the Cerro Verde open pit, the Lluclla normal fault system separates basement metamorphic rocks from overlying strata of latest Jurassic age (Fig. III.3) deposited in the "Arequipa basin" (Geyer, 1983). The Agua Salada normal fault separates Upper-Jurassic strata from the basement and Jurassic intrusions at the NE of the LCH (Fig. III.3). Northeast of the Agua Salada fault, the parallel Huanca normal fault controls a half-graben where the continental Huanca Formation is preserved. The Chachani, Misti and Pichu Pichu volcanoes appear to be standing along the footwall edge of the Quinistacas normal fault, where metamorphic basement crops out (Fig. III.3) (James and Brooks, 1976).

Other normal faults can be observed in the Majes and Tambo valleys (Fig. III.1), but are covered beneath the Clemesí surface. Near Torán, in the Majes valley, the local normal fault dips ~40° to the NNE and places gently-dipping Late Paleozoic strata over the metamorphic basement (a geometry commonly observed in the coastal area) (Fig. III.3). However, partial inversion in the Neogene of this fault has resulted in a ~175 m offset of the Miocene/basement contact and a local flexure of Miocene strata that dies out upsection.

Near Cerro Verde, the NE-trending Cenicienta normal fault (Fig. III.3) juxtaposes the "Jurassic batholith" (composed by diorites and gabbros and dated at ~200-175 Ma; Demouy et al., 2012) with its volcano-sedimentary counterpart (the ~215-180 Ma Chocolate and Socosani formations; Boekhout et al., 2013). Given the contrast in original structural level between these coeval units, the vertical offset on the Cenicienta fault is likely to be $\geq$ 3 km. Furthermore, this NE-trending fault is post-dated by the ~84–78 Ma-old Tiabaya pluton (Fig. III.4) and thus formed between ~175 and ~84 Ma (Sempere et al., 2002). Jurassic extension is also documented in the Cantera Cayhua area (Fig. III.4) by ductile deformation in Liassic plutonic rocks, which on average is characterized by top-to-the-southeast shearing. These observations are consistent with the Jurassic basin deepening to the southeast (Vicente, 1981).

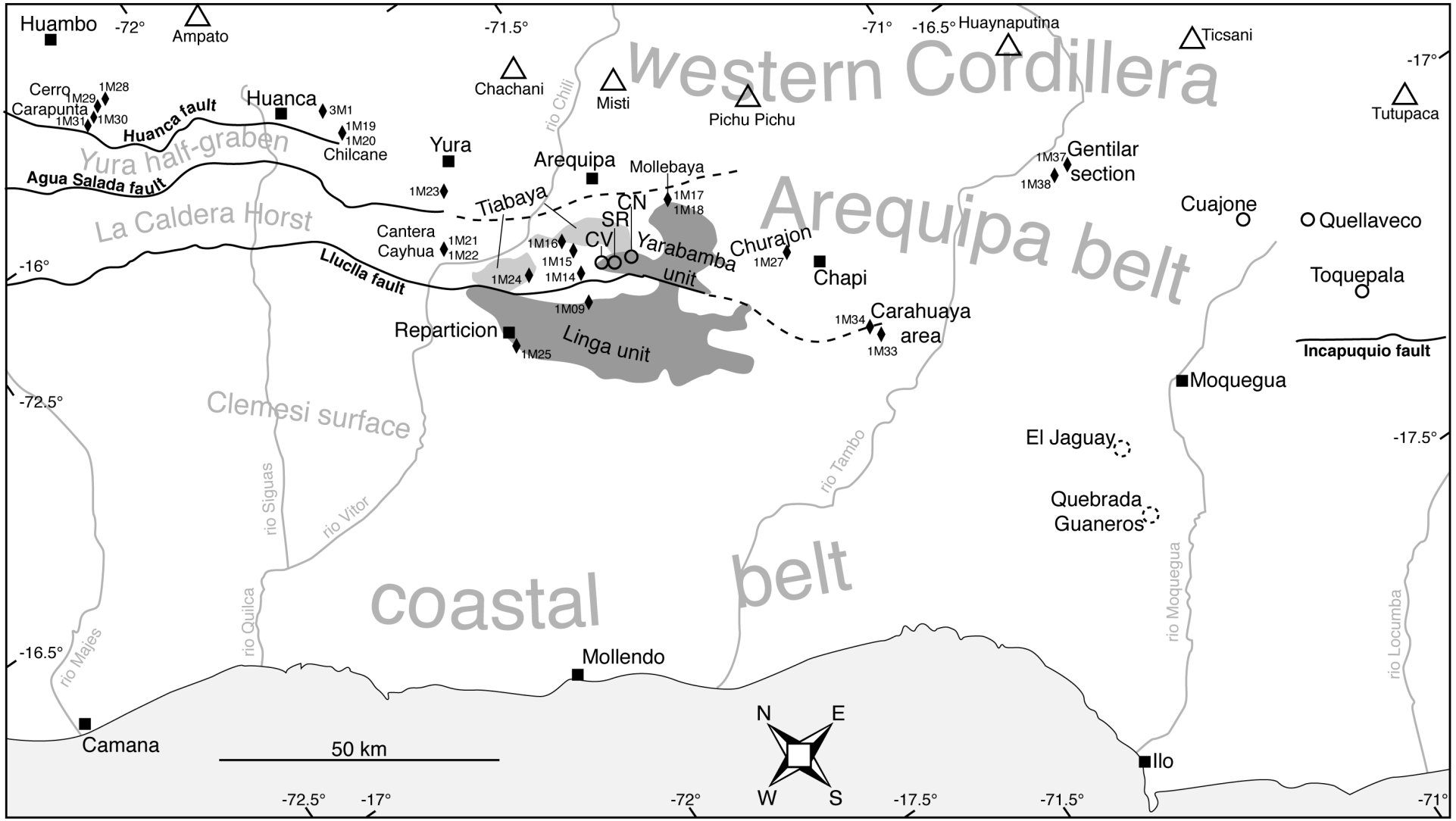

Figure III.4: Simplified map of the forearc of southern Peru showing the main locations names used in the text. Names of faults are in bold and located on their downwarped side. Black squares: cities; open triangles: volcanoes; black diamonds: samples sites; open circles: major dated porphyry copper deposits (CV: Cerro Verde; SR: Santa Rosa and CN: Cerro Negro); open dotted circles: location of relevant outcrops.

III. 3 – Stratigraphy of the Arequipa belt

As stated above, we focus in this chapter on the Arequipa belt, this area includes numerous accessible, diverse, and good-quality outcrops and therefore is an ideal location to study the geological evolution of the present-day forearc of southern Peru. We hereunder compile data from the literature and our own observation to present the geological evolution of this region.

III. 3. A – Basement.

In the Arequipa belt, the basement crops out, in limited areas, as metamorphic rocks in the footwalls of the Agua Salada, Lluclla, and Quinistacas normal faults (the hanging walls consisting of Mesozoic strata), making that most of its outcrops are located in the LCH (Fig. III.3).

III. 3. B – Plutonic rocks

The basement and its Late Triassic to mid-Cretaceous cover are intruded by plutons that, where dated, reflect two major pulses of emplacement, namely the ~200–175 Ma and ~90–62 Ma intervals (Demouy et al., 2012). In the southeastern part of the study area, the Churajón quartz-diorite unit (see location on Fig. III.4) represents a minor pulse at ~160.5 Ma, but is thought to have been emplaced into the coeval backarc (Demouy et al., 2012). The available geochemical data indicate that at least both major pulses were emplaced in a magmatic arc whose source was considered to be juvenile (Mamani et al., 2010; Demouy et al., 2012). These two pulses therefore reflect that the subduction-related volcanic arc approximately coincided with the Arequipa belt during the respective intervals, namely between ~200 and ~175 Ma on its migration toward the southwest, and between ~90 and at least ~62 Ma on its migration toward the northeast (Fig. III.2). In the Arequipa belt, the ~200–175 Ma pulse built the "Liassic batholith" and, after a magmatic lull, magmatism resumed abruptly at ~90 Ma and built the "Late Cretaceous batholith" (which includes a few Early Paleocene rocks; Demouy et al., 2012).

Linga and Yarabamba plutons and magmatic flare-up. Southwest of Cerro Verde, the Linga unit belongs to the "Late Cretaceous batholith". It consists of a variety of plutonic rocks ranging from minor gabbros to dominant diorites, tonalites and monzonites, and was emplaced

into strata of Late Jurassic age that, at NE and SW, homogeneously dip 45° to the southwest. The Linga unit has yielded so far a total of 11 zircon U-Pb ages (including a new age reported below; Mukasa, 1986; Demouy et al., 2012). Eight of these ages range between 70.2 ± 0.7 and 64.8 ± 0.4 Ma, and the younger one is 61.6 ± 0.4 Ma, all being distributed over much of the pluton. The other two ages, respectively from its NE and SW borders, are 89.8 ± 0.7 and 87.1 ± 1.0 Ma, suggesting the main mass of the pluton was emplaced into a ~90–87 Ma-old intrusion and probably split it. In what follows, we thus use the term 'Linga unit' to refer to the main magmatic volume, which crystallized between ~70 and ~62 Ma, unless specified otherwise.

Northeast of the Linga unit, in the footwall of the Lluclla normal fault, i.e. in the LCH (Fig. III.1), the Yarabamba plutonic unit (Fig. III.4) consists dominantly of diorites and intruded the basement and Liassic strata. Yarabamba unit yielded five zircon U-Pb ages ranging from 67.4 ± 0.7 to 62.1 ± 0.6 Ma (Mukasa, 1986; Demouy et al., 2012).

Taken altogether, the ages obtained on the voluminous and coeval Linga and Yarabamba plutonic units document that the Cerro Verde area underwent a significant magmatic flare-up between ~70 and possibly as late as ~62 Ma (Fig. III.2; Demouy et al., 2012).

III. 3. C – Late Triassic to mid-Cretaceous stratigraphic succession.

The Arequipa belt is characterized by a ≥3 km-thick Late Triassic to mid-Cretaceous stratigraphic succession (Fig. III.3 and III.5), which in the northwest provides many of the Mesozoic stratotypes for southern Peru (Benavides, 1962; Jenks, 1948; Vicente, 1981; Vicente et al., 1982). The stratigraphic contact of this succession with the basement is only known in the Cerro Verde area, where the volcanic to volcaniclastic Chocolate Formation (~215–185 Ma; Boekhout et al., 2013) directly overlies metamorphic rocks (Sempere et al., 2012). In contrast with the coastal belt, the Late Carboniferous–Middle Triassic Yamayo Group thus appears to be absent or of reduced thickness in the Arequipa belt (Fig. III.2; III.3 and III.5).

The Late Triassic to mid-Cretaceous succession in the Arequipa belt (Fig. III.4) reflects the presence of the subduction arc in this area during the Late Triassic and early Liassic (Chocolate Formation) and its subsequent migration toward the southwest, which caused a marine backarc basin to develop (Fig. III.2; Sempere et al., 2002). Facies and paleocurrent distribution indicates that this arc apparently consisted of a discontinuous stringer of volcanic islands from ~215 to

~90 Ma. The turning point at which the arc started to migrate backwards (i.e., toward the northeast) is tentatively estimated to be ~130 Ma (Fig. III.2).

A marine transgression developed in the backarc basin starting ~110 Ma, leading to the deposition of a ~250–650 m-thick limestone unit, the Arcurquina Formation (Jenks, 1948), until ~90 Ma (Fig. III.2 and III.5; Callot et al., 2008). The persistence of thick and widespread carbonate deposition between ~110 and ~90 Ma implies that the regional climate was hot and dominantly arid during that time.

The Arcurquina marine limestones are overlain by the ~200 m-thick Querque Formation (Fig. III.5; Vicente et al., 1979) also locally known as the Chilcane Formation (Benavides, 1962). This formation crops out only northwest of Yura (Fig. III.4) and consists of fine-grained red beds intercalated with few limestone strata and many thick evaporite beds, indicating that the regional climate continued to be dominantly arid. One of the limestone beds yielded a Coniacian (~90-~85 Ma) ammonite (Callot et al., 2008).

This rapid evolution from a backarc which had been predominantly marine since ~185 Ma (Boekhout et al., 2013) toward distal alluvial to shallow coastal environments (Fig. III.2), indicates that a significant regression developed starting ~90 Ma (Jaillard, 1994; Callot et al., 2008). This change was accompanied by a complete switch in basin polarity: whereas the backarc had deepened toward the southwest until ~90 Ma, around this date it started to be fed from the southwest with reddish, fine- to coarse-grained, volcaniclastic detritus (Callot et al., 2008). It has to be noted that the Querque formation generally exhibits some deformation, because it either suffered the abrupt emplacement of the overlying Late Cretaceous slump deposits, or was involved in it.

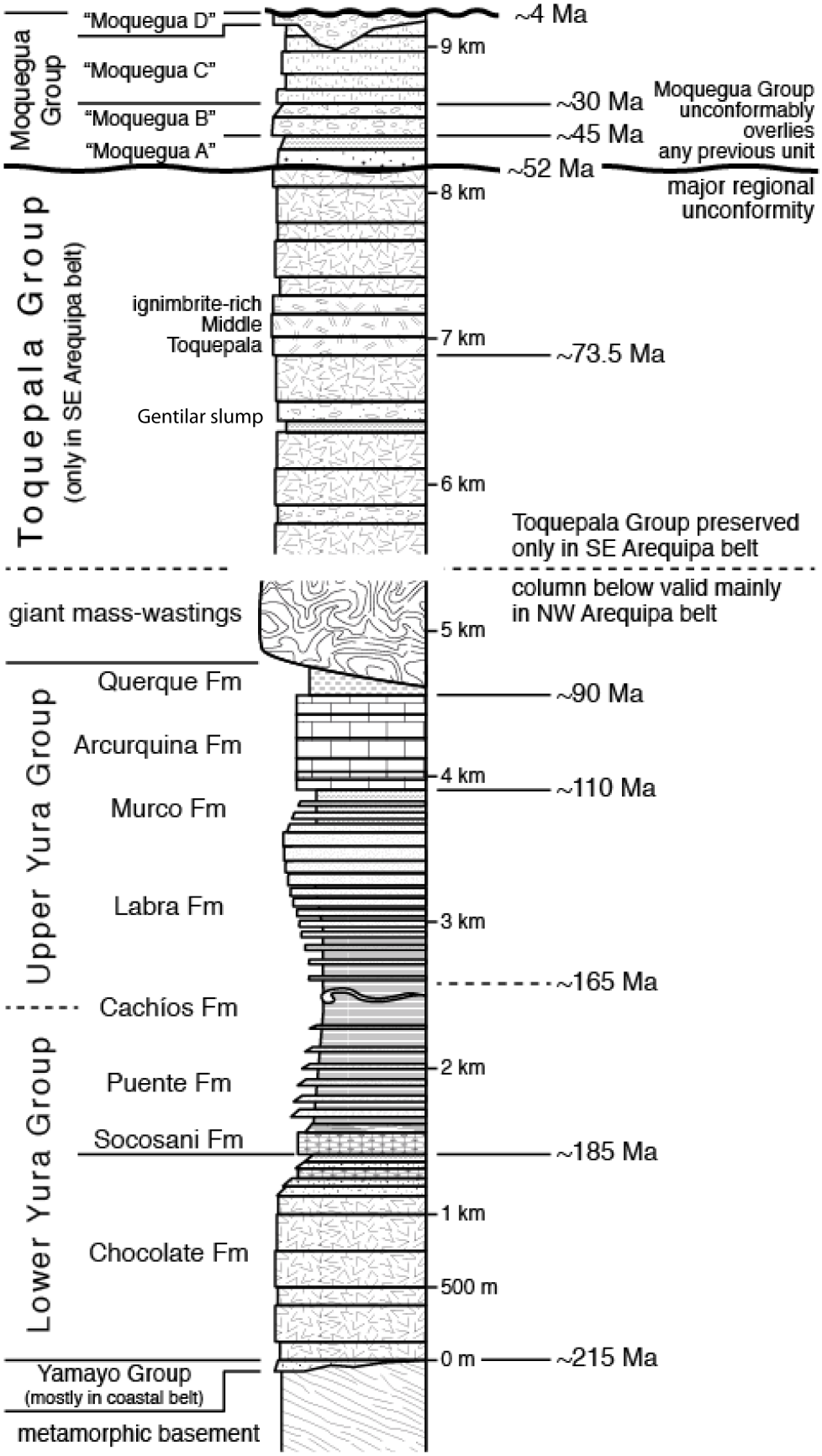

Figure III.5: Stratigraphic log for the Arequipa belt region from a literature compilation and our own observation and data.

III. 3. D – Late Cretaceous slump deposits.

The Late Triassic to mid Cretaceous succession described above is overlain by what has been described as the 'Ayabacas Formation' (Callot et al., 2008). In the study area, this unit appears to consist of a number of coalescent large-scale slump deposits (Fig. III.5) that involve deformed and/or fragmented masses of Late Jurassic to Late Cretaceous strata (Yura, Huanca, and Huambo areas) or ~10–100 m-sized olistoliths of Upper Yura quartzarenites and mid-Jurassic graywackes (Carahuaya area; Fig. III.4). These deposits may apparently reach a total thickness well in excess of 0.5 km and we suggest below that, in the Arequipa belt, they formed during the ~84–77 Ma interval. However, they do not consist of one single gravitational collapse event as the Ayabacas Formation of Callot et al. (2008), for this reason we will here refer to "the Late Cretaceous slump deposits".

III. 3. E – Toquepala Group.

Southeast of ~71.7°W a >3 km-thick volcanic units crops out (Fig. III.3), the Toquepala Group (Fig. III.5). It consists of a variety of volcanic and volcaniclastic rocks. Most lavas are andesitic and altered, especially in its lower section, which remains undated. The Middle Toquepala Group is characterized by coalescent, thick ignimbrites (Fig. III.4), on which we provide below new ages, whereas its upper section hosts major porphyry copper deposits and related rocks dated between ~62 and ~52 Ma (Clark et al., 1990; Quang et al., 2003; Simmons et al., 2013).

Logical correlation with the plutonic data in the Arequipa belt suggests that the Toquepala Group started to accumulate when plutonism resumed in the Arequipa belt i.e. ~90 Ma ago (see section III. 3 E). This assumption implies that the Querque Formation, which is only known northwest of Yura, is a time-equivalent of the lowermost Toquepala Group (Fig. III.4), implying in turn that Late Cretaceous slump deposits may have affected the lowermost Toquepala Group. The Lower Toquepala Group indeed includes in the Gentilar section (Fig. III.4) a ~30 m-thick member characterized by slumped volcaniclastic strata, termed here the Gentilar slump deposit.

III. 3. F – Copper-bearing late volcanic systems.

Porphyry suites, including large copper deposits, occur in the LCH (Cerro Verde, Santa Rosa) and its southeastern extension (Cuajone, Quellaveco, Toquepala) (Fig. III.4). Moreover, the remnants of a copper-bearing paleovolcano crop out at Cerro Negro, ~5 km ESE of Cerro Verde (Table III.1; Fig. III.3 and III.6). It has to be noted that porphyries typically emplace between 1.5 and 3–4 km beneath the top of (paleo)volcanoes, in magmatic conducts that connect(ed) plutonic reservoirs with the surface of the volcanic arc (Sillitoe, 1973, 2010). It is therefore noteworthy that, at the five localities mentioned above, the porphyries intrude plutons that had formed slightly earlier and likely at a deeper structural level (Fig. III.6; Table III.1).

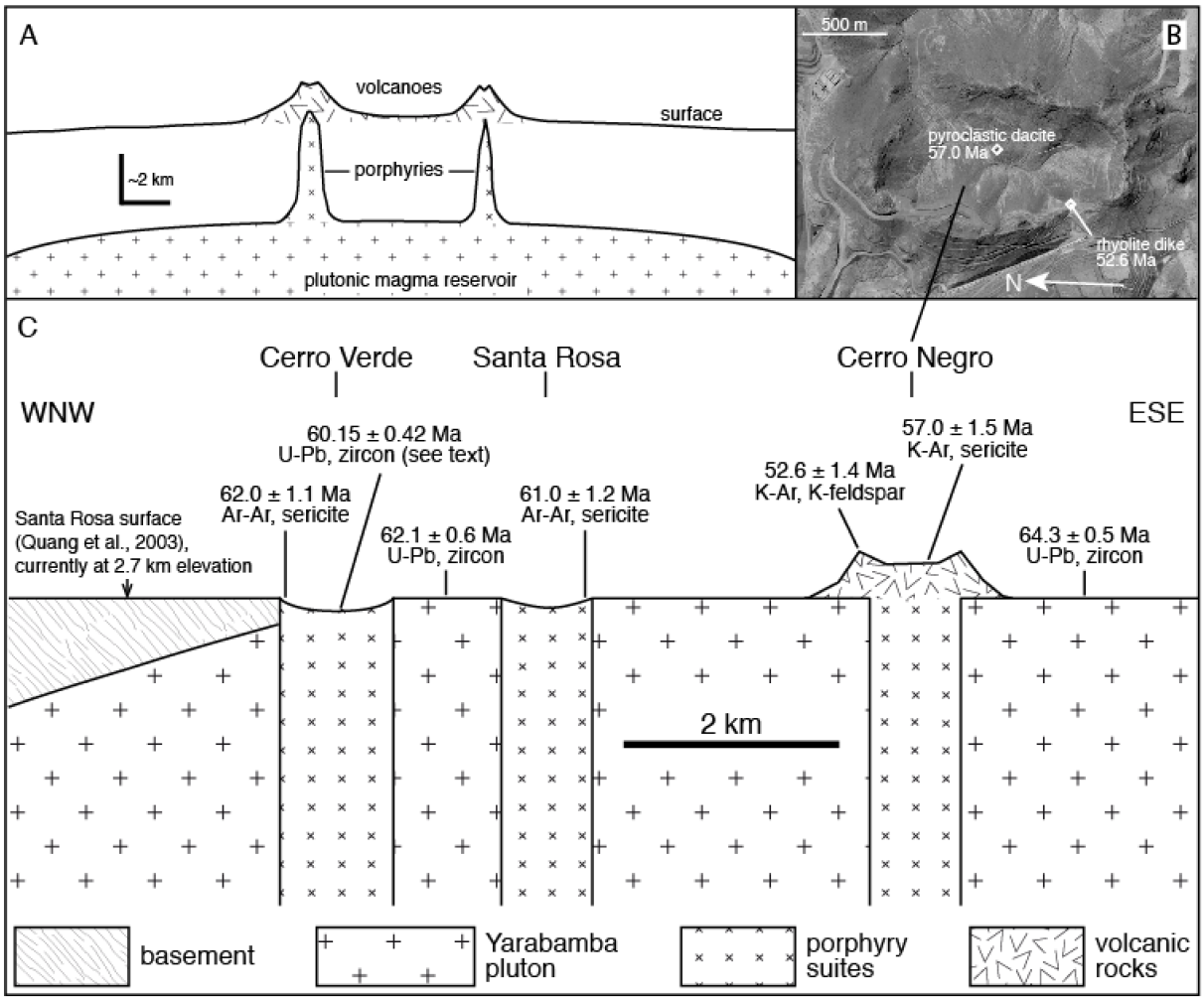

Figure III.6: A. Cartoon cross-section illustrating the emplacement model for porphyries after Sillitoe (2010). B. Satellite image of the Cerro Negro paleovolcanoe (16.548°S–71.556°W) and localization of the different disponible ages. C. Sketch of the geological relationships in the Cerro Verde mining district. No vertical scale. See references for ages in Table III.1

	Cerro Verde	Santa Rosa	Cerro Negro	Cuajone	Quellaveco	Toquepala
Volcanic rocks (at or near paleosurface)			52.6 ± 1.4* 57.0 ± 1.5**			
Porphyries (1.5–4 km depth)	59.8 ± 0.6 60.5 ± 0.6			53.5 ± 0.5 55.6 ± 0.6 56.2 ± 0.7	54.3 ± 0.6 55.9 ± 0.3 58.41 ± 0.5	54.3 ± 0.6 56.8 ± 0.6
Hydrothermal alteration	61.8 ± 0.7° 62.0 ± 1.1°	61.0 ± 1.2°		52.4 ± 1.7°		
Intruded pluton (≥3 km depth)	62.1 ± 0.6		64.3 ± 0.5	64.2 ± 0.9 65.1 ± 0.8	59.5 ± 0.2	61.4 ± 0.8
References	*Mukasa, 1986; Quang et al., 2003*	*Quang et al., 2003*	*Bidgood, 2000; Demouy et al., 2012*	*Simmons et al., 2013; Clark et al., 1990*	*Sillitoe and Mortensen, 2010*	*Simmons et al., 2013*

Table III.1: Published ages related to Late Cretaceous – Lower Paleogene magmatic activity in the Arequipa Belt of southern Peru. All ages are U-Pb on zircon, except for: * = K-Ar age on K-feldspar; ** = K-Ar age on sericite and ° = Ar/Ar age on sericite. See references for details.

In particular, in the Cerro Verde area, a subhorizontal erosional surface, the Santa Rosa «pediment » of Quang et al. (2003), affects plutonic rocks as young as ~62 Ma and is covered by volcanic rocks as old as ~57 Ma (Fig. III.6; Table III.1). This imply that at least 2 km of exhumation occurred between ~62 and ~57 Ma. We also note that porphyry copper deposits emplaced during this period of exhumation. In particular, northeast of Moquegua (Fig. III.4), copper-bearing porphyry suites show that volcanic systems were active as late as 53.5 ± 0.5 Ma (zircon U-Pb age; Simmons et al., 2013) or 52.2 ± 1.2 Ma (muscovite ^{40}Ar-^{39}Ar age; Clark et al., 1990) (Table III.1), indicating that the volcanic arc was still located along the Arequipa belt at that time. The arc subsequently left the Arequipa belt and rapidly migrated ~100-150 km to the north (Fig. III.2), where it generated the Andahuaylas-Yauri batholith (Perelló et al., 2003). The oldest dates obtained in this batholith are ~48 Ma (Perelló et al., 2003; Carlotto, 2013). The northward volcanic arc migration from the Arequipa Belt to the Adahuaylas-Yauri batholith in Cuzco region occured between ~52 and ~48 Ma. It was most likely due to slab flattening (Clark et al., 1990; Sandeman et al., 1995; James and Sacks, 1999; Carlotto, 2013). The arc remained in this northern position between ~45 and ~31 Ma (Perelló et al., 2003), started to migrate back

southwestwards about 30 Ma ago (Mamani et al., 2010), and currently coincides with the Western Cordillera. The Arequipa belt has therefore belonged to the Andean forearc since ~50 Ma (Fig. III.2).

III. 3. G – Major regional unconformity.

The top of the Late Paleozoic to Lower Eocene age stratigraphic succession described above is capped by an unconformity at least erosional and generally angular. The base of the Moquegua Group that overlain the unconformity has been estimated to be ~50 Ma (Roperch et al., 2006). This unconformity clearly post-dates the major extensional deformation episode characterized by normal faulting and tilting (Fig. III.3), which affected coherently the previous succession, as young as ~60 Ma. This major unconformity thus expresses that significant extensional deformation developed in the Arequipa region during the ~60-50 Ma interval.

III. 3. H – Moquegua Group.

All Cenozoic terrestrial forearc deposits of southern Peru, east of ~74.4°W, form the Moquegua Group. Depending on the area, these mostly continental deposits overlie the basement, Mesozoic sedimentary or plutonic rocks, and/or Toquepala volcanic rocks, locally displaying (and generally implying) stratigraphic onlap. The Moquegua Group was deposited in independent sub-basins and encompasses four units that are labelled "Moquegua A" to "Moquegua D" and characterized as follows.

a – Lower Moquegua subgroup.

Because the "Moquegua A" (MoqA) and "Moquegua B" (MoqB) units share a number of features and were deposited in the same areas, locally without a clear discontinuity between them, they are grouped here in the "Lower Moquegua subgroup" (MoqA+B). The 100–200 m-thick MoqA unit consists of dominantly fine-grained red beds, locally with gypsum. Its base, and thus the base of the entire Moquegua Group, is a major discontinuity that we infer to be diachronous.

The 150–250 m-thick MoqB unit is coarser than the MoqA but highly variable in lithology, depending on location in the sub-basins. Dominantly coarse conglomerates of fluvial

origin laterally grade into reddish sandstones and siltstones deposited in apparently endorrheic alluvial environments, locally including gypsum and/or aeolian sandstones.

Both the MoqA and MoqB units include very little to no bedded pyroclastic material and therefore display a dominant reddish tinge. This scarcity of visible contemporaneous volcanic material is likely to reflect that the coeval arc was located ~100-150 km to the north, and that it generated almost no ignimbrites and pyroclastites significant enough to reach the study area (although the Andahuaylas-Yauri batholith was clearly productive; Perelló et al., 2003). However, the base and top of the MoqB unit are respectively dated at 44.5 ± 0.4 Ma and 30.4 ± 0.5 Ma from tuff layers, albeit in distinct areas (^{40}Ar-^{39}Ar ages; Roperch et al., 2006). The age of the volcanic event represented by the lower tuffite is thus similar to one of the oldest ages known in the Andahuaylas-Yauri batholith. These age constraints allow calculating depositional rates for the MoqB unit in the 10–20 m/Myr range, but are likely to have varied in time and space.

Both units also commonly exhibit synsedimentary extensional features and therefore accumulated during active normal faulting. Several outcrops show that these normal faults are post-dated by the Moquegua C (MoqC) unit, which only rarely shows distributed extensional features.

b – "Moquegua C" unit.

In contrast with the Lower Moquegua, the MoqC unit consists of dominantly tuffaceous volcaniclastic strata and intercalated lacustrine deposits, pyroclastic beds, and large ignimbrite flows, and therefore exhibits a dominantly whitish color. This 200-600 m-thick unit was deposited over a significantly broader area than the MoqA+B. Its base is dated 30 Ma in the Moquegua area and its top is markedly diachronous, ranging from ~23 to possibly ~13 Ma (Sempere et al., 2004; 2014; Roperch et al., 2006). Depositional rates for the MoqC unit are estimated to have been in the 40–70 m/Myr range, but are likely to have varied in time and space.

c – "Moquegua D" unit.

The "Moquegua D" (MoqD) unit is distinct in that it accumulated after a period of marked erosion (Fig. III.2C and III.3). It mostly consists of locally up to 300 m-thick conglomerates that infill incised paleovalleys (especially in the Río Tambo valley) and/or onlap over erosional paleosurfaces (south and west of Arequipa); it also includes large ignimbrite flows and tuffs. Its base is diachronous, locally as old as ~14 Ma but otherwise ~10 Ma; its top is slightly younger than 4.9 Ma, and estimated to be ~4.5 Ma (Sempere et al., 2004; 2014). Depositional rates for the

MoqD vary considerably with locality, and show a maximum value of ~60 m/Myr in the lower Tambo valley. Except for pyroclastic deposition, erosion has apparently prevailed everywhere since ~4.5 Ma.

III. 3. I – Huanca red beds.

In the northwest part of the study area and northeast of the Huanca normal fault, the Ayabacas Formation is unconformably overlain by the ~2.5 km-thick, SW-dipping Huanca Formation (Fig. III.3). This markedly coarsening-upward unit is apparently devoid of volcanic layers and includes (1) a ~0.3 km-thick basal member consisting of red mudstones, siltstones, and sandstones, which rapidly grades laterally and vertically into (2) a ~2.2 km-thick main member composed of conglomerates and minor coarse red sandstones. Clasts in the conglomerates mostly consist of quartzarenites, limestones and altered andesites, but severely weathered plutonic rocks appear in the uppermost part of the unit at Chilcane (Fig. III.4). Most clasts are subrounded (to subangular) and their maximum diameter increases upwards to reach sizes well in excess of 0.5 m (>1 m in the case of andesites). These conglomerates have long been considered to represent syntectonic deposits of the early Andes, and traditionally thought to be of Late Cretaceous (Vicente et al., 1979; Vicente, 1989) or Paleogene age (Cruz, 2002). We document below that the Huanca red beds are most likely a partial time-equivalent of the Lower Moquegua subgroup.

III. 3. J – Liquirca Formation.

In the same part of the study area, the Huanca red beds are unconformably overlain by a ~500 m-thick whitish unit of tuffaceous volcaniclastic deposits of very variable grain size. Lacking a proper name and being undated, we refer to this unit as the Liquirca Formation and document below that it is younger than ~18 Ma. The Liquirca and Huanca formations are unconformably covered by the Ampato-Sabancaya volcanic plateau, of latest Neogene age.

III. 4 – SAMPLING

III. 4. A – Rationale and targets

A major issue emerges from the geology of the Arequipa region as reviewed above. It is indeed striking that the magmatic arc flare-up reported between ~70 and ~62 Ma near Cerro Verde (Demouy et al., 2012) was immediately followed in the same area by batholith exhumation between ~62 and 57 Ma (Fig. III.6). Moreover, regional extensional deformation characterized by normal faulting and tilting affects coherently the stratigraphic succession below a regional unconformity roughly ~60-50 Ma in age. Slightly after, the arc migrated northwards between ~52 and ~45 Ma. Because this close succession of events may document a causal chain and therefore provide precise clues regarding the Andean evolution, targets in this study were identified on this basis (Table III.2). I focused on fission-track dating, and zircon U-Pb dating. The methods and protocols used are detailed in chapter II and in appendices.

III. 4. B – Sampling

a – Magmatic flare-up

In order to better define and understand the mentioned magmatic flare-up, we collected for zircon U-Pb dating four samples of volcanic rocks (three from the ignimbrite-rich Middle Toquepala Group, and one from a ~30 m-thick rhyolite dike emplaced in a normal fault). Because the Linga unit emplaced during the flare-up, we addressed the issue of its cooling and thermal impact in the area by collecting two samples, respectively taken from its northeast (1M09) and southwest (1M25) borders for apatite fission-track dating.

b – La Caldera Horst

We sampled the LCH for fission-track dating, mainly at Mollebaya, Cantera Cayhua, and in the Cerro Verde area (Fig. III.4). Samples were collected at altitudes ranging from 1650 m (Cantera Cayhua) to 2959 m (Churajón), but most of them are from elevations between 2125 and 2525 m (Table III.2). Samples included seven pre-Cretaceous rocks as well as two samples of Late Cretaceous plutonic rocks older than 75 Ma (1M16, 1M24; Fig. III.4). We collected these nine

samples from rocks that pre-date the assumed flare-up development. Because no plutonic rocks are known in the Yura half-graben northeast of the LCH, we sampled a rhyolite dike that provided a tenth >75 Ma-old sample (1M23) for comparison with the other areas.

c – Huanca red beds

We collected four samples (1M28 to 1M31) along the ~2 km-thick Huanca section at Cerro Carapunta (Table III.2, Fig. III.3) because we thought this unit could represent syntectonic deposits of possible Late Cretaceous and/or Paleogene age. Additionally, ~42 km to the southeast, at Chilcane, we sampled the very coarse uppermost part of the Huanca conglomerates (Fig. III.4) (this horizon lie ~2.5 km above the base of the unit). In this conglomerate, we sampled the matrix (sample 1M20) but also similar-looking plutonic (dioritic) clasts with diameter size >0.4 m and displaying intense weathering (sample 1M19).

We processed these six detrital samples for zircon U-Pb dating and zircon and apatite fission-track dating, expecting apatites and zircons from the Huanca red beds to provide information about the crystallization and exhumation history of their sources, as well as a proxy for their time of deposition. Because this unit is ≤2.5 km-thick and was buried beneath ≤1 km of younger strata, it seems unlikely that its fission-tracks in apatite were significantly annealed during burial. Moreover, we observed no evidence of contact metamorphism or hot fluid circulation at the sites we sampled. Furthermore, we sampled an ignimbrite located ~30 m above the Liquirca/Huanca contact for zircon U-Pb dating in order to place a lower bound on the age of the Huanca red beds.

Sample	Lithology	Unit	structural domain	locality or area	Lat.(°)	Long.(°)	Elev. (m)	zU-Pb	zft	aft
pre-Cretaceous rocks in La Caldera horst										
1M14	metarenite	basement	LCH	Cerro Verde area	-16.51331	-71.63135	2514		x	x
1M17	pegmatitic dykes	basement	LCH	Mollebaya	-16.48177	-71.4617	2549			x
1M18	metarenite	basement	LCH	Mollebaya	-16.4816	-71.46413	2522		x	
1M15	gabbro	Liassic mafic plutonic unit	LCH	Cerro Verde area	-16.47991	-71.61873	2370	o		x
1M21	foliated diorite	Liassic mafic plutonic unit	LCH	Cantera Cayhua	-16.36188	-71.78576	1646	o	x	x
1M22	aplite	dyke in 1M21 Liassic diorite	LCH	Cantera Cayhua	-16.36188	-71.78576	2975	x		x
1M27	quartz-diorite	Churajón laccolith	LCH	Churajón	-16.67595	-71.34001		o		x
~90-76 Ma magmatism										
1M09	quartz-diorite	base of Linga laccolith	Linga graben	Cerro Verde area	-16.55688	-71.44484	2480	o		x
1M16	quartz-diorite	Late Cretaceous plutons	LCH	Cerro Verde area	-16.46333	-71.62493	2274	o		x
1M23	dacite	dyke in Chocolate Fm	Yura half-graben	~6 km SW of Yura	-16.28733	-71.73173	2380	o		x
1M24	diorite	Late Cretaceous plutons	LCH	6 km SW of Uchumayo	-16.547026	-71.70082	2126	o		x
~70-62 Ma magmatic flare-up (volcanic rocks)										
1M34	rhyolite	dyke in normal fault	Linga graben	14.5 km S of Chapi	-16.84973	-71.29853	2302	x		
1M33	ignimbrite	middle Toquepala	Linga graben	16.6 km SSE of Chapi	-16.86699	-71.28114	2086	x		
1M37	ignimbrite	at local base of middle Toquepala		47 km ESE of Chapi	-16.81929	-70.88352	2145	x		
1M38	ignimbrite	at local top of middle Toquepala		45 km ESE of Chapi	-16.81664	-70.88352	2256	x		

Table III.2: Summary of all samples analyzed in this study. x, this work; o, literature

Table III.2 (suite)

Sample	Lithology	Unit	structural domain	locality or area	Lat.(°)	Long.(°)	Elev. (m)	zU-Pb	zft	aft
~70-62 Ma magmatic flare-up (plutons)										
1M25	granodiorite	top of Linga laccolith	Linga graben	2 km SW of Repartición	-16.54084	-71.79558	1707	x		x
Huanca red beds and Liquirca Formation										
1M28	red, mid- to fine-grained sandstone	~0.1 km above base of Huanca Fm	Huanca half-graben	Cerro Parapunta	-15.88321	-72.09644	4055	x	x	
1M29	conglomerate matrix	~0.9 km above base of Huanca Fm	Huanca half-graben	Cerro Parapunta	-15.89284	-72.12676	4086	x		x
1M30	red coarse sandstone with conglomeratic layers	~1.2 km above base of Huanca Fm	Huanca half-graben	Cerro Parapunta	-15.89489	-72.13488	4144	x	x	x
1M31	conglomerate matrix	~2.0 km above base of Huanca Fm	Huanca half-graben	Cerro Parapunta	-15.90835	-72.1454	4234	x	x	x
1M20	conglomerate matrix	~2.5? km above base of Huanca Fm	Huanca half-graben	Chilcane	-16.12189	-71.81254	2992	x	x	x
1M19	>30 cm-sized plutonic clasts in conglomerate	~2.5? km above base of Huanca Fm	Huanca half-graben	Chilcane	-16.12189	-71.81254	2992	x	x	x
1M73+ 3M1	ignimbrite	~30 m above base of Liquirca Fm	Huanca half-graben	6 km SE of Huanca	-16.07003	-71.8352	3618	x		x

Table III.2: Summary of all samples analyzed in this study. x, this work; o, literature

III. 5 – RESULTS

III. 5. A – Overview

Zircon U-Pb, zircon fission-track, and apatite fission-track results obtained on basement and magmatic rocks are presented in Tables III.3, III.4 and III.5, respectively; those obtained on detrital grains from the Huanca red beds are displayed in Tables III.6, III.7 and III.8, respectively. All 'central ages', 'peak ages' and 'minimum ages' (Galbraith and Laslett, 1993) reported below for fission-track results were calculated using RadialPlotter (Vermeesch, 2012, 2009) with logarithmic transformations. Peak fitting algorithm was set to automatic. Reported uncertainties are 2s.

III. 5. B – Latest Campanian–Danian magmatic flare-up

a – Volcanic rocks

The Gentilar section of the Toquepala Group exposes a ~430 m thick member composed of coalescent ignimbrites (Figs. III.4). We obtained zircon U-Pb ages of 73.3 ± 0.6 and 72.2 ± 0.9 Ma respectively on its lowermost and uppermost flows (samples 1M37 and 1M38) (Table III.3). An ignimbrite flow from the Middle Toquepala (sample 1M33) in the Carahuaya area (Fig. III.4) yielded a 69.4 ± 0.9 Ma zircon U-Pb age (Table III.3). Moreover, a ^{40}Ar-^{39}Ar age of 66.3 ± 1.0 Ma on the groundmass of an andesite flow from El Jaguay, ~16 km west of Moquegua has been obtained (F. Boekhout, pers. comm., 2014).

b – Rhyolite dike

Also in the Carahuaya area, a ~30 m-thick rhyolite dike (sample 1M34) intrudes a normal fault that separates the Toquepala Group in the east from the local Carahuaya slump deposit in the west. We obtained a zircon U-Pb age of 64.3 ± 0.5 Ma on this rhyolite dike (Table III.3).

c – Linga unit

We obtained a zircon U-Pb age of 68.7 ± 0.6 Ma on a granodiorite (1M25) sampled at the SW border of the Linga unit near Repartición (Fig. III.4 and Table III.3). The same sample yielded an apatite fission-track central age of 57 ± 12 Ma (Table III.5) with a mean D_{par} value of 1.71 mm. This sample thus underwent rapid cooling from ~800° (assumed temperature of crystallization) to ~100°C most likely between ~69 and ~57 Ma. At the base of the >6 km-thick laccolith, a diorite (sample 1M09) dated at 89.8 ± 0.7 Ma (zircon U-Pb age; Demouy et al.; 2012) yielded an apatite fission-track age of 92 ± 24 Ma, and a D_{par} value of 2.7 mm (this study), suggesting that the rocks from sample 1M09 cooled rapidly from 800°C to ~100°C likely around ~90 Ma.

III. 5. A – La Caldera Horst

a – Mollebaya

Near Mollebaya, at 2525 m elevation and ~2 km southwest of the inferred extension of the Agua Salada normal fault (Fig. III.4), we obtained an apatite fission-track age of 58 ± 13 Ma with a mean D_{par} of 1.93 mm on a pegmatitic vein intruding Proterozoic amphibolites (sample 1M17, Table III.5). A metarenite located 260 m to the west (sample 1M18) yielded a zircon fission-track age of 56 ± 5 Ma (this study, Table III.4). Although they were obtained on nearby samples and on two minerals with distinct closure temperatures, these two ages are indistinguishable.

b – Cantera Cayhua

At Cantera Cayhua, a foliated diorite (sample 1M21, Fig. III.4) is cut by ~0.1 m-thick subvertical aplite dikes (sample 1M22). We obtained a zircon U-Pb age of 176.0 ± 1.2 Ma on one of the aplite dikes (Table III.3). The diorite (sample 1M21) provided a zircon fission-track age of 66 ± 7 Ma (Table III.4). Consistent apatite fission-track ages of 57 ± 10 (D_{par} 2.13) and 59 ± 13 Ma were obtained for the diorite and the aplite dike, respectively (Table III.5). This indicates that the Cantera Cayhua area underwent cooling from ~300° to ~100°C between ~73 and ~46 Ma.

						Apparent ages (Ma)			
Sample	**Lab**	**Lithology**	**Unit**	**Lat.**	**Long.**	**N**	**$^{206}Pb/^{238}U$**	**± 2σ**	**MSWD**
1M22	LMV	aplite	dyke in Liassic mafic plutonic unit	-16.36188	-71.78576	16	176.0	1.2	0.28
1M25	LMV	granodiorite	top of Linga laccolith	-16.54084	-71.79558	6	68.7	0.6	0.18
1M33	UNIL	ignimbrite	middle Toquepala	-16.86699	-71.28114	12	69.4	0.9	7.1
1M34	LMV	rhyolite	dyke in normal fault	-16.84973	-71.29853	30	64.3	0.5	0.35
1M37	UNIL	ignimbrite	at local base of middle Toquepala	-16.81929	-70.88352	17	73.3	0.6	4.8
1M38	UNIL	ignimbrite	at local top of middle Toquepala	-16.81664	-70.88352	9	72.2	0.9	4.9
1M73 / 3M1	UNIL	ignimbrite	~30 m above base of "white strata" unit	-16.07003	-71.83520	12	16.5	0.3	5

Table III.3: Zircon U-Pb ages. Age determination were performed with different settings in each laboratory, experimental conditions are described in the supplementary materials.

c – Late Cretaceous, >75 Ma-old magmatism

We collected sample 1M24 at 2131 m elevation from a diorite in the western Tiabaya unit dated at 76.7 ± 0.4 Ma (zircon U-Pb age *(Demouy et al., 2012)*; Table III.2), and obtained an apatite fission-track age of 67 ± 10 Ma (D_{par} 2.56 µm). This indicates rapid cooling from ~800° to ~100°C most likely between ~76 Ma (crystallization age) and ~67 Ma. In the Tiabaya eastern unit, we collected a quartz diorite (sample 1M16) dated 82.3 ± 0.4 (Demouy et al., 2012) which yielded a 73 ± 23 Ma apatite fission-track central age.

a – Cerro Verde area

In addition of 1M16 we collected in the Cerro Verde area two other samples from different units. A basement arenite, sample 1M14, located ~1.4 km beneath the Lluclla fault plane and currently at 2505m elevation yielded zircon and apatite fission-track ages respectively of 53 ± 10 and 37 ± 9 Ma. Moreover, we collected at 2363 m elevation a gabbro (sample 1M15) dated at 200.0 ± 1.1 Ma (Demouy et al., 2012), it yielded a central age of 47 ± 8 Ma zircon fission-track age.

b – Churajón

Although it is consistent with the ages reported elsewhere in the LCH, the apatite fission-track age of 49 ± 25 Ma obtained at Churajón on a quartz-diorite (sample 1M27) dated 160.5 ± 0.8 Ma (zircon U-Pb age; Demouy et al., 2012) is poorly constrained as only four grains could be analyzed.

Sample	Unit	Lat. (°)	Long. (°)	Elev. (m)	N	ρd	rse(ρd)	Nd	P(χ^2) (%)	D (%)	Pooled age (Ma)	Central age (Ma)
1M14 (MN)	basement	-16.51331	-71.63135	2514	29	215622	1.31	9115	0.84	23	53 ± 9	53 ± 10
1M18 (EH)	basement	-16.48160	-71.46413	2522	20	197600	1.25	10126	63	<< 1	56 ± 5	56 ± 5
1M21 (EH)	Liassic mafic plutonic unit	-16.36188	-71.78576	1646	21	200000	1.13	9115	94	<< 1	66 ± 7	66 ± 7

Table III.4: Zircon fission-track ages. Age determinations were performed by M. Noury (MN) with ζ = 128 ± 9 and E. Hardwick (EH) with ζ = 174 ± 3 for glass dosimeter CN1. N, number of grains counted; ρ d, dosimeter track density (fluence); rse(ρd), relative standard error on fluence; Nd, number of tracks counted to determine the reported fluence; P(χ^2), probability that the single grain ages represent one population; D, age dispersion. Pooled and Central ages are reported associated with 2σ standards errors

Sample	Unit	Crystallization age	Latitude (°)	Longitude (°)	Elevation (m)	N	ρ_d	rse(ρ_d)	U (ppm)	P(χ^2) (%)	D (%)	Pooled age (Ma)	Central age (Ma)	Mean D_{par}
1M09	base of Linga laccolith	89.8 ± 0.7 Ma (d)	-16.55688	-71.44484	2480	20	597455	1.29	8.97	35	22	88 ± 20	92 ± 24	2.7
1M14	basement	-	-16.51331	-71.63135	2514	16	642932	1.14	6.76	39	8	37 ± 9	37 ± 9	1.51
1M15	mafic plutonic unit	200.0 ± 1.1 Ma (d)	-16.47991	-71.61873	2370	20	597348	1.11	45.3	54	4	47 ± 8	47 ± 8	2.5
1M16	Late Cretaceous plutons	82.3 ± 0.4 Ma (d)	-16.46333	-71.62493	2274	10	633551	1.09	11.79	57	35	69 ± 15	73 ± 23	2.38
1M17	basement	-	-16.48177	-71.4617	2549	19	597455	1.29	20.76	81	<< 1	58 ± 13	58 ± 13	1.92
1M21	mafic plutonic unit	Liassic (d)	-16.36188	-71.78576	1646	20	619568	1.11	12.54	73	1	56 ± 10	57 ± 10	2.13
1M22	dyke in 1M21 diorite	176.0 ± 1.2 Ma (n)	-16.36188	-71.78576	2975	18	614966	1.15	13.65	29	13	59 ± 12	59 ± 13	-
1M23	dyke in Chocolate Fm	≈ 76 Ma (n)	-16.28733	-71.73173	2380	20	600582	1.23	10.55	66	5	43 ± 10	43 ± 10	2.28
1M24	Late Cretaceous plutons	76.7 ± 0.4 Ma (d)	-16.547026	-71.70082	2126	20	605673	1.24	19.04	88	1	67 ± 10	67 ± 10	2.56
1M25	top of Linga laccolith	68.7 ± 0.5 Ma (n)	-16.54084	-71.79558	1707	20	600983	1.31	12.84	2	27	56 ± 10	57 ± 12	1.77
1M27	Churajón laccolith	160.5 ± 0.8 Ma (d)	-16.67595	-71.34001	2975	4	586337	1.11	4.44	70	<< 1	49 ± 25	49 ± 25	-

Table III.5: Apatite fission-track ages. All fission-track age determinations were performed by M. Noury with $\zeta = 254 \pm 12$ for glass dosimeter IRMM540. N, number of grains counted; ρd, dosimeter track density (fluence); rse(ρd), relative standard error on fluence; U, mean uranium content in the analyzed grains (in ppm); P(χ^2), probability that the single grain ages represent one population; D, age dispersion. Pooled and Central ages are reported associated with 2σ standards errors. Sources for crystallization ages: (d) Demouy et al. (2012); (n) this study.

III. 5. B – Yura half-graben

South of Yura and North of Cantera Cayhua, we obtained a zircon U-Pb age of 76.1 ± 0.1 Ma and an AFT age of 43 ± 10 Ma for a rhyolite dike (sample 1M23) that cuts across the Chocolate formation (Fig. III.3).

III. 5. C – Huanca red beds

a – U-Pb dating of detrital zircons

Kernel density (KD) plots of zircon U-Pb ages show that the age signal is composed of different populations (Table III.6 and Fig. III.8). The proportion of >500 Ma-old zircons clearly increases upsection, while that of younger zircons decreases (except in the uppermost sample 1M20, which yielded a younger population). Most of the grains are >220 Ma, except for the uppermost and two lower samples where a 90–110 Ma component predominates. Older peaks appear at ~250 Ma, ~600 Ma, 1.1–1.3 Ga, and 1.9–2.3 Ga. The youngest detrital zircon U-Pb ages are found in the uppermost sampled horizon and cluster around 81.9 ± 1.0 Ma. The dioritic clasts from the same horizon (grouped in 1M19) all yielded nearly identical zircon U-Pb ages of on average 80.6 ± 0.4 Ma.

b – Age of the base of the Liquirca Formation

We obtained a U-Pb age of 16.5 ± 0.3 Ma on 13 zircon grains extracted from the ignimbrite located ~30 m above the base of the Liquirca Formation (sample 3M1, Table III.3), which unconformably overlies the Huanca red beds.

c – Fission-track analysis of detrital zircons and apatites

Depending on the sample, the zircon fission-track age distribution shows 1 to 3 populations (Table III.7). All samples yielded peak ages between ~62 and ~54 Ma except 1M31. However, in samples 1M28 and 1M31 the younger population peaks instead respectively at 54 ± 7 and 38 ± 15 Ma. The proportion of zircon fission-track ages older than 110 Ma increases upsection (Table III.7), excepting the uppermost sample 1M20 which likely have different source area (Fig. III.4).

The distribution of apatite fission-track ages (Table III.8) shows 1 or 2 age peaks in each sample (Fig. III.8). All samples (except 1M31) yielded a peak centered between 78 and 83 Ma, but the proportion of apatites with >100 Ma ages increases upsection (Fig. III.8). The uppermost sample 1M20 carries a signal younger than all other samples, with a peak age of 39 ± 10 Ma representing 33 % of the grains.

Excepting sample 1M31, apatite and zircon fission-track minimum ages are increasingly younger upsection, as are zircon fission-track minimum ages (Fig. III.8). These minimum ages range from 41 ± 15 to 92 ± 13 Ma for apatites, and from 38 ± 12 to 65 ± 19 Ma for zircons, which however appear systematically younger that the formers (Table III.7 and III.8).

In sample, 1M28, from ~100 m above the base of the Huanca Formation, the only zircon fission-track age population peaks at 54 ± 10 Ma (representing 84 % of all dated zircons) and yields a minimum age of 37 ± 16 Ma. The entire AFT age population forms one peak at 83 ± 10 Ma, but individual ages as young as 37 ± 23 Ma were measured.

Sample 1M19, from the uppermost Huanca Formation, groups dioritic clasts that yielded a consistent zircon U-Pb age of 80.6 ± 0.4 Ma. These clasts yielded a zircon fission-track age of 48 ± 6 Ma, and AFT peak ages of 34 ± 14 Ma (9 %) and 87 ± 17 Ma (91 %). The zircon and apatite minimum ages calculated for this sample are 48 ± 6 and 51 ± 10 Ma, respectively.

	Lithology	stratigraphic position	Lat. (°)	Long. (°)	N	Age range	P1	P2	P3	P4	CA	MA	P(χ^2)	D (%)
1M28	red, mid- to fine-grained sandstone	~0.1 km above base of Huanca Fm	-15.88321	-72.09644	78	94 - 3002	103 ± 1 (41%)	131 ± 2 (43%)	1194 ± 40 (7%)	1956 ± 46 (9%)	179 ±39	101 ±2	<< 0.01	95
1M29	conglomerate matrix	~0.9 km above base of Huanca Fm	-15.89284	-72.12676	93	100 - 3422	109 ± 1 (35%)	599 ± 10 (21%)	1205 ± 17 (24%)	2247 ± 32 (20%)	496 ±124	104 ±2	<< 0.01	120
1M30	red coarse sandstone with conglomeratic layers	~1.2 km above base of Huanca Fm	-15.89489	-72.13488	104	86 - 2897	164 ± 5 (7%)	607 ± 7 (33%)	1210 ± 12 (42%)	2310 ± 32 (18%)	947 ±128	114 ±7	<< 0.01	68
1M31	conglomerate matrix	~2.0 km above base of Huanca Fm	-15.90835	-72.14540	101	158 - 3231	250 ± 8 (6%)	596 ± 8 (30%)	1147 ± 12 (41%)	2201 ± 28 (23%)	994 ±120	201 ±16	<< 0.01	60
1M20	conglomerate matrix	top of the Huanca Fm, ~2.5 km (?) above its base	-16.12189	-71.81254	116	79 - 2388	84 ± 1 (14%)	252 ± 5 (10%)	587 ± 6 (35%)	1308 ± 13 (40 %)	565 ±98	82 ±2	<< 0.01	94
1M19	>30 cm-sized plutonic clasts in conglomerate	top of the Huanca Fm, ~2.5 km (?) above its base	-16.12189	-71.81254	74	78 - 86	80.6 ± 0.4	-	-	-	80.6	0.4	MSWD =0.94	

Table III.6: Detrital zircon U-Pb ages. All ages determinations were performed by J.-L. Paquette at Laboratoire Magmas et Volcans (Clermont Ferrand). N, number of grains analyzed; P1, P2, P3 and P4 are the population peaks, CA the central age and MA the minimum age calculated using RadialPlotter (Vermeesch, 2012); P(χ^2), probability that the single grain ages represent one population; D, individual grain age dispersion. All ages are reported associated with 2σ standards errors. The bracketed percentages in the P1 to P4 columns indicate the proportion of the total population belonging to this peak.

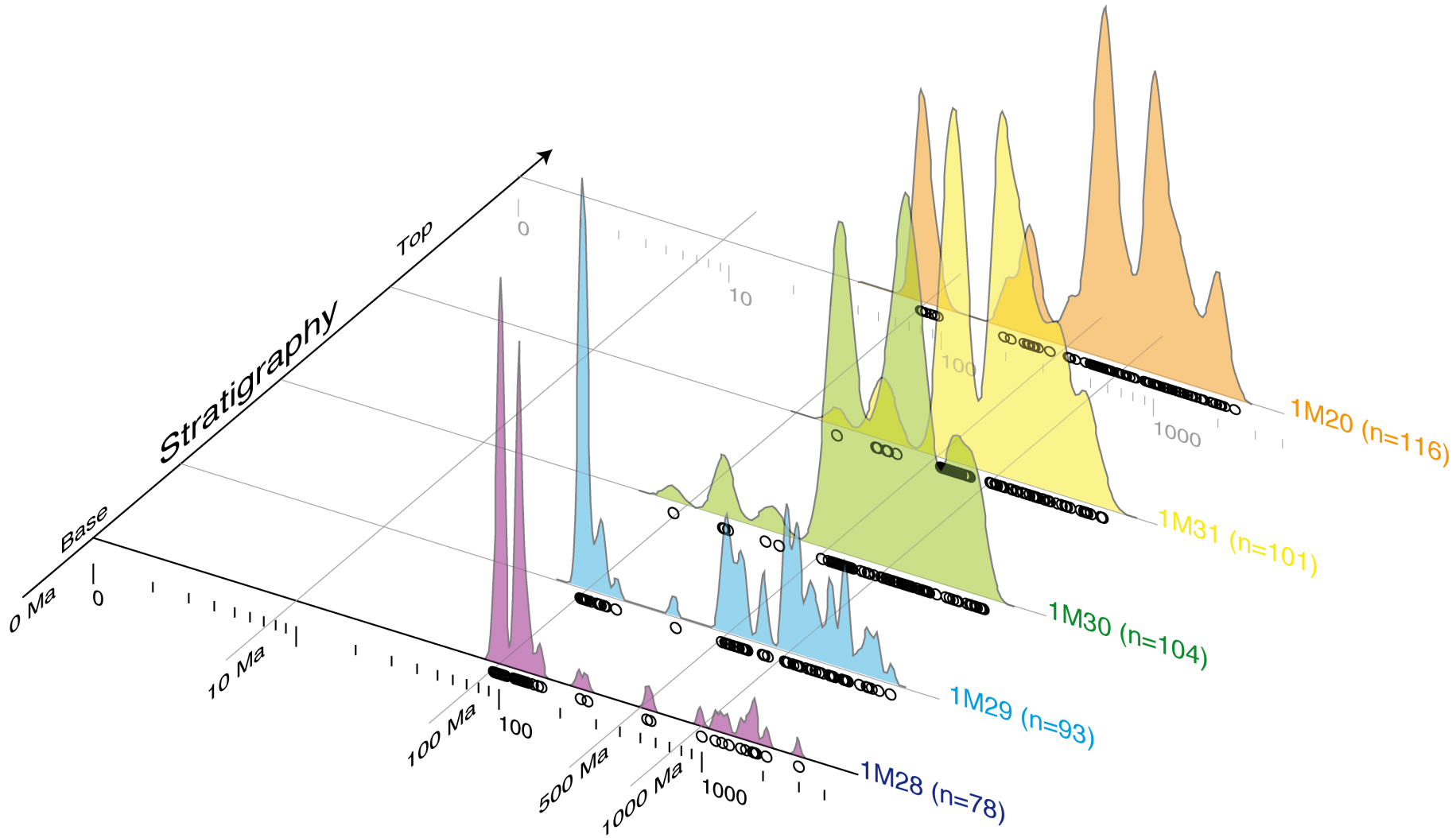

Figure III.7: Kernel density plots (Vermeesch, 2012) of zircon U-Pb ages obtained on the matrix of conglomerates from the Huanca basin

	Lithology	stratigraphic position	Lat. (°)	Long. (°)	N	Age range	P1	P2	P3	CA	MA	D (%)
1M28	red, mid- to fine-grained sandstone	~0.1 km above base of Huanca Fm	-15.88321	-72.09644	68	12 - 258	-	57 ± 10 (100%)	-	56 ± 7	50 ± 9	23
1M30	red coarse sandstone with conglomeratic layers	~1.2 km above base of Huanca Fm	-15.89489	-72.13488	100	31 - 1210	-	62 ± 18 (25%)	169 ± 36 (75%)	118 ± 16	65 ± 20	47
1M31	conglomerate matrix	~2.0 km above base of Huanca Fm	-15.90835	-72.14540	100	23 - 408	38 ± 15 (16%)	-	120 ± 26 (84%)	91 ± 13	48 ± 12	53
1M20	conglomerate matrix	top of Huanca Fm, ~2.5 km (?) above its base	-16.12189	-71.81254	69	10 - 726	18 ± 8 (4%)	60 ± 14 (52%)	153 ± 48 (44%)	79 ± 14	38 ± 12	56
1M19	>30 cm-sized plutonic clasts in conglomerate	top of Huanca Fm, ~2.5 km (?) above its base	-16.12189	-71.81254	53	30 - 108	48 ± 6 (100%)	-	-	48 ± 6	48 ± 6	0

Table III.7: Detrital zircon fission-track ages. All age determinations were performed by M. Noury with $\zeta = 128.42 \pm 8.86$ for glass dosimeter CN1. N, number of grains counted; P1, P2 and P3 are the population peaks, CA the central age and MA the minimum age calculated using RadialPlotter (Vermeesch, 2012); D, individual grain ages dispersion. All ages are reported associated with 2σ standards errors. All samples failed the χ^2 test with $P(\chi^2)=0$. The bracketed percentages in the P1, P2 or P3 columns indicate the proportion of the total population belonging to this peak.

	Lithology	stratigraphic position	Lat. (°)	Long. (°)	N	Age range	P1	P2	CA	MA	D (%)
1M28	red, mid- to fine-grained sandstone	~0.1 km above base of Huanca Fm	-15.88321	-72.09644	100	37 - 304	83 ± 10 (100%)		83 ± 6	79 ± 11	12
1M29	conglomerate matrix	~0.9 km above base of Huanca Fm	-15.89284	-72.12676	100	45 - 283	78 ± 9 (94%)	184 ± 66 (6%)	83 ± 6	77 ± 6	20
1M30	red coarse sandstone with conglomeratic layers	~1.2 km above base of Huanca Fm	-15.89489	-72.13488	93	32 - 886	81 ± 10 (100%)		84 ± 8	62 ± 17	26
1M31	conglomerate matrix	~2.0 km above base of Huanca Fm	-15.90835	-72.1454	59	47 - 626	100 ± 16 (100%)		101 ± 14	92 ± 13	17
1M20	conglomerate matrix	top of Huanca Fm, ~2.5 km (?) above its base	-16.12189	-71.81254	39	20 - 269	39 ± 10 (33%)	80 ± 16 (67%)	63 ± 10	41 ± 15	33
1M19	>30 cm-sized plutonic clasts in conglomerate	top of Huanca Fm, ~2.5 km (?) above its base	-16.12189	-71.81254	24	23 - 312	34 ± 14 (9%)	87 ± 17 (91%)	81 ± 16	51 ± 20	33

Table III.8: Detrital apatite fission-track ages. All age determinations were performed by M. Noury with $\zeta = 254 \pm 12$ for glass dosimeter IRMM540. N, number of grains counted; P1 and P2 are the population peaks, CA the central age and MA the minimum age calculated using RadialPlotter (Vermeesch, 2012); D, individual grain age dispersion. All samples failed the χ^2 test except 1M28 and 1M31 ($P(\chi^2) = 0.35$ and 0.58 respectively). All ages are reported associated with 2σ standards errors. The bracketed percentages in the P1 or P2 columns indicate the proportion of the total population belonging to this peak.

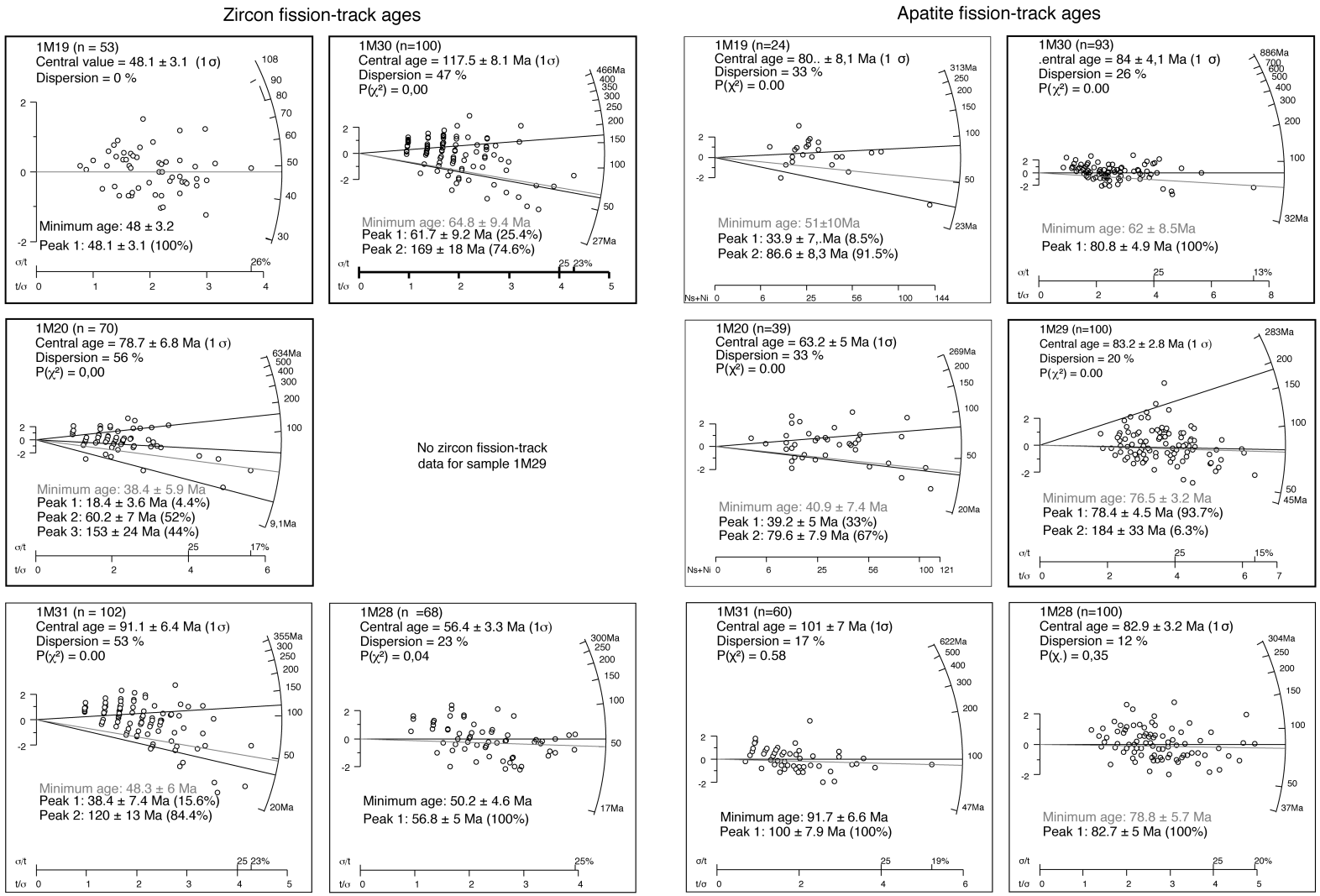

Figure III.8: Radial plots and computed central, peak(s) and minimum ages (in grey) of apatite and zircon fission-track analyses carried on the Huanca red beds sediments.

III. 6 – DISCUSSION

The observations and data presented above highlight a three-step evolution of the arc in the Arequipa belt, which apparently followed a simple, logical succession: an initial stage of arc growth (~90–74 Ma) gave way to a flare-up of the arc (~74–62 Ma), which in turn was followed by its extensional collapse (~62–52 Ma). We furthermore show that extensional conditions persisted in the region during the ~52–30 Ma interval.

III. 6. A – Initial stage of arc growth: ~90–74 Ma

a – Magmatic record

Zircon U-Pb ages by Mukasa (1986) and Demouy et al. (2012) and this study outline the growth history of the arc along the Arequipa belt (Fig. III.9). Initial pulse is documented by two zircon U-Pb ages from the SW and NE of the Linga unit (samples 1M25 and 1M09), which define a ~90–87 Ma interval. The oldest age close to the LCH, 89.8 ± 0.7 Ma (Demouy et al., 2012), is only slightly younger than a 90.7 ± 0.2 Ma age obtained for a granite located in Quebrada Guaneros (Boekhout, pers. comm., 2014) ~30 km southwest of the inferred extension of the LCH (Fig. III.3), suggesting that establishment of the arc in the LCH and initiation of arc growth occurred close to 90 Ma. This 90.7 Ma granite intrudes the Lower Toquepala and implies that the base of the Toquepala Group is older than ~91 Ma in the southwest. The Lower Toquepala Group is thus likely diachronous from SW to NE reflecting the migration of the arc during the Upper Cretaceous.

In the LCH, the Tiabaya-SE and Tiabaya-NW plutons (Fig. III.4)(Demouy et al., 2012) yielded seven ages. They define a second, longer and more voluminous 'Tiabaya pulse' during the ~84–76 Ma interval (Fig. III.9). The rhyolite dike dated at 76.1 ± 0.1 Ma in the Yura half-graben, and the diorite clasts in the upper Huanca conglomerates dated at 80.6 ± 0.4 Ma near Chilcane, may also be ascribed to this magmatic pulse.

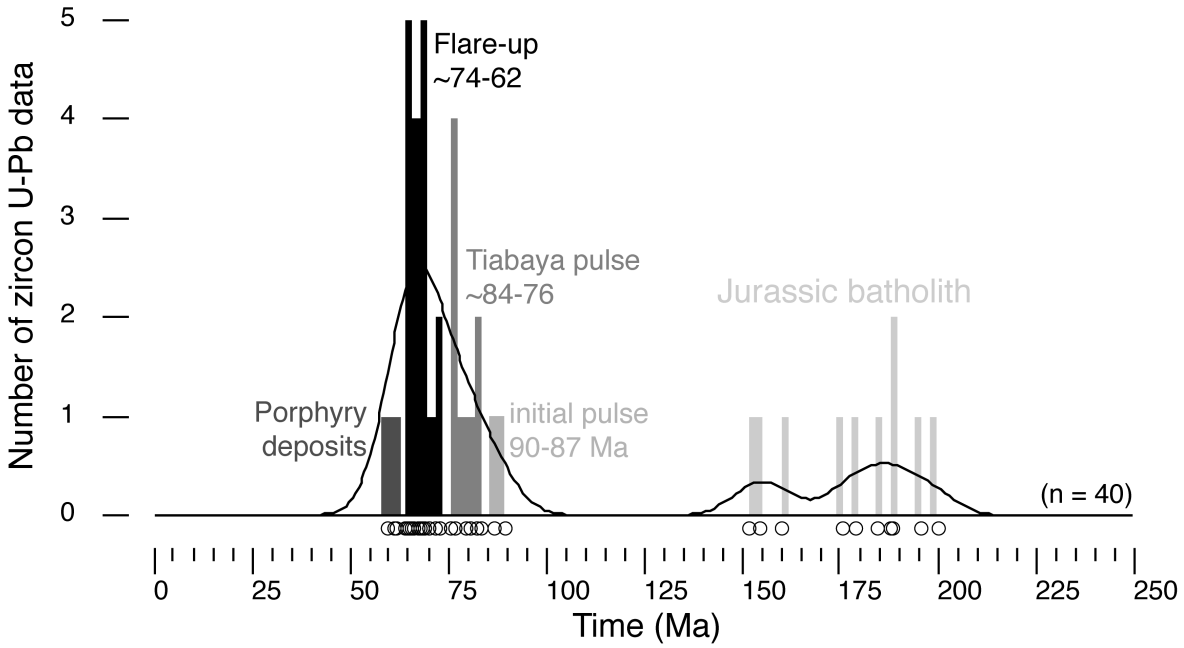

Figure III.9: Histogram and kernel density estimate (black line) for all the zircon U-Pb data available on plutonic and hypo-volcanic rocks in the Arequipa region of Southern Peru (from Mukasa, 1986; Demouy et al., 2012 and this study). The different magmatic "pulses" mentioned in the text are labeled.

b – Stratigraphic record

Continentalization of backarc. Invasion of the marine Peruvian backarc basin by reddish detrital material derived from the west began in the latest Turonian, i.e. ~90 Ma (Jaillard, 1994). In southern Peru, this change is marked by the sharp contact between the Albian to Turonian Arcurquina limestones and the overlying Querque red beds and evaporites (Fig. III.2 and III.5). Because a limestone bed in the Querque Formation yielded a Coniacian ammonite (Callot et al., 2008), this marine regression also occurred at ~90 Ma in the Arequipa belt. Thus, this regression coincided with the onset of arc growth in the LCH.

Large slump deposits. Our mapping and observations require revising aspects of Callot et al.'s (2008) conclusions about the 'Ayabacas Formation'. In the Arequipa region, our recognition of large-scale slump deposits of varied lithologies in distinct areas show that this unit does not consist of one single giant gravitational collapse but more likely of several events affecting different portions of the margin. The Carahuaya mass-wasting deposit (Fig. III.4), for instance, overlies stratified mid-Jurassic graywackes, which are also found as olistoliths within it, unlike the typical Ayabacas Formation of Callot et al. (2008).

Cincha-Lluta slump deposit. In the Yura half-graben, the sliding sole of this slump deposit was previously described as "the Cincha-Lluta overthrust" (Vicente et al., 1979; Vicente, 1989) but our observations and mapping rule out that this surface and the deformation in the overlying mass are of strictly-speaking tectonic origin. Indeed, the slump deposit exhibits a marked asymmetry in its composition, as it consists of broken and tilted large-size blocks of bedded Upper Yura quartzarenites in the southwest, and of folded and faulted mid-Cretaceous limestones and Coniacian red beds (the Querque Formation) in the northeast (Figs. III.2 and III.3).

The Cincha-Lluta slump deposit overlies and involves the Querque Formation in the northeastern exposures, implying it is younger than this unit. The plastic deformation style observed in some Querque and Arcurquina strata involved in the slumps imply also that these formations were not completely lithified before the mass-wasting event (Callot et al., 2008). We can thus approach the age of the Cincha-Lluta mass-wasting event by estimating the age of the top of the Querque Formation (Fig. III.5). This latter unit is best exposed in the Cerro Carapunta section (Fig. III.4) where it is ~200 m-thick, whereas the Arcurquina Formation is ~650 m-thick there. As this latter unit accumulated during the ~110–90 Ma interval, we can estimate depositional rates of ~32.5 m/Myr in the area. Assuming a similar rate for the Querque Formation allows to estimate that its top is ~84 Ma. The age of the Cincha-Lluta mass-wasting event could therefore be ~84 Ma or younger.

Gentilar slump deposit. At Gentilar (Fig. III.4), the ~1.65 km-thick Lower Toquepala Group exhibits a >30 m-thick member characterized by slumped volcaniclastic strata, about ~400 m below the 73.6 ± 0.6 Ma basal ignimbrite of the Middle Toquepala (this study, table III.3 and Fig. III.5). We can calculate an average accumulation rate of ~100 m/Myr for the Lower Toquepala assuming that the base of the Lower Toquepala Group is ~90 Ma, and thus estimate an age of ~77.5 Ma for this slump event.

Age and cause of slump events. Although they are approximate, our two estimates for Cincha-Lluta and Gentilar slump deposits bracket the Late Cretaceous mass-wasting events in the Arequipa belt of southern Peru to the ~84–77 Ma interval. This period coincides with arc growth (Fig. III.9) and, in particular, with the Tiabaya pulse of pluton emplacement. Moreover, the sedimentary compositional asymmetry of the Cincha-Lluta deposit is best explained having been derived from the southwest, where the growing arc was located. This

suggests that increasing slopes along the flanks of the growing arc may have destabilized its stratified cover, triggering large-scale mass-wasting directed away from the arc.

III. 6. B – Arc flare-up: ~74–62 Ma

Demouy et al. (2012) recognized that a magmatic flare-up occurred in the Cerro Verde area during the latest Cretaceous and earliest Paleocene, on the basis of zircon U-Pb dating of plutonic rocks in the Linga and Yarabamba units (Fig. III.4). Our own approach has been to identify and date volcanic products generated by the flare-up, and to assess its effects on country rocks in the Cerro Verde area.

a – Volcanic record

The ignimbrite member of the Middle Toquepala Group (Fig III.5) documents the initiation of the flare up event in the Arequipa belt. Considerable volumes of coalescent ignimbrites emplaced during this event. Here, we dated at Gentilar its base and top respectively at 73.3 ± 0.6 and 72.2 ± 0.9 Ma (Table III.3). It has to be noted that these two samples are separated by ~430 m of ignimbrites, which thus erupted in 1.1 ± 1.5 Ma. The two other zircon U-Pb ages (Table III.3) obtained in the Carahuaya area on an ignimbrite in the Middle Toquepala (69.4 ± 0.9 Ma – sample 1M33) and a ~30 m-thick rhyolite dike (64.3 ± 0.5 Ma – sample 1M34) fall in the range of those obtained on the Linga and Yarabamba plutons (Demouy et al., 2012) as the 66.3 ± 1.0 Ma ^{40}Ar-^{39}Ar age on the groundmass of an andesite flow from El Jaguay (Fig. 4) (Boekhout, pers. comm., 2014). These five new ages thus represent volcanic counterparts of the plutonic flare-up initially recognized in the Linga and Yarabamba units (Fig. III.9). This observation confirms that production of large ignimbrite volumes generally reflects emplacement of a large plutonic body at depth (de Silva and Gosnold, 2007; Ducea, 2001).

b – Plutonic record

Emplacement timing. The oldest "flare-up" crystallization ages available from the Linga pluton, namely 70.2 ± 0.7 Ma (Mukasa, 1986), 68.7 ± 0.5 Ma (Demouy et al., 2012), and 68.7 ± 0.6 Ma (this paper) are younger than the zircon U-Pb ages obtained on ignimbrites produced by the flare-up (see above the section "volcanic record"). The simplest explanation of this offset is that abrupt invasion of voluminous magma at depth first caused ignimbrite eruptions, whereas crystallization in underlying thick magma bodies was somewhat delayed. Moreover, the available zircon U-Pb ages indicate that the main part of the plutonic rocks from the Linga and Yarabamba units crystallized between ~70 and ~64 Ma (Fig. III.9).

Volume of intrusion. Based on the shapes of 125 laccoliths, and 21 granitoid plutons, McCaffrey and Petford (1997) proposed the following empirical power-law linking the width (L) and the thickness (T) of intrusives bodies: $T = 0.12*L^{0.88}$ for laccoliths and $T = 0.29*L^{0.80}$ for plutons. Considering that the Linga unit is 45 km-long in map-view, it emplaced as a ~3.4 to ~6 km-thick body. If we assume that it was an ellipsoid shaped body of at least 10 km-wide, it implies that 800 to 1500 km^3 of magma were emplaced to form the sole Linga unit. Adding the Yarabamba unit, 20 km-long, we obtain at least, 1000 km^3 of magma emplaced in 8 Ma (that is to say 125 km^3/Ma).

Depth of intrusion. The Linga unit was emplaced into quartzarenites and shales of latest Jurassic age. We estimate that the Late Jurassic to mid-Cretaceous sedimentary pile overlying the unit was no more than 0.5 km. Late Cretaceous volcanic strata, namely the Lower Toquepala Group, must have accumulated also because the arc was located along the LCH (Tiabaya units). The Lower Toquepala being generally ~1.5 km-thick in the region, we thus estimate that the Linga unit was emplaced ~2 km beneath the arc surface. This seems to be confirmed by preliminary Al-in-hornblende thermobarometry analyses (Demouy, pers. comm., 2014). Considering a geothermal gradient between 40 and 50°C/km for this arc (present-day average values for the Cascade volcanic range; Blackwell et al., 1990), temperature at this depth before intrusion must have been in the 80–120°C range.

Cooling of the Late Cretaceous batholith. Excepting sample 1M24 from a ~77 Ma granite (Demouy et al., 2012), the three other samples from the Late Cretaceous batholith (1M09, 1M16 and 1M25; Table III.5) yielded dispersed single grain ages. Due to low uranium content in these samples (Table III.5), we were not able to measure lengths of horizontal

confined tracks. However, we measured D_{par}, a proxy of the grain chemistry and annealing rate (Donelick et al., 2005). There is no correlation between the measured single grain ages and D_{par}. The dispersion is thus not due to differential annealing rates between apatites grains of different compositions but more likely to a rapid initial cooling followed by a long residence time in the partial annealing zone of the apatite. This interpretation of the apatite fission-track single grain age dispersion is coherent with our estimation of the temperature at the depth of the intrusion. The fact that the sample 1M09 from a diorite that crystallized at ~90 Ma, before the flare up, yielded a 92 ± 22 Ma age reveals that the Late Cretaceous batholith (emplaced between ~74 and 62 Ma) had neither a far-reaching nor a lasting thermal effect on the country rocks.

III. 6. C – Extensional collapse of the arc: ~62–52 Ma (~10 Myr)

We have seen above that important volumes of magma emplaced during the 74-62 Ma period (Fig. III.9). These magmas have εHf values coherent with an input of mantle-derived magmas (Mamani et al., 2010; Demouy et al., 2012). Moreover, based on geological and geochemical data, Mamani et al. (2010) argue that crustal thickening began at ~90 Ma. Indeed, according to these authors, during the 310-90 Ma period, low Dy/Yb, Sm/Yb and $^{87}Sr/^{86}Sr$ ratios associated with high εNd values suggest that the crust was thin, confirming the tectonic stretching of the margin previously identified by Sempere et al. (2002). However, a slight increase in Dy/Yb, Sm/Yb and $^{87}Sr/^{86}Sr$ ratios associated with lower εNd values starting ~90 Ma was interpreted as reflecting incipient crustal thickening of the present-day forearc crust (Mamani et al., 2010). Thus, the magmatic flare-up recorded in the Arequipa belt during the 74-62 Ma must have contributed to thicken the crust, transferring mantle-derived material to the upper crust. Now, any crustal growth beyond a stability threshold is expected to end in gravitational collapse, and our mapping shows that the overall structure displayed by the Arequipa belt is markedly of extensional origin.

We hereunder investigate the timing of extension in the LCH because the main axis of the subduction arc is likely to have been located along the LCH (and its SE extension) during the ~90–52 Ma interval. Indeed, the LCH exposes the structurally deepest rocks known in the Arequipa belt (Fig. III.2). Moreover coeval plutonic to volcanic rocks concentrate along this central feature bounded by the major Lluclla and Agua Salada normal faults.

a – Exhumation in the LCH: ~62–57? Ma

Magmatic record and age of exhumation. In the Cerro Verde open pit, the quartz-monzonite porphyry related to the copper deposit yielded U-Pb ages of 60.5 ± 0.6 and 59.8 ± 0.6 Ma on fine and coarse zircon fractions, respectively (Mukasa, 1986). Furthermore, a pyroclastic dacite and a porphyric rhyolite dike from the Cerro Negro paleovolcano yielded K-Ar ages of 57.1 ± 1.5 Ma (on sericite) and 52.6 ± 1.4 Ma (on K-feldspar) respectively (Bidgood, 2000). This paleovolcano directly sits on the Santa Rosa "erosional pediment" (Quang et al., 2003) established on the Yarabamba plutonic unit, which yielded zircon U-Pb ages of 64.3 ± 0.5 (Demouy et al., 2012) and 62.1 ± 0.6 Ma nearby (Mukasa, 1986; Fig. III.6). Such relationships imply that the Cerro Verde area underwent rapid exhumation during an interval of time bracketed by the youngest age obtained on the Yarabamba unit (62.1 ± 0.6 Ma) and the oldest age available from the overlying volcanic rocks (57.1 ± 1.5 Ma).

Estimating that the Yarabamba unit was emplaced at least at 2–3 km depth until ~62 Ma and was cropping out at ~57 Ma around the Cerro Negro paleovolcano, the exhumation rate must have been at least in the 0.4–0.6 km/Myr range. Although this estimate can only be rough due to the uncertainties on the initial depth of the Yarabamba pluton and on the duration of denudation it points to rapid exhumation in the LCH around ~60 Ma. Moreover, if K-Ar ages on sericite and K-feldspar are partially reset, real crystallization dates could be older and exhumation rates much higher.

Insights from in-situ fission-track data. In the LCH, three zircon fission-track ages were obtained on pre-Cretaceous rocks (sample 1M14, 1M18 and 1M21; Table III.4) and have in average an age of 58 ± 8 Ma. The seven apatite fission-track ages obtained in the same structural area (we exclude Linga unit, located in the Lluclla fault hanging wall) have on average an age of 55 ± 16 Ma (Table III.5). This smoothing of our data set thus results in mean zircon and apatite fission-track ages that point to the LCH having been rapidly cooled from ~240°C to ~50°C during the ~58–55 Ma interval, in good agreement with the ~60 Ma age of exhumation deduced from the geological relationships near Cerro Verde (Fig. III.6). Because erosion was low due to the arid climate (Hartley et al., 2005), Late Cretaceous to early Tertiary rapid cooling of rocks from the LCH was likely the effect of extensional exhumation. We note also that the 43 ± 10 Ma apatite fission-track age of sample 1M23 in the Yura half-Graben, is relatively young when compared to apatite fission-track ages in the LCH, confirming that the

rocks buried in the Yura half-graben cooled later than the LCH.

b – Emplacement of porphyry copper deposits: ~61-52 Ma

Porphyry emplacement at 60.2 ± 0.8 Ma at Cerro Verde (Mukasa, 1986), appears to have coincided exactly with the onset of extensional exhumation in the same area. Furthermore, the fact that other porphyry suites along the southeast extension of the Arequipa belt, namely Cuajone, Quellaveco, and Toquepala (Fig. III.4), also intrude plutons which had crystallized slightly earlier (Sillitoe and Mortensen, 2010; Simmons et al., 2013) and likely at a deeper level, imply that porphyry suites were all emplaced during the extensional collapse of the arc to which these volcanic systems were belonging. One may therefore wonder whether a causal link existed between the arc flare-up and subsequent collapse, which we document here, and the formation of these large porphyry copper deposits.

III. 6. D – A simple causal chain involving crustal thickening

Although the observation of outcropping plutonic volumes does not allow assessing correctly the amount of crustal thickening generated by arc magmatism, the succession of the three stages reconstructed in the Arequipa belt (Fig. III.10) does shed light on this issue. We observe that initial magmatic growth of the arc caused an increase in topography, and therefore some thickening of its crust, as reflected by transportation of oxidized detrital material from the arc into the backarc (terminating marine conditions) and subsequent large-scale mass-wasting away from the arc (Fig. III.2 & III.10). The flare-up that followed indicates that magmatic production and therefore growth increased with time, which suggests that the crust continued to thicken during this stage. Any protracted arc growth is logically expected to end in gravitational collapse if the arc crust is overthickened beyond a stability threshold, and we indeed observe that extensional collapse closely followed the magmatic flare-up.

The case here documented in western South America is consistent with at least one case from western North America. In California, Kidder et al. (2003) reconstructed that magmatic activity in the Mesozoic arc was especially intense during the 93–81 Ma interval, coinciding with crustal thickening. The termination of magmatism between 81 and 76 Ma was immediately followed by exhumation, coinciding with extensional collapse along the arc and

bringing deep rocks to the surface within 8 Myr at a very high, >2–3 km/Myr rate. We therefore propose that a 3-step evolution of growth—flare-up—collapse (Fig. III.10) may be characteristic for the evolution of many arcs world-wide.

III. 6. E – Persistence of extension in the forearc: ~52–30 Ma

a – Northward arc migration: ≤52–≥45 Ma

We have shown that the arc was located along the Arequipa belt until at least ~52 Ma (Fig. III.10), and ~150 km more to the north starting at least at ~45 Ma, meaning that the implied migration occurred during a ≤ 7 Myr-long interval. The extensional collapse in the Arequipa belt could not be a consequence of this northward migration because in the Cerro Verde area it was initiated between ~62 and ~60 Ma and was already significant by ~57 Ma. However, this migration of the arc resulted in the Arequipa belt being located in the Andean forearc after ~50 Ma, a context favorable to protracted extensional deformation.

b – Moquegua Group

Basal age. The conspicuous extensional deformation of pre-Cenozoic rocks that characterizes the current forearc is post-dated by the Moquegua Group (Fig. III.2 and III.5). Given that there is no volcanic evidence that the lower part of this group was deposited during the late activity of the Toquepala arc, it is unlikely that its base is older than ~52 Ma.

Placing the base of the Moquegua Group at ~52 Ma results in an average depositional rate of ~30 m/Myr for the MoqA unit, which is consistent with rates calculated for the MoqC unit in the region. However, this value is 2–3 times the average rate estimated for the MoqB unit, which suggests that subsidence and thus extension were more intense during the MoqA (compared to MoqB) depositional period, i.e. between ~52 and ~45 Ma.

Syndepositional extension and subsequent evolution. It has to be noted that some synsedimentary extensional features are commonly observed throughout the Lower Moquegua subgroup, i.e. from ~52 to 30 Ma. It indicates that the forearc SW of the Lluclla fault was submitted to continuous extension over ~22 Myr. The fact that these extensional features are post-dated by the MoqC unit reflects that some change in tectonic regime occurred ~30 Ma ago.

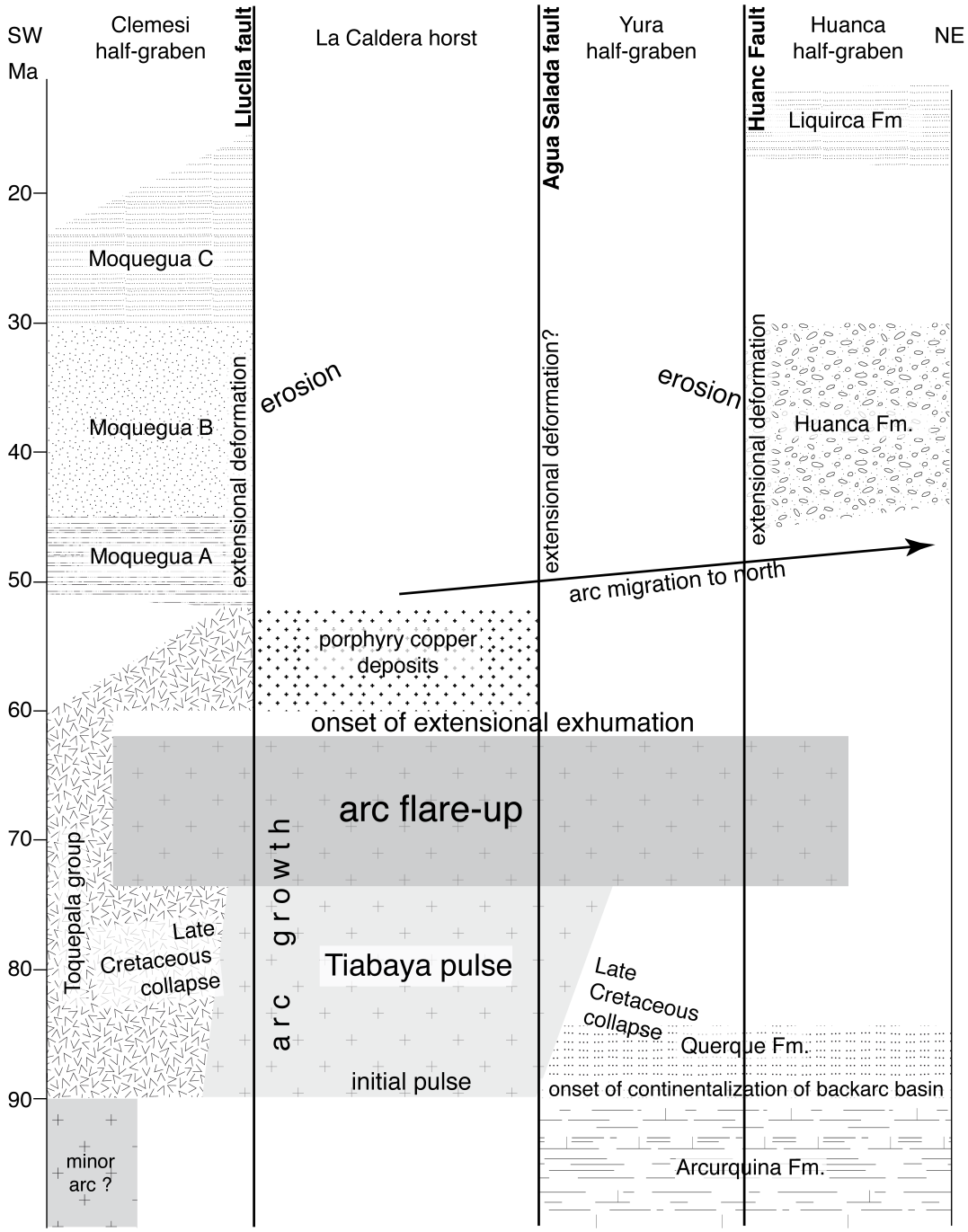

Figure III.10: Transversal schematized stratigraphy summarizing the main events affecting the forearc of southern Peru.

c – Huanca Formation

All strata in the Huanca Formation are younger than ~84 Ma, as this unit overlies the Querque Formation and Cincha-Lluta collapse, and are older than the overlying Liquirca Formation. The Huanca Formation dips 25–45° to the southwest toward the Huanca fault. In contrast, the overlying Liquirca Formation gently dips to the northeast by ~10–15° near its base and displays a growth-strata geometry. This geometry implies that the Huanca Formation was dipping by ~35–55° toward SW prior to accumulation of the Liquirca Formation. Growth strata geometry in this latter unit implies that its tilting toward the NE was synsedimentary and due to a SW-dipping fault, likely located at the foot of the present-day volcanoes. We hereunder investigate the age of these deposits in order to better constrain the age of these formations and the period of extension.

Age constraints from detrital grains. The time of deposition of a bed is necessarily younger than the time of initial crystallization and cooling of its individual detrital grains. In the absence of later thermal resetting, ages obtained on detrital zircons and apatites provide chronostratigraphic constraints. Therefore, either the minimum age as defined by Galbraith and Laslett (1993) for fission-track ages of each sample can be used to infer the time of deposition, or the youngest individual grain age in each sample can be used.

Lowermost sample. The three youngest U-Pb ages obtained on detrital zircons from sample 1M28, from ~100 m above the base of the Huanca Formation, are 94.4 ± 3.6, 94.8 ± 3.6, and 96.3 ± 3.5 Ma. In contrast, the ZFT age population peaks at 57 ± 10 Ma and yields a minimum age of 50 ± 9 Ma (Table III.7). The entire AFT age population forms one peak at 83 ± 10 Ma (Table III.8). As apatite fission-track ages are systematically older than zircon fission-track ages, these data imply that fission-track in apatite and therefore zircon have not been affected by a post-depositional thermal imprint in the lower part of the Huanca Formation. Given the zircon fission-track ages, Huanca Formation cannot be of Cretaceous age, confirming Cruz's conjecture (2002). Considering the 50 ± 9 Ma zircon fission-track minimum age peak, and in the absence of ash or fossils in the sampled strata, we propose that the Huanca Formation began to accumulate approximately at the same time as the Moquegua Group, i.e. starting ~52 Ma.

Uppermost samples. Samples 1M19 and 1M20 were collected in the same horizon near the top of the Huanca Formation. The diorite clasts of sample 1M19 have an

homogeneous average zircon U-Pb age of 80.6 ± 0.4 Ma (Table III.6) and a zircon fission-track peak age of 48 ± 6 Ma (Table III.7), whereas the youngest apatite fission-track age population (9% of the grains) peaks at 34 ± 14 Ma, resulting in a 51 ± 20 Ma apatite minimum age peak (Table III.8). Taking into account the reported uncertainties, these data imply that the upper part of the Huanca Formation was deposited after ~48 Ma, and possibly as late as the Upper Eocene (considering the younger apatite fission-track single grain ages population.

The Huanca Formation and the Lower Moquegua subgroup thus now appear to be time-equivalents (deposited in the ~52-30 Ma period). This is consistent with the fact that they both display reddish conglomeratic facies with almost no pyroclastic beds. The Huanca and Lower Moquegua Formations post-date the onset of exhumation along the LCH at ~60 Ma, and respectively accumulated along its northeast and southwest sides.

Age and context of accumulation. Considering that the ~2.5 km-thick Huanca Formation accumulated during the ~52–30 Ma interval allows to estimate a rough depositional rate of ~110 m/Myr, which is 2–6 times higher than those estimated for sub-units of the Moquegua Group southwest of the LCH. This implies that the Huanca Formation accumulated in a more subsident domain and therefore suggests significant coeval activity along the nearby Huanca normal fault. Depositional facies and paleocurrents confirm that this fault controlled the position of an elongated, dominantly proximal fluvial system that was draining part of the Arequipa belt during that time (Cruz, 2002).

Age of the base of the Liquirca Formation. The ignimbrite ~30 m above the contact between the Huanca and Liquirca formations is now dated at 16.5 ± 0.3 Ma. Considering depositional rate in the 20–60 m/Myr range, equivalent to rates estimated elsewhere in the region, the base of the Liquirca Formation can be estimated to be ~18-17 Ma in age. The Liquirca Formation thus appears to represent a partial time-equivalent of the MoqC unit, with which it shares similarities such as a highly tuffaceous component and a resulting whitish color.

Weathering in uppermost conglomerates of the Huanca Formation. The marked angular unconformity between the Huanca and overlying Liquirca formations is consistent with the ~30 Ma change in tectonic regime reported above, and indicates that the former was tilted down to the southwest by ~45° before ~18 Ma. The proposed chronology implies that the upper part of the Huanca conglomerates was exposed and thus submitted to weathering

and probably some erosion between >30 and ~18 Ma, i.e. during >12 Myr. In agreement, the large diorite clasts in the SW-dipping uppermost Huanca Formation show an alteration so intense that it precludes that they were transported in such a state, implying in-situ weathering. The fact that no paleosoil is preserved at the top of the unit is likely to reflect pre-Liquirca erosion.

d – Exhumation recorded by the Huanca Formation

Source area. The lower 500 m of the conglomeratic part of the Huanca Formation are dominated by subangular to subrounded andesite clasts (Cruz, 2002). It reveals that volcanic arc accumulations formed the first dominant unit to undergo erosion at that time, and points to the Toquepala Group as the most likely source unit for this member. This is coherent with the present-day absence of Late Cretacous–Early Paleogene volcanic rocks (the Toquepala Group) northwest of Cerro Verde; despite the fact that the coeval arc extended there (as documented by plutonic rocks). In contrast with the area extending southeast of Cerro Verde where this thick unit has been preserved, the Toquepala Group, which was covering the LCH during or after the Oligocene, has thus been totally eroded. However, because zircon fission-track minimum ages are always younger than apatite fission-track ages obtained in the Huanca section, at least part of the apatites and zircons in the Huanca red beds were derived from distinct source rocks and/or areas.

The upper ~1.2 km of the Huanca conglomerates in the Cerro Carapunta section are mostly composed of subrounded to subangular clasts from andesite flows (presumably also from the Toquepala Group), mid-Cretaceous limestones, and Upper Yura quartzarenites. However, plutonic clasts are observed only in the uppermost Huanca Formation at Chilcane (Fig. III.4). It appears thus likely that a dominant fraction of the Huanca clastic material was derived from the LCH (and therefore also from the quartzarenites and limestones that compose the Cincha-Lluta slump deposit along its northeast flank). Because of the abundance of quartzarenite clasts, which increases upsection, it is expected that a significant mineral fraction of the conglomerate matrices may have been recycled from these ~150–130 Ma-old sandstones and not directly from older rocks in the source area. It has to be noted that the material from which these quartzarenites formed was derived from the northeast (Sempere et al., 2002) by Jurassic to lower Cretaceous fluvial systems thought to have sampled regions as

remote as the Amazonian craton (Chew et al., 2008). This also explains the large amount of ≥ 250 Ma zircon U-Pb and fission-track ages found in the samples from Cerro Carapunta section.

U-Pb data. Late Cretaceous zircons, most likely derived from the arc in the LCH, are common in the two stratigraphically lower samples, whereas they are absent from the two upper samples from the Huanca basin (Cerro Carapunta) section (Fig. III.4), suggesting that denudation progressively affected deeper rocks. No zircons younger than ~79 Ma were found, but this does not preclude that younger volcanic rocks have existed in the LCH (according to our experience, no andesite from southern Peru has yielded zircons so far). This indicates that the ~73.5–62 Ma magmatic flare-up evidenced in the Cerro Verde area did not generate intrusions bearing zircons in the source area of the Huanca Formation in the Cerro Carapunta section (Fig. III.4), which therefore did not include Cerro Verde and neighboring areas. Ignimbrites characteristic of the Middle Toquepala are likely to have included zircons but may not have been deposited in the area or were eroded away before accumulation of the Huanca Formation. However, at Chilcane (Fig. III.4), the two consistent ages, from dioritic clasts and their matrix in the uppermost sampled horizon of the Huanca red beds, indicate that a ~81 Ma-old diorite was largely cropping out in the source area of the upper Huanca Formation, most probably in the nearby LCH.

Fission-track data. A fraction of the dated zircon grains yielded >200 Ma zircon fission-track ages, and this old fraction increases upsection. Because fission-track in apatites and zircons are not annealed at the base of the Huanca Formation, it suggests that the source area initially mainly exposed the Late Cretaceous batholith, and that rocks bearing zircons with >200 Ma cooling ages were unroofed later. Such zircons had crystallized and cooled below 240°C before ~200 Ma and therefore are likely to have been recycled from the Upper Yura quartzarenites.

However, a large fraction of detrital apatite and zircon fission-track individual grain ages groups around ~60 Ma (Fig. III.8). The detrital age distributions from the Huanca Formation thus reflect the cooling ages obtained on rocks from the LCH, confirming the identification of the LCH as the main source area. It is probable that the apatite fission-track signal is mainly derived from the Late Cretaceous batholith and little from the Jurassic batholith and Proterozoic basement, in which apatites have proven to be generally scarce.

e – Liquirca and Moquegua C Formations

The ignimbrite here dated at 16.5 ± 0.3 Ma by the zircon U-Pb method (Table III.3) between Chilcane and Huanca appears to be identical with the Lluclla ignimbrite dated at ~16.2 Ma in the Majes and Siguas valleys (Fig. III.4), i.e. southwest across the LCH, by the ^{40}Ar-^{39}Ar method in several studies (Roperch et al., 2006; Thouret et al., 2007; Schildgen et al., 2009). In the Majes valley, this ignimbrite is located ~550 m above the base of the MoqC unit and ~50 m below the marked erosional unconformity at the base of the MoqD unit. In contrast, in the Chilcane-Huanca area it is found only ~30 m above the base of the local ~500 m-thick Liquirca Formation, interpreted as the lateral equivalent of the MoqC unit.

The base of the MoqC unit thus appears to be highly diachronous, as it is dated to ~30 Ma near Moquegua (Roperch et al., 2006), post-dated west of the study area by a number of ~25-23 Ma-old volcanic deposits (Noble et al., 1985; Thouret et al., 2007; Schildgen et al., 2009), and assumed to be also ~30 Ma in the Majes valley (implying a consistent depositional rate of ~40 m/Myr for the MoqC). This contrast reflects considerable lateral differences in relief and subsidence in the Cenozoic forearc during the Late Oligocene and Miocene.

III. 6. F – Comparison with plate convergence history

Plate convergence reconstructions of Pardo-Casas and Molnar (1987)) and by Sdrolias and Müller (2006) indicate that the convergence direction probably became dominantly trench-normal roughly between ~70 and ~60 Ma (ages on chron 30-31 in Pardo-Casas and Molnar; 1987 and emended following Cande and Kent; 1995). The convergence rate remained however low, until it significantly increased between ~55 and ~50 Ma. The convergence rate peaked at ~40 Ma and subsequently dropped significantly.

There are thus some parallels between the evolution we have reconstructed and the plate convergence history. In particular, the arc flare-up (~74 – 62 Ma) apparently developed during a significant, albeit poorly constrained, change in the direction of convergence. The Late Cretaceous and Paleocene convergence history is however too poorly defined to tell whether and how the details of the arc growth, flare-up and collapse in the Arequipa belt were directly related or not to this change. Furthermore, a sharp increase in convergence rate between ~55 and ~50 Ma strongly correlates with the initiation of arc migration northwards.

However, this event apparently did not cause compressional deformation, at least in the upper crust of the Arequipa region.

III. 7 – CONCLUSIONS

Our results lead to a refined knowledge of the geologic evolution of the Arequipa belt and neighboring areas in the Central Andes. Our novel mapping and new data shed significant light on the succession of events that shaped the present-day geology of southern Peru (Fig. III.10). The Arequipa belt now appears as a well-preserved taphrogen of Early Paleogene age, confirming previous mapping of large-scale normal faults (Sébrier et al., 1985; Schildgen et al.; 2009).

Development of the Arequipa taphrogen was centered along the main subduction arc, which had established there at ~90 Ma. Between ~84 and ~76 Ma, this arc grew triggering the destabilization of its stratigraphic cover along its flanks during large-scale mass-wasting events. Acceleration of arc growth resulted in a magmatic flare-up, whose ignimbritic earliest products are now dated ~73.5 Ma. This flare-up lasted until ~62 Ma (Fig. III.9) and is documented at least from latitudes ~10°S to ~20°S, and in the distal backarc record of Bolivia. Geological observations and related in-situ and detrital fission-track data demonstrate that extensional exhumation started ~62–60 Ma. Since then, extension prevailed in the forearc and waned until ~30 Ma (Fig. III.10).

As no compressional features are observed, we interpret the generalized extension in the forearc closely following the arc growth and flare-up as gravitational collapse of the crust that had been previously overthickened by magmatic addition. The collapse resulted in the observed taphrogen, and was accompanied by large-scale normal faulting and block tilting. Our data do not preclude, however, that extension and exhumation were somewhat diachronous along the Arequipa belt. Sedimentation resumed in the downwarped areas (Moquegua and Huanca basins) starting ~52 Ma (Fig. III.10), post-dating most of the extensional tilting of previous rocks and recording syndepositional normal faulting.

To sum-up, the ~38 Myr-long evolution of the main Andean arc while it was located along the Arequipa belt (~90–52 Ma) may thus be described as a trilogy, namely growth—flare-up—collapse (Fig. III.10). This relatively detailed evolution of the present-day forearc we

have reconstructed is clearly dominated by arc magmatism and subsequent extension. A marked increase in plates convergence rate synchronous with the northward migration of the arc between ~52 and ~45 Ma strongly suggests that the former triggered the later. However, plate convergence history in southern Peru is poorly constrained prior to ~60 Ma, and for now it seems impossible to relate it accurately to the reconstructed succession of events prior to 60 Ma.

Last but not least, the switch from lithospheric thinning to crustal thickening undergone by the southern Peruvian margin near ~90 Ma (Mamani et al., 2010) thus appears to have been mostly caused by a considerable magmatic growth of the subduction arc between 90 and 62 Ma (Fig. III.10), and not by compressional tectonics as traditionally assumed (Sempere et al., 1997). The dominance of extensional features in the Arequipa region is largely due to the gravitational collapse of the arc that developed starting ~62–60 Ma and to the persistence of extensional conditions (Fig. III.10) in a region that has belonged to the forearc since ~52 Ma.

References

Beck, S.L., and Zandt, G., 2002, The nature of orogenic crust in the central Andes: Journal of Geophysical Research: Solid Earth, v. 107, p. 2230, doi: 10.1029/2000JB000124.

Beck, S.L., Zandt, G., Myers, S.C., Wallace, T.C., Silver, P.G., and Drake, L., 1996, Crustal-thickness variations in the central Andes: Geology, v. 24, p. 407–410.

Benavides, V., 1962, Estratigrafía pre-Terciaria de la región de Arequipa: Boletín de la Sociedad geológica del Perú, v. 38, p. 5–63.

Bidgood, T., 2000, Geologia del yacimiento Cerro Negro, *in* Primer volumen de monografias de yacimientos minerales peruanos: historia, exploracion y geologia, Lima, Instituto de Ingenieros de Minas del Peru, p. 227–230.

Blackwell, D.D., Steele, J.L., Kelley, S., and Korosec, M.A., 1990, Heat flow in the state of washington and thermal conditions in the Cascade Range: Journal of Geophysical Research: Solid Earth, v. 95, p. 19495–19516, doi: 10.1029/JB095iB12p19495.

Boekhout, F., Sempere, T., Spikings, R., and Schaltegger, U., 2013, Late Paleozoic to Jurassic chronostratigraphy of coastal southern Peru: Temporal evolution of sedimentation along an active margin: Journal of South American Earth Sciences, v. 47, p. 179–200, doi: 10.1016/j.jsames.2013.07.003.

Boekhout, F., Spikings, R., Sempere, T., Chiaradia, M., Ulianov, A., and Schaltegger, U., 2012, Mesozoic arc magmatism along the southern Peruvian margin during Gondwana breakup and dispersal: Lithos, v. 146–147, p. 48–64, doi: 10.1016/j.lithos.2012.04.015.

Callot, P., Sempere, T., Odonne, F., and Robert, E., 2008, Giant submarine collapse of a carbonate platform at the Turonian–Coniacian transition: The Ayabacas Formation, southern Peru: Basin Research, v. 20, p. 333–357, doi: 10.1111/j.1365-2117.2008.00358.x.

Cande, S.C., and Kent, D.V., 1995, Revised calibration of the geomagnetic polarity timescale for the Late Cretaceous and Cenozoic: Journal of Geophysical Research, v. 100, p. 6093, doi: 10.1029/94JB03098.

Carlotto, V., 2013, Paleogeographic and tectonic controls on the evolution of Cenozoic basins in the Altiplano and Western Cordillera of southern Peru: Tectonophysics, v. 589, p. 195–219, doi: 10.1016/j.tecto.2013.01.002.

Casquet, C., Fanning, C.M., Galindo Francisco, M. del C., Pankhurst, R.J., Rapela, C.W., and Torres, P., 2010, The Arequipa Massif of Peru: New SHRIMP and isotope constraints on a Paleoproterozoic inlier in the Grenvillian orogen: Journal of South American earth sciences, v. 29, p. 128–142.

Chew, D.M., Magna, T., Kirkland, C.L., Mišković, A., Cardona, A., Spikings, R., and Schaltegger, U., 2008, Detrital zircon fingerprint of the Proto-Andes: Evidence for a Neoproterozoic active margin? Precambrian Research, v. 167, p. 186–200, doi: 10.1016/j.precamres.2008.08.002.

Clark, A.H., Farrar, E., Kontak, D.J., Langridge, R.J., Arenas, M.J., France, L.J., McBride, S.L., Woodman, P.L., Wasteneys, H.A., Sandeman, H.A., and Archibald, D.A., 1990, Geologic and geochronologic constraints on the metallogenic evolution of the Andes of southeastern Peru: Economic Geology, v. 85, p. 1520–1583.

Cruz, M., 2002, Estratigrafía y evolución tectono-sedimentaria de los depósitos sin-orogénicos del cuadrángulo de Huambo (32-r, Cuadrante-II): las formaciones Ashua y Huanca. Departamento de Arequipa:.

Demouy, S., Paquette, J.-L., de Saint Blanquat, M., Benoit, M., Belousova, E.A., O'Reilly, S.Y., García, F., Tejada, L.C., Gallegos, R., and Sempere, T., 2012, Spatial and temporal evolution of Liassic to Paleocene arc activity in southern Peru unraveled by zircon U–Pb and Hf in-situ data on plutonic rocks: Lithos, v. 155, p. 183–200, doi: 10.1016/j.lithos.2012.09.001.

Donelick, R.A., O'Sullivan, P.B., and Ketcham, R.A., 2005, Apatite Fission-Track Analysis: Reviews in Mineralogy and Geochemistry, v. 58, p. 49–94, doi: 10.2138/rmg.2005.58.3.

Ducea, M., 2001, The California Arc: thick granitic batholiths, eclogitic residues, lithospheric-scale thrusting, and magmatic flareup: GSA today, p. 4–10.

Dunai, T.J., López, G.A.G., and Juez-Larré, J., 2005, Oligocene–Miocene age of aridity in the Atacama Desert revealed by exposure dating of erosion-sensitive landforms: Geology, v. 33, p. 321–324, doi: 10.1130/G21184.1.

Galbraith, R.F., and Laslett, G.M., 1993, Statistical models for mixed fission track ages: Nuclear Tracks and Radiation Measurements, v. 21, p. 459–470, doi: 10.1016/1359-0189(93)90185-C.

Geyer, O., 1983, Obertithonische Ammoniten-fauna von Peru: Zblatt Geol. Palaetont., v. 1, p. 335–350.

Hartley, A.J., Chong, G., Houston, J., and Mather, A.E., 2005, 150 million years of climatic stability: evidence from the Atacama Desert, northern Chile: Journal of the Geological Society, v. 162, p. 421–424, doi: 10.1144/0016-764904-071.

Isacks, B.L., 1988, Uplift of the Central Andean Plateau and Bending of the Bolivian Orocline: J. Geophys. Res., v. 93, p. 3211–3231, doi: 10.1029/JB093iB04p03211.

Jaillard, E., 1994, Kimmeridgian to Paleocene tectonic and geodynamic evolution of the Peruvian (and Ecuadorian) margin, *in* Cretaceous tectonics of the Andes, Earth Evolution Sciences, Braunschweig, Vieweg, p. 101–167.

James, D.E., 1971, Andean crustal and upper mantle structure: Journal of Geophysical Research, v. 76, p. 3246–3271, doi: 10.1029/JB076i014p03246.

James, D.E., and Brooks, C., 1976, Preliminary Rb/Sr data on the minimum age of the central Andean Precambrian basement complex: Yb. Carnegie Instn. Wash., v. 75, p. 213–216.

James, D.E., and Sacks, I.S., 1999, Cenozoic formation of the Central Andes; a geophysical perspective, *in* Geology and ore deposits of the Central Andes, Special Publication, Skinner B. J., p. 1–25.

Jenks, W.F., 1948, Geología de la Hoja de Arequipa al 200,000: Boletín del Instituto Geológico del Perú, v. 9.

Kidder, S., Ducea, M., Gehrels, G., Patchett, P.J., and Vervoort, J., 2003, Tectonic and magmatic development of the Salinian Coast Ridge Belt, California: Tectonics, v. 22, p. 1058, doi: 10.1029/2002TC001409.

Kono, M., Fukao, Y., and Yamamoto, A., 1989, Mountain building in the central Andes: Journal of Geophysical Research: Solid Earth, v. 94, p. 3891–3905, doi: 10.1029/JB094iB04p03891.

Mamani, M., Wörner, G., and Sempere, T., 2010, Geochemical variations in igneous rocks of the Central Andean orocline (13°S to 18°S): Tracing crustal thickening and magma generation through time and space: Geological Society of America Bulletin, v. 122, p. 162–182.

Martignole, J., and Martelat, J.-E., 2003, Regional-scale Grenvillian-age UHT metamorphism in the Mollendo–Camana block (basement of the Peruvian Andes): Journal of Metamorphic Geology, v. 21, p. 99–120, doi: 10.1046/j.1525-1314.2003.00417.x.

McCaffrey, K.J.W., and Petford, N., 1997, Are granitic intrusions scale invariant? Journal of the Geological Society, v. 154, p. 1–4, doi: 10.1144/gsjgs.154.1.0001.

Mukasa, S.B., 1986, Zircon U-Pb ages of super-units in the Coastal batholith, Peru: Implications for magmatic and tectonic processes: Geological Society of America Bulletin, v. 97, p. 241–254.

Myers, J.S., 1975, Vertical crustal movements of the Andes in Peru: Nature, v. 254, p. 672–674, doi: 10.1038/254672a0.

Noble, D.C., Sébrier, M., Megard, F., and McKee, E.H., 1985, Demonstration of two pulses of Paleogene deformation in the Andes of Peru: Earth and Planetary Science Letters, v. 73, p. 345–349, doi: 10.1016/0012-821X(85)90082-2.

Pardo-Casas, F., and Molnar, P., 1987, Relative motion of the Nazca (Farallon) and South American Plates since Late Cretaceous time: Tectonics, v. 6, p. 233–248, doi: 10.1029/TC006i003p00233.

Perelló, J., Carlotto, V., Zárate, A., Ramos, P., Posso, H., Neyra, C., Caballero, A., Fuster, N., and Muhr, R., 2003, Porphyry-Style Alteration and Mineralization of the Middle Eocene to Early Oligocene Andahuaylas-Yauri Belt, Cuzco Region, Peru: Economic Geology, v. 98, p. 1575–1605, doi: 10.2113/gsecongeo.98.8.1575.

Quang, C.X., Clark, A.H., Lee, J.K.W., and B, J.G., 2003, 40Ar-39Ar ages of hypogene and supergene mineralization in the Cerro Verde-Santa Rosa porphyry Cu-Mo cluster, Arequipa, Peru: Economic Geology, v. 98, p. 1683–1696.

Roperch, P., Sempere, T., Macedo, O., Arriagada, C., Fornari, M., Tapia, C., García, M., and Laj, C., 2006, Counterclockwise rotation of late Eocene–Oligocene fore-arc deposits in southern Peru and its significance for oroclinal bending in the central Andes: Tectonics, v. 25, p. TC3010, doi: 10.1029/2005TC001882.

Sandeman, H.A., Clark, A.H., and Farrar, E., 1995, An Integrated Tectono-Magmatic Model for the Evolution of the Southern Peruvian Andes (13-20°S) since 55 Ma: International Geology Review, v. 37, p. 1039–1073, doi: 10.1080/00206819509465439.

Schildgen, T.F., Hodges, K.V., Whipple, K.X., Pringle, M.S., van Soest, M.C., and Cornell, K., 2009, Late Cenozoic structural and tectonic development of the western margin of the Central Andean Plateau in southwest Peru: Tectonics, v. 28, doi: 10.1029/2009tc002590.

Sdrolias, M., and Müller, R.D., 2006, Controls on back-arc basin formation: Geochemistry, Geophysics, Geosystems, v. 7, p. Q04016, doi: 10.1029/2005GC001090.

Sébrier, M., Mercier, J.-L., Mégard, F., Laubacher, G., and Carey-Gailhardis, E., 1985, Quaternary normal and reverse faulting and the state of stress in the central Andes of south Peru: Tectonics, v. 4, p. 739–780, doi: 10.1029/TC004i007p00739.

Sempere, T., Boekhout, F., Noury, M., Taipe, E., García, F., Jacay, J., Spikings, R.A., and Schaltegger, U., 2012, Reinstauración del Grupo Yamayo (Bellido y Guevara, 1963), y su significado en la evolución de la margen peruana del Carbonífero al Triásico, *in* XVI Congresso Peruano de Geologia, Lima.

Sempere, T., Butler, R.F., Richards, D.R., Marshall, L.G., Sharp, W., and Swisher, C.C., 1997, Stratigraphy and chronology of Upper Cretaceous–lower Paleogene strata in Bolivia and northwest Argentina: Geological Society of America Bulletin, v. 109, p. 709–727.

Sempere, T., Carlier, G., Soler, P., Fornari, M., Carlotto, V., Jacay, J., Arispe, O., Néraudeau, D., Cárdenas, J., Rosas, S., and Jiménez, N., 2002, Late Permian–Middle Jurassic lithospheric thinning in Peru and Bolivia, and its bearing on Andean-age tectonics: Tectonophysics, v. 345, p. 153–181, doi: 10.1016/S0040-1951(01)00211-6.

Sempere, T., Folguera, A., and Gerbault, M., 2008, New insights into Andean evolution : an introduction to contributions from the 6th ISAG symposium (Barcelona, 2005): Tectonophysics, v. 459, p. 1–13, doi: 10.1016/j.tecto.2008.03.011.

Sempere, T., Fornari, M., Acosta, J., Flores, A., Jacay, J., Peña, D., Roperch, P., and Taipe, E., 2004, Estratigrafía, geocronología, paleogeografía y paleotectónica de los depósitos de antearco del sur del Perú, *in* Resúmenes extendidos del XII Congreso Peruano de Geología, Lima, Sociedad Geológica del Perú, p. 533–536.

Sempere, T., and Jacay, J., 2008, Anatomy of the Central Andes: Distinguishing between Western, Magmatic Andes and Eastern, Tectonic Andes, *in* Proceedings of the 7th International Symposium of Andean Geodynamics (ISAG), Nice, France, p. 505–507.

Sempere, T., Noury, M., García, F., and Bernet, M., 2014, Elementos para una actualización de la estratigrafía del grupo Moquegua, sur del Perú, *in* Resúmenes extendidos del XVII Congreso Peruano de Geología, Lima.

Sillitoe, R.H., 1973, Environments of formation of volcanogenic massive sulfide deposits: Economic Geology, v. 68, p. 1321–1325, doi: 10.2113/gsecongeo.68.8.1321.

Sillitoe, R.H., 2010, Porphyry Copper Systems: Economic Geology, v. 105, p. 3–41, doi: 10.2113/gsecongeo.105.1.3.

Sillitoe, R.H., and Mortensen, J.K., 2010, Longevity of Porphyry Copper Formation at Quellaveco, Peru: Economic Geology, v. 105, p. 1157–1162, doi: 10.2113/econgeo.105.6.1157.

De Silva, S.L., and Gosnold, W.D., 2007, Episodic construction of batholiths: Insights from the spatiotemporal development of an ignimbrite flare-up: Journal of Volcanology and Geothermal Research, v. 167, p. 320–335, doi: 10.1016/j.jvolgeores.2007.07.015.

Simmons, A.T., Tosdal, R.M., Wooden, J.L., Mattos, R., Concha, O., McCracken, S., and Beale, T., 2013, Punctuated Magmatism Associated with Porphyry Cu-Mo Formation in the Paleocene to Eocene of Southern Peru: Economic Geology, v. 108, p. 625–639, doi: 10.2113/econgeo.108.4.625.

Suárez, G., Molnar, P., and Burchfiel, B.C., 1983, Seismicity, fault plane solutions, depth of faulting, and active tectonics of the Andes of Peru, Ecuador, and southern Colombia: Journal of Geophysical Research: Solid Earth, v. 88, p. 10403–10428, doi: 10.1029/JB088iB12p10403.

Thouret, J.-C., Wörner, G., Gunnell, Y., Singer, B., Zhang, X., and Souriot, T., 2007, Geochronologic and stratigraphic constraints on canyon incision and Miocene uplift of the Central Andes in Peru: Earth and Planetary Science Letters, v. 263, p. 151–166, doi: 10.1016/j.epsl.2007.07.023.

Tosdal, R.M., Clark, A.H., and Farrar, E., 1984, Cenozoic polyphase landscape and tectonic evolution of the Cordillera Occidental, southernmost Peru: Geological Society of America Bulletin, v. 95, p. 1318–1332.

Vermeesch, P., 2012, On the visualisation of detrital age distributions: Chemical Geology, v. 312–313, p. 190–194, doi: 10.1016/j.chemgeo.2012.04.021.

Vermeesch, P., 2009, Radialplotter: a java application for fission track, luminescence and other radial plots: Radiation Measurments, v. 44, p. 409–410.

Vicente, J.-C., 1989, Early Late Cretaceous overthrusting in the Western Cordillera of Southern Peru, *in* Geology of the Andes and its Relation to Hydrocarbon and Mineral ressources, Circum-Pacific Council for Energy and Mineral Ressources Earth Science Series, Houston, Texas, Ericksen, G. E., Cañas Pinochet, M.T., and Reinemund, J. A., p. 91–117.

Vicente, J.-C., 1981, Elementos de la estratigrafía mesozoica sur-peruana, *in* Cuencas sedimentarias del Jurásico y Cretácico de América del Sur, Buenos Aires, Volkheimer, W., Musacchio, E. A., p. 319–351.

Vicente, J.-C., Beaudouin, B., Chávez, A., and León, I., 1982, La cuenca de Arequipa (Sur Perú) durante el Jurásico-Cretácico inferior., *in* Quinto Congreso Latinoamericano de Geología, Buenos-Aires, p. 121–153.

Vicente, J.-C., Sequeiros, F., Valdivia, M.A., and Zavala, J., 1979, El sobre-escurrimiento de Cincha-Lluta: elemento del accidente mayor andino al NW de Arequipa: Boletín de la Sociedad geológica del Perú, v. 61, p. 67–107.

Chapter IV – Thermochronologic evidence for Eo-Oligocene orogen-parallel extension in the forearc of southern Peru.

This chapter is similar to a paper submitted to Lithosphere in collaboration with Matthias Bernet, Thibaud Simon-Labric (U-Th/He analyses), Taylor F. Schildgen ($^{40}Ar/^{39}Ar$ analyses) and Thierry Sempere.

The Central Andean margin has been active continuously since at least the late Jurassic. However, important rigid block rotations (around their vertical axis) responsible for the present-day croissant-shape of the orogen and for deformation phases that led to plateau formation and uplift started broadly at the same time, during the Eocene. Although important block rotations occurred in the forearc, a zone prone to recording changes in subduction dynamics, the tectono-thermal Cenozoic evolution of this area remains poorly known.

Here we use thermochronology to constrain the tectono-thermal history of the present-day forearc of the Central Andes. We sampled 16 new sites between Atiquipa and Ilo (Peru) and present results for biotite and muscovite $^{40}Ar/^{39}Ar$, zircon and apatite fission-track, and zircon (U-Th)/He analyses. Combined with previously published data, our results show that the gneissic basement was near (or at) the surface in the Neo-Proterozoic, and no major thermal event occurred since then. Nonetheless, some zones were heated to temperatures of ~220°C between ~175–105 Ma.

Apatite fission-track ages along the coast show two shifts from younger (60 Ma) to older (~90 Ma) ages, coinciding with two major normal fault zones that strike perpendicular to the orogen and delineate blocks tilted to the NW. Given these ages, the faults were active after 60 Ma. Eocene to early Miocene forearc deposits covering the basement show that paleogeographic highs were located in the NW during the Eocene, but jumped to the SE before ~25 Ma. We propose that this block tilting along the coast was triggered by orogen-parallel Eo-Oligocene extension that accommodated counterclockwise block rotation in the southern Peruvian forearc during the formation of the Bolivian Orocline.

IV. 1 – Introduction

The Central Andes are characterized by the occurrence of the second largest elevated plateau in the world and by an important curvature: the Bolivian Orocline (Fig. IV.1). Previous studies have shown that the beginning of crustal shortening (Sempere et al., 1990; Horton, 2005) broadly corresponds to the onset of rigid block rotations that led to the present-day curvature of the orogen (MacFadden et al., 1990; Beck et al., 1994; MacFadden et al., 1995; Somoza et al., 1999; Beck, 1998; Randall, 1998; Taylor et al., 2005; Roperch et al., 2006; Taylor et al., 2007; Arriagada et al., 2008; Eichelberger et al., 2013). In particular, in their 2D reconstruction of paleogeography (Fig. IV.1), Arriagada et al. (2008) calculated that the oroclinal bending was accompanied by ~200 to 260 km of stretching parallel to the margin between ~10 and ~30°S between 4~0 and ~25 Ma. However, the influence of these rotations on the history of exhumation is poorly documented in the forearc, where vertical-axis rotations can reach ~55°.

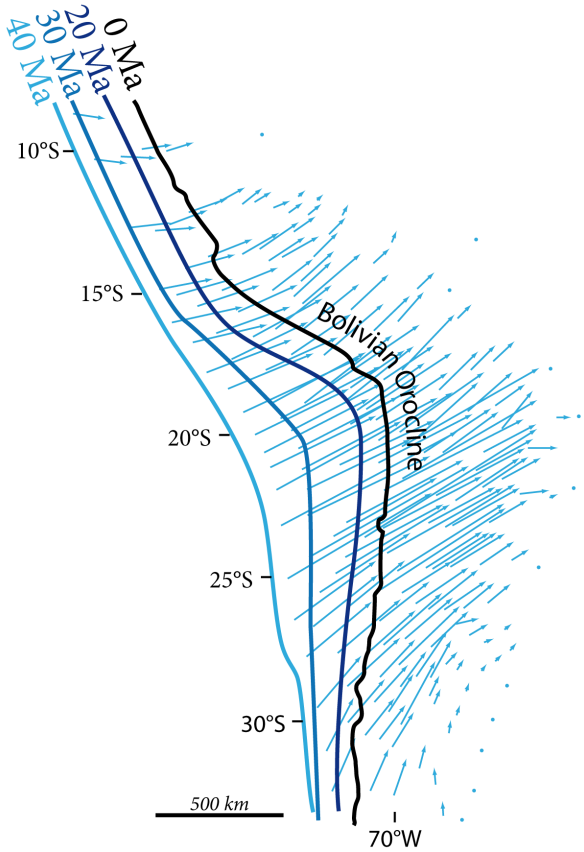

Figure IV.1: Infered position of the south American western coastline through time (thick lines) after Roperch et al. (2006), and total (40 Ma to present) displacement vectors (arrows) for restoration of paleomagnetic data after Arriagada et al. (2008). In southern Peru, paleomagnetic rotations recorded in rocks older than ~40 Ma are maximum whereas rocks younger than ~25 Ma do not show evidences of tectonic rotation.

In the southern part of the Bolivian Orocline (coastal northern Chile), Juez-Larré et al., 2010 report results of a low-temperature thermochronology study on a ~2000 m vertical profile in a coastal diorite pluton. These authors describe an Eocene cooling event that they attribute to a change in subduction dynamics when the Farallon–Phoenix ridge entered the subduction zone below the present-day Central Andes. However, different studies investigating the thermal history of the present-day forearc of southern Peru (Schildgen et al., 2007; Schildgen et al., 2009a; Gunnell et al., 2010; Wipf et al., 2008) yielded comparable ages along the coast of southern Peru, where the Farallon–Phoenix ridge entered the subduction zone later, likely during the Oligocene (Sdrolias and Müller, 2006) and questionning the signification of cooling ages in southern Peru.

This study assesses the history of deformation and exhumation linked to oroclinal bending in the forearc. We focus on the forearc of southern Peru between ~14 and ~17°S, where rotations were the most important (Arriagada et al., 2008). Moreover, the large basement block that crops out there (the Atico - Mollendo block, Fig. IV.2) has been little affected by the different Mesozoic magmatic arcs that developed along the margin, minimizing the difficulty of differentiating between post-magmatic cooling and exhumational cooling in thermal history reconstructions. We use mica $^{40}Ar/^{39}Ar$, zircon and apatite fission-track, and zircon (U-Th)/He data together with previously published data to characterize the spatio-thermal evolution of the forearc. This approach allows us to describe post-cooling tilting of blocks due to orogen-parallel extension accommodated on faults that strike perpendicular to the coastline. Together with the sedimentary architecture of the Cenozoic forearc deposits, we better constrain offset on the faults and their timing of activity with respect to bending of the Bolivian Orocline.

IV. 2 – Geological setting

The forearc of southern Peru (15°–18°S) is bounded to the southwest by the Pacific coastline and to the northeast by the present-day volcanic arc, which is often referred to as the Western Cordillera (Fig. IV.2). An escarpment up to ~1000 m high defines most of the coastline. This region has been located above a major subduction zone since at least the Early Paleozoic, and possibly since ~650 Ma (Chew et al., 2008). Magmatic activity has been continuously active along the margin of southern Peru since at least the Early Jurassic

(Demouy et al., 2012; Boekhout et al., 2012). It has to be noted that the associated forearc-arc-backarc system was not static over this period but migrated through time (Fig. I.7), first toward the southwest between ~200 and ~130 Ma, then toward the NE between ~130 and ~30 Ma and again toward the SW and its actual position since ~30 Ma (Mamani et al., Fig. I.7). In order to reflect this migration of the arc through time, we propose a simplified tectonostratigraphic map of the study area (Fig. IV.3) in which we grouped together, for each of the three steps of the arc migration, the rocks respectively deposited in a backarc, arc and forearc context. Concerning the plutonic rocks, we have also grouped together intrusives associated to the same periods (Fig. IV.3).

IV. 2. A – Stratigraphy

The present-day forearc of southern Peru provides the best exposed and preserved Proterozoic basement inlier of the Pacific South American coast, the Arequipa Massif (Cobbing and Pitcher, 1972 ; Fig. IV.2). The basement crops out along ~600 km of coast between ~14°S and ~17°S (Cocachacra), and outcrops extend from the coast to ~100 km inland in the Arequipa area. The Arequipa Massif is composed of ultra-high temperature (> 900°C) Proterozoic granulites between Cocachacra and Camaná (Martignole and Martelat, 2003; Loewy et al., 2004; Casquet et al., 2010) and gneiss northwest of Camaná and in the Arequipa area (Fig. IV.2 & IV.3). The gneisses are unconformably overlain in the San Juan de Marcona area by the Upper Neo-Proterozoic, glaciogenic Chiquerio Formation (the youngest detrital zircons yielded ~700 Ma crystallization ages), which experienced greenschist facies metamorphism during the Early Paleozoic (Chew et al., 2007; Chew and Kirkland, 2011). We hereunder refer to the Atico – Mollendo block as the ~225 km-long and ~30 km-large block of Proterozoic rocks outcropping between 16.1°S and 17.2°S (Fig. IV.2).

In southern Peru, Phanerozoic rocks intrude and overlie the Arequipa Massif (Fig. IV.3). Ordovician-Silurian subduction-related granitoids (470–460 Ma, (Loewy et al., 2004; Casquet et al., 2010)) intrude the basement block croping out between Atico and Mollendo. Carboniferous to Triassic continental to deep marine deposits of the Yamayo Group overlie the basement and outcrop mainly near Atico and Ocoña (Fig. IV.3) (Narvaez and Garcia, 1962; Sempere et al., 2012; Boekhout et al., 2013).

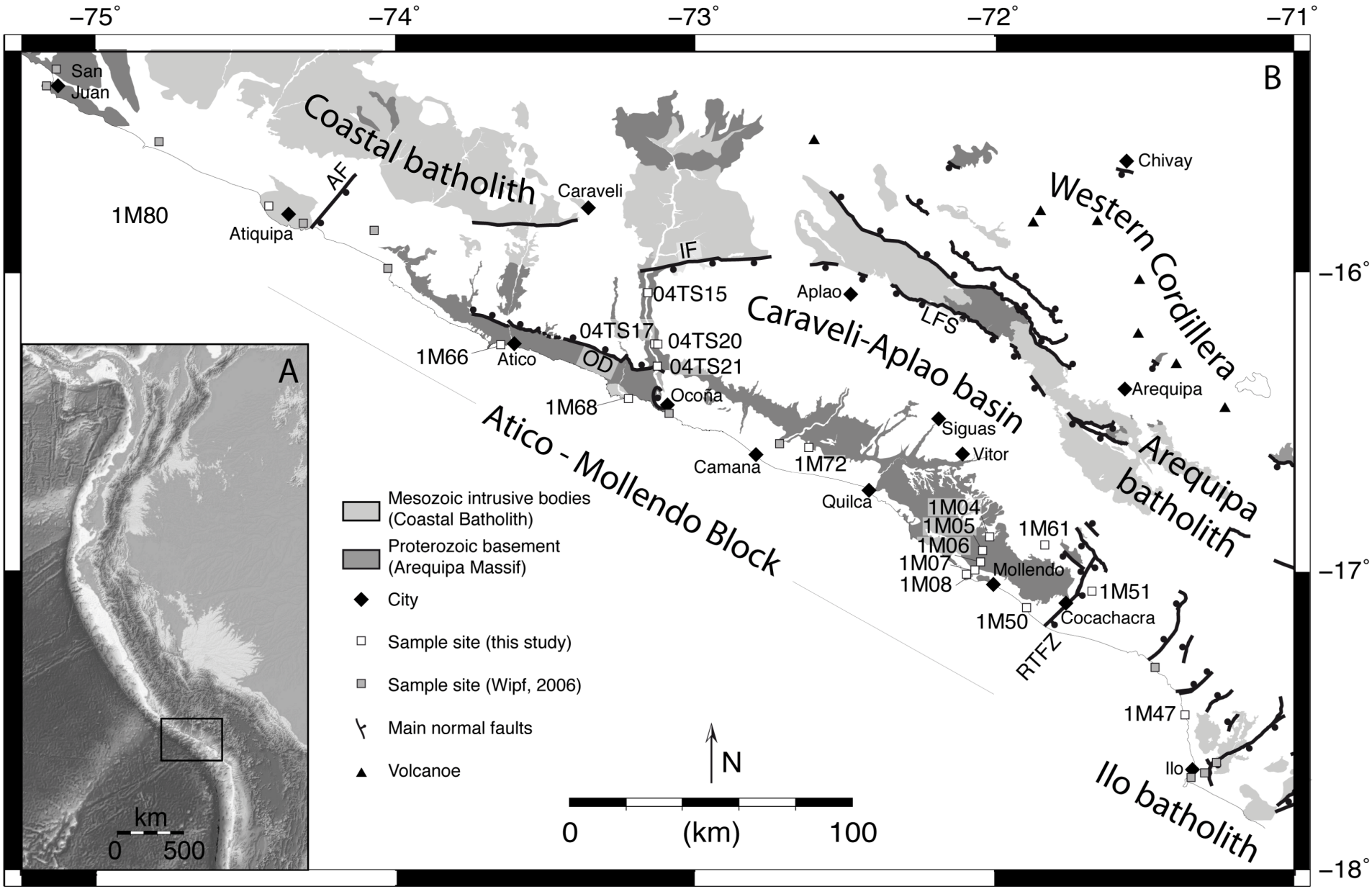
−75°
−74°
−73°
−72°
−71°
−16°
−17°
−18°
B
A
San Juan
1M80
Atiquipa
AF
Coastal batholith
Caraveli
IF
04TS15
Aplao
LFS
Caraveli-Aplao basin
Western Cordillera
Chivay
Arequipa
Arequipa batholith
1M66
Atico
04TS17
04TS20
04TS21
OD
Ocoña
1M68
Camana
1M72
Siguas
Vitor
Quilca
Atico - Mollendo Block
1M04
1M05
1M06
1M07
1M08
1M61
Mollendo
1M51
1M50
Cocachacra
RTFZ
1M47
Ilo
Ilo batholith
Mesozoic intrusive bodies (Coastal Batholith)
Proterozoic basement (Arequipa Massif)
City
Sample site (this study)
Sample site (Wipf, 2006)
Main normal faults
Volcanoe
N
0
(km)
100
km
0
500

As stated above, the subduction arc was active almost continuously between ~200 and 60 Ma, a period during which it migrated through time (e.g. Mamani et al., 2010; Demouy et al., 2012). Numerous plutonic rocks associated with this magmatic activity crops out in the present-day forearc of southern Peru, forming the "Coastal Batholith" (Fig. IV.2). It is composed by Lower Jurassic (200-175 Ma) plutons cropping out mainly in the Arequipa area (Demouy et al., 2012) and Upper Jurassic (175-150 Ma) plutons intruded by Lower Cretaceous (110-106 Ma) magmatic bodies which crop out in the coastal area, south of 17.1°S, building the composite Ilo Batholith (Demouy et al., 2012; Boekhout et al., 2012) (Fig. IV.2 & IV.3). Upper Cretaceous to Paleocene plutons (90 – 60 Ma) outcrop at least at ~40 km from the coastline, in particular, they intrude the Lower Jurassic plutons in the Arequipa region (Fig. IV.3). It has to be noted that there is no evidence of Mesozoic magmatic activity in the Atico-Mollendo block (Demouy et al., 2012), suggesting that the arc did not intruded the gneiss and migmatites of the basement in this area (Fig. IV.2 & IV.3). Volcanic products of Jurassic to Lower Cretaceous age (Chocolate and Toquepala Formations, Fig. IV.3) overlie the previously described rocks, and crop out mainly near Atiquipa, north of Ilo and in main river valleys (for example near Aplao). Additionally, a sedimentary succession of ~185–50 Ma marine backarc deposits outcrops ~50 km northeast of Aplao and ~50 km southeast of Arequipa (Jenks, 1948; Sempere et al., 2002; Boekhout et al., 2013).

Eocene to Pliocene deposits of the Moquegua Group (Marocco, 1984; Sempere et al., 2004; Decou et al., 2011, 2013), unconformably overlie the previous stratigraphic succession between Caravelí and La Joya (Fig. IV.3). These continental forearc sediments deposited in the "Caravelí-Aplao basin" (Fig. IV.2) between ~50 and ~4.5 Ma. We propose the first map of these deposits (Fig. IV.3) (from satellital pictures) in the forearc of southern Peru, following the subdivisions of Roperch et al., 2006. Finally, Upper Oligocene to Miocene deltaic deposits of the Camaná Formation (Pecho and Morales, 1969; Sempere et al., 2004; Roperch et al., 2006; Alván and von Eynatten, 2014) crop out on the coastline, mainly at the outlet of the Camaná river (Fig. IV.3).

(*previous page)* Figure IV.2: A. Location (black square) of the study area in northwestern South-America. B. Schematic map of the study area showing the sites sampled for thermochronology (this study and Wipf, 2006) and the main geologic features mentioned in text. AF: Atiquipa fault; IF: Iquipi fault; LFS: Lluclla fault system; OD: Ocoña detachment; RTFZ: Río Tambo fault zone.

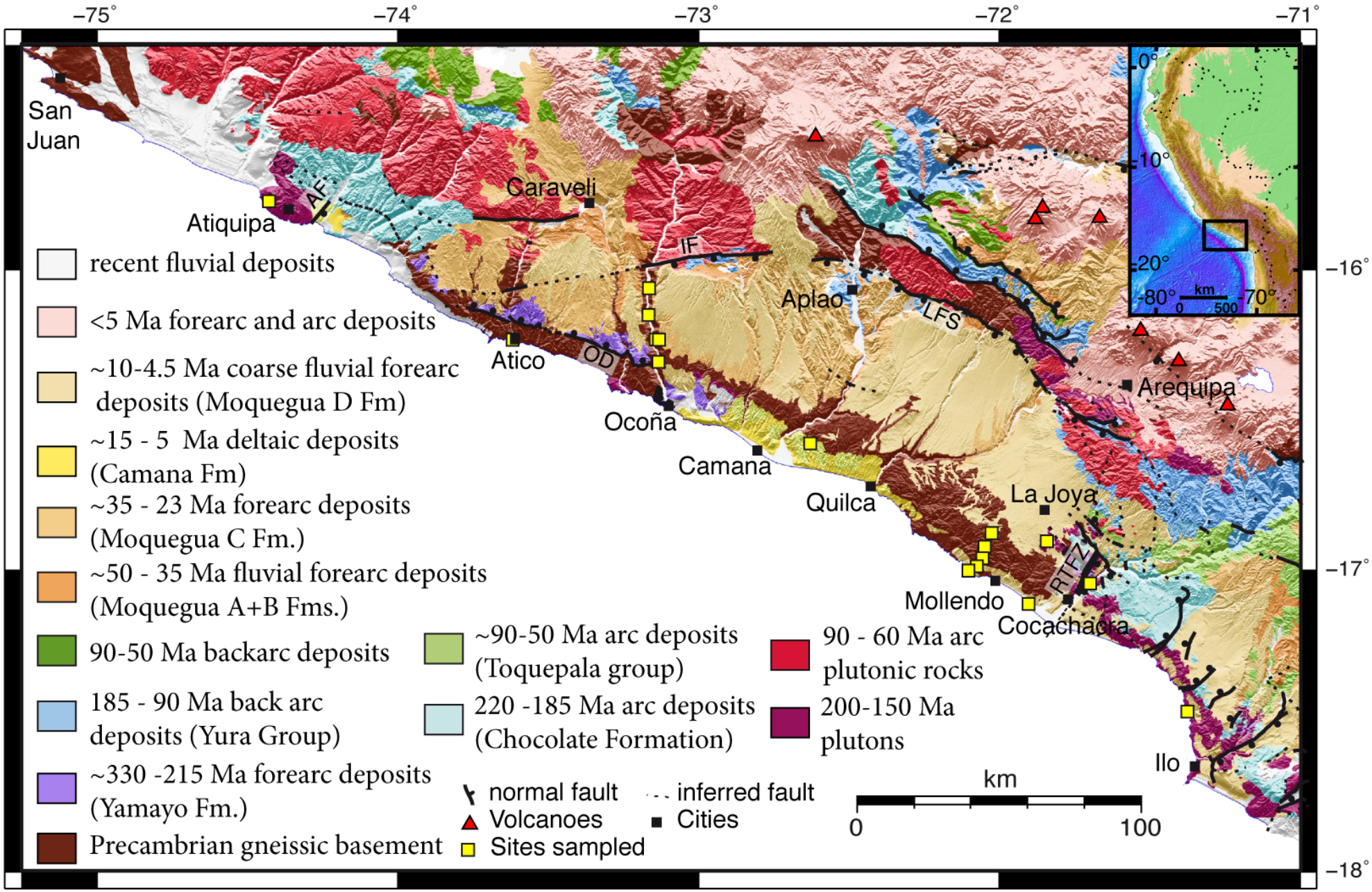

Figure IV.3: Tectono-stratigraphic map of southern Peru (after the 1:100,000 geological maps by INGEMMET) and its location in northwestern South America. AF: Atiquipa Fault; OD: Ocoña detachment; IF: Iquipi fault; LFS: Lluclla Fault System; RTFZ: Río Tambo fault zone.

IV. 2. B – Structural setting

It has been proposed that the Arequipa Massif is composed of different tectonically juxtaposed metamorphic domains because ages and grades of metamorphism are diachronous in the massif (Martignole and Martelat, 2003; Casquet et al., 2010). The fault zones bounding each domain are, however, not precisely described.

An important low angle normal fault zone (the Ocoña detachment) likely controlled the deposition of the Carboniferous to Triassic continental conglomerates of the Yamayo Group (Taipe, 2004) (Fig. IV.3). This detachment is particularly well exposed in the Ocoña valley where it creates a structural slab in the landscape (Fig. I.6).

The Coastal Batholith, which is composed of plutons of Jurassic to Lower Paleocene ages, typically strikes parallel to the coastline. In southern Peru, it is deflected near Caravelí to the southeast (Fig. IV.3). There, the Iquipi Fault seems closely related to the deflection (Roperch et al., 2006). This fault connects to the Lluclla Fault system (Demouy et al., 2012), which marks the southwestern border of the Coastal Batholith between Aplao and Arequipa (Fig. IV.2).

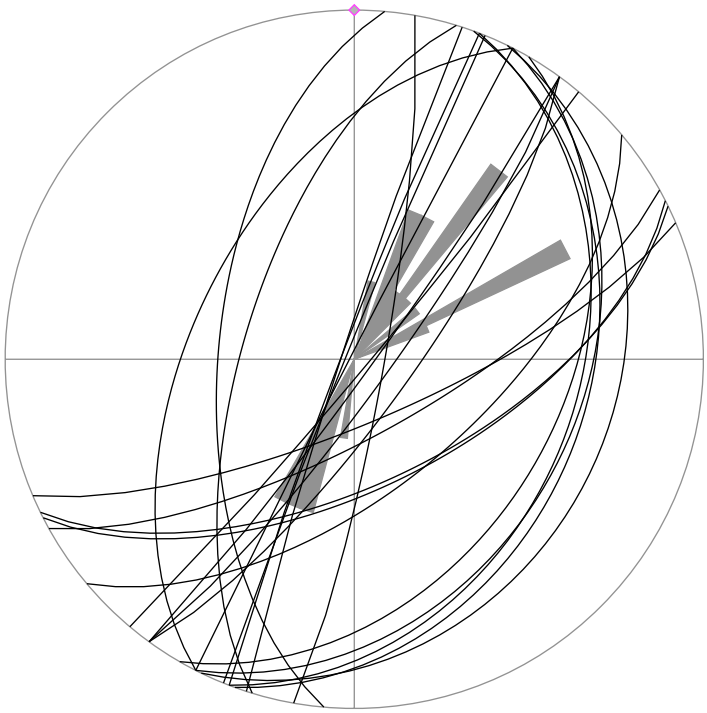

Figure IV.4: Stereographic plot showing the measured fault planes in the Atiquipa fault zone (black lines) and the corresponding rose diagram with 5° boxes (grey areas), large circle corresponds to 20% of the data (N=22).

Another important fault zone striking perpendicular to the coastline is inferred by (Roperch et al., 2006) in the Río Tambo valley. This "Río Tambo fault zone" (RTFZ) bounds the Camaná–Mollendo block to the southeast (Fig. IV.2). Numerous other faults striking perpendicular to the coastline are also reported in INGEMMET geological maps for Clemesí (Bellido et al., 1963), Ilo (Narvaez and Garcia, 1962) and Locumba (Narvaez and Jaen, 1962) areas, in particular between Ilo and Cocachacra. Near Atiquipa, we map a normal fault that was previously undescribed (Fig. IV.4). This fault outcrops on the Panamerican highway at "Playa La Caleta" bounding the Camaná–Mollendo block at northeast. It consists of a ~50 m large breccia that affects the Atiquipa diorite on its southeastern border. We could not find any striated plane in the analyzed outcrops but we measured fault planes striking broadly N035 (Fig. IV.4). The origin of these fault zones striking perpendicular to the coast was undocumented prior to this work.

IV. 3 – Methods

In this study we sampled along the coastline to better constrain the cooling history of the Arequipa Massif (Fig. IV.2). We focused our sampling on the Camaná –Mollendo block, composed of UHT migmatites intruded by Ordovician granitoids. This area lacks Mesozoic intrusive rocks and allows determining exhumational cooling instead of post-magmatic cooling.

A total of 17 localities (Fig. IV.2) were sampled for this study, 12 of which for apatite and zircon fission-track analysis, one for zircon (U-Th)/He dating, and four for $^{40}Ar/^{39}Ar$ dating on biotite and muscovite. Ten samples were collected from the Proterozoic basement, four from Ordovician plutonic rocks, two from Jurassic plutons, and one from a granite of unknown crystallization age. Sample preparation protocols are described in detail in the Appendix sections A ($^{40}Ar/^{39}Ar$ dating), B (zircon (U-Th)/He dating), and C (fission-track dating).

IV. 4 – RESULTS

IV. 4. A – Mica $^{40}Ar/^{39}Ar$ dating

We present four $^{40}Ar/^{39}Ar$ step-heating analyses on biotite and one on muscovite from the Ocoña canyon (Table IV.1), see the method for data collection in Appendix A. All samples exhibit very well defined plateau ages (Fig. IV.5). These samples were collected between the river outlet and the Iquipi fault ~50 km upstream (Fig. IV.2). Ages range from 816.7 ± 4.3 Ma upstream to 468.1 ± 2.6 Ma downstream (~15 km from the outlet). An important shift in cooling ages occurs between 35 and 25 km from the outlet, where biotite $^{40}Ar/^{39}Ar$ ages change from 816.7 ± 4.3 Ma (04TS15) to 468.1 ± 2.6 Ma (04TS21) getting closer to a granite on which whole rock Rb-Sr analysis yielded a 539 ± 90 Ma age (Cobbing et al., 1977). Additionnally, we sampled two gneisses in the canyon separated by ~500 m of elevation ~25 km from the outlet. Biotite $^{40}Ar/^{39}Ar$ analyses yielded ages of 483.1 ± 5.5 Ma and 470.3 ± 2.7 Ma respectively for the lower sample (04TS17) and upper sample (04TS20). Moreover, we obtained a muscovite $^{40}Ar/^{39}Ar$ age of 467.7 ± 2.6 Ma for the upper sample (Table IV.1).

Sample name	Latitude (°S)	Longitude (°W)	Altitude (m)	Mineral dated	Age (Ma)	2σ error (Ma)
04TS15	16.058445	73.168030	319	biotite	816.74	4.27
04TS17	16.225813	73.149583	275	biotite	483.1	5.45
04TS20	16.227267	73.144233	680	biotite	470.33	2.71
04TS21	16.301944	73.135556	100	biotite	468.1	2.62
04TS20	16.227267	73.144233	680	muscovite	467.67	2.60

Table IV.1: ^{40}Ar-^{39}Ar analyses results. All samples are from Precambrain gneiss and were analyzed by T. F. Schildgen according to the protocol defined in Appendix A.

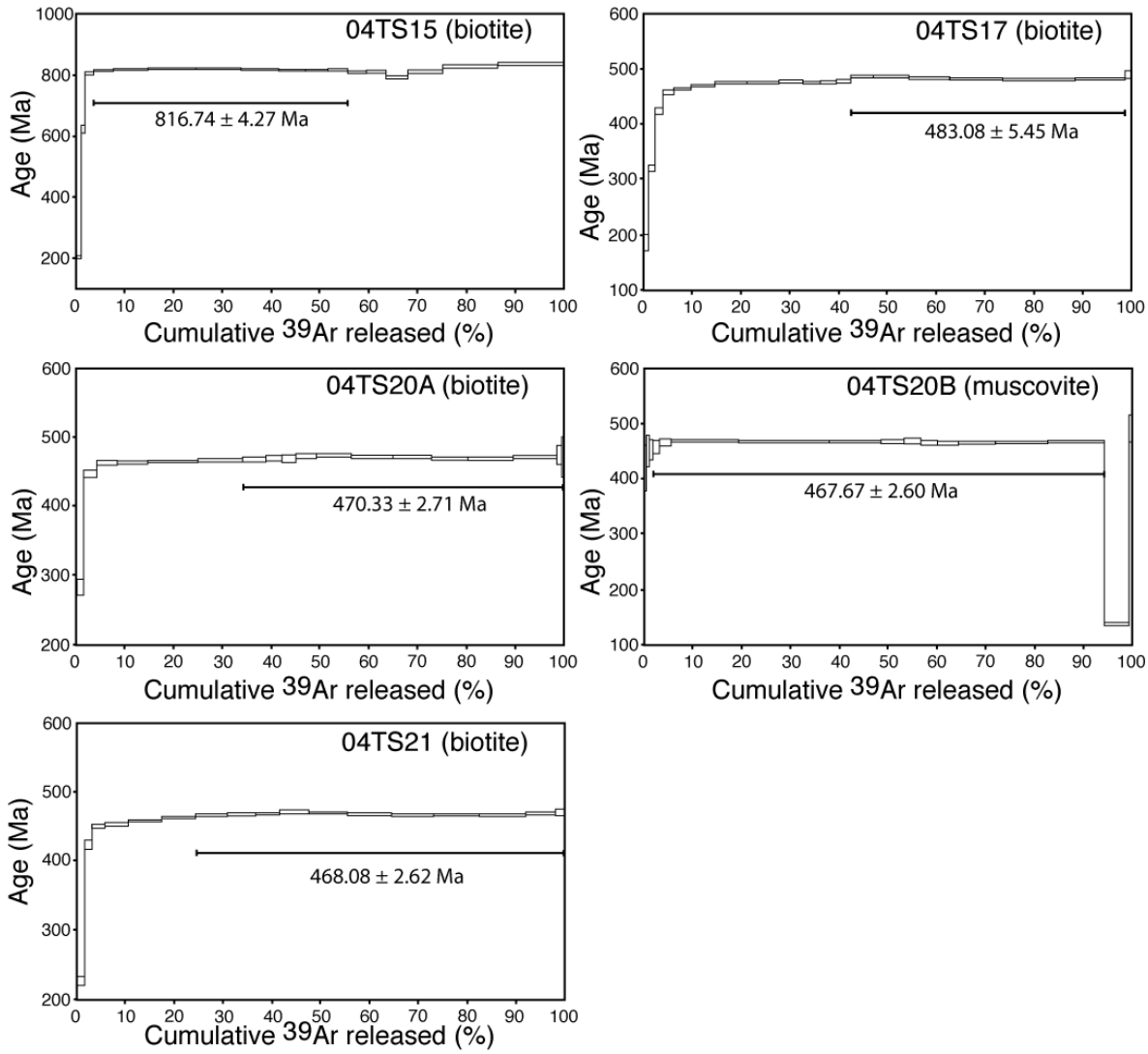

Figure IV.5: $^{40}Ar/^{39}Ar$ age spectra for samples from the Ocoña Canyon.

IV. 4. B – Zircon (U-Th)/He dating

Zircon (U-Th)/He analysis (Appendix B) of sample 1M04 (Fig. IV.2, Table IV.2) at 1200 m elevation yielded a mean age of 158.6 ± 6.6 Ma. This age is within the 2σ uncertainty of the zircon fission-track age (149 ± 39 Ma) obtained on the same sample.

Sample	grain morphology	4He (nmol/g)	U (ppm)	Th (ppm)	eU (ppm)	Rs (um)	Corrected Age (Ma)	± 2s (Ma)
1M04z1	abraded	50.42	40.2	132.4	71.3	66.4	163.2	1.8
1M04z2	very abraded	53.75	56.6	99.4	79.9	68.9	153.9	1.9

Table IV.2: Analytical data for (U-Th)/He on zircon age determinations from sample 1M04.

IV. 4. C – Apatite and zircon fission-track dating

From our 12 new sampled sites in the Atico–Mollendo block (Fig. IV.2) we obtained 9 zircon fission-track ages (Table IV.3) and 8 apatite fission-track ages (Table IV.4). Five of these locations (samples 1M04 to 1M08) are along a profile across the coastal escarpment ~10 km NW of Mollendo (Fig. IV.3). We sampled this transect at ~250 m elevation increments, from the coastline to 1200 m elevation. Zircon fission-track ages in this transect range from 227 ± 65 Ma (1M08) to 145 ± 38 Ma (1M06). Due to the scarcity of apatites in the Proterozoic ultra-high temperature migmatites and their low uranium content, we obtained only two reliable apatite fission-track ages on this transect. Sample 1M08, located on the coastline, yielded an age of 83 ± 20 Ma and sample 1M06, located in the middle of the transect at 565 m elevation, yielded an age of 55 ± 11 Ma. These fission-track ages are equivalent within 2σ uncertainty, and this transect did not yield an age-elevation relationship.

Seven samples from the coastal area between Atico (16.2°S) and Ilo (17.5°S) from 1125 m elevation to sea level yielded zircon fission-track ages between 244 ± 62 Ma (1M72) and 61 ± 13 Ma (1M47) (Table IV.3). Apatite fission-track ages range from 93 ± 28 Ma (1M51) to 63 ± 10 Ma (1M50) (Table IV.4). Due to the low uranium content in apatites, it was not possible to measure confined horizontal track lengths in these samples, neither in the samples from the Mollendo transect.

Sample name	Lithology	Latitude (°S)	Longitude (°W)	Elevation (m)	Central age (Ma)	2σ error (Ma)	N	Nd	ρd (10^5)	rse (ρd)	P(χ^2) (%)	D (%)
1M04	Proterozoic migmatite	16.87171	72.02515	1180	149	39	19	7335	1.83	1.21	93	0
1M05	Proterozoic migmatite	16.91787	72.04906	863	194	41	20	9115	2.14	1.40	89	0
1M06	Proterozoic migmatite	16.95583	72.05595	565	145	38	20	9115	2.15	1.38	43	17
1M07	Proterozoic migmatite	16.9823	72.07451	280	148	40	19	7335	1.84	1.20	64	2
1M08	Proterozoic migmatite	16.99694	72.10288	5	227	65	20	9115	2.15	1.33	31	19
1M47	Ordovician anatectic gneiss	17.4656	71.37315	0	61	13	20	7335	1.88	1.17	12	9
1M50	Undated granite	17.10783	71.90193	5	128	70	7	9115	2.21	1.06	0	112
1M66	Ordovician granite	16.938801	71.593492	30	110	28	20	7335	1.92	1.19	19	22
1M72	Ordovician granite	16.57268	72.62976	600	244	62	16	9115	2.24	1.07	66	3

Table IV.3: zircon fission-track analyses results. Age determinations were performed with ζ = 128 ± 9 for glass dosimeter CN1 according to protocol defined in Appendix C. N, number of grains counted; ρd, dosimeter track density (fluence) in tracks per cm-2; rse(ρd), relative standard error on fluence; Nd, number of tracks counted to determine the reported fluence; P(χ^2), probability that the single grain ages represent one population; D, age dispersion. Central age has been computed with the RadialPlotter software (Vermeesch, 2009).

Sample name	Lithology	Latitude (°S)	Longitude (°W)	Elevation (m)	Central age (Ma)	2σ error (Ma)	N	Nd	ρd (10^5)	rse (ρd)	P(χ^2) (%)	D (%)
1M06	Proterozoic migmatite	16.95583	72.05595	565	55	10.5	19	8323	6.01	1.13	25	13
1M08	Proterozoic migmatite	16.99694	72.10288	5	83	20	20	7814	5.91	1.44	29	21
1M50	Undated granite	17.10783	71.90193	5	63	10	24	7814	6.1	1.13	37	9
1M51	Jurassic Granite	17.03928	71.69701	171	93	28	12	8965	7.1	1.07	42	5
1M61	Jurassic Granitoïd	16.89878	71.84192	1125	65	11	20	8323	6.13	1.13	32	9
1M66	Ordovician granite	16.938801	71.593492	30	74	11	19	7814	6.16	1.15	11	12
1M68	Undated granite	16.41116	73.23413	0	74	12	20	7814	6.19	1.18	71	1
1M72	Ordovician granite	16.57268	72.62976	600	65	14	19	8965	6.82	1.27	29	13

Table IV.4: Apatite fission-track analyses results. All fission-track age determinations were performed with $\zeta = 254 \pm 12$ for glass dosimeter IRMM540 according to protocol defined in Appendix C. N, number of grains counted; ρd, dosimeter track density (fluence) in tracksper cm-2; rse(ρd), relative standard error on fluence; Nd, number of tracks counted to determine the reported fluence; P(χ^2), probability that the single grain ages represent one population; D, age dispersion. Central age has been computed with the RadialPlotter software (Vermeesch, 2009).

IV. 5 – Discussion

IV. 5. A – Compilation of thermochronological ages

A compilation of all ages available for coastal southern Peru (Table IV.5 ; Wipf, 2006; Schildgen et al., 2007; Schildgen et al., 2009a) does not show age-elevation relationship, not even in the vertical transect sampled near Mollendo. This is understandable as data cover a large region that is faulted. It is thus difficult to explain the large differences in fission-track ages (~40 Ma for apatite fission-track ages and more than 100 Ma for zircon fission-track ages) with a uniform denudation rate along the coastal area of southern Peru.

Over the six apatite (U-Th)/He dates available, three are comprised between 55 and 65 Ma. Apatite fission-track dates cluster at both ~60-70 and ~90-100 Ma, however there is no relationship between calculated central fission-track age and corresponding mean track-length measured (Wipf, 2006). Zircon (U-Th)/He dates cluster at ~150-160 Ma (Fig. IV.6) whereas zircon fission-track dates are, in contrast, widely dispersed between 61 ± 13 and 531 ± 99 Ma (Fig. IV.6). These data thus document very slow long-term exhumation rates in this area (Wipf, 2006; Schildgen et al., 2007; Schildgen et al., 2009a).

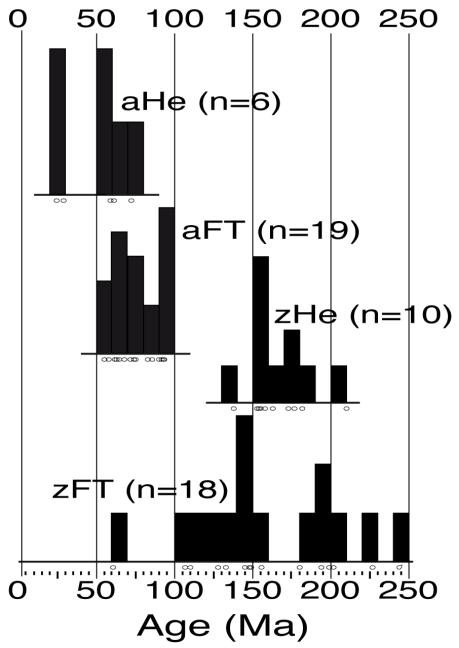

Figure IV.6: Histograms of ages available in the coastal area of Southern Peru (Wipf et al., 2008; Schildgen et al., 2007; Schildgen et al., 2009a) in function of the method used. aHe: apatite (U-Th)/He; aFT: apatite fission-track; zHe: zircon (U-Th)/He; zFT: zircon fission-track.

Sample name	Source	Location	Elevation (m)	Lithology	Age of formation	Method	Age	Age err
1M08	This study	Mollendo	5	Migmatite	Precambrian	aft	83	20
1M50	This study	Punta de bonbon	5	Granite	-	aft	63	10
1M51	This study	Cocachacra	171	Granite	163.8 ± 0.9 (a)	aft	93	28
1M61	This study	Pampa La Joya	1125	Granitoid	161.9 ± 0.9 (a)	aft	65	11
1M66	This study	Atico	30	Granite	-	aft	74	11
1M68	This study	Pescadores	0	Granite	-	aft	68	11
1M72	This study	Camana	650	Granite	447 (b)	aft	65	14
MW34	Wipf et al., 2008	San Juan de Marcona	348	Granodiorite	-	aft	55.4	7.4
MW35	Wipf et al., 2008	San Juan de Marcona	82	Gneiss	-	aft	62	10
MW41	Wipf et al., 2008	Canyon rio Ocona	307	Monzonite	-	aft	92	8
MW42	Wipf et al., 2008	Puerto Viejo	63	Granite	-	aft	90	51
MW44	Wipf et al., 2008	Atiquipa	176	Monzonite	-	aft	58	6.4
MW45	Wipf et al., 2008	Puerto de las Lomas	75	Granie	-	aft	75	20
MW52	Wipf, 2006	Ilo	32	Jurassic Granite	154.9 ± 4.8 (c)	aft	93.8	23.2
MW53	Wipf, 2006	Ilo	320	-	-	aft	85.8	10.4
MW54	Wipf, 2006	Ilo	630	-	-	aft	90	12
MW59	Wipf, 2006	Yerba Buena	230	Basement	-	aft	93.1	13.8
MW63	Wipf, 2006	Ocona	220	Migmatite	~1000 (d)	aft	71.8	9.4
1M06	This study	Mollendo	565	Migmatite	Proterozoic	aft	55	10.5
04TS17	Schildgen et al., 2007	Canyon rio Ocona	1011	-	-	aHe	59.3	1.1
04TS18	Schildgen et al., 2007	Ocona	415	-	-	aHe	72.5	
04TS21	Schildgen et al., 2007	Ocona	73	Schist?	-	aHe	61.4	15.4

Table IV.5: Compilation of data available in coastal belt of southern Peru. (a) zircon U-Pb, Boekhout et al., 2012; (b) biotite K-Ar date, Stewart et al., 1974; (c) hornblende K-Ar date, McBride (1977); (d) zircon U-Pb, Casquet et al., 2010. aft: apatite fission-track; aHe: apatite (U-Th)/He; btArAr: biotite Ar/Ar; muArAr: muscovite Ar/Ar; zft: zircon fission-track; zHe: zircon (U-Th)/He.

Sample name	Source	Location	Elevation (m)	Lithology	Age of formation	Method	Age	Age err
05TS12	Schildgen et al., 2007	Canyon rio Ocona	360	-	-	aHe	24.6	12.9
MW44	Wipf, 2006	Atiquipa	176	-	-	aHe	29	7
MW53	Wipf, 2006	Ilo	320	Granodiorite - Tonalite	-	aHe	59.3	12
04TS15	This study	Ocona	319	Gneiss	Proterozoic	btArAr	816.74	4.27
04TS16	This study	Ocona	271	Gneiss	Proterozoic	btArAr	786	3
04TS17	This study	Ocona	275	Gneiss	Proterozoic	btArAr	483.1	5.45
04TS20	This study	Ocona	680	Gneiss	Proterozoic	btArAr	470.33	2.71
04TS21	This study	Ocona	100	Gneiss	Proterozoic	btArAr	468.1	2.6
04TS20	This study	Ocona	680	Gneiss	Proterozoic	muArAr	467.67	2.6
1M04	This study	Mollendo	1180	Migmatite	Proterozoic	zft	149	39
1M05	This study	Mollendo	863	Migmatite	Proterozoic	zft	194	41
1M06	This study	Mollendo	565	Migmatite	Proterozoic	zft	145	38
1M07	This study	Mollendo	280	Migmatite	Proterozoic	zft	148	40
1M08	This study	Mollendo	5	Migmatite	Proterozoic	zft	227	65
1M47	This study	Ilo	0	Anatectic granitoid	464 ± 4 (d)	zft	61	13
1M66	This study	Atico	30	Granite	-	zft	110	28
1M72	This study	Camana	600	Granite	447 (b)	zft	244	62
1M50	This study	Punta de bonbon	5	Granite	-	zft	128	70
MW103	Wipf, 2006	Camana	64	-	-	zft	353	63
MW104	Wipf, 2006	Corire	380	-	-	zft	531	99
MW34	Wipf, 2006	San Juan de Marcona	348	Granodiorite	-	zft	348	63

Table IV.5: Compilation of data available in coastal belt of southern Peru. (a) zircon U-Pb, Boekhout et al., 2012; (b) biotite K-Ar date, Stewart et al., 1974; (c) hornblende K-Ar date, McBride (1977); (d) zircon U-Pb, Casquet et al., 2010. aft: apatite fission-track; aHe: apatite (U-Th)/He; btArAr: biotite Ar/Ar; muArAr: muscovite Ar/Ar; zft: zircon fission-track; zHe: zircon (U-Th)/He.

Sample name	Source	Location	Elevation (m)	Lithology	Age of formation	Method	Age	Age err
MW42	Wipf, 2006	Puerto Viejo	63	Granite	-	zft	156	47
MW44	Wipf, 2006	Atiquipa	176	Monzonite	-	zft	202	33
MW45	Wipf, 2006	Puerto de las Lomas	75	Granite	-	zft	180	34
MW52	Wipf, 2006	Ilo	32	Jurassic Granite	-	zft	107	14
MW53	Wipf, 2006	Ilo	320	-	-	zft	133	15
MW63	Wipf, 2006	Ocona	220	Migmatite	Proterozoic	zft	199	54
04TS16a	Schildgen et al., 2007	Canyon rio Ocona	225	Gneiss	Proterozoic	zHe	158	7.3
04TS16b	Schildgen et al., 2007	Canyon rio Ocona	225	Gneiss	Proterozoic	zHe	153	7.7
04TS18a	Schildgen et al., 2007	Canyon rio Ocona	415	Gneiss	Proterozoic	zHe	182	8.34
04TS18b	Schildgen et al., 2007	Canyon rio Ocona	415	Gneiss	Proterozoic	zHe	173	8.23
04TS20a	Schildgen et al., 2007	Canyon rio Ocona	650	Gneiss	Proterozoic	zHe	210	9.86
04TS20b	Schildgen et al., 2007	Canyon rio Ocona	650	Gneiss	Proterozoic	zHe	177	8.1
04TS21a	Schildgen et al., 2007	Canyon rio Ocona	73	Gneiss	Proterozoic	zHe	155	5.3
04TS21b	Schildgen et al., 2007	Canyon rio Ocona	73	Gneiss	Proterozoic	zHe	138	4.9
1M04z2	This study	Mollendo	1180	Migmatite	Proterozoic	zHe	163.2	1.8
1M04z3	This study	Mollendo	1180	Migmatite	Proterozoic	zHe	153.9	1.9

Table IV.5: Compilation of data available in coastal belt of southern Peru. (a) zircon U-Pb, Boekhout et al., 2012; (b) biotite K-Ar date, Stewart et al., 1974; (c) hornblende K-Ar date, McBride (1977); (d) zircon U-Pb, Casquet et al., 2010. aft: apatite fission-track; aHe: apatite (U-Th)/He; btArAr: biotite Ar/Ar; muArAr: muscovite Ar/Ar; zft: zircon fission-track; zHe: zircon (U-Th)/He.

IV. 5. B – Lateral variations of thermochronological ages

To better illustrate the lateral variations in thermochronological ages along the coastal area, we projected the different dates onto a graduated line parallel to the coast (Fig. IV.7). We focused on apatite and zircon fission-track ages because the available zircon and apatite (U-Th)/He ages from the literature are too scattered (Table IV. 5) and because the latter can be strongly affected by recent changes in topographic relief. We show that apatite and zircon fission-track ages do not follow the same lateral trend. Both exhibit well defined lateral shifts in age, but these shifts are not located at the same place along the coastline (Fig. IV.7).

a – Zircon fission-track ages.

Zircon fission-track ages greatly vary laterally along the coast of southern Peru. In particular, two zones centered on Atico and on the Ilo batholith exhibit younger ages that increase with distance from these zones. The composite Ilo Batholith (Fig. IV.2) emplaced during two episodes of magmatism, respectively 173–152 Ma and 110–106 Ma (Boekhout et al., 2012). The 107 ± 15 Ma zircon fission-track age and the modelled T-t paths reported by Wipf (2006) for the Ilo batholith indicate that the Albian plutons likely emplaced in the upper crust, cooled rapidly to temperatures <100°C, and stayed at least between 80 and 30 Ma at temperatures between 60 and 80°C. We interpret that the 133 ± 15 Ma zircon fission-track age reported by Wipf (2006) in the same region correspond to partial annealing of fission-track in a Middle Jurassic plutonic body due to the 110–106 Ma magmatic pulse. The emplacement of the Ilo Batholith may also have partially annealed fission-track in zircons from the migmatites of the Mollendo transect.

It is more difficult to explain the 61 ± 13 Ma zircon fission-track age obtained for a mylonitic granite (which yielded a zircon U-Pb age of 446 ± 6 Ma, Casquet et al., 2010) north of Ilo. However, Roperch and Carlier (1992) described a secondary magnetization of the Jurassic volcanic deposits of the Chocolate Formation and attributed it to a Late Cretaceous tectonomagmatic event to which this age could be related. However, there is no evidence of Upper-Cretaceous to Paleocene intrusions in the Atico-Mollendo Block (Fig. IV.3).

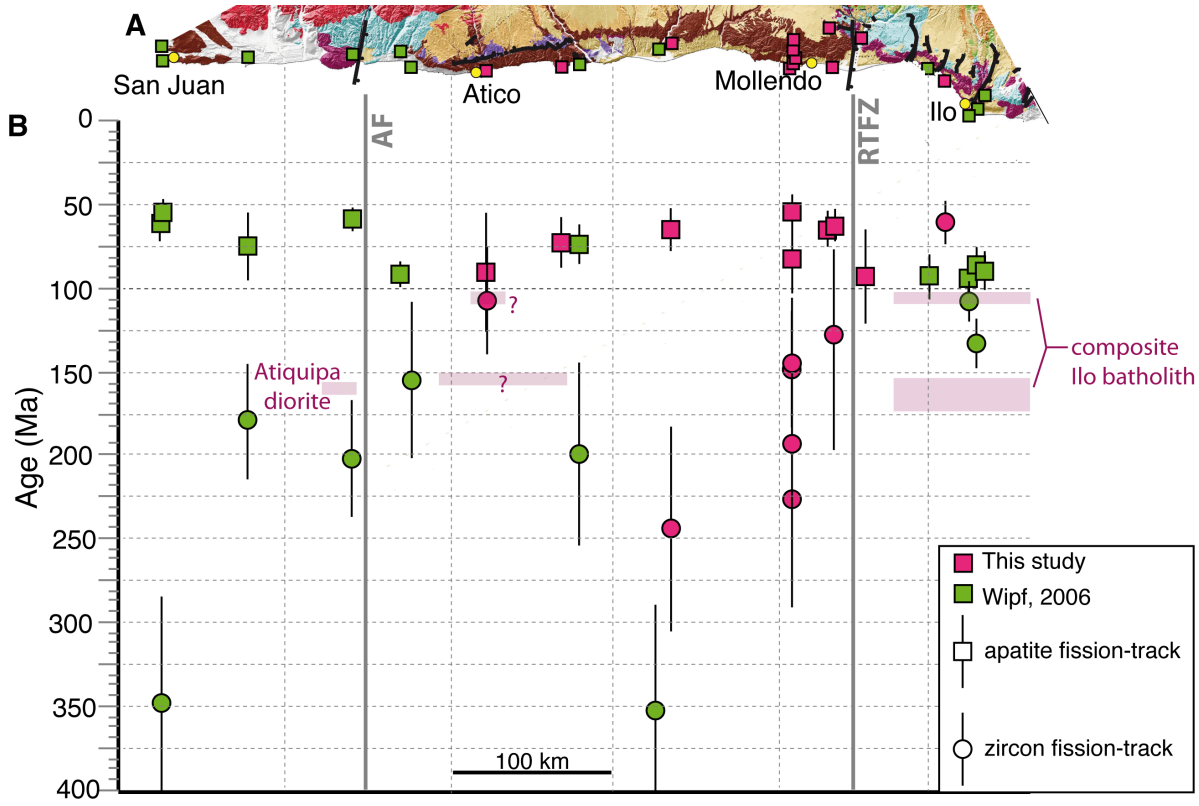

Figure IV.7: A. Geological map and location of the zircon and apatite fission-track samples used to analyze patterns of thermochronological ages in the study area. B. Corresponding plot of the different apatite (squares) and zircon (circles) fission-track ages along the coastline. AF: Atiquipa fault; RTFZ: Río Tambo fault zone.

Concerning the younger zircon fission-track ages in the region of Atico, they reflect the thermal structure of the crust during the Albian, when the arc was located in the present-day coastal area (second pulse of emplacement in the Ilo batholith). It is thus possible that a pluton, which does not crop out, emplaced at depth during this period, partially resetting the zircon fission-track ages in the Atico region (Fig. IV.8). Besides, previous thermochronological studies along the Atico–Mollendo block that yielded Jurassic and Lower Cretaceous ages support this interpretation of a Mesozoic thermal event due to magmatic emplacement in the Atico–Mollendo block. In particular, the basement that crops out in the Ocoña valley has been dated by different techniques. There, Stewartet al. (1974) obtained K-Ar dates on biotite and muscovite of 209 ± 5 Ma and 210 ± 5 Ma from a staurolite schist. They also report biotite K-Ar ages of ~204 Ma on a quartz-diroite and of ~157 Ma on a foliated diorite. Moreover, we obtained a 162.2 ± 1.1 Ma zircon U-Pb age on the Atiquipa diorite (sample 1M80, see Fig. IV.2 and Appendix D). Finally, Schildgen et al. (2009b) obtained 12

zircon (U-Th)/He ages ranging between 210 ± 9.9 Ma and 98.4 ± 3.8 Ma (the mean age of all individual ages is 145.7 ± 18.6 Ma). However, in the same valley, we obtained very well defined Proterozoic to Ordovician biotite $^{40}Ar/^{39}Ar$ plateau ages (between 816.7 ± 4.3 and 468.1 ± 2.6 Ma), as well as a 467.7 ± 2.6 Ma muscovite $^{40}Ar/^{39}Ar$ plateau age.

Zircons from the Precambrian basement likely accumulated radiation damage during at least the Ordovician–Triassic period, as the temperature of the rocks was most likely lower than 400°C during this period (based on the biotite $^{40}Ar/^{39}Ar$ cooling ages). Because of the radiation damage that accumulated in the zircon crystal, the fission-track partial annealing zone temperature range for the zircons in the basement rocks is probably quite low (Garver et al., 2005; Reiners and Brandon, 2006). For this reason, we infer that the restricted areas of the forearc with partially reset zircon fission-track ages were not hotter than 180-220°C.

To summarize, zircon (U-Th)/He and the majority of zircon fission-track ages range from 200 to 120 Ma (Table IV.5 and Fig. IV.7). This large dispersion of ages within individual thermochronological systems could be explained by reheating of the Arequipa Massif in some areas during the Jurassic to Early Cretaceous period, when the volcanic arc was located on the present-day coast line. This thermal event partially reset thermochronological systems with low effective closure temperatures (zircon fission-track and zircon (U-Th)/He). However, higher temperature systems, such as the muscovite $^{40}Ar/^{39}Ar$ system with an effective closure temperature of 300–350°C (Robbins, 1972; Hames and Bowring, 1994), were not affected by these localized Jurassic to Early Cretaceous thermal event, as the Proterozoic to Ordovician biotite $^{40}Ar/^{39}Ar$ plateau ages illustrate (Fig. IV.5).

During the Late Triassic–Early Cretaceous, lithospheric thinning and extension prevailed in the present-day coastal area of southern Peru. Volcaniclastic deposits of the Chocolate Formation, whose base is dated near Chala at 177.1 ± 2.2 Ma by $^{40}Ar/^{39}Ar$ dating on whole rock (Roperch and Carlier, 1992), accumulated rapidly in the back-arc basin that was undergoing a subsidence rate of 3.5 km/Ma (Boekhout et al., 2012). The present-day coastal area of southern Peru was also the site of intense magmatic activity. Indeed, this period corresponds to the intrusion of the composite Ilo Batholith in two phases, between 173–153 Ma and 110–106 Ma (Boekhout et al., 2012). It is thus likely that the large dispersion of zircon fission-track ages in restricted areas along the Atico–Mollendo block of coastal southern Peru is due to a partial annealing of fission-tracks in zircons at temperatures ≤ 220°C during the

Middle Jurassic–Early Cretaceous (175–105 Ma). Lithospheric thinning as well as heat conduction from the volcanic arc and burial under volcaniclastic deposits of the Chocolate Formation are good candidates to explain the partial annealing of fission tracks in zircon and the total resetting of lower temperature systems.

b – Apatite fission-track ages.

It is noteworthy that the apatite fission-track ages in the coastal area are comprised between 55 and 90 Ma and thus correspond to the period of emplacement of the Coastal and Arequipa batholiths (Fig. IV.2). However, we do not think that the Upper Cretaceous–Lower Paleocene magmatic arc influenced the apatite fission-track system. Indeed, the coastal strip we here consider has been in a forearc setting since ~100 Ma and the volcanic arc was located at least ~30 km away during the 90-60 Ma period. Yet, in these contexts, geothermal gradients are low because isotherms are depressed above the cold subducting oceanic slab and heat flux anomalies due to magma chambers in volcanic arcs are restricted to ~10 km around the volcanoes (Blackwell et al., 1990). Thus, the geothermal gradient was probably only slightly higher (likely 15°C/km) than the present-day one during the Late Cretaceous–Paleocene period. In addition, we found the older apatite fission-track ages in the area closest to where the Upper Cretaceous-Lower Paleocene magmatic arc had been located. We are thus confident that since ~100 Ma, volcanic arc activity has not affected the apatite fission-track ages from the coastal belt.

The plot of apatite fission-track ages projected along the coastline (Fig. IV.7) shows two lateral age shifts. The first is located NW of Chala and is related to the Atiquipa fault zone. The second age shift occurs NW of the Río Tambo valley, and corresponds to the Río Tambo fault system (Roperch et al., 2006) (Fig. IV.7). Both of these normal, SE-dipping fault zones strike perpendicular to the coast and bound the Atico–Mollendo block. The age shifts are thus located at the boundaries of this block.

In the domain intruded by the Ilo Batholith, SE of the Río Tambo fault system, apatite fission-track ages cluster between ~85 and 95 Ma. They are slightly younger than the two available zircon fission-track ages, which are equivalent to zircon crystallization ages (110-106 Ma, (Boekhout et al., 2012 ; Fig. IV.7), and rather correspond to post-emplacement cooling than exhumational cooling. The northwesternmost domain corresponds to the footwall of the

Atiquipa fault, there all apatite fission-track ages are equivalent within uncertainty at ~60–65 Ma (Fig. IV.7). At the NW end of the Atico-Mollendo block, older apatite fission-track ages cluster at ~90 Ma in the hanging wall of the Atiquipa fault zone whereas there is no known ~90 Ma intrusive in the area. From there, apatite fission-track ages progressively decrease along the Atico-Mollendo block towards the SE to around 60 Ma in the footwall of the RTFZ (Fig. IV.7). To explain these lateral varitions of fission-track ages, we propose that the coastal area of the Arequipa-Massif passed through the fission-track partial annealing zone of apatite during the 90-60 Ma period and that the Atico-Mollendo block, located between the Atiquipa and the Río Tambo fault systems, was tilted towards the NW afterwards (Fig. IV.8).

If we assume that the exhumation rate of the coastal area was constant at 0.13 km/Ma since 90 Ma (maximum exhumation rate calculated in the case of a 15°C/km geothermal gradient considering all samples dated with at least two different thermochronometers), the 30 Ma difference between the older and younger ages in the Atico–Mollendo block corresponds to a vertical difference of 4 km maximum. As the distance between the older and younger ages is ~175 km, the vertical difference corresponds to a tilt of ~1.3°. If we consider that the Atiquipa normal fault dips 60° towards the SE, then the slip on the fault is 4.6 km.

This interpretation of NW-tilting of the Atico-Mollendo block between the Atiquipa and Río Tambo fault zones (striking NE-SW) based on our thermochonology data is supported by additional observations. First, within the hanging wall of the Atiquipa fault zone, where the block is supposed to have subsided the most, the Chocolate volcanic succession and its underlying Pennsylvanian basin are the thickest and best preserved (Fig. IV.7). Second, in the footwall of the Río Tambo fault zone, where exhumation should be the greatest, the higher metamorphic grade rocks of the Atico–Mollendo block (and of the Arequipa Massif) are found, including ultra-high temperature (>900°C) granulites (Fig. IV.8). Moreover, no Proterozoic basement crops out southeast of this fault zone, suggesting that their exposure is a result of the tilting. The same kind of tilt appears to affect the northwestern domain of the study area (NW of the Atiquipa fault), as metamorphic grade evolves from gneisses 50 km NW of the Atiquipa fault to greenschist facies Neoproterozoic glacioeustatic sediments (Chiclayo Formation) farther NW (San Juan de Marcona) (Fig. IV.3). Because younger apatite fission-track ages cluster around 65-60 Ma (Fig. IV.7), we infer that the normal faults tilting the Atico-Molendo block were active after, or maybe during this period.

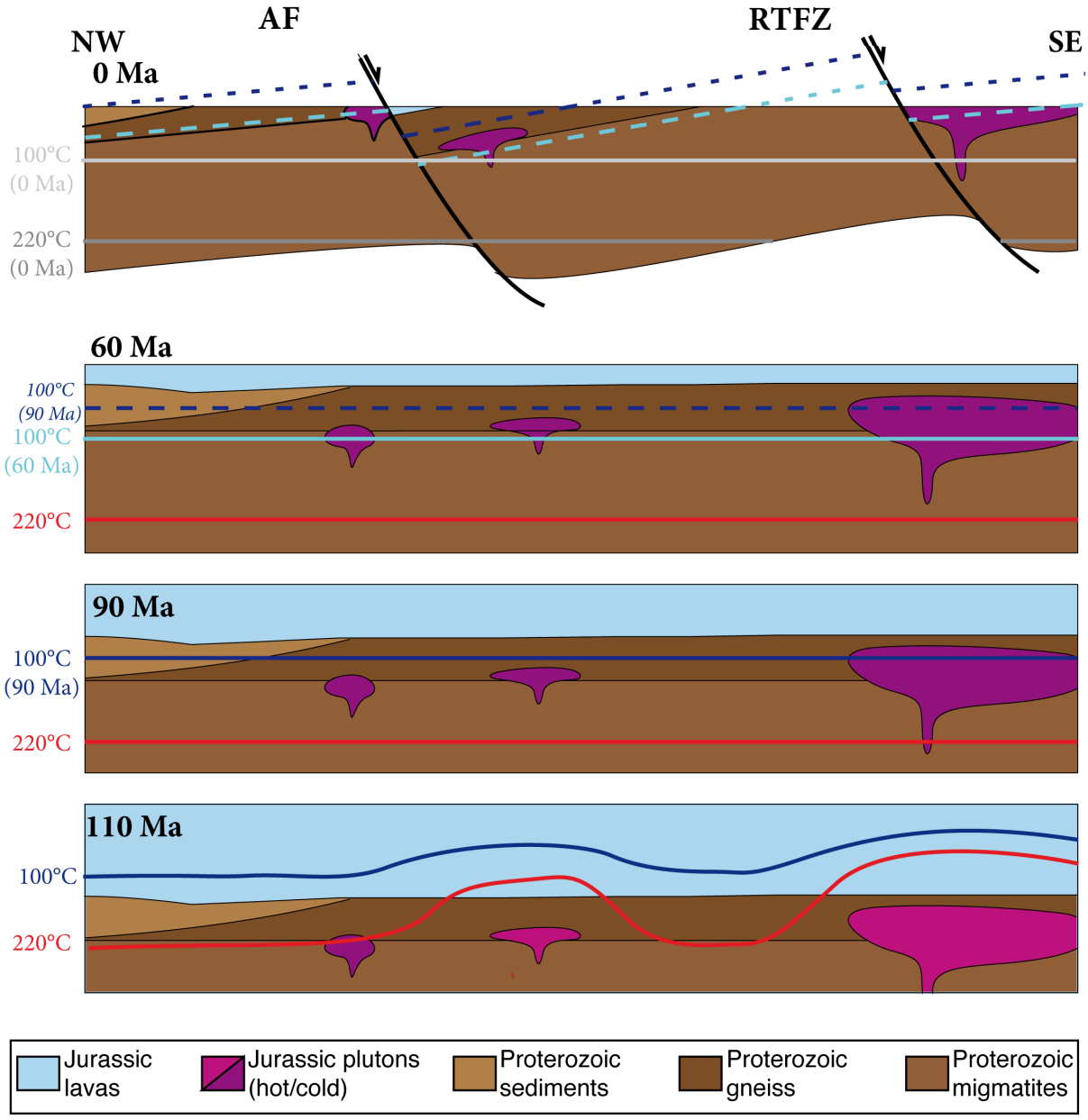

Figure IV.8: Schematic cross-sections along the present-day coast of southern Peru showing the exhumation history of the area. Solid lines correspond to isotherms, dotted line are apatite fission-track isochrones.

IV. 5. C – Architecture of the Caravelí–Aplao Paleogene basin and timing of deformation

To better constrain the duration of Atico–Mollendo block tilting, we next discuss the paleogeography of the present-day coastal area of southern Peru in Paleogene times (Fig. IV.9). To do so, we focus on the sedimentary architecture of the Cenozoic forearc deposits (Moquegua Group) in the Caravelí-Aplao basin (Fig. IV.2) overlying the basement and Mesozoic rocks of the Coastal Belt (Fig. IV.3). These mainly continental deposits filled three sub-basins located between the Arequipa Batholith and the Coastal Belt (Sempere et al., 2004; Roperch et al., 2006; Decou et al., 2011, 2013), with an onset of deposition that has been estimated at ~50 Ma in some areas (Roperch et al., 2006). The Moquegua Group is subdivided into four units, from base to top, the Moquegua A (MoqA) to Moquegua D (MoqD) (Sempere et al., 2004; Roperch et al., 2006). The first map of these deposits (grouping Moquegua A and B) is proposed in Fig. IV.3.

a – Sedimentary architecture of the Moquegua A/B deposits.

Seaward progradation of the Moquegua A/B deposits defines a significant diachronism at the base of the unit. Importantly, the more proximal sedimentary facies of the Moquegua A/B deposits (coarse fluvial conglomerates) are located in the northwest portion of the Caravelí–Aplao basin, whereas deposits towards the southeast are increasingly distal (Fig. IV.9 ; Sempere et al., 2004). This pattern suggests that areas sourcing the Moquegua A and B deposits were located in the present-day Arequipa Batholith and in the northwest sector of the study area (Quicacha area), while lower topography characterized the Vitor region in the southeast (Fig. IV.9; Huamán, 1985; Sébrier et al., 1988).

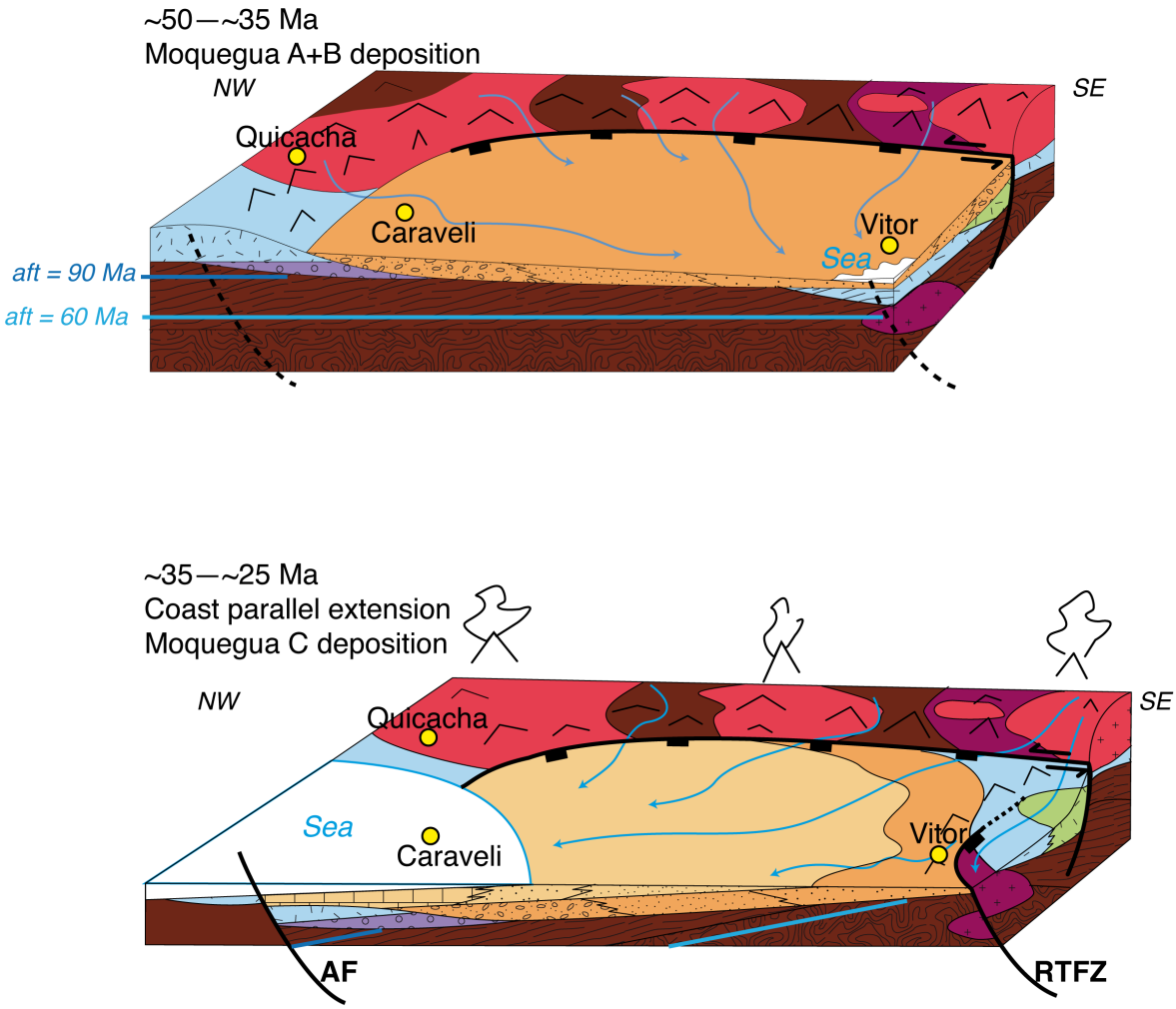

Figure IV.9: Schematic sketch of the Moquegua basin paleogeography during the Paleogene. AF: Atiquipa Fault; RTFZ: Río Tambo fault zone. Note the change of sourcing areas after ~35 Ma.

b – Sedimentary architecture of the Moquegua C deposits.

In contrast to the Moquegua A/B deposits, the Moquegua C deposits, mainly tuffaceous volcanic strata whose base is estimated at ~30 Ma (Roperch et al., 2006), are distal in the Caravelí region and record a marine incursion (Caravelí limestones) interbedded with volcanic products dated at 25 Ma (Noble et al., 1985). The Moquegua C deposits are more proximal (indicated by the presence of intercalated fluvial conglomerates) in the Siguas valley and bevel towards the SE (there are no Moquegua C deposits in the Vitor valley). This pattern suggests that an important paleotopographic change occurred during the early Oligocene: topographic highs that were located in the NW of the coastal area (Quicacha) shifted to the SE (Vitorarea; Fig. IV.9).

During the deposition of the Moquegua C unit, deltaic sediments were deposited at the outlet of the Río Camaná (Fig. IV.3). In particular, according to a sedimentological study of the Camaná fan delta deposits by Alván and von Eynatten (2014), the late Oligocene lower Camaná sediments (subunit A2) were deposited while the coastline was migrating seaward despite a rising sea-level at the time. These authors thus proposed that the lower Camaná deposits record a period of coastal uplift during the Late Oligocene–Early Miocene period. However, this time span is not well constrained. Additionally, in the hanging wall of the Atiquipa fault, highly deformed red conglomerates and whitish fine grained marine deposits crop out. Considering their facies and position, they could be lateral equivalents of the Camaná A and B deposits.

We interpret these changes in sedimentary architecture as due to block tilting between the Río Tambo and Atiquipa fault zones (respectively at the SE and NW ends of the study area; Fig. IV.9). The sedimentary facies of the Eocene to early Miocene Moquegua and Camaná Formations deposits permit us to infer that the tilting began before 25 Ma (based on Caravelí limestones deposits) and may have continued until at least the early Miocene (20 Ma, based on highly deformed lateral equivalents of Camaná B deposits in the hanging wall of the Atiquipa normal fault). It should also be noted that in the ~35 km NW of both the Atiquipa and Río Tambo fault zones, there are no preserved outcrops of Moquegua A/B and C deposits (Fig. IV.3). This lack of preservation could be due to higher tilting of the hanging walls near the fault zones, which triggered enhanced erosion during block tilting (Fig. IV.9).

IV. 5. D – Coast-parallel extension

Authors of different paleomagnetic studies (Roperch et al., 2006; Arriagada et al., 2008) have inferred that bending during the formation of the Bolivian Orocline triggered coast-parallel extension. In particular, in their 2D reconstruction of paleogeography, Arriagada et al. (2008) calculated that the oroclinal bending was accompanied by ~200 to 260 km of stretching parallel to the margin between ~10 and ~30°S. In the context of the southern Peruvian forearc, paleomagnetic studies have shown that the lower Eocene or older units show more rotation than younger units, and the magnitude of rotation increases from southeast (Arica) to northwest (Caravelí) (Roperch and Carlier, 1992; Somoza et al., 1999; Arriagada et al., 2006;

Roperch et al., 2006; Taylor et al., 2005, 2007). In particular, the Mesozoic rocks of the Arequipa belt record the same rotation as the ~45 Ma Moquegua A/B deposits (Roperch et al., 2006). In contrast, the upper Eocene to Oligocene deposits of the upper Moquegua B to lower Moquegua C units record half the rotation of the underlying Moquegua deposits (Roperch et al., 2006). It is also noteworthy that rotations in upper Oligocene and Miocene rocks are negligible after 25 Ma in southern Peru, and after 18 Ma in northern Chile (Somoza et al., 1999; Arriagada et al., 2006; Roperch et al., 2006). Thus, it is possible to constrain the period of rotation in the forearc of southern Peru between ~40 and 25 Ma. If the Atiquipa and Río Tambo fault zones accommodated the coast-parallel extension that prevailed in the forearc of southern Peru during the development of the Bolivian Orocline, they should have been active during the late Eocene to early Miocene period (~40 to 25 Ma). This timing is consistent with our interpretation of block tilting towards the NW after 60 Ma along the coast of southern Peru and with the observed sedimentary architecture of the Paleogene Moquegua deposits, which record a change in sedimentary provenance before 25 Ma (Fig. IV.7).

IV. 6 – Conclusions

Thermochronologic data available for coastal southern Peru between San Juan de Marcona and Ilo show patterns that can be interpreted in conjunction with details of the local geology to illustrate the timing and probable mechanisms of deformation.

In the San Juan de Marcona area, Upper Neo-Proterozoic greenschist meta-sediments (maximum age of ~700 Ma) unconformably overlie high grade metamorphic gneisses of the Arequipa Massif. Exhumation of the Arequipa Massif during the Neo-Proterozoic is recorded by biotite 40Ar/39Ar cooling ages in coastal southern Peru to be old as 817 ± 4 Ma, implying that no major thermal event (>350°C) occurred since then. However, zircon fission-track ages of this study as well as zircon (U-Th)/He data of Schildgen et al. (2009b) indicate a moderate heating in restricted areas of the Arequipa Massif to temperatures ≤ 220°C during the Middle Jurassic to Early Cretaceous period. This moderate and localized heating was only able to partially reset the zircon fission-track system. However, it did not affect the whole Arequipa Massif, as demonstrated by some Paleozoic low-temperature thermochronologic ages. We interpret this localized heating to be related to the Jurassic volcanic arc activity, while the

margin was subjected to intense extension. Lithospheric thinning as well as heat conduction from the volcanic arc and burial under volcaniclastic deposits of the Chocolate Formation are good candidates to explain the partial resetting of fission tracks in zircon only in select areas.

Important normal faults zones strike perpendicular to the coastline of the present-day forearc of southern Peru. Apatite fission-track age patterns show that these faults delineate a large, NW-tilted block between Atico and Mollendo. This tilt explains the lateral variation of apatite fission-track ages, which decrease toward the SE, whereas the metamorphic grade of the local bedrock increases in this direction. We suggest this tilt occurred in the Paleogene or later and attribute it to the coast-parallel extension that affected the southern Peruvian forearc during the formation of the Bolivian Orocline by map-view rotation of rigid blocks (Arriagada et al., 2008). Our interpretation is supported by the sedimentary architecture of the Paleogene to early Miocene Moquegua basin, which suggests that paleogeographic highs migrated from the northwest during the Eocene to the southeast in the Oligocene (before ~25 Ma). Some coastal deposits in the Atiquipa fault zone also indicate that tilting may have continued until the early Miocene, but further work is needed to better constrain the period of tilting.

References

Alván, A., and von Eynatten, H., 2014, Sedimentary facies and stratigraphic architecture in coarse-grained deltas: Anatomy of the Cenozoic Camaná Formation, southern Peru (16°25′S to 17°15′S): Journal of South American Earth Sciences, v. 54, p. 82–108, doi: 10.1016/j.jsames.2014.04.008.

Arriagada, C., Cobbold, P.R., and Roperch, P., 2006, Salar de Atacama basin: A record of compressional tectonics in the central Andes since the mid-Cretaceous: Tectonics, v. 25, p. TC1008, doi: 10.1029/2004TC001770.

Arriagada, C., Roperch, P., Mpodozis, C., and Cobbold, P.R., 2008, Paleogene building of the Bolivian Orocline: Tectonic restoration of the central Andes in 2-D map view: Tectonics, v. 27, p. TC6014, doi: 10.1029/2008TC002269.

Beck, M.E., 1998, On the mechanism of crustal block rotations in the central Andes: Tectonophysics, v. 299, p. 75–92, doi: 10.1016/S0040-1951(98)00199-1.

Beck, M.E., Burmester, R.R., Drake, R.E., and Riley, P.D., 1994, A tale of two continents: Some tectonic contrasts between the central Andes and the North American Cordillera, as illustrated by their paleomagnetic signatures: Tectonics, v. 13, p. 215–224, doi: 10.1029/93TC02398.

Bellido, E., Guevara, C., and Comisión Carta Geológica Nacional, 1963, Geología del cuadrángulo de Clemesi (hoja 35-t): Lima, Com. de la Carta Geológica Nacional.

Blackwell, D.D., Steele, J.L., Kelley, S., and Korosec, M.A., 1990, Heat flow in the state of washington and thermal conditions in the Cascade Range: Journal of Geophysical Research: Solid Earth, v. 95, p. 19495–19516, doi: 10.1029/JB095iB12p19495.

Boekhout, F., Sempere, T., Spikings, R., and Schaltegger, U., 2013, Late Paleozoic to Jurassic chronostratigraphy of coastal southern Peru: Temporal evolution of sedimentation along an active margin: Journal of South American Earth Sciences, v. 47, p. 179–200, doi: 10.1016/j.jsames.2013.07.003.

Boekhout, F., Spikings, R., Sempere, T., Chiaradia, M., Ulianov, A., and Schaltegger, U., 2012, Mesozoic arc magmatism along the southern Peruvian margin during Gondwana breakup and dispersal: Lithos, v. 146–147, p. 48–64, doi: 10.1016/j.lithos.2012.04.015.

Casquet, C., Fanning, C.M., Galindo Francisco, M. del C., Pankhurst, R.J., Rapela, C.W., and Torres, P., 2010, The Arequipa Massif of Peru: New SHRIMP and isotope constraints on a Paleoproterozoic inlier in the Grenvillian orogen: Journal of South American earth sciences, v. 29, p. 128–142.

Chew, D., and Kirkland, C., 2011, The Chiquerío Formation, southern Peru: The Geological Record of Neoproterozoic Glaciations, p. 481–486.

Chew, D., Kirkland, C., Schaltegger, U., and Goodhue, R., 2007, Neoproterozoic glaciation in the Proto-Andes: Tectonic implications and global correlation: Geology, v. 35, p. 1095–1098, doi: 10.1130/G23768A.1.

Chew, D.M., Magna, T., Kirkland, C.L., Mišković, A., Cardona, A., Spikings, R., and Schaltegger, U., 2008, Detrital zircon fingerprint of the Proto-Andes: Evidence for a Neoproterozoic active margin? Precambrian Research, v. 167, p. 186–200, doi: 10.1016/j.precamres.2008.08.002.

Cobbing, E.J., Ozard, J.M., and Snelling, N.J., 1977, Reconnaissance geochronology of the crystalline basement rocks of the Coastal Cordillera of southern Peru: Geological Society of America Bulletin, v. 88, p. 241–246, doi: 10.1130/0016-7606(1977)88<241:RGOTCB>2.0.CO;2.

Cobbing, E.J., and Pitcher, W.S., 1972, Plate Tectonics and the Peruvian Andes: Nature, v. 240, p. 51–53, doi: 10.1038/10.1038/physci240051a0.

Decou, A., von Eynatten, H., Dunkl, I., Frei, D., and Wörner, G., 2013, Late Eocene to Early Miocene Andean uplift inferred from detrital zircon fission track and U–Pb dating of Cenozoic forearc sediments (15–18°S): Journal of South American Earth Sciences, v. 45, p. 6–23, doi: 10.1016/j.jsames.2013.02.003.

Decou, A., von Eynatten, H., Mamani, M., Sempere, T., and Wörner, G., 2011, Cenozoic forearc basin sediments in Southern Peru (15–18°S): Stratigraphic and heavy mineral constraints for Eocene to Miocene evolution of the Central Andes: Sedimentary Geology, v. 237, p. 55–72, doi: 10.1016/j.sedgeo.2011.02.004.

Demouy, S., Paquette, J.-L., de Saint Blanquat, M., Benoit, M., Belousova, E.A., O'Reilly, S.Y., García, F., Tejada, L.C., Gallegos, R., and Sempere, T., 2012, Spatial and temporal evolution of Liassic to Paleocene arc activity in southern Peru unraveled by zircon U–Pb and Hf in-situ data on plutonic rocks: Lithos, v. 155, p. 183–200, doi: 10.1016/j.lithos.2012.09.001.

Eichelberger, N., McQuarrie, N., Ehlers, T.A., Enkelmann, E., Barnes, J.B., and Lease, R.O., 2013, New constraints on the chronology, magnitude, and distribution of deformation within the central Andean orocline: Tectonics, v. 32, p. 1432–1453, doi: 10.1002/tect.20073.

Garver, J.I., Reiners, P.W., Walker, L.J., Ramage, J.M., and Perry, S.E., 2005, Implications for Timing of Andean Uplift from Thermal Resetting of Radiation-Damaged Zircon in the Cordillera Huayhuash, Northern Peru: Journal of Geology, v. 113, p. 117–138.

Gunnell, Y., Thouret, J.-C., Brichau, S., Carter, A., and Gallagher, K., 2010, Low-temperature thermochronology in the Peruvian Central Andes: implications for long-term continental denudation, timing of plateau uplift, canyon incision and lithosphere dynamics: Journal of the Geological Society, v. 167, p. 803–815, doi: 10.1144/0016-76492009-166.

Hames, W.E., and Bowring, S.A., 1994, An empirical evaluation of the argon diffusion geometry in muscovite: Earth and Planetary Science Letters, v. 124, p. 161–169, doi: 10.1016/0012-821X(94)00079-4.

Horton, B.K., 2005, Revised deformation history of the central Andes: Inferences from Cenozoic foredeep and intermontane basins of the Eastern Cordillera, Bolivia: Tectonics, v. 24, p. TC3011, doi: 10.1029/2003TC001619.

Huamán, D., 1985, Evolution tectonique cénozoïque et néotectonique du piémont pacifique dans la région d'Arequipa (Andes du Sud-Pérou) [Thèse de doctorat de 3ème cycle]: Université de Paris-Sud, 220 p.

Jenks, W.F., 1948, Geología de la Hoja de Arequipa al 200,000: Boletín del Instituto Geológico del Perú, v. 9.

Juez-Larré, J., Kukowski, N., Dunai, T.J., Hartley, A.J., and Andriessen, P.A.M., 2010, Thermal and exhumation history of the Coastal Cordillera arc of northern Chile revealed by thermochronological dating: Tectonophysics, v. 495, p. 48–66, doi: 10.1016/j.tecto.2010.06.018.

Loewy, S.L., Connelly, J.N., and Dalziel, I.W.D., 2004, An orphaned basement block: The Arequipa-Antofalla Basement of the central Andean margin of South America: Geological Society of America Bulletin, v. 116, p. 171–187, doi: 10.1130/B25226.1.

MacFadden, B.J., Anaya, F., and Swisher, C.C., 1995, Neogene paleomagnetism and oroclinal bending of the central Andes of Bolivia: Journal of Geophysical Research: Solid Earth, v. 100, p. 8153–8167, doi: 10.1029/95JB00149.

MacFadden, B. J., Anaya, F., Perez, H., Naeser, C. W., Zeitler, P. K., and Campbell Jr, K. E., 1990, Late Cenozoic paleomagnetism and chronology of Andean basins of Bolivia: Evidence for possible oroclinal bending: Journal of Geology, v. 98, p. 541–555.

Mamani, M., Wörner, G., and Sempere, T., 2010, Geochemical variations in igneous rocks of the Central Andean orocline (13°S to 18°S): Tracing crustal thickening and magma generation through time and space: Geological Society of America Bulletin, v. 122, p. 162–182.

Marocco, R., 1984, Dynamique du remplissage d'un bassin intramontagneux cénozoïque andin : le bassin Moquegua (Sud du Pérou): Cahiers ORSTOM.Série Géologie, v. 14, p. 117–140.

Martignole, J., and Martelat, J.-E., 2003, Regional-scale Grenvillian-age UHT metamorphism in the Mollendo–Camana block (basement of the Peruvian Andes): Journal of Metamorphic Geology, v. 21, p. 99–120, doi: 10.1046/j.1525-1314.2003.00417.x.

Narvaez, S., and Garcia, W., 1962, Geologia del cuadrangulo de Ilo (hoja 36-t):.

Narvaez, S., and Jaen, H., 1962, Geologia del cuadrangulo de Locumba (hoja 36-u):.

Noble, D.C., Sébrier, M., Megard, F., and McKee, E.H., 1985, Demonstration of two pulses of Paleogene deformation in the Andes of Peru: Earth and Planetary Science Letters, v. 73, p. 345–349, doi: 10.1016/0012-821X(85)90082-2.

Pecho, V., and Morales, G., 1969, Geología de los cuadrangulos de Camana y le Yesera: Boletín del Servicio Geologico Minero, 21.

Randall, D.E., 1998, A new Jurassic–Recent apparent polar wander path for South America and a review of central Andean tectonic models: Tectonophysics, v. 299, p. 49–74, doi: 10.1016/S0040-1951(98)00198-X.

Reiners, P.W., and Brandon, M.T., 2006, Using Thermochronology to Understand Orogenic Erosion: Annual Review of Earth and Planetary Sciences, v. 34, p. 419–466, doi: 10.1146/annurev.earth.34.031405.125202.

Robbins, G.A., 1972, Radiogenic argon diffusion in mscovite under hydrothermal conditions [M.S. Thesis]: Brown University.

Roperch, P., and Carlier, G., 1992, Paleomagnetism of Mesozoic rocks from the central Andes of southern Peru: Importance of rotations in the development of the Bolivian orocline: Journal of Geophysical Research: Solid Earth, v. 97, p. 17233–17249, doi: 10.1029/92JB01291.

Roperch, P., Sempere, T., Macedo, O., Arriagada, C., Fornari, M., Tapia, C., García, M., and Laj, C., 2006, Counterclockwise rotation of late Eocene–Oligocene fore-arc deposits in southern Peru and its significance for oroclinal bending in the central Andes: Tectonics, v. 25, p. TC3010, doi: 10.1029/2005TC001882.

Schildgen, T.F., Ehlers, T.A., Whipp, D.M., van Soest, M.C., Whipple, K.X., and Hodges, K.V., 2009a, Quantifying canyon incision and Andean Plateau surface uplift, southwest Peru: A thermochronometer and numerical modeling approach: Journal of Geophysical Research: Earth Surface, v. 114, p. F04014, doi: 10.1029/2009JF001305.

Schildgen, T.F., Hodges, K. V., Whipple, K.X., Reiners, P.W., and Pringle, M. S., 2007, Uplift of the western margin of the Andean plateau revealed from canyon incision history, southern Peru: Geology, v. 35, p. 523–526, doi: 10.1130/G23532A. 1.

Schildgen, T.F., Hodges, K.V., Whipple, K.X., Pringle, M.S., van Soest, M.C., and Cornell, K., 2009b, Late Cenozoic structural and tectonic development of the western margin of the Central Andean Plateau in southwest Peru: Tectonics, v. 28, doi: 10.1029/2009tc002590.

Sdrolias, M., and Müller, R.D., 2006, Controls on back-arc basin formation: Geochemistry, Geophysics, Geosystems, v. 7, p. Q04016, doi: 10.1029/2005GC001090.

Sébrier, M., Lavenu, A., Fornari, M., and Soulas, J.-P., 1988, Tectonics and uplift in Central Andes (Peru, Bolivia and Northern Chile) from Eocene to present: Géodynamique,.

Sempere, T., Boekhout, F., Noury, M., Taipe, E., García, F., Jacay, J., Spikings, R.A., and Schaltegger, U., 2012, Reinstauración del Grupo Yamayo (Bellido y Guevara, 1963), y su significado en la evolución de la margen peruana del Carbonífero al Triásico, *in* XVI Congresso Peruano de Geologia, Lima.

Sempere, T., Carlier, G., Soler, P., Fornari, M., Carlotto, V., Jacay, J., Arispe, O., Néraudeau, D., Cárdenas, J., Rosas, S., and Jiménez, N., 2002, Late Permian–Middle Jurassic lithospheric thinning in Peru and Bolivia, and its bearing on Andean-age tectonics: Tectonophysics, v. 345, p. 153–181, doi: 10.1016/S0040-1951(01)00211-6.

Sempere, T., Fornari, M., Acosta, J., Flores, A., Jacay, J., Peña, D., Roperch, P., and Taipe, E., 2004, Estratigrafía, geocronología, paleogeografía y paleotectónica de los depósitos de antearco del sur del Perú, *in* Resúmenes extendidos del XII Congreso Peruano de Geología, Lima, Sociedad Geológica del Perú, p. 533–536.

Sempere, T., Hérail, G., Oller, J., and Bonhomme, M.G., 1990, Late Oligocene-earlyMiocene major tectonic crisis and related basins in Bolivia: Geology, v. 18, p. 946–949.

Somoza, R., Singer, S., and Tomlinson, A., 1999, Paleomagnetic study of upper Miocene rocks from northern Chile: Implications for the origin of Late Miocene-Recent tectonic rotations in the southern Central Andes: Journal of Geophysical Research: Solid Earth, v. 104, p. 22923–22936, doi: 10.1029/1999JB900215.

Stewart, J.W., Evernden, J.F., and Snelling, N.J., 1974, Age Determinations from Andean Peru: A Reconnaissance Survey: Geological Society of America Bulletin, v. 85, p. 1107–1116, doi: 10.1130/0016-7606(1974)85<1107:ADFAPA>2.0.CO;2.

Taipe, E., 2004, Détachement en extension et sédimentation : Les bassins Pennsylvaniens d'Atico et Ocoña (Sud Pérou) [Mémoire de DEA]: Université Paul Sabatier, 38 p.

Taylor, G.K., Dashwood, B., and Grocott, J., 2005, Central Andean rotation pattern: Evidence from paleomagnetic rotations of an anomalous domain in the forearc of northern Chile: Geology, v. 33, p. 777–780, doi: 10.1130/G21876.1.

Taylor, G.K., Grocott, J., Dashwood, B., Gipson, M., and Arévalo, C., 2007, Implications for crustal rotation and tectonic evolution in the central Andes fore arc: New paleomagnetic results from the Copiapó region of northern Chile, 26°–28°S: Journal of Geophysical Research: Solid Earth, v. 112, p. B01102, doi: 10.1029/2005JB003950.

Wipf, M.A., 2006, Evolution of the Western Cordillera and Coastal Margin of Peru: Evidence from low-temperature Thermochronology and Geomorphology [PhD]: Swiss Federal Institute of Technology, 152 p.

Wipf, M., Zeilinger, G., Seward, D., and Schlunegger, F., 2008, Focused subaerial erosion during ridge subduction: impact on the geomorphology in south-central Peru: Terra Nova, v. 20, p. 1–10, doi: 10.1111/j.1365-3121.2007.00780.x.

Chapter V –
Neogene crustal flow-driven subsidence of Altiplano edges defines two episodes of Andean crustal thickenning

Over a large region, the Central Andean crust is >60 km thick. However, how and when this overthickness was acquired remains debated. Although, it is currently believed that the Andes built-up incrementally during the last 30 My. New data from coastal southernmost Peru show that the orogenic evolution is more complex. Indeed, the Andean crust locally thickenned between ~23 and ~10 Ma and again since ~4.5 Ma. This is reflected by surface uplift, but significant subsidence occurred between ~10 and ~4.5 Ma. This chronology, combined with regional geological data, suggests that subsidence at ~10 Ma resulted from ductile flow away from overthickenned crust. This evolution sheds new light on the Central Andean crustal overthickening, which was markedly diachronous and whose last episode has developed since ~4.5 Ma in the absence of any significant tectonic shortening.

V. 1 – Introduction

High mountain ranges rise on Earth where the crust is overthickened, as in the well-known case of continental collisions. Considerable crustal overthickening may however also develop in subduction settings devoid of continental collision. For example, within the Central Andes, the Bolivian Orocline (Fig. V.1) is characterized by a ≥200 km wide, >3.6 km high plateau underlain by >60 km thick crust (James, 1971; Isacks, 1988; Beck and Zandt, 2002). Although, how this crustal ovethickness has been achieved in the absence of continental collision still remains unclear (Sempere et al., 2008).

The currently dominant paradigm favors that Andean crustal thickening resulted from tectonic shortening (Isacks, 1998; Lamb and Davies, 2003) caused by "ocean-continent collision" (Yuan et al., 2000). This hypothesis is however at odds with the fact that little to no tectonic shortening is observed along the Andean Pacific side (James, 1971; Tosdal et al., 1984; Kono et al., 1989; Sempere and Jacay, 2008). A claim that the Central Andes underwent rapid surface uplift through delamination of the lower lithosphere during the Late Miocene (Garzione et al., 2008) was later disproved, favoring instead the idea that major crustal thickening and related surface uplift have developed more or less continuously since ~30 Ma (Ehlers and Poulsen, 2009; Mamani et al., 2010). In any case, crustal overthickening had the important consequence of increasing the tickness of the ductile lower crust. It results that most of the Central Andean mountains sit over a ≥50 -km-thick 'layer' of relatively low-viscosity material (Yuan et al., 2000). This has implications for regional tectonics and implies special rheological behavior including lateral flow (Husson and Sempere, 2003; Picard et al., 2008). Moreover, crustal thickening generates surface uplift via isostatic compensation of crustal masses either added by lower crustal flow or removed by normal faulting and/or erosion. Thus, determining the timing of incision and sedimentation is crucial for studying orogenic evolution.

Here we investigate the Andean surface uplift issue by focusing on its history in coastal southern Peru. This region is interesting in three ways. First, because regional crustal thickening in the Bolivian Orocline (Fig. V.1) is thought to have resulted in lateral flow of the overthickened ductile crust along but also across the orogen (Husson and Sempere, 2003; Yang et al., 2003; Gerbault et al., 2005). Coastal regions of the Central Andes are thus expected to have recorded the regional uplift history, in particular because the nearby Pacific Ocean

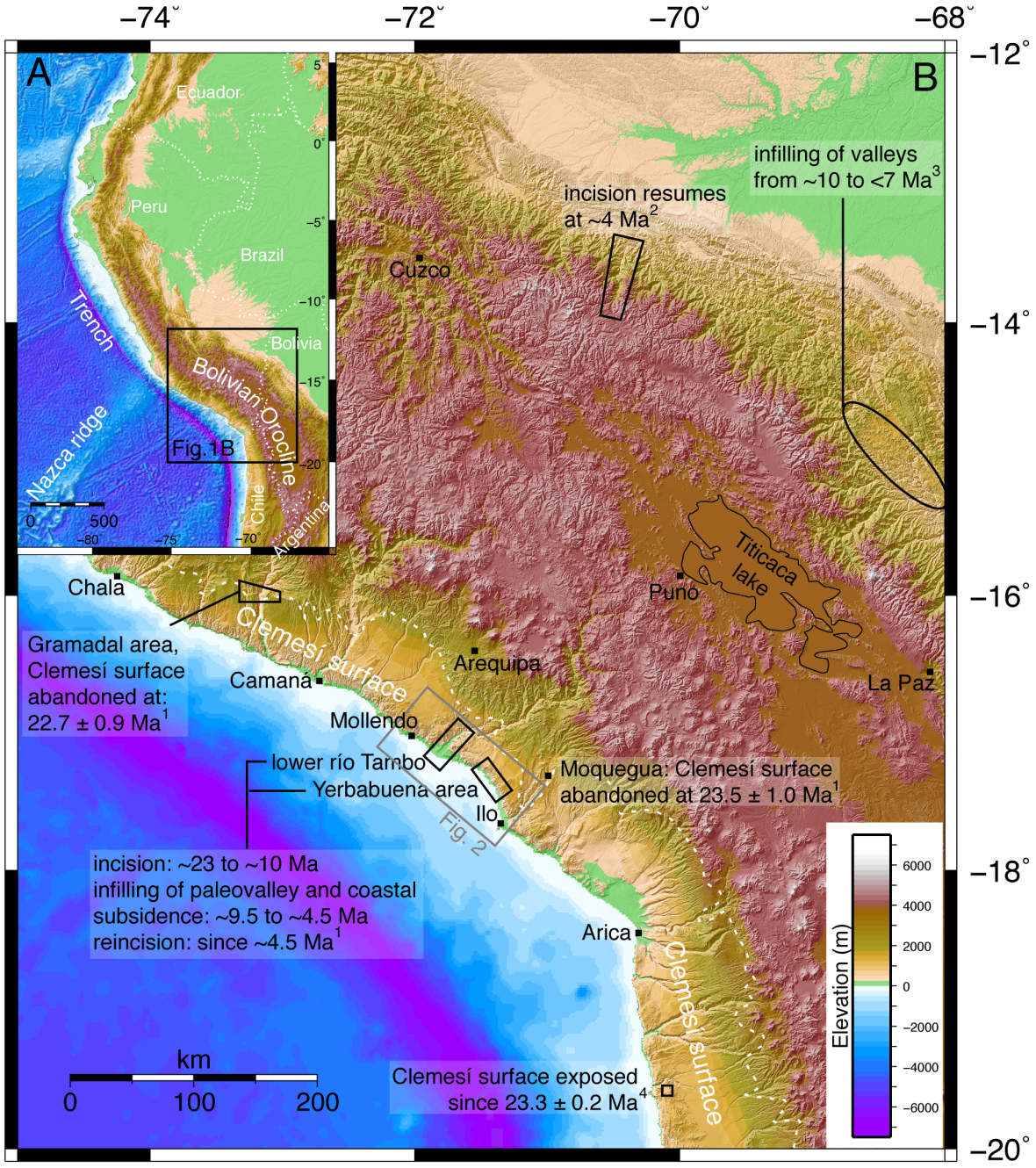

Figure V.1: A. Location in northwestern South America, geographic borders (white dotted lines) and location of main geological features; B. Location of the different areas mentioned in text and timing of the different events concerning the Andean surface uplift. The white dotted line marks the approximate northeast limit of the Clemesí surface. References: [1]: this paper; [2]: Lease & Ehlers (2013); [3]: Mosolf et al. (2011); [4]: Dunai et al. (2005).

imposed a base level controlling geomorphic markers. Second, the coastal forearc of southern Peru allows to study crustal thickenning since its inferred onset at ~30 Ma because marked aridity characterises the central andean forearc since the mid-Cretaceous (Hartley et al., 2005). This very dry climate has helped to preserve geomorphic features dating back at least since the Oligocene (Dunai et al., 2005). Finally, this region is devoid of significant tectonic shortening (James, 1971; Tosdal et al., 1984; Kono et al., 1989; Sempere and Jacay, 2008), permitting us to minimize the effects of tectonic thrusting from the observed surface uplift. We hereunder focus on the current lower Río Tambo valley and nearby Yerbabuena coastal area (cf. Fig. V.1) which provide key outcrops that allow improving the chronology of events related to regional surface uplift.

V. 2 – Chronology of regional surface uplift

V. 2. A – Lower Río Tambo valley

In the lower Río Tambo valley, a number of geomorphic markers reveal the following history. A 40-70 km wide flat surface now at ~1-km elevation, here referred to as the Clemesí surface, extended over 400 km over the bedrock (Fig. V.1). It was incised by the ~1 km deep valleys which were later filled in by ≥400 m thick fluvial conglomerates (e.g. the paleo-Tambo valley). The present-day Tambo valley was incised into these deposits and into bedrocks, and is currently being filled in by fluvial conglomerates. We hereunder date the different steps of this evolution compiling data from the literature and providing new zircon U-Pb dates (Table V.1).

a – Clemesí surface formation

The elevated Clemesí surface covers bedrock of diverse ages but also caps the undeformed sediments of the Oligo-Miocene "Moquegua C" Formation (Roperch et al., 2006). In particular, near the city of Moquegua and in the Gramadal area, the Clemesí surface caps gravels interbedded with dated ignimbrites (Fig. V.2) permitting to estimate for each locality, depositional rates and therefore age for the Clemesí surface.

Sample lithology and location	Lat. (°)	Long. (°)	Method	Age (Ma ± 2s)	Reference
Dating the Clemesi surface: Moquegua area					
Ignimbrite (base of a ~100m thick gravels member)	-17.249471	-70.922281	Biotite Ar/Ar	24.3 ± 0.1	Roperch et al., 2006
Rhyolitic pumice (~45m under the Clemesi surface)	-17.252691	-70.927608	K-feldspar Ar/Ar	23.9 ± 0.5	Thouret et al., 2007
Dating the Clemesi surface: Gramadal area					
Tuff at the base of the marine strata	-15.945833	-73.315833	Plagioclase K-Ar	25.5 ± 2.0	Noble et al., 1985
Pumice fragments in the middle of the marine intercalation	-15.945833	-73.319444	Biotite Ar/Ar	24.5 ± 1.6	Noble et al., 1985
Tuff (~60m under the Clemesi surface)	-15.998893	-73.08575	K-feldspar Ar/Ar	23.8 ± 0.2	Schildgen et al., 2009
			Biotite Ar/Ar	24.1 ± 0.1	Schildgen et al., 2009
Dating paleo-river incision:					
Tuff at the base of the deltaic Camana B Formation	-16.495398	-72.93402	Biotite Ar/Ar (mean of 3 dates)	20.8 ± 0.1	M. Fornari, pers. comm., 2014
Dating paleo-Tambo infill:					
Ignimbrite (base of the paleo Rio Tambo infill)	-16.96269	-71.65139	Zircon U-Pb	10.1 ± 0.1	This study
Ignimbrite (base of the paleo Rio Tambo infill)	-16.99095	-71.64498	Zircon U-Pb	9.5 ± 0.2	This study
Ignimbrite (top of the paleo Rio Tambo infill)	-16.94	-71.69	Biotite Ar/Ar	4.9 ± 0.3	Quang et al., 2005
Ignimbrite (top of the paleo Rio Tambo infill)	-16.95	-71.68	Biotite Ar/Ar	5.0 ± 0.3	Quang et al., 2005
Dating the marine abrasion surface:					
Tuffite (20m above the marine abrasion surface)	-17.27704	-71.45998	Zircon U-Pb (younger grain)	6.2 ± 0.3	This study
Tuffite (50m above the marine abrasion surface)	-17.278413	-71.456904	Biotite Ar/Ar	5.9 ± 0.8	M. Fornari, pers. comm., 2014
Sandstone (70m above the marine abrasion surface)	-17.37743	-71.39596	Zircon U-Pb (younger grain)	5.8 ± 0.2	This study

Table V.1: Summary of all data presented in this study.

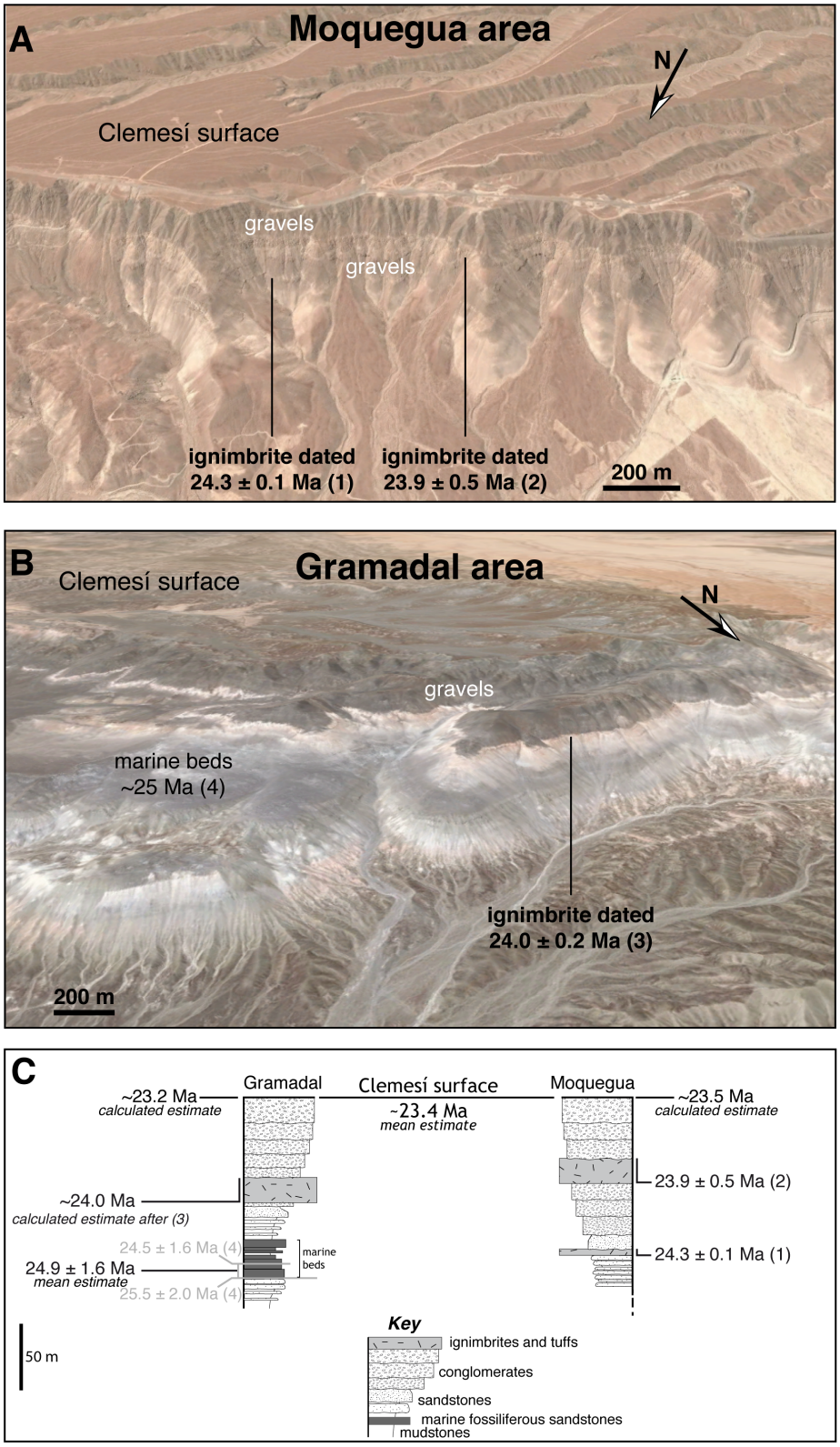

Figure V.2: Relevant datations allowing to date the Clemesí surface. 3D satellite views (©Google Earth) of the stratigraphy in: A) the Moquegua area (©2014 DigitalGlobe image) and B) the Gramadal area (©2014 Cnes/Spot Image). C: Stratigraphic logs for each of these areas and dated strata. References for dated strata: (1) Roperch et al., 2006; (2) Thouret et al. 2007; (3) Schildgen et al., 2009; (4) Noble et al., 1985.

At 6.5 km south of Moquegua, the Clemesí surface caps a ~100 m thick member of gravels (Fig. V.2) whose base is dated by a 24.3 ± 0.1 Ma ignimbrite (Table V.1; Roperch et al., 2006). Another ignimbrite located 50 m above the basal ignimbrite (and ~45 m under the Clemesí surface) yielded a 23.9 ± 0.5 Ma age (Table V.1; Thouret et al., 2007). We thus calculate an average depositional rate of ~125 m/My and estimate the abandonment of the Clemesí surface near Moquegua at ~23.5 (Fig. V.2).

About 290 km to the northwest, in the Gramadal area, Huamán (1985) and later Cruzado and Rojas (2005) described in detail a section where the same elevated surface extends ~60 m above gravels that directly overlie an ignimbrite dated at ~24.0 Ma (mean age calculated from two $^{40}Ar/^{39}Ar$ respectively on K-feldspar and biotite from Schildgen et al., 2009; Table V.1). Fifty meters beneath this ignimbrite, they found marine strata interbedded with pyroclastic products dated at ~25 Ma (Noble et al., 1985) (Table V.1 and Fig. V.2). The mean depositional rate in this area is thus ~60 m/My and the abandonment of the Clemesí surface in the Gramadal area can be estimated at ~23.2 Ma (Fig. V.2). Moreover, the last indisputably marine bed in the section is located ~28 m below the base of the ~24.0 Ma ignimbrite. We thus estimate the end of marine conditions in this area at ~24.6 Ma.

Despite the ~290 km distance between the two considered sections, we observe a nearly synchronous gravel invasion at ~24.3 Ma and obtain fairly consistent independent ages of ~23.4 Ma for the abandonment of the Clemesí surface (respectively of 23.5 and 23.2 Ma; Fig. V.2). We also show that at least in the Gramadal area, the regional scale sedimentary system was abandoned only ~2 My after having been connected to the Pacific Ocean.

b – Onset of valley incision and carving of the coastal escarpment.

The Clemesí surface, thus represents the fossilized surface of a regional-scale sedimentary system that had been active at low elevations. Abandonment at ~23.4 Ma of this coastal plain coincided with a relative fall of the base level triggering incision of rivers. For example, the Río Tambo paleovalley reached ≥1000 m deep, as its bottom is not visible in the current valley (Fig. V.3). Deltaic to marine deposits accumulated at the outlet of these river systems. Those near Camaná (Fig. V.1) include a volcanic tuff dated 20.8 ± 0.1 Ma (Table V.1; M. Fornari, pers. comm. 2014) and many volcanic clasts transported from the magmatic arc >100 km to the northeast, confirming an early age for the incision of at least the Camaná –

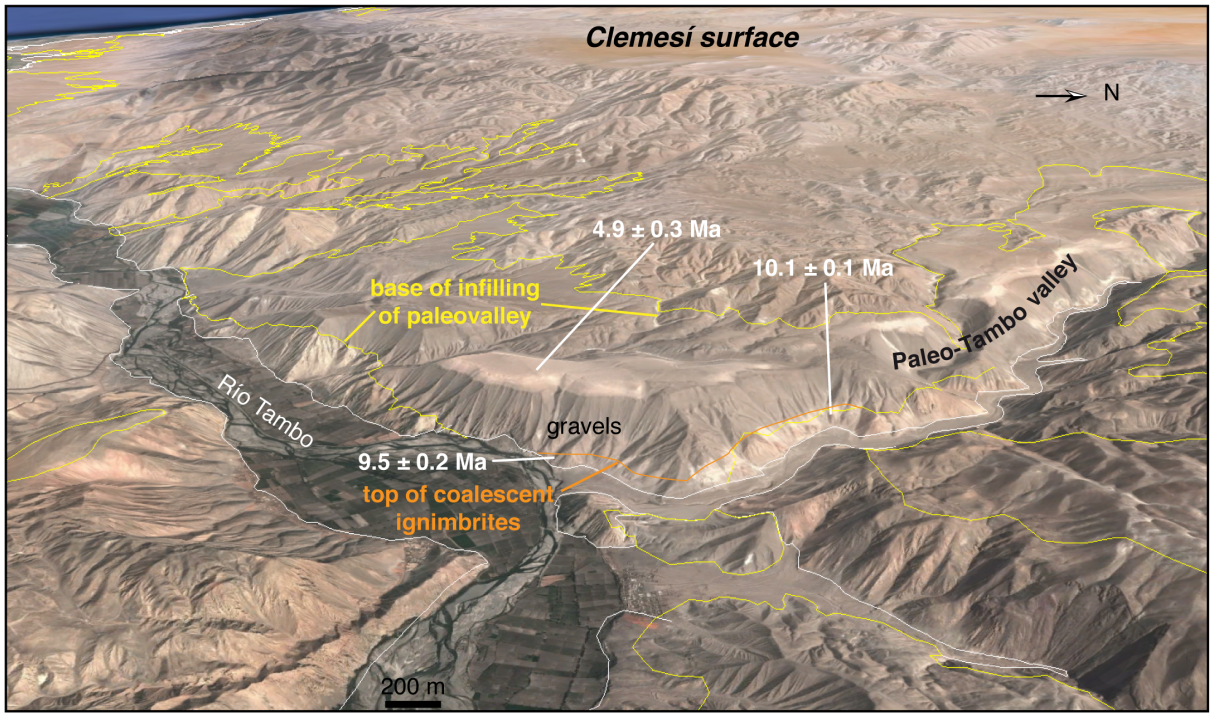

Figure V.3: 3D satellite view (©2014 DigitalGlobe, Landsat Image) of the present-day río Tambo in the region of El Toro. Yellow line marks the base of the infilling in the paleo-Tambo valley. Dates in black correspond to zircon U-Pb ages on ignimbrites (this study and (Quang et al., 2005). Orange line corresponds to the approximate location of the top of the two coalescent ignimbrites at the base of the paleo-Tambo valley infilling.

Majes river (Sempere et al., 2004; Roperch et al., 2006). The Clemesí surface stands now at least at ~1 km elevation and is bounded on its Pacific side by a ~1 km high coastal escarpment (Fig. V.4). The apparent absence of faults associated with this escarpment suggests it was generated by wave erosion while uplift progressed (Hartley and Jolley, 1995).

c – Infill of the Tambo paleovalley.

The paleo-Tambo valley infill mainly consists of coarse conglomerates of fluvial origin, but its 30–70 m thick basal member is formed by at least two coalescent ignimbrites (Fig. V.3). We dated it by zircon U-Pb (Table V.1 and Appendix D) at respectively at 10.1 ± 0.1 (sample 2M05, reworking zircons of older ages) and 9.5 ± 0.2 Ma (sample 3M3; Appendix D). The 290 m thick conglomerates filling the central part of the paleovalley are capped by a third ignimbrite dated in two different sites 4.9 ± 0.3 and 5.0 ± 0.3 Ma (Table V.1; Quang et al., 2005) (Fig. V.3). These ages imply that the relative base level rise that caused paleovalley

aggradation (at an average rate of ~64 m/My) lasted from >9.5 to 4.9 Ma. More regionally, the 4.9 Ma upper ignimbrite is locally overlain by up to 25 m of fluvial conglomerates, similar to those infilling the Tambo paleovalley, suggesting that fluvial infilling may have lasted until ~4.5 Ma, when incision resumed and carved the present-day valley.

d – Incision rates.

The average incision rate is being ~83 m/Ma since ~4.5 Ma whereas between ~23 and ≥10.1 Ma, incision rate had been at least of 77 m/My because the Tambo paleovalley has been incised by more than 1 km. Moreover, the Tambo paleovalley incision reached deeper than the current valley floor, implying that the Clemesí surface was at least as high as today at ~11 Ma.

V. 2. B – Yerbabuena coastal area

Parallelly, in the Yerbabuena coastal area (Fig. V.1), marine and fan-delta deposits overlie an ancient wave-cut surface (Fig. V.4) which is 1 to 5 km wide and gently dipping to the SW. These strata are bounded seaward by a ~150 m high cliff falling into the ocean, and landward by a "coastal escarpment" which is 0.6 to 1.0 km high (Fig. V.4). In turn, this escarpment bounds the Clemesí surface that was abandoned at ~23.4 Ma (see section V.2.a) and now stands 1.1–1.4 km above sea level in this area (Fig. V.4).

These relationships imply a similar uplift history than the one reconstructed in the lower Río Tambo valley. The regional uplift leading to the abandonment of the Clemesí surface was accompanied by the carving of the coastal escarpment by wave erosion. At the same time, a gently-dipping abrasion surface at the foot of the escarpment was being shaped below sea-level. Processes on this submarine surface switched from erosion to sedimentation during a period of coastal subsidence during which the surface lowered below the wave-abrasion depth. This surface subsidence allowed the preservation of the Yerbabuena marine and fan-delta deposits on the submarine surface. However, the area later switched back to erosion when coastal uplift resumed. The present-day shoreline is clearly abrasive as a flat wave cut platform is forming in front of the 100 m high active coastal cliff.

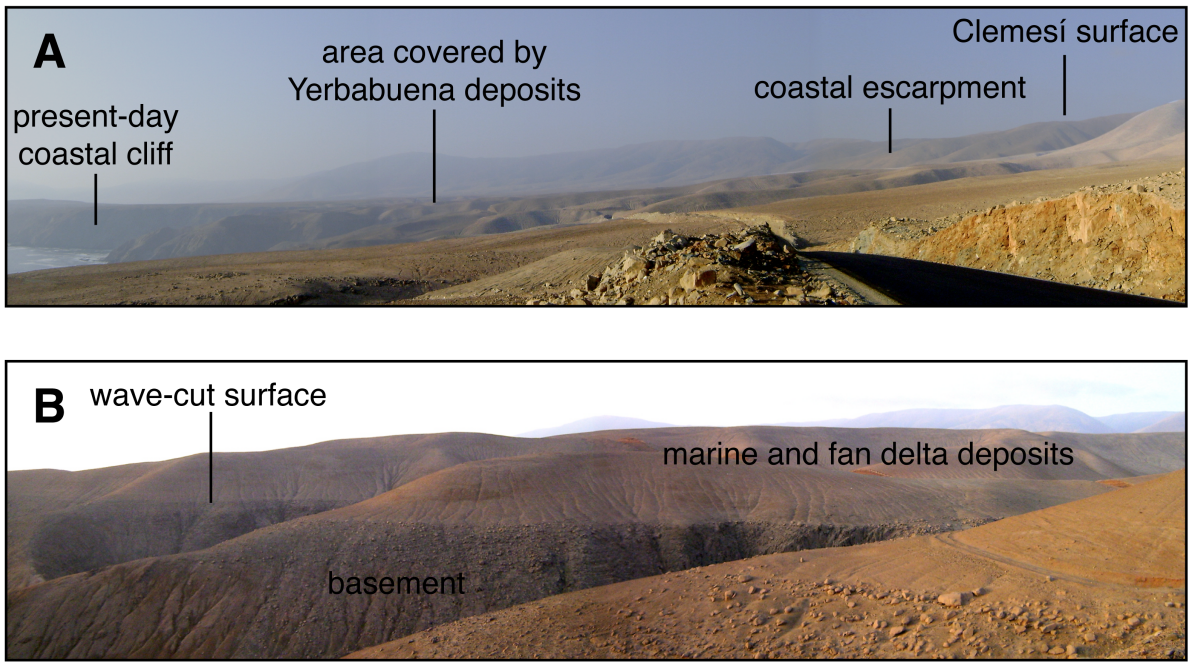

Figure V.4: Panoramic landscapes of the Yerbabuena area. A. View of the main geomorphologic features of the area. B. Miocene marine and fan delta deposits overlying the basement via an abrasion surface.

The Yerbabuena marine beds grade into fan-delta deposits that rapidly thicken and coarsen against the coastal escarpment (Fig. V.4). Toward the ocean, they are generally ~50-m-thick and include a variety of sedimentary facies ranging in grain size from coarse sandstones with marine shells to conglomerates that include >1m size blocks likely fallen from the nearby escarpment. In this succession, we sampled for zircon U-Pb dating a tuffite located ~20 m above the marine abrasion surface (sample 1M74; Table V.1 and Appendix D), it yielded mainly Middle Jurassic zircons, likely derived from the nearby Ilo Batholith and one 6.2 ± 0.3 Ma zircon grain (Table V.1). A 5.9 ± 0.8 Ma $^{40}Ar/^{39}Ar$ on biotite age was also obtained on a tuff bed located ~50 m above the marine abrasion surface (Table V.1; M. Fornari, pers. comm., 2014). These ages and thicknesses allow to estimate approximately a ~60 m/My depositional rate. We thus tentatively assign a ~6.5 Ma age to the base of these marine deposits that were thus depositing at the end of the fluvial infilling in the lower Tambo valley. In addition, we sampled a magnetite-rich sandstone (1M76; Table V.1 and Appendix D) located ~70 m above the marine abrasion surface, from which the youngest detrital zircons show a U-Pb age peak at 5.8 Ma ± 0.2 Ma confirming the upper-Miocene age of the Yerbabuena deposits (younger grain being 5.5 ± 0.2 Ma).

Our combined data in the Yerbabuena strip indicate that coastal subsidence started prior to ~6.5 Ma, allowing marine and fan-delta sediments to accumulate on the previous marine abrasion surface. The area was uplifted after ~5.5 Ma and then submitted to subaerial erosion, to form the current coastal cliff. Although less constrained, this chronology is consistent with the one reconstructed in the lower Tambo valley. In particular, average depositional rates are very similar (~60-65 m/My).

V. 3 – Base level variations.

Our observations in the lower Tambo valley and Yerbabuena coastal area corroborate the fact that the coastal region underwent significant base level variations since ~23.4 Ma (Fig. V.5). After a period during which a sedimentary depositional surface formed near sea level, base level lowered at ~23.4 Ma of at least 1000 m, carving the paleo Río Tambo valley, the coastal escarpment and its associated marine abrasion surface. Between ~9.5 and ~4.5 Ma base level rised, permitting the deposition of at least 50 m of marine and fan-delta deposits on the wave-cut surface as well as the 300 m conglomeratic infill of the paleo Río Tambo valley. Since ~4.5 Ma, base level dropped at least of 400 m to incise the present-day Río Tambo valley and carved the 100 m high coastal cliff. It has to be noted that the valleys bottom are flat and covered by fluvial deposit, which may indicate that base level is currently rising again.

These variations of base level are clearly uncorrelated in magnitude and in time to coeval global sea level fluctuations (Fig. V.5). Indeed, global sea level rised at ~24 Ma with high levels lasting until ~14.5 Ma. This evolution was followed by a sea-level fall ending with a sharp drop at ~12 Ma, when global sea level started a slow, irregular and moderate rise culminating at ~4.5 Ma; since then sea level is mostly lowering (Hardenbol et al., 1998). Such an uncorrelated behaviour of base level and global sea level fluctuations (Fig. V.5) confirms that the observed geomorphic succession in the lower Tambo valley and Yerbabuena coastal strip must be primarily interpreted in terms of surface uplift and subsidence.

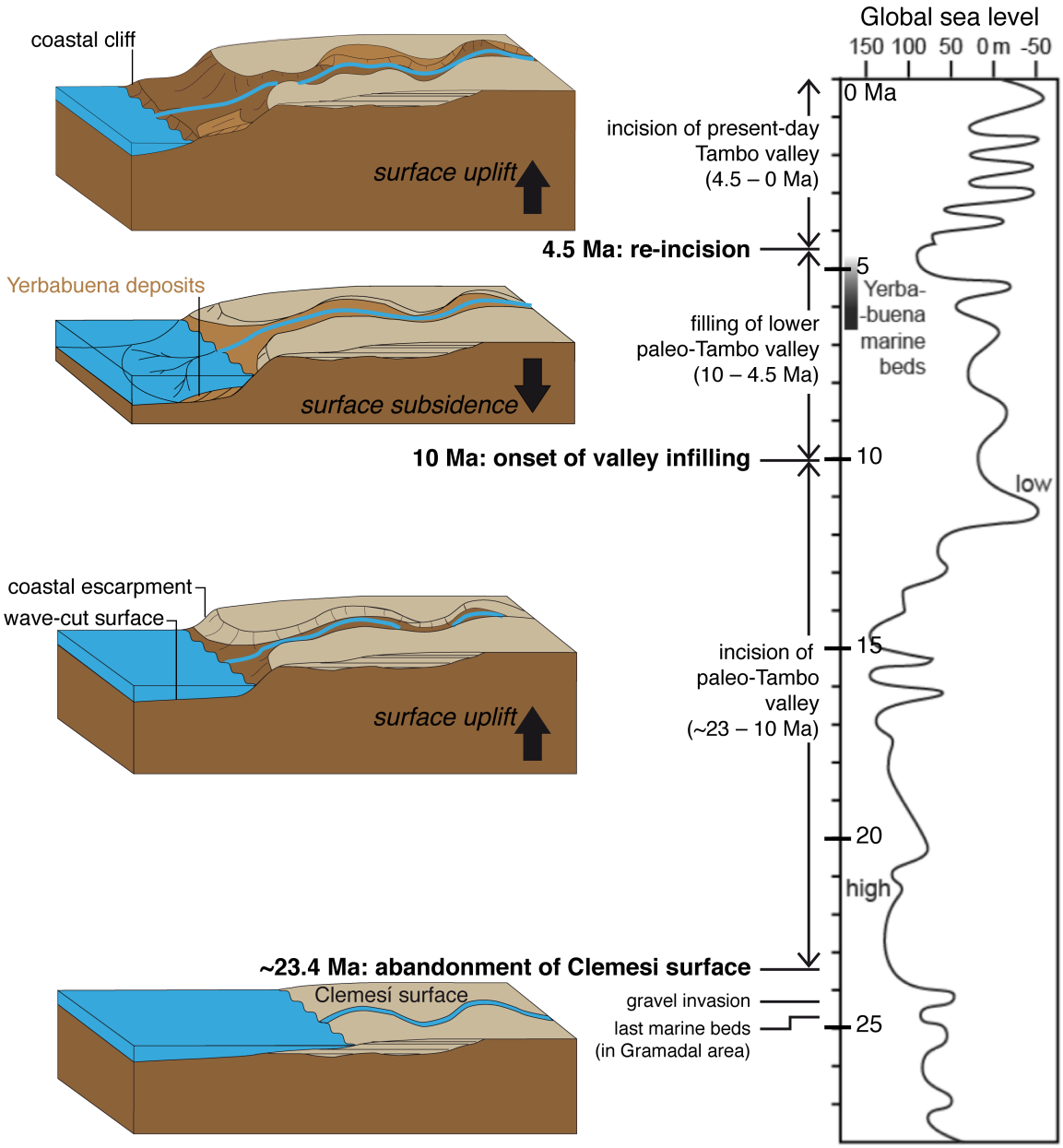

Figure V.5: Sketchs (not to scale) summarizing the evolution of the Río Tambo and Yerbabuena area since the Middle Oligocene (left), we report for comparison the coeval global sea-level fluctuations (right - each tick on the vertical axis correspond to 1 Ma; after Hardenbol et al., 1998)

V. 4 – Regional perspective

Other data from southern Peru and nearby Chile and Bolivia (Fig. V.1) are in agreement with the evolution and timing of uplift in the río Tambo and Yerbabuena areas described in the previous sections. First, in coastal northernmost Chile a surface sampled at ~950 m elevation and only ~10 km away from the ocean, has undergone continuous exposure since 23.3 ± 0.2 Ma (Dunai et al., 2005). This makes this surface similar to the Clemesí surface in southern Peru that was abandoned at ~23 Ma (this study). Second, our deduction that surface uplift affected coastal southern Peru beginning ~23 Ma ago also agrees with the observation that surface uplift above 2.0 to 2.5 km elevation in Andean southern Peru developed during the ~23–19 Ma interval (Picard et al., 2008). This age also falls within the ~30–19 Ma interval supported by geochemical data for a major increase in crustal thickening along the magmatic arc (Fig. V.6; Mamani et al., 2010).

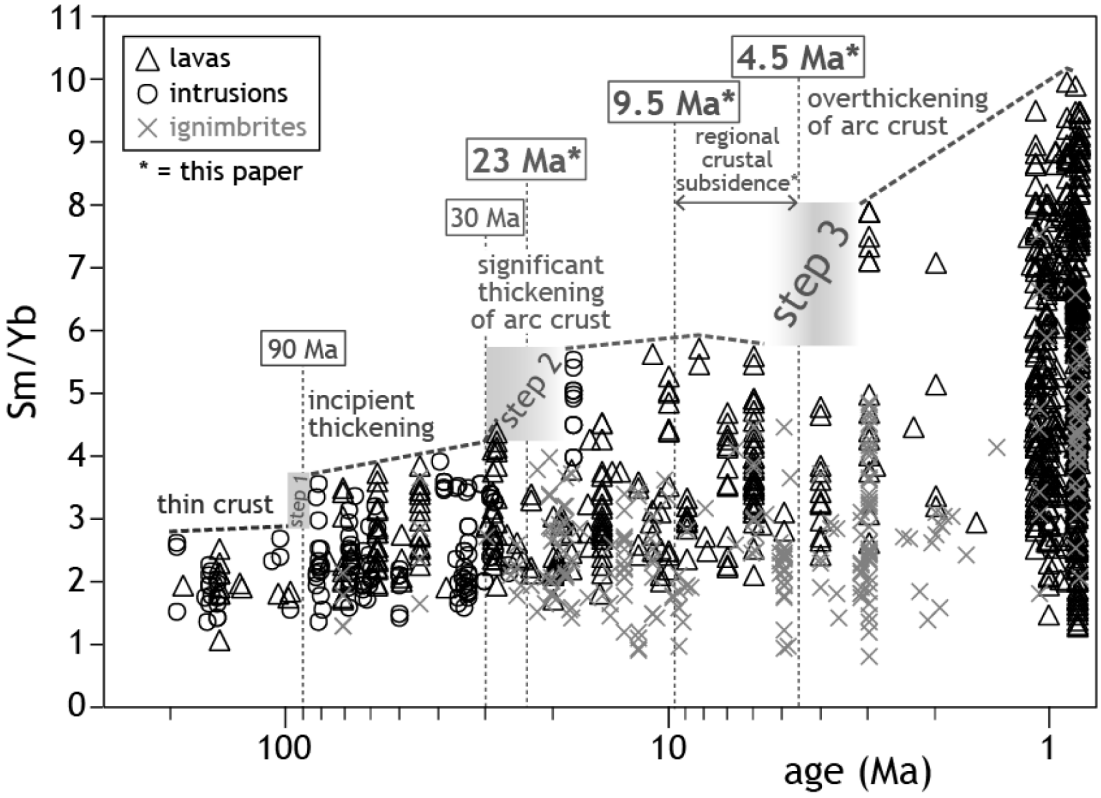

Figure V.6: Plot of Sm/Yb ratios versus rock ages (note the logarithmic age axis) since ~200 Ma in southern Peru and northernmost Chile, from Mamani et al. (2010). The Sm/Yb ratio indicates the involvement of garnet, whose abundance increases in the lower crust during crustal thickening. The envelope formed by maximum Sm/Yb values (inclined dashed lines) therefore provides a qualitative proxy for the degree of crustal thickening in the arc crust. The vertical dashed lines indicate the different episodes of crustal thickening recognized by Mamani et al. (2010), updated here by including the findings reported in this paper (*).

Moreover, the crustal subsidence we evidence between ~9.5 and ~4.5 Ma on the Pacific piedmont of this segment of the Bolivian Orocline (Fig. V.5) was coeval with a similar phenomenon on its Amazonian-side counterpart. Indeed, in western Subandean Bolivia (Fig. V.1), a high-relief paleotopographic surface including deeply incised paleovalleys, now at ~0.6 to 1.6 km elevation, was buried between ~10 and <7 Ma by more than 500 m of fluvial conglomerates that include pyroclastic deposits dated 9.2 ± 0.1 and 7.4 ± 0.5 Ma by sanidine $^{40}Ar/^{39}Ar$ dating (Mosolf et al., 2011). These conglomerates were reexposed to erosion afterwards as they are now being incised by the Río Tipuani.

Finally, resumption of fluvial incision is observed at ~4 Ma on the northeastern edge of Andean plateau margin (Lease and Ehlers, 2013), and at ~4.5 Ma in coastal southern Peru (this study). We also note that these ages fall within the ~5.5–3.5 Ma age range that can be deduced from geochemical data for the resumption of crustal thickening along the magmatic arc (Mamani et al., 2010; Fig. V.6).

V. 5 – A LOWER CRUSTAL FLOW DRIVEN EVOLUTION

Thus, the geological record in the Mollendo-Ilo area but also in northern Chile (Dunai et al., 2005), and in the Amazonian edge of the Bolivian (Mosolf et al., 2011) and southern Peruvian Andes (Fig. V.1) together point to surface uplift having developed from ~23 to 10 Ma and since ~4.5 Ma whereas geochemical data (Mamani et al., 2010) point to crustal thickenning in the corresponding Andean region since ~30 Ma (Fig. V.6). Inbetween these two episodes of comparable magnitude, subsidence occurred permitting valley infilling. Such symmetrical correspondences 400 km across the orogen implie that the episodes of uplift and subsidence we evidence here developed at the scale of this segment of the Bolivian Orocline.

As stated above, there is no significant tectonic shortening in the Mollendo-Ilo area, permitting to reject the effects of tectonic thrusting from the observed surface uplift in the southern Peruvian forearc. We also rule out that the resumption of the incision at ~4.5 Ma was triggered by enhanced precipitation during the Pliocene global climate change. Indeed, even if more rainfall affected the eastern Altiplano from 4 to 3 Ma on (Fedorov et al., 2013), precipitation in the forearc region decreased at that time (Molnar and Cane, 2007) and cannot explain the carving of the present-day Tambo valley. Thus, we come to the conclusion that only a deep process affecting the orogen in its entire width can explain the simultaneous

surface uplift and incision of the orogen edges.

Lateral support of high elevations can be achieved in the absence of internal deformation in particular in subduction context if the subduction interface is anomalously strong. However, it seems difficult to transfer these forces across the orogen (more than 500 km away from the trench). Increased slab boyancy (due to subduction of thicker oceanic lithosphere for example) could also triger surface uplift of the upper plate by isostatic compensation. However, since ~30 Ma the volcanic arc is migrating toward the southwest suggesting that the slab dip is increasing. Moreover, geochemical data support increased differentiation and crustal assimilation through time, which is not consistent with surface uplift triggered by mantle upwelling (dynamic topography) but more with crustal thikening. In this respect it has to be noted that crustal thickness is highly anormal under the present-day Central Andes as demonstrated by different geophysical studies (e.g. James, 1971; Isacks, 1988; Beck and Zandt, 2002). We thus propose that surface uplift and subsidence are related to variations in crustal thickness over time at the scale of the Bolivian Orocline.

Between ~10 and ~4.5 Ma an important subsidence occurred. This episode marked by valley infilling on both sides of the orogen (this study and Mosolf et al., 2011) is likely due to crustal thinning at the scale of the ~15.5-17.5°S segment of the Bolivian orocline. We propose that, in a context of overall crustal thickening, crustal thinning resulted from lower crustal ductile flow away from this segment of the orogen which had been previously overthickened. Indeed, lower crustal ductile flow is likely to have redistributed mass along and across the Bolivian Orocline, thus modifying crustal thickness over time (Husson and Sempere, 2003; Yang et al., 2003; Picard et al., 2008; Gerbault et al., 2005).

However, we note that these concordant results across the orogen markedly contrast with chronologies published on the Ocoña valley (Thouret et al., 2007; Schildgen et al., 2009 and 2010), only ~200 km northwest of the lower Tambo valley (Fig. V.1). In the former, incision apparently started between ~11 and ~8 Ma, i.e. when the latter was being filled in, and ended between ~5 and ~3 Ma, i.e. when incision resumed regionally more to the southeast. A possible way to reconcile these apparently opposed chronologies is to assume that ductile flow transferred lower crustal material from the southeast (producing subsidence in the Tambo area) to the northwest (producing uplift in the Ocoña region). This idea also agrees with the southeast-to-northwest propagation of surface uplift, and hence of crustal

thickening, documented by Picard et al. (2008). Though, this marked diachroneity may be seen as a confirmation of the prominent role played by lower crustal ductile flow along the Andean overthickened axis in forcing diachronous variations in crustal thickness.

V. 6 – Concluding remarks

We therefore conclude that redistribution of lower crust by ductile flow provides a simple explanation for the geomorphic features dealt with in this paper. The fact that the Tambo paleovalley bottom reaches at least as deep as the current valley floor whereas mean sea level was higher than today at ~10 Ma, implies that the Clemesí abandoned surface was at least as high as today in the Middle Miocene. This strongly suggests that crustal thickness of the forearc of this Andean segment was comparable to today's thickness, or possibly even larger, and thus that the crust of this segment of the Bolivian Orocline had already been overthickened between ~23 and ~10 Ma.

Because the brittle-ductile transition always lies at 10 to 15 km depth, crustal overthickening mainly thickens the ductile lower crust and thus causes it to flow away in order to decrease this local overthickness. In the Bolivian Orocline axis, important crustal thickening initiated at ~30 Ma (Mamani et al., 2010) and ended in lower crustal ductile flow toward regions of lower thickness (Husson and Sempere, 2003). Thus, along the forearc of southern Peru, surface uplift starting ~23 Ma reflects coeval thickening of the local crust. In contrast, subsidence between ~10 and ~4.5 Ma in both coastal southernmost Peru and western Subandean Bolivia indicates crustal thinning due to lower crustal flow away from this segment of the Bolivian Orocline, possibly toward the northwest (Picard et al., 2008). We propose that resumption of river incision and thus of surface uplift in both coastal and Subandean southern Peru at ~4.5 Ma reflected renewed crustal thickening, in particular because these regions are contrastingly characterized by hyperaridity and high rainfall, respectively. Although our findings do not shed a definite light on the cause(s) of initial crustal overthickening, the absence of large-scale tectonic shortening in this Andean segment since at least 5 Ma reveals that mantle-derived magmatic additions to the crust (Mamani et al., 2010; Fig. V.6) are likely to have played a significant role since then.

References

Beck, S.L., and Zandt, G., 2002, The nature of orogenic crust in the central Andes: Journal of Geophysical Research: Solid Earth, v. 107, p. 2230, doi: 10.1029/2000JB000124.

Cruzado, H.A., and Rojas, C.A., 2005, Incursión marina en una cuenca continental de ante-arco: eustatismo o tectónica? [Tesis de grado]: Universidad Nacional San Antonio Abad del Cusco, 145 p.

Dunai, T.J., López, G.A.G., and Juez-Larré, J., 2005, Oligocene–Miocene age of aridity in the Atacama Desert revealed by exposure dating of erosion-sensitive landforms: Geology, v. 33, p. 321–324, doi: 10.1130/G21184.1.

Ehlers, T.A., and Poulsen, C.J., 2009, Influence of Andean uplift on climate and paleoaltimetry estimates: Earth and Planetary Science Letters, v. 281, p. 238–248, doi: 10.1016/j.epsl.2009.02.026.

Fedorov, A.V., Brierley, C.M., Lawrence, K.T., Liu, Z., Dekens, P.S., and Ravelo, A.C., 2013, Patterns and mechanisms of early Pliocene warmth: Nature, v. 496, p. 43–49, doi: 10.1038/nature12003.

Garzione, C.N., Hoke, G.D., Libarkin, J.C., Withers, S., MacFadden, B., Eiler, J., Ghosh, P., and Mulch, A., 2008, Rise of the Andes: Science, v. 320, p. 1304–1307, doi: 10.1126/science.1148615.

Gerbault, M., Martinod, J., and Hérail, G., 2005, Possible orogeny-parallel lower crustal flow and thickening in the Central Andes: Tectonophysics, v. 399, p. 59–72, doi: 10.1016/j.tecto.2004.12.015.

Hardenbol, J., Thierry, J., Farley, M.B., Jacquin, T., de Graciansky, P.-C., and Vail, P.R., 1998, Mesozoic and Cenozoic Sequence Chronostratigraphic Framework of European Basins, chart 1, *in* Mesozoic and Cenozoic Sequence Stratigraphy of European Basins, SEPM Special Publication 60, P.-C. de Graciansky, J. Hardenbol, T. Jacquin & P. R. Vail, p. 363–364.

Hartley, A.J., Chong, G., Houston, J., and Mather, A.E., 2005, 150 million years of climatic stability: evidence from the Atacama Desert, northern Chile: Journal of the Geological Society, v. 162, p. 421–424, doi: 10.1144/0016-764904-071.

Hartley, A.J., and Jolley, E.J., 1995, Tectonic implications of Late Cenozoic sedimentation from the Coastal of northern Chile (22-24°S): Journal of the Geological Society, v. 152, p. 51–63.

Huamán, D., 1985, Evolution tectonique cénozoïque et néotectonique du piémont pacifique dans la région d'Arequipa (Andes du Sud-Pérou) [Thèse de doctorat de 3ème cycle]: Université de Paris-Sud, 220 p.

Husson, L., and Sempere, T., 2003, Thickening the Altiplano crust by gravity-driven crustal channel flow: Geophysical Research Letters, v. 30, p. 1243, doi: 10.1029/2002GL016877.

Isacks, B.L., 1988, Uplift of the Central Andean Plateau and Bending of the Bolivian Orocline: J. Geophys. Res., v. 93, p. 3211–3231, doi: 10.1029/JB093iB04p03211.

James, D.E., 1971, Andean crustal and upper mantle structure: Journal of Geophysical Research, v. 76, p. 3246–3271, doi: 10.1029/JB076i014p03246.

Kono, M., Fukao, Y., and Yamamoto, A., 1989, Mountain building in the central Andes: Journal of Geophysical Research: Solid Earth, v. 94, p. 3891–3905, doi: 10.1029/JB094iB04p03891.

Lamb, S., and Davis, P., 2003, Cenozoic climate change as a possible cause for the rise of the Andes: Nature, v. 425, p. 792–797, doi: 10.1038/nature02049.

Lease, R.O., and Ehlers, T.A., 2013, Incision into the Eastern Andean Plateau During Pliocene Cooling: Science, v. 341, p. 774–776, doi: 10.1126/science.1239132.

Mamani, M., Wörner, G., and Sempere, T., 2010, Geochemical variations in igneous rocks of the Central Andean orocline (13°S to 18°S): Tracing crustal thickening and magma generation through time and space: Geological Society of America Bulletin, v. 122, p. 162–182.

Molnar, P., and Cane, M.A., 2007, Early Pliocene (pre–Ice Age) El Niño–like global climate: Which El Niño? Geosphere, v. 3, p. 337–365, doi: 10.1130/GES00103.1.

Mosolf, J.G., Horton, B.K., Heizler, M.T., and Matos, R., 2011, Unroofing the core of the central Andean fold-thrust belt during focused late Miocene exhumation: evidence from the Tipuani-Mapiri wedge-top basin, Bolivia: Basin Research, v. 23, p. 346–360, doi: 10.1111/j.1365-2117.2010.00491.x.

Noble, D.C., Sébrier, M., Megard, F., and McKee, E.H., 1985, Demonstration of two pulses of Paleogene deformation in the Andes of Peru: Earth and Planetary Science Letters, v. 73, p. 345–349, doi: 10.1016/0012-821X(85)90082-2.

Picard, D., Sempere, T., and Plantard, O., 2008, Direction and timing of uplift propagation in the Peruvian Andes deduced from molecular phylogenetics of highland biotaxa: Earth and Planetary Science Letters, v. 271, p. 326–336, doi: 10.1016/j.epsl.2008.04.024.

Quang, C.X., Clark, A.H., Lee, J.K.W., and Hawkes, N., 2005, Response of Supergene Processes to Episodic Cenozoic Uplift, Pediment Erosion, and Ignimbrite Eruption in the Porphyry Copper Province of Southern Perú: Economic Geology, v. 100, p. 87–114, doi: 10.2113/100.1.0087.

Roperch, P., Sempere, T., Macedo, O., Arriagada, C., Fornari, M., Tapia, C., García, M., and Laj, C., 2006, Counterclockwise rotation of late Eocene–Oligocene fore-arc deposits in southern Peru and its significance for oroclinal bending in the central Andes: Tectonics, v. 25, p. TC3010, doi: 10.1029/2005TC001882.

Schildgen, T.F., Balco, G., and Shuster, D.L., 2010, Canyon incision and knickpoint propagation recorded by apatite 4He/3He thermometry: Earth and Planetary Science Letters, v. 293, p. 377–387, doi: 10.1016/j.epsl.2010.03.009.

Schildgen, T.F., Ehlers, T.A., Whipp, D.M., van Soest, M.C., Whipple, K.X., and Hodges, K.V., 2009, Quantifying canyon incision and Andean Plateau surface uplift, southwest Peru: A thermochronometer and numerical modeling approach: Journal of Geophysical Research: Earth Surface, v. 114, p. F04014, doi: 10.1029/2009JF001305.

Sempere, T.; Folguera, A., and Gerbault, M., 2008, New insights into Andean evolution: an introduction to contributions from the 6th ISAG symposium (Barcelona, 2005): Tectonophysics, v. 459, p. 1–13, doi: 10.1016/j.tecto.2008.03.011.

Sempere, T., Fornari, M., Acosta, J., Flores, A., Jacay, J., Peña, D., Roperch, P., and Taipe, E., 2004, Estratigrafía, geocronología, paleogeografía y paleotectónica de los depósitos de antearco del sur del Perú, *in* Resúmenes extendidos del XII Congreso Peruano de Geología, Lima, Sociedad Geológica del Perú, p. 533–536.

Sempere, T., and Jacay, J., 2008, Anatomy of the Central Andes: Distinguishing between Western, Magmatic Andes and Eastern, Tectonic Andes, *in* Proceedings of the 7th International Symposium of Andean Geodynamics (ISAG), Nice, France, p. 505–507.

Thouret, J.-C., Wörner, G., Gunnell, Y., Singer, B., Zhang, X., and Souriot, T., 2007, Geochronologic and stratigraphic constraints on canyon incision and Miocene uplift of the Central Andes in Peru: Earth and Planetary Science Letters, v. 263, p. 151–166, doi: 10.1016/j.epsl.2007.07.023.

Tosdal, R.M., Clark, A.H., and Farrar, E., 1984, Cenozoic polyphase landscape and tectonic evolution of the Cordillera Occidental, southernmost Peru: Geological Society of America Bulletin, v. 95, p. 1318–1332.

Yang, Y., Liu, M., and Stein, S., 2003, A 3-D geodynamic model of lateral crustal flow during Andean mountain building: Geophysical Research Letters, v. 30, p. 2093, doi: 10.1029/2003GL018308.

Yuan, X., Sobolev, S.V., Kind, R., Oncken, O., Bock, G., Asch, G., Schurr, B., Graeber, F., Rudloff, A., Hanka, W., Wylegalla, K., Tibi, R., Haberland, C., Rietbrock, A., et al., 2000, Subduction and collision processes in the Central Andes constrained by converted seismic phases: Nature, v. 408, p. 958–961, doi: 10.1038/35050073.

Chapter VI – Summary and outlook

The main objective of this dissertation was to better constrain coupling between magmatic, tectonic and sedimentary processes, and the thermal evolution of the forearc of southern Peru. By using an integrated approach combining various geochronological and thermochronological methods together with geological mapping, geomorphic analysis, and a compilation of previously published ages, we provided new insights on the evolution of the south Peruvian margin since the Mesozoic and on the crustal thickening issue in the Central Andean orogen. In particular, this dissertation focused on three key periods of the margin evolution: the onset of crustal thickening at ~90 Ma; the beginning of formation of the Bolivian Orocline by rotation of rigid blocks and the Neogene crustal thickening of the Central Andean orogen. Here we summarize our main contributions (Fig. VI.1).

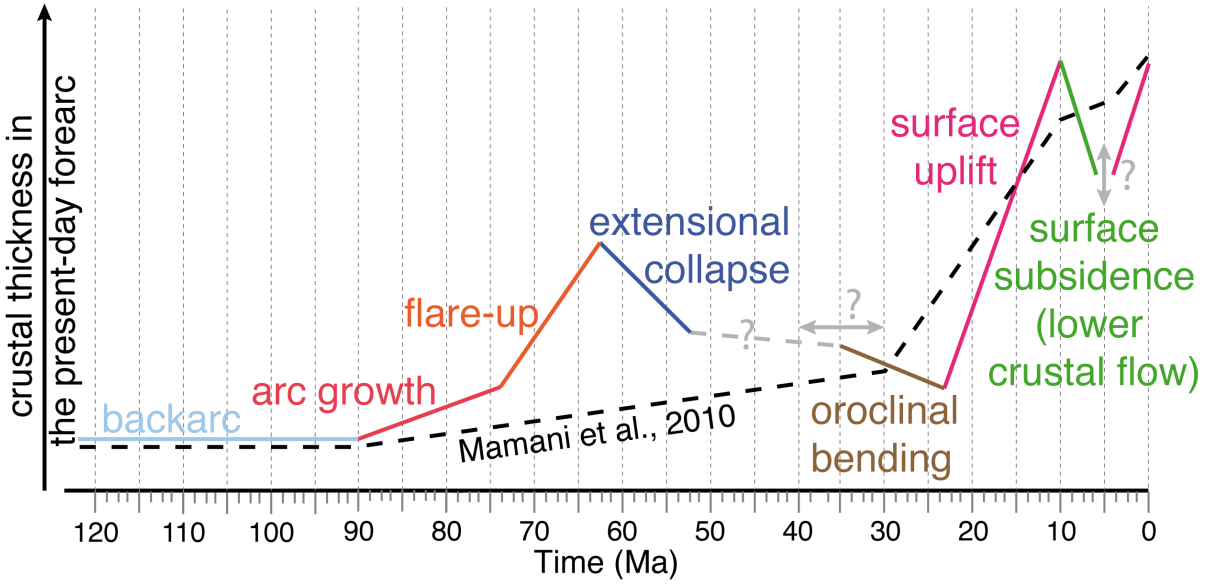

Figure VI. 1: Diagram showing the schematic evolution of crustal thickness in the present-day forearc of southern Peru as proposed in this dissertation (in color). The evolution based on geochemical data proposed by Mamani et al. (2010) is reported for comparison (black doted line). No vertical scale.

VI. 1 – From crustal thinning to thickening

In the Arequipa belt of Southern Peru we evidence a three step evolution of the magmatic arc between 90 and ~50 Ma. After more than 200 My of lithospheric thinning, and migration of the volcanic activity locus, the arc established during the Upper-Cretaceous – Paleocene in an area located ~150-200 km from the present-day trench. An initial arc growth

between ~90 and 74 Ma triggered important mass wasting in the backarc followed rapidly by an important regression expressed by the continentalization of the sediments in the backarc basin. Arc growth resulted in magmatic flare-up from ~74 to ~62 Ma which is documented from ~10 to ~20°S of latitude. The switch from lithospheric thinning to crustal thickening undergone by the southern Peruvian margin near ~90 Ma thus appears to have been mostly caused by a considerable magmatic growth of the subduction arc between 90 and 62 Ma, and not by compressional tectonics as traditionally assumed. These important addition of mantle derived magmas to the crust were followed by extensional collapse of the arc starting at ~62-60 Ma. Extension was accompanied by large-scale normal faulting and block tilting, and recorded by in-situ and detrital apatite and zircon fission-track data. Extension prevailed in the forearc since then and waned until ~30 Ma as recorded by the syn-sedimentary extensional deformation in the Paleogene forearc deposits.

VI. 2 – Bolivian Orocline building and orogen parallel extension

Deformation in the Eastern Cordillera that led to plateau formation and surface uplift as well as initiation of block rotations in the forearc during the formation of the Bolivian Orocline started around 30 Ma. We investigated the tectono-thermal evolution of the coastal belt of southern Peru a zone prone to recording changings in subduction dynamics. We showed that the gneissic basement was near (or at) the surface in the Neo-Proterozoic, and that no major thermal event occurred since then. Nonetheless, some localised zones were heated to temperatures of ~220°C between ~175–105 Ma likely due to the passing through in the area of the Jurassic magmatic arc. New field observations, lateral variation of apatite fission-track ages and sedimentary architecture of the Eocene to Miocene forearc deposits in the Caravelí-Aplao basin reveal that important normal faults zones strike perpendicular to the coastline of the southern Peruvian margin delineating large north-westward tilted blocks. We showed that this tilt occurred in the Paleogene or later and we attributed it to the orogeny-parallel extension that affected the southern Peruvian forearc during the building of the Bolivian Orocline by counterclockwise rotation of rigid blocks.

VI. 3 – Neogene crustal thickening and lower crustal flow

Geomorphic features in the Lower Río Tambo valley and in the Yerbabuena coastal strip reveals that the coastal forearc of southern Peru experienced two periods of surface uplift, between ~23 and ~10 Ma and since ~4.5 Ma, separated by a period of surface subsidence (from ~10 to ~4.5 Ma). Because the same chronology has been described on the other side of the Central Andean orogen, we interpreted this evolution as resulting from an important Neogene crustal thickening that eventually triggered lower crustal flow from the axis of the Bolivian Orocline toward the northwest. Renewed crustal thickening occurred since 4.5 Ma. Because there is no evidence of crustal shortening in the forearc of southern Peru, we proposed that crustal thickening in this area was mainly triggerred by mantle-derived addition to the crust.

VI. 4 – Outlook

In this study we confirm that the coastal belt of southern Peru is thermally stable since at least the Upper Cretaceous. It would be interesting to investigate in detail the modes and timing of exhumation by the Ocoña detachment fault of the largest block of ultra-high temperature in the world. Indeed, the Jurassic volcanic arc deposits are not affected by this important detachment fault visible in the Ocoña valley and such a study may reveal important details on the early evolution of the subduction zone.

We note that in the Arequipa area just after the end of the magmatic flare up and extensional collapse, the arc migrated drastically northward likely due to an important slab flattening during a marked increase in plate convergence. This questions the causal relationships between the different phenomena listed above. Investigating at a regional scale the detailed evolution of arcs may help to better understand subduction zones dynamics and processes that caused for example porphyry copper emplacement and slab flattening. In this kind of contexts, it however remains difficult to extract cooling due to post-emplacement thermal relaxation from exhumational cooling. Characterize the emplacement depth of the magmatic bodies as well as hunt and consider all the geological and geomorphological constraints available thus appear crucial to better understand exhumation rates and modes.

Another striking feature of the Central Andean orogen in southern Peru is its orogenic volume that markedly decrease from the Bolivian Orocline axis toward the north. Yet, I confirm that lower crustal flow may have affected the Central Andean orogen during the Neogene and it would be interesting to investigate the possible diachronisms that could be induced by the migration of the crustal flow front toward the northwest. In this framework, we began a pilot study on modern river sediments for detrital fission-track analyses on rivers draining the Altiplano and the present-day forearc towards the west (see Appendices J and K).

The forearc of southern Peru thus offers a wide variety of possibilities for future work. Indeed, because it was not affected by terrane accretion nor tectonic shortening and thanks to the arid climate that prevails in this region since at least the Oligocene, it records the subduction and orogen evolution and is likely to give many more new insights on processes related to active margins.

Résumé étendu

Introduction

Les Andes contrastent avec d'autres orogènes majeurs tels que les Alpes ou l'Himalaya car elles ne résultent pas de la collision de deux plaques continentales, mais de la subduction de la plaque océanique Nazca sous la plaque continentale Amérique du Sud. En particulier, les Andes Centrales du sud du Pérou se sont formées dans un contexte de subduction pure, aucun terrain allochtone n'ayant été accrété à la marge depuis l'initiation de la subduction au Protérozoïque (Loewy et al., 2004; Cawood, 2005). Par ailleurs, cette région est caractérisée par un volume orogénique bien plus important que celui des Andes Septentrionales ou Méridionales : l'orogène y est extrêmement large et la croûte y atteint des épaisseurs de 70 km (Beck et al., 1996 ; Assumpção et al, 2013; Chulick et al., 2013; van der Meijde et al., 2013).

Cependant, quand et comment ce sur-épaississement crustal a été acquis reste débattu. En effet, la subduction a été presque continue au niveau de la marge des Andes Centrales depuis au moins ~215 Ma (Boekhout et al., 2012), mais l'acquisition de l'altitude (subséquente à l'épaississement crustal) n'a commencé qu'après ~30 Ma, alors que la déformation compressive commençait dans la Cordillère Orientale (Sempere et al., 1990a ; Horton, 2005) et que l'Orocline Bolivien commençait à se former (Roperch et al., 2006). Il semble donc que l'épaississement crustal, et par conséquent l'acquisition d'une topographie élevée, ne soit pas lié à l'ensemble de l'histoire de la subduction mais à son passé récent ; posant la question des processus à l'origine de l'épaississement crustal en contexte de subduction océan-continent.

Afin de tenter de répondre à cette question, une approche possible consiste à comparer les chronologies de différents phénomènes résultants de différents processus. Par exemple, on peut comparer les phénomènes magmatiques tels qu'une augmentation de la production de magma (liée à la subduction) avec les enregistrements sédimentaires (liés à l'érosion et donc à la formation de la topographie par isostasie) et avec la chronologie de l'exhumation des roches profondes constituant le socle (liée à la tectonique, l'érosion et la formation de la topographie).

Dans cette optique, l'avant-arc sud péruvien est une région idéale car il fournit de vastes affleurements de socle, de roches plutoniques liées à l'arc et l'arrière-arc ainsi que de roches sédimentaires d'âges différents. Par ailleurs, comme il n'y a pas eu d'épisode d'accrétion, cette région permet de comparer la chronologie de l'exhumation des roches profondes avec celle des processus magmatiques et sédimentaires associés et ce, sur une longue période de temps.

De plus, comme le niveau de base de l'océan Pacifique est proche, l'avant-arc des Andes Centrales est susceptible d'avoir enregistré le soulèvement de la surface associée à l'épaississement crustal actuel observé entre la côte et l'arc volcanique (la croûte y passant de 30 à 70 km d'épaisseur). Enfin, la région présente de nombreuses caractéristiques d'une extension et au contraire pas ou peu de preuves de raccourcissement crustal (James, 1971 ; Myers, 1975 ; Tosdal et al., 1984), ceci bien que le sur-épaississement de la croûte continentale soit généralement considéré comme le résultat d'un raccourcissement tectonique. Or, un sur-épaississement crustal se traduit généralement par un effondrement gravitaire en extension (collapse de la croûte) et/ou une importante érosion en surface. Je me propose donc de mieux contraindre l'évolution géologique de l'avant-arc sud péruvien (entre 15 et 18°S) en étudiant l'évolution thermique et les couplages qui ont pu exister entre les processus magmatiques, tectoniques et sédimentaires au cours des 200 derniers millions d'années dans la région. Pour ce faire j'utilise des méthodes de datation absolue et thermochronologiques couplées à une analyse tectono-sédimentaire des dépôts d'avant-arc d'âge Méso-Cénozoïque.

Architecture d'une zone de subduction

Toutes les zones de subduction présentent la même architecture schématique (Fig.A ; Stern, 2002) (Fig. I.1) : une plaque océanique (le « panneau plongeant» ou « slab ») s'enfonce dans le manteau sous la « plaque supérieure ». A la frontière entre les deux plaques, il existe une « fosse » océanique. En général, à 150–200 km de cette fosse, sur la plaque supérieure, se trouve un alignement de volcans appelé « arc volcanique ». La zone entre la fosse et l'arc est nommée « l'avant-arc » et est souvent subsidente, conduisant à la formation d'un « bassin d'avant-arc », la zone située de l'autre côté de l'arc est appelée « arrière-arc ».

Quand la plaque océanique plonge dans le manteau, la température et la pression auxquelles elle est soumise augmentent déclenchant la déshydratation du panneau plongeant. Ceci a pour effet d'hydrater le coin de manteau (c'est à dire le matériel situé entre la plaque supérieure et la plaque plongeante) dont le point de fusion diminue entrainant la fusion partielle du matériel mantellique. Les magmas dérivés de cette fusion montent dans la plaque supérieure pour former l'arc volcanique. Par conséquent, dans la plupart des cas, en ajoutant du matériel magmatique d'origine mantellique à la croûte les processus de subduction

déclenchent l'épaississement de cette dernière. Par ailleurs, la position de l'arc volcanique est directement liée au pendage du panneau plongeant. Quand le slab est plat, l'arc volcanique est situé loin de la fosse tandis que lorsque que le slab est plus vertical, l'arc se trouve proche de la fosse.

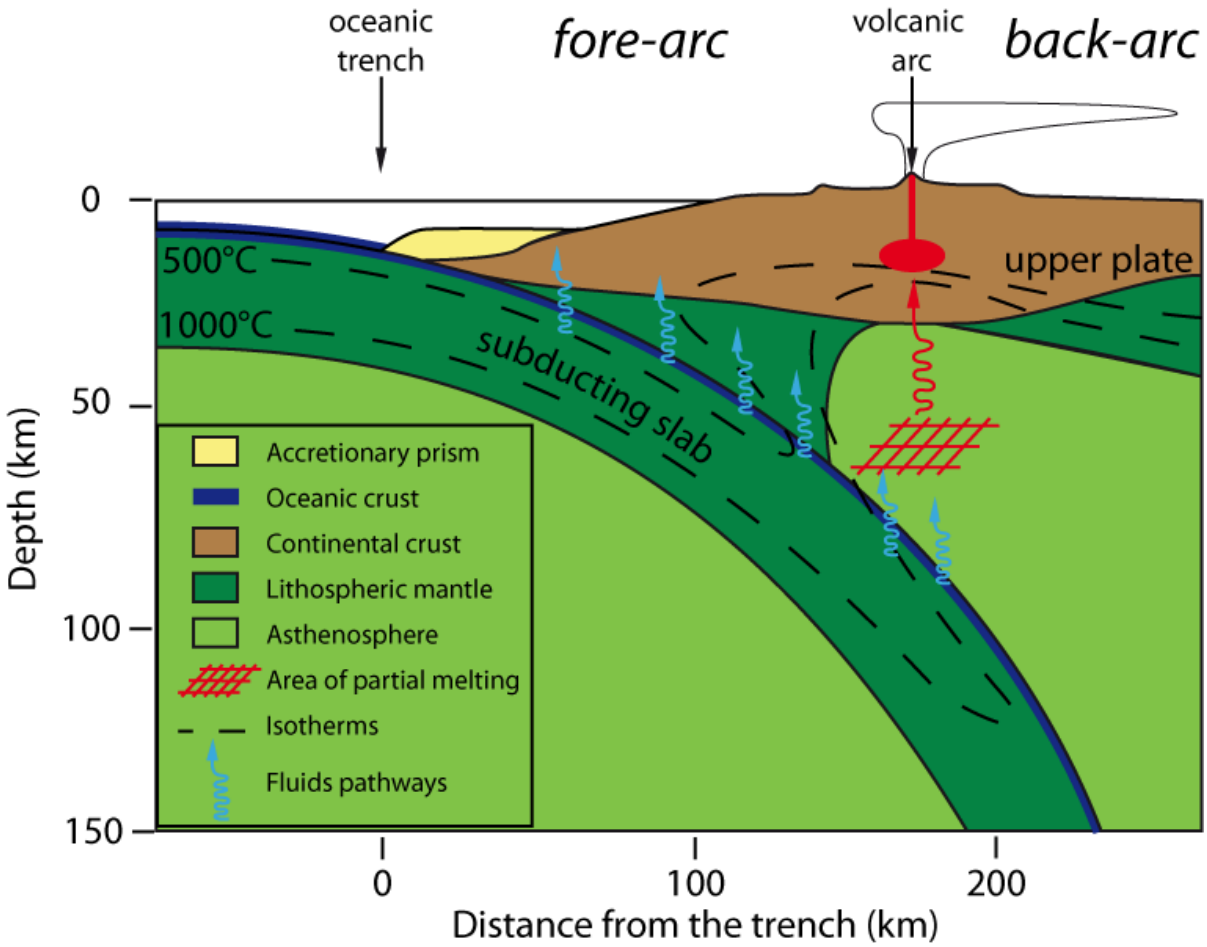

Figure A : Architecture schématique d'une zone de subduction (en coupe). Les flèches verticales indiquent la position de la fosse et de l'arc volcanique. La zone hachurée en rouge correspond à la région du coin de manteau où a lieu la fusion partielle. « fore-arc » : avant-arc ; « back-arc » : arrière-arc ; « subducting slab » : panneau plongeant.

Contexte géologique : évolution de la marge sud-péruvienne

Au sud du Pérou, le socle est composé de roches métamorphiques Protérozoïques (majoritairement des gneiss et des migmatites) formant le Massif d'Arequipa. Les premiers plutons avec une signature géochimique de subduction intrudent le socle à l'Ordovicien (Mukasa and Henry, 1990 ; Loewy et al., 2004 ; Mišković et al., 2009). Entre le Permien supérieur et le Jurassique moyen, la marge sud-péruvienne est en extension (Sempere et al., 2002). Puis entre ~215 et ~90 Ma, un important basin d'arrière arc marin se développe. Ce type de basin possède une architecture sédimentaire typique, les facies sédimentaires permettent donc de déduire la position relative de l'arc au moment de leur dépôt. Il est donc possible de reconstruire la migration de l'arc au cours du temps à partir de la stratigraphie régionale et de l'âge des différents plutons (Figure B).

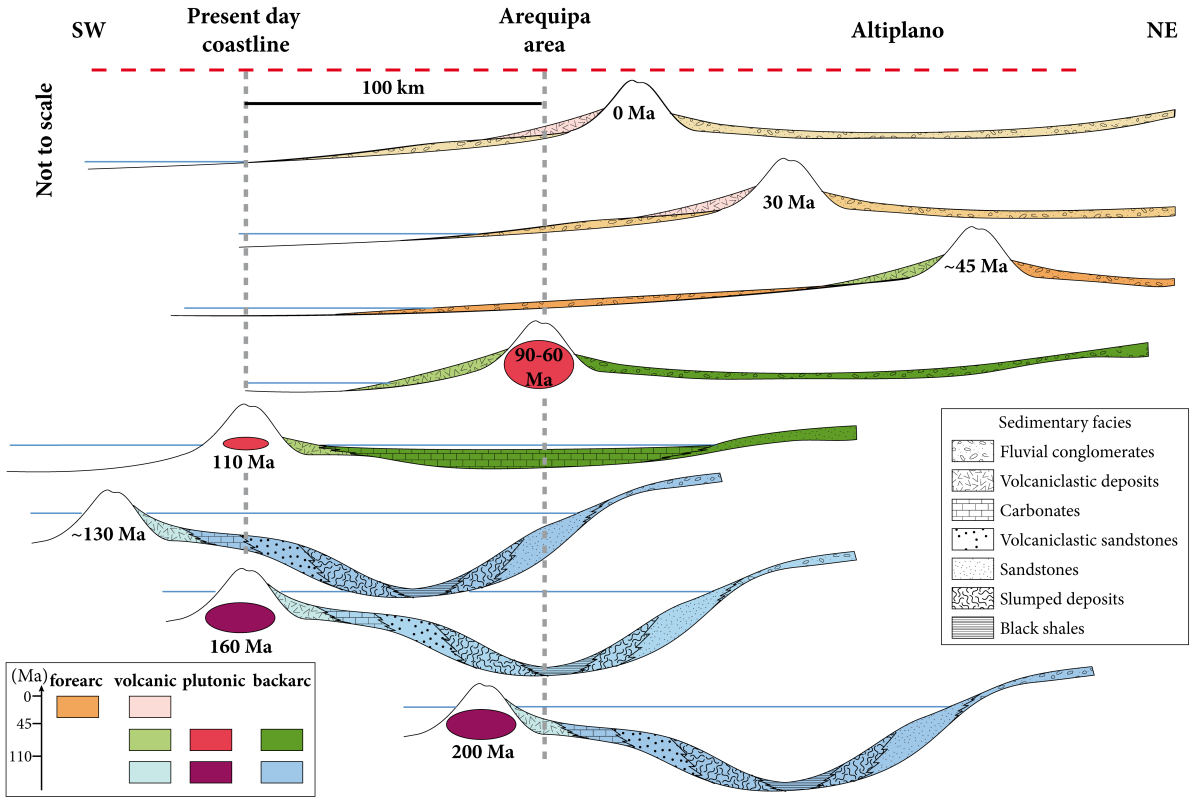

Figure B : Coupes schématiques orientées NE-SW à travers l'avant-arc actuel du sud du Pérou (noter la position de la côte actuelle ainsi que celle de la région d'Arequipa) montrant la migration latérale au cours du temps du système avant-arc/arc/arrière-arc et des faciès sédimentaire associés (d'après une compilation des données de la littérature).

Selon Demouy et al. (2012), l'activité magmatique était concentrée dans la région d'Arequipa il y a environ 200 Ma, elle migre ensuite vers le sud-ouest et le littoral actuel ou se forme le batholithe d'Ilo entre 175 et 152 Ma (Fig. B). Dans la région d'Arequipa, les dépôts dans le bassin d'arrière-arc enregistrent cette migration, les sédiments évoluant graduellement depuis des laves vers des grès volcaniclastiques, des shales puis des grès propres déposés sur la pente amazonienne du bassin d'arrière-arc (Fig. B). Autour de 130 Ma, l'arc est localisé dans une zone actuellement immergée et commence à migrer de nouveau vers le continent. Entre 110 et 106 Ma, l'arc est de nouveau au niveau du littoral actuel et quelques plutons intrudent le batholithe d'Ilo (Fig. B ; Boekhout et al., 2012). A ce moment, une importante transgression a lieu dans le bassin d'arrière-arc et une plateforme carbonatée s'y développe. A ~90 Ma, l'arc volcanique est de nouveau dans la région d'Arequipa (Fig. B ; Demouy et al., 2012) et la plateforme carbonatée s'effondre dans un grand glissement gravitaire (Callot et al., 2008). Une diminution rapide du niveau de base du bassin d'arrière-arc est alors enregistrée et le bassin d'arrière-arc se continentalise (Fig. B). Par ailleurs, à partir de ce moment, les sédiments qui provenaient auparavant majoritairement du nord-est (c'est à dire du coté amazonien du bassin d'arrière-arc) commencent à venir du sud-ouest où l'arc était localisé. Il est important de noter que l'activité magmatique reste localisée dans la région d'Arequipa jusqu'au Paléocène (~60 Ma ; Fig. B ; Demouy et al., 2012). Pendant toute cette période, d'importants volumes de magmas se mettent en place ainsi que des gisements de cuivre porphyrique (Mukasa et al., 2012 ; Quang et al., 2013). Par ailleurs, la signature géochimique des magmas semble indiquer que la croûte continentale commence à s'épaissir à cette période (Mamani et al., 2010). Vers ~45 Ma, l'arc est situé dans l'actuel Altiplano, la région d'Arequipa est donc alors localisée dans l'avant-arc (Fig. B), des dépôts continentaux s'y accumulent dans le bassin de Caravelí-Aplao. Vers 30 Ma, les premières déformations tectonique affectent la Cordillère Orientale (en Bolivie) (Sempere et al., 1990b ; Uba et al., 2006), l'Orocline Bolivien se forme (Roperch et al., 2006) et l'arc commence à migrer de nouveau vers le sud-ouest et sa localisation actuelle (Fig. B).

On peut donc définir trois périodes dans l'histoire de l'évolution de la marge en se basant sur la direction de migration de l'arc volcanique : ~200–110 Ma (l'arc migre vers le SW), 110–45 Ma (l'arc migre vers le NE) et 45–0 Ma (l'arc migre de nouveau vers le SW).

Afin de refléter cette migration, nous proposons une nouvelle charte tectono-stratigraphique (Fig. C) et la carte géologique associée (Fig. D) où nous combinons des unités qui étaient précédemment cartographiées séparément.

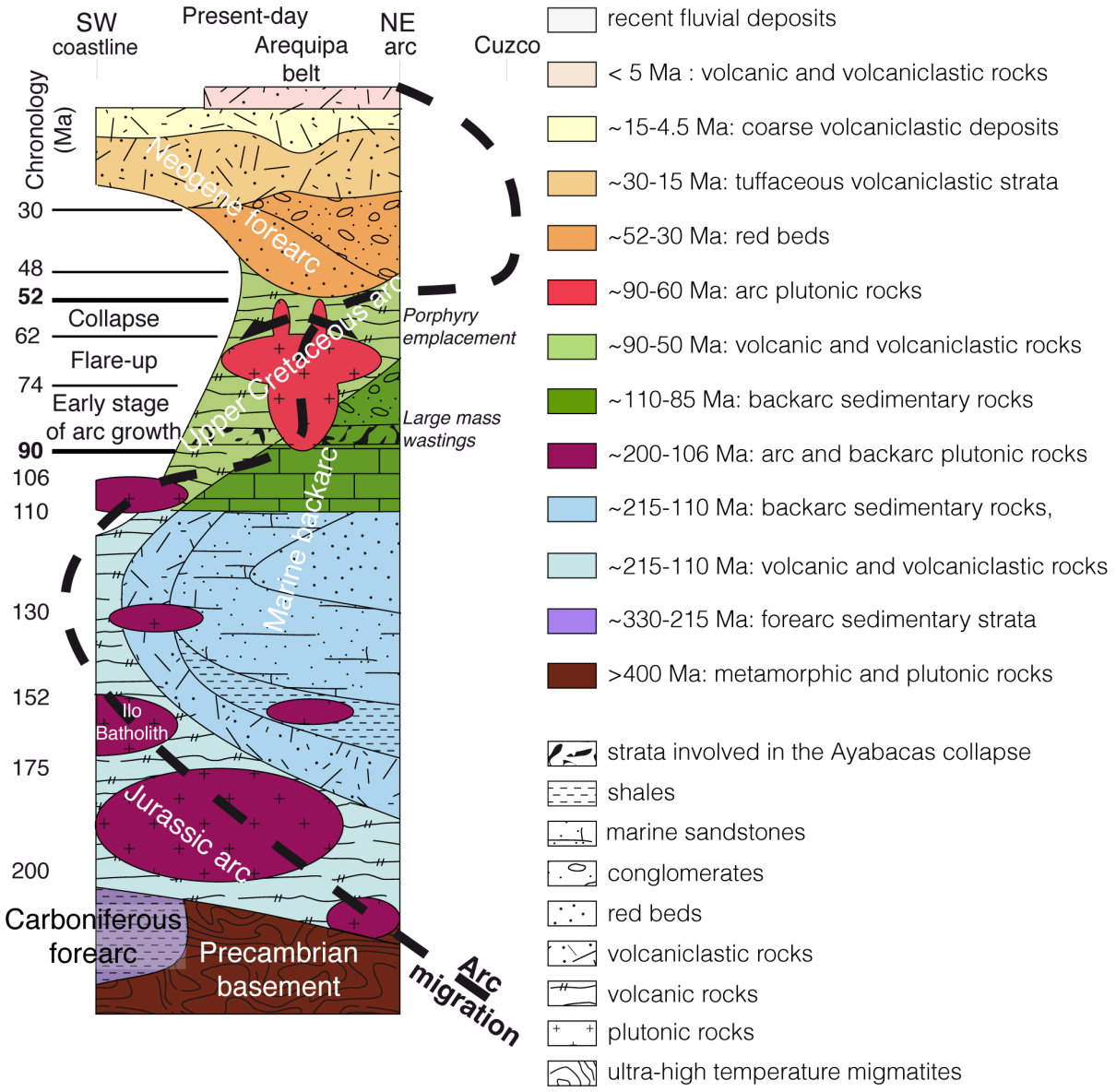

Figure C : Charte tectono-stratigraphique pour le sud du Pérou ; la verticale de droite correspond à la stratigraphie approximative sur la côte actuelle, celle de gauche à la stratigraphie supposée présente sous l'arc volcanique (telle qu'exposée dans la région de Huambo). Noter la migration de l'arc au cours du temps (ligne pointillée noire). Les tons clairs correspondent aux dépôts d'arc, les plus foncés à ceux d'arrière-arc.

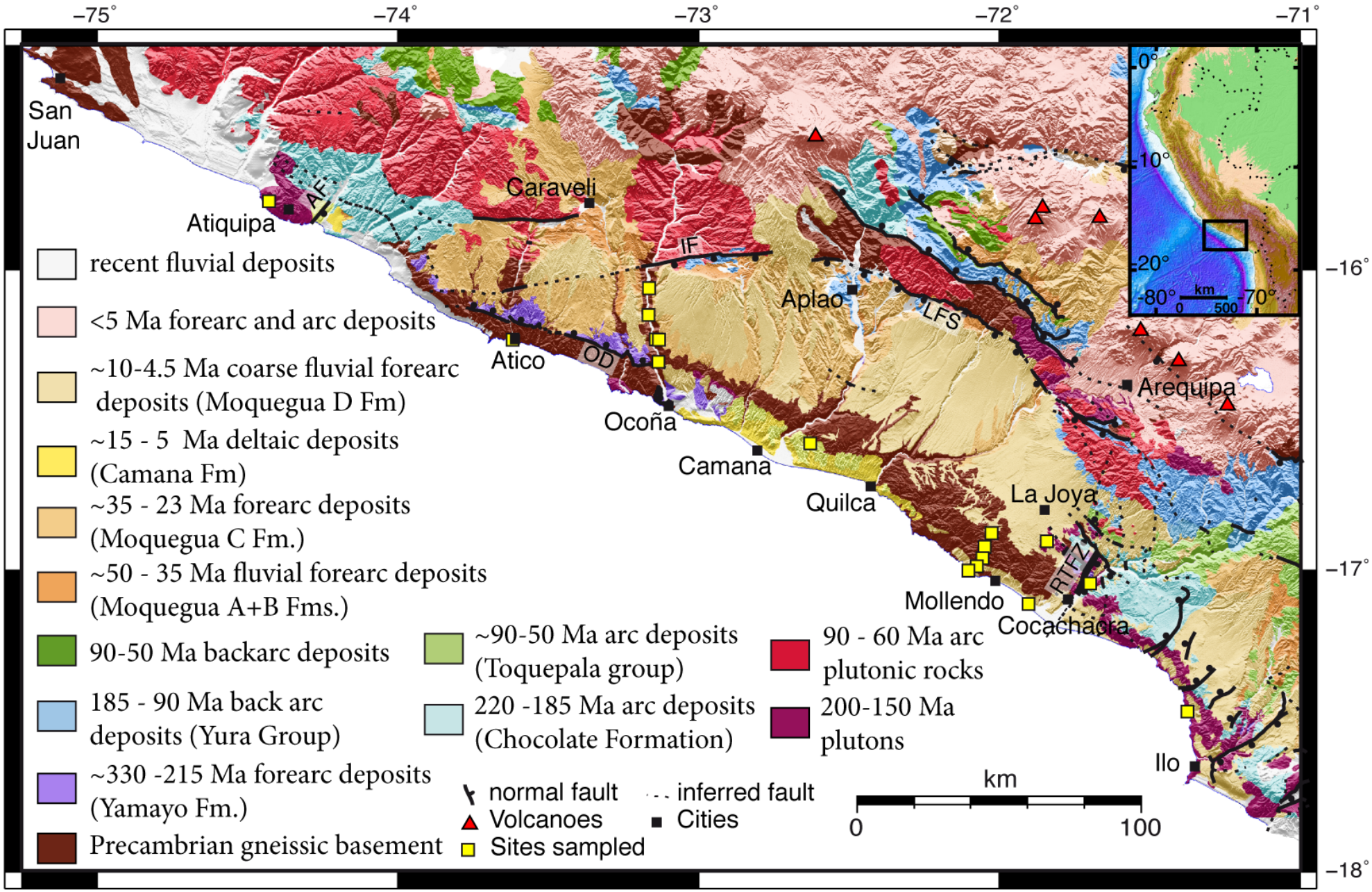

Figure D : Carte tectono-stratigraphique du Sud du Pérou (d'après les cartes géologiques au 1 :100.000 publiées par l'INGEMMET). AF: Faille d'Atiquipa ; OD: Detachement d'Ocoña ; IF: Faille d'Iquipi ; LFS: Système de failles de Lluclla ; RTFZ: Zone de failles du Río Tambo.

Principales contributions

Cette thèse a pour but de mieux contraindre les couplages entre les processus magmatiques, tectoniques et sédimentaires ainsi que l'évolution thermique de l'avant-arc du sud du Pérou. En utilisant une approche combinant différentes méthodes de datations (en particulier thermochronologiques) combinée avec une nouvelle carte tectono-stratigraphique, une analyse géomorphologique et une compilation des données publiées antérieurement pour la région, elle apporte de nouvelles contraintes sur l'évolution de la marge sud péruvienne depuis le Mésozoïque ainsi que sur l'histoire de l'épaississement crustal dans les Andes Centrales (Fig. E). En particulier, cette thèse s'attarde sur trois périodes clefs de l'évolution de la marge : le début de l'épaississement crustal autour de ~90 Ma ; le début de la formation de l'Orocline Bolivien et l'épaississement crustal au Néogène des Andes Centrales.

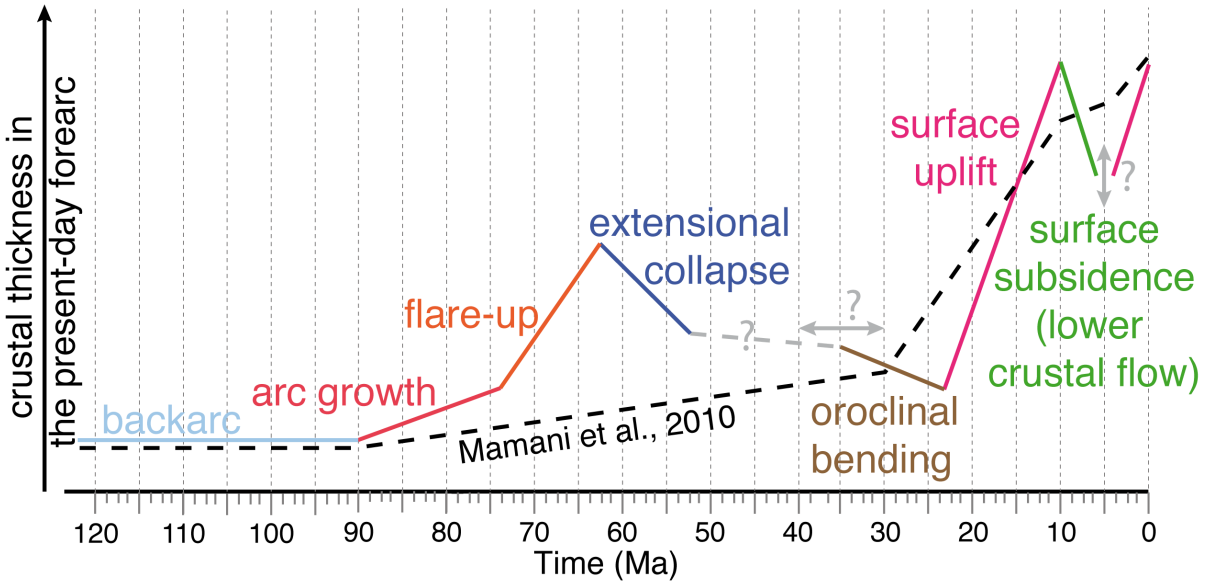

Figure E : Diagramme montrant l'évolution schématique de l'épaisseur crustale de l'avant-arc sud péruvien au cours du temps tel que proposé dans cette thèse (en couleur). L'évolution basée sur les données géochimiques propose par Mamani et al. (2012) est reportée pour comparaison (ligne noire en pointillés). Pas d'échelle verticale.

De l'amincissement à l'épaississement crustal

Dans la région d'Arequipa, au sud du Pérou, nous mettons en évidence une évolution en trois étapes de l'arc magmatique entre ~90 et ~50 Ma (Fig. E). Après plus de 200 Myr d'amincissement crustal et de migration de l'arc volcanique, celui–ci s'établit entre ~90 et ~50 Ma dans une région localisée à environ 150-200 km de la fosse actuelle. Entre ~90 et 74 Ma, la croissance initiale de l'arc dans cette région induit de larges glissements de terrain sous-marins depuis les pentes de l'arc vers le bassin d'arrière-arc. S'ensuit une régression rapide reflétée par la continentalisation rapide des sédiments déposés dans le bassin d'arrière-arc. La croissance de l'arc continue et s'accélère entre ~74 et ~62 Ma, période durant laquelle d'importants volumes de magma se mettent en place dans la croûte (« flare-up » magmatique entre ~10 et ~20°S). En l'absence de déformation compressive, cette importante addition de magmas dérivés du manteau à la croûte supérieure a entrainé la déstabilisation gravitaire de cette dernière au niveau de l'arc, qui s'est effondré à partir de ~62-60 Ma. L'effondrement a été accompagné par une extension à grande échelle à l'origine de nombreuses failles normales orientées NW-SE (Fig. D) et délimitant de grands blocs basculés. Par exemple la faille normale de Lluclla met en contact des grès jurassiques avec un gneiss précambrien alors que selon la stratigraphie régionale ces faciès sédimentaires ne se retrouvent que ~3 km au dessus du socle. L'exhumation liée à cette extension est par ailleurs enregistrée dans les données traces de fission sur apatites et zircons (in-situ et détritiques). Par ailleurs, une surface d'érosion affectant un granite daté à ~62 Ma est couverte par un paléo-volcan dont les laves les plus anciennes ont ~57 Ma.

Le passage, autour de ~90 Ma, de l'amincissement lithosphérique à l'épaississement crustal au niveau de la marge sud péruvienne semble donc avoir été causé principalement par la croissance magmatique considérable de l'arc entre 90 et 62 Ma, et non par une tectonique compressive comme généralement supposé. L'extension a ensuite dominé dans l'avant-arc tout en diminuant progressivement jusque vers ~30 Ma comme l'indiquent les déformations syn-sédimentaires dans les dépôts d'avant-arc paléogènes.

Formation de l'Orocline Bolivien et extension parallèle à l'orogène

Les données thermochronologiques (Fig. F) montrent que le socle de l'avant-arc sud-péruvien était proche de la surface dès le Néo-Protérozoïque. Aucun événement thermique majeur ne l'a affecté depuis hormis dans certaines zones localisées qui ont subi un réchauffement modéré (autour de 220°C) entre ~175 et 105 Ma lors du passage de l'arc sur le littoral actuel au Jurassique (Fig. G). Par ailleurs, les âges par traces de fission sur apatites obtenus le long de la côte actuelle montre que les roches du socle sont passées sous ~90°C entre ~90 et ~55 Ma (Fig. F). De plus, ces âges sont corrélés latéralement à la position de failles normales perpendiculaires à la côte (Fig. F), délimitant de grands blocs basculés (Fig. G). L'analyse de l'architecture sédimentaire dans le bassin éo-miocène de Caravelí-Aplao permet de dater le basculement autour de ~35 Ma. Nous attribuons la formation de ces blocs basculés à l'extension parallèle à l'orogène induite lors de la formation de l'Orocline Bolivien (à partir de 40 Ma) par rotation de blocs rigides autour de leur axe vertical.

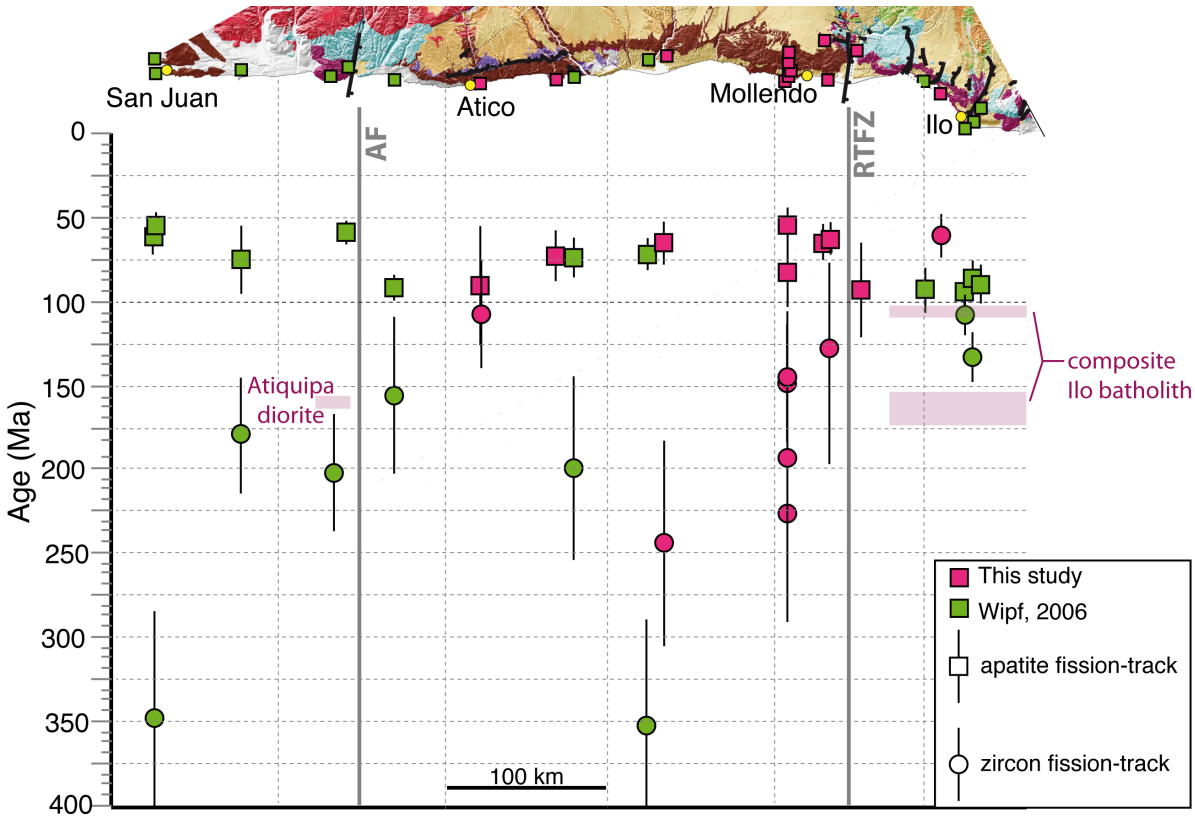

Figure F : A. Carte géologique et distribution des âges par traces de fission sur apatites (carrés) et sur zircons (cercles) disponibles le long du littoral sud-Péruvien. Noter que les âges trace de fission sur zircons sont très dispersés alors que les âges sur apatites sont mieux contraints et sont corrélés à la position de failles normales perpendiculaires à la côte actuelle (et donc à l'orogène).

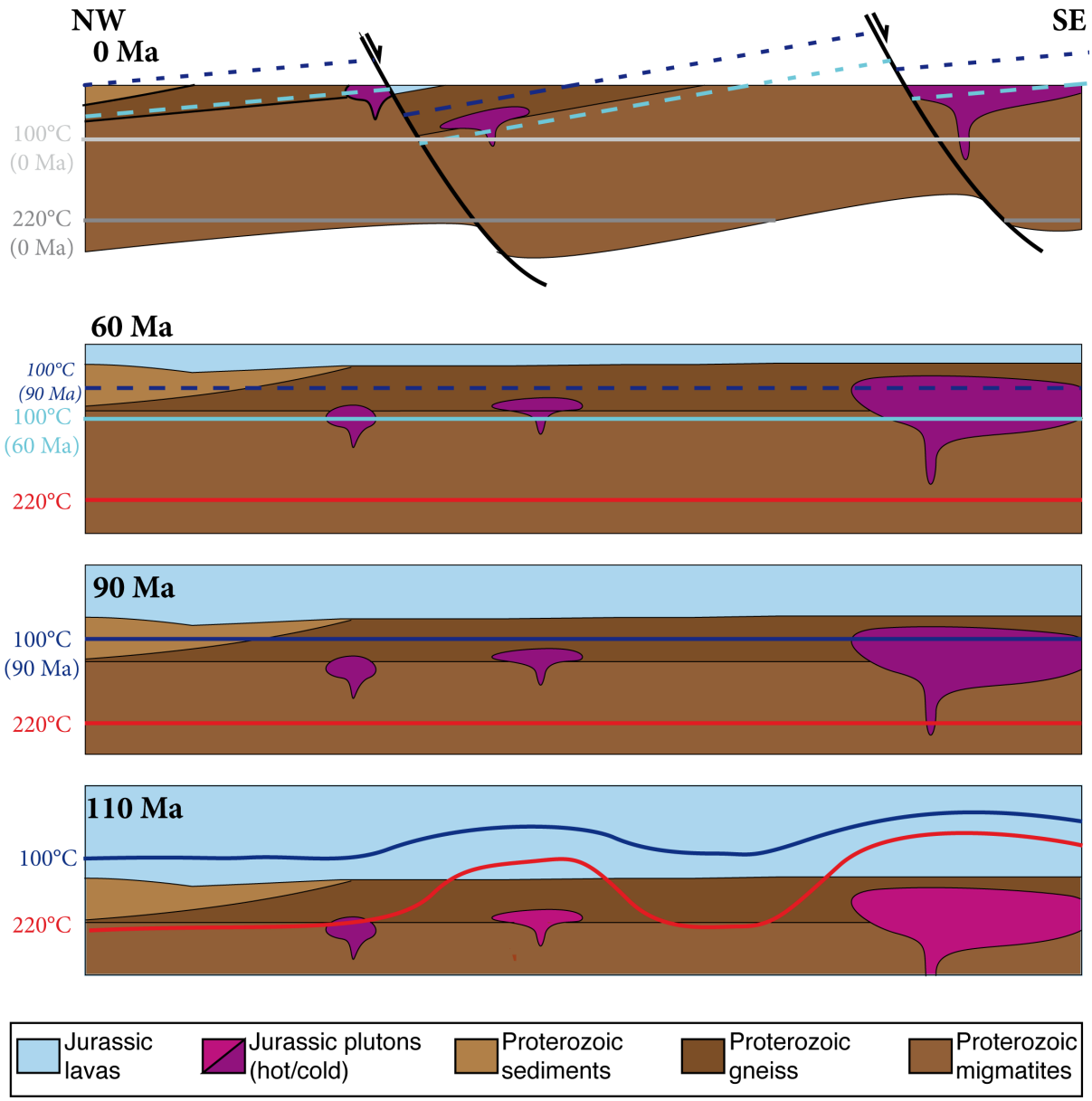

Figure G : Coupes schématiques le long du littoral actuel retraçant l'histoire d'exhumation dans la région. Noter que la structuration en blocs basculés s'acquiert après 60 Ma. Les lignes pleines correspondent aux isothermes, les pointillées aux isochrones des âges traces de fission sur apatites.

Epaississement crustal néogène et écoulement de la croûte inférieure

L'analyse géomorphologique de la vallée inférieure du Rio Tambo et de la bande côtière dans la région de Yerbabuena montre que l'avant-arc sud péruvien a connu deux épisode de soulèvement des surfaces, entre ~23 et ~10 Ma et depuis ~4,5 Ma. Ces deux épisodes ont été séparés par une période de forte subsidence entre ~10 et ~4,5 Ma. Ces épisodes ne sont pas en phase avec les variations eustatiques (Fig. H). Par ailleurs, il n'y a pas d'évidence de raccourcissement tectonique dans l'avant-arc du sud du Pérou, nous proposons donc que le soulèvement de la surface soit dû à un épaississement crustal induit par l'ajout de magmas dérivés du manteau à la croûte.

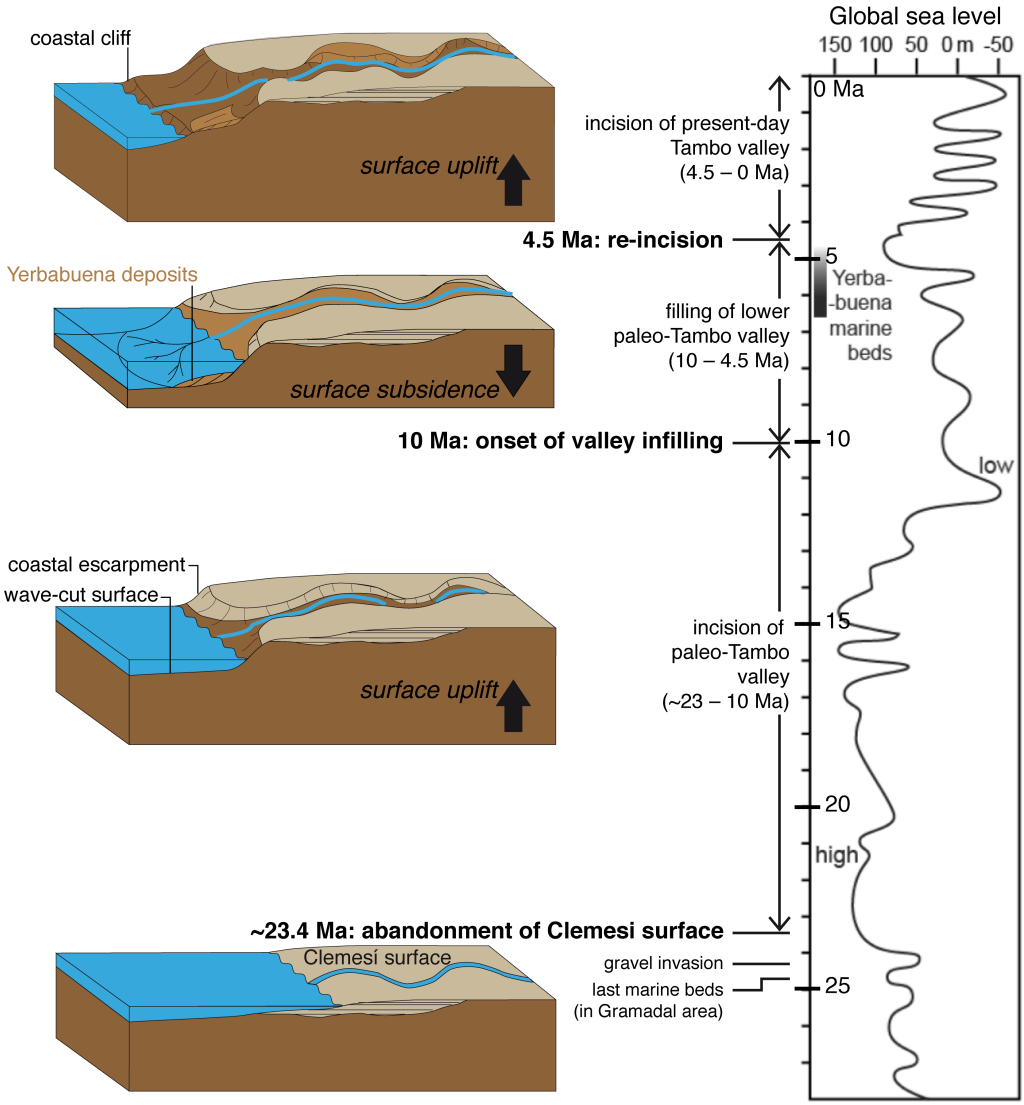

Figure H: Schémas (pas d'échelle) résumant l'évolution géomorphologique de la vallée inférieure du Río Tambo et de la région côtière de Yerbabuena depuis l'Oligocène Moyen (gauche). Les variations eustatiques globales sont reportées pour comparaison (droite ; l'échelle vertical est graduée en Ma ; d'après Hardenbol et al., 1998).

La même chronologie a été décrite sur le versant amazonien des Andes Centrales (Fig. I) alors que les variations climatiques entre ces deux régions sont en opposition de phase (lorsque le climat est aride dans l'avant-arc, il est humide sur le versant amazonien). Nous interprétons donc cette évolution comme reflétant un important épaississement crustal au Néogene qui déclenche finalement un écoulement de la croûte inférieure ductile depuis l'axe de l'Orocline Bolivien vers le nord-ouest.

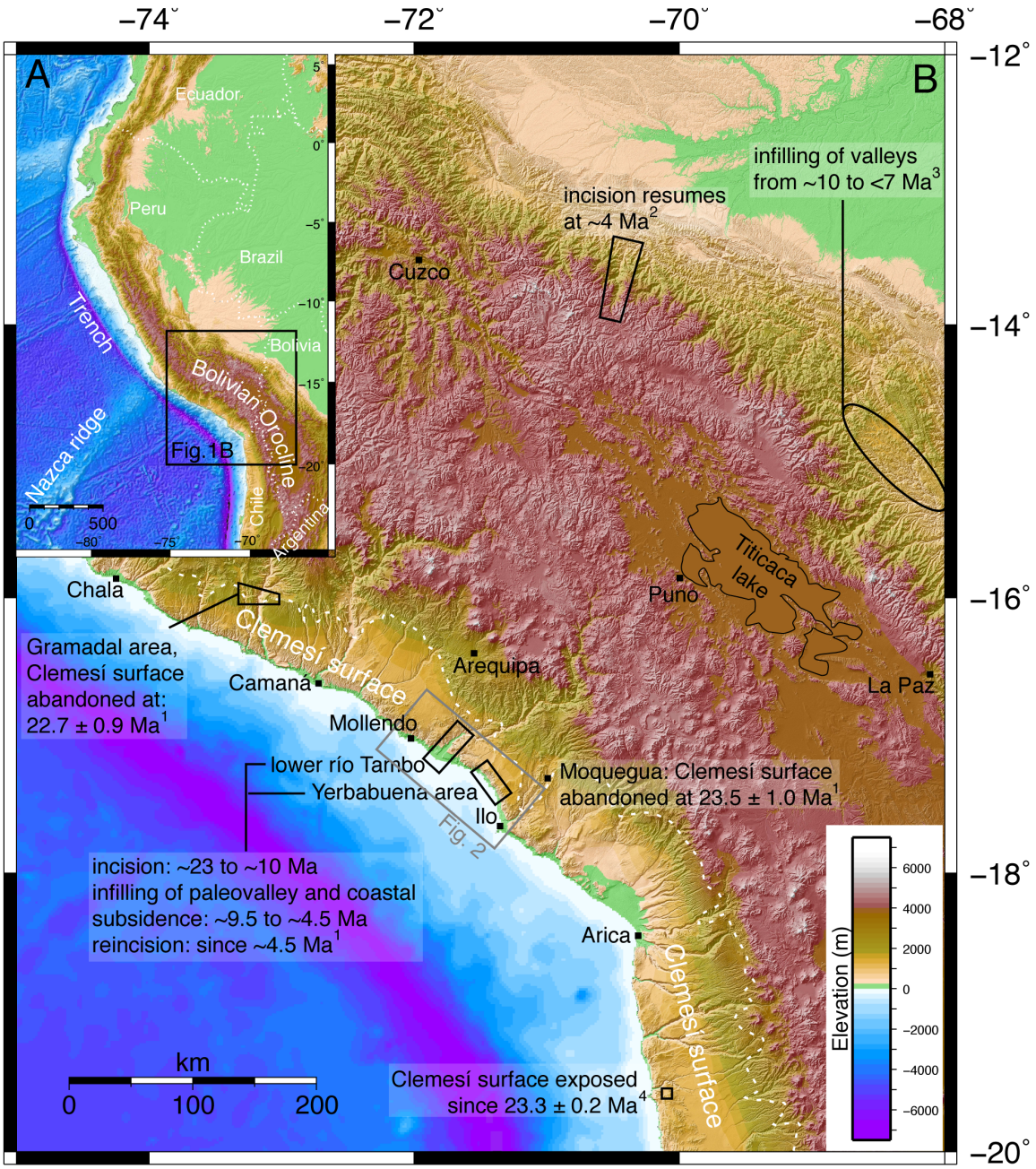

Figure I: Position et chronologie des différents évènements concernant le soulèvement des surfaces andines. La ligne pointillée blanche marque approximativement la limite NE de la surface Clemesi. Références : [1]: cette étude ; [2]: Lease & Ehlers (2013); [3]: Mosolf et al. (2011); [4]: Dunai et al. (2005).

Perspectives

Il serait intéressant d'étudier en détails les modes et la chronologie de l'exhumation au niveau du détachement d'Ocoña. En effet, cette faille permet d'exhumer le plus grand bloc de migmatites ultra-haute température du monde. Cependant, les dépôts volcaniclastiques jurassiques de la région ne sont pas affectés par cet important détachement, une telle étude permettrait certainement de mieux contraindre l'histoire précoce de la zone de subduction.

De plus, juste après la fin de l'épisode de flare-up dans la région d'Arequipa, l'effondrement de la croûte et la mise en place des porphyres, l'arc migre subitement et drastiquement vers le nord (Fig. B). Cette migration est probablement due à une diminution du pendage du panneau plongeant alors que la vitesse de convergence des plaques Nazca et Amérique du sud augmente. Ce synchronisme pose le problème des éventuelles relations causales entre les différents phénomènes énumérés. Une étude détaillée à l'échelle régionale de l'évolution des arcs volcaniques pourrait aider à mieux comprendre la dynamique des zones de subduction et, par exemple, les différents processus à l'origine de la mise en place des porphyres de cuivre ou de l'horizontalisation de la plaque plongeante.

Dans ce type de contextes, il reste cependant difficile d'extraire le refroidissement dû à la relaxation thermique des plutons (après leur mise en place) du refroidissement lié à l'exhumation des roches. Il semble donc essentiel de caractériser la profondeur de mise en place des corps magmatiques mais aussi de rechercher et considérer l'ensemble des contraintes géologiques et géomorphologiques disponibles afin de mieux contraindre les taux et les modes d'exhumation.

Enfin, une autre caractéristique importante des Andes Centrales est son volume orogénique qui diminue nettement depuis l'axe de l'Orocline bolivien vers le nord. Cette étude confirme qu'un écoulement de la croûte inférieure ductile peut avoir affecté l'orogène au Néogène. Il serait donc intéressant d'étudier les diachronismes possibles qui pourraient avoir été induits par la migration du front de l'écoulement de la croûte vers le nord-ouest.

L'avant-arc du sud du Pérou offre donc de nombreuses possibilités de travaux futurs. En effet, parce qu'il n'a pas été affecté par l'accrétion de terrains allochtones ni par un raccourcissement tectonique et parce qu'un climat aride y règne depuis au moins l'Oligocène, cette région enregistre l'évolution de la subduction et de l'orogène et est susceptible de fournir encore de nombreuses contraintes sur les processus liés aux marges actives.

Méthodes

Principes

La géo-thermochronologie est une méthode de datation qui utilise la décroissance radioactive ou la fission spontanée d'un atome père en un atome fils pour obtenir l'âge depuis lequel le système étudié (un minéral) a refroidi sous sa « température de fermeture » T_c. Ces méthodes de datations sont toutes basées sur la loi de décroissance radioactive qui lie le temps *t* depuis lequel le système minéralogique est dit « fermé » à la quantité d'atomes pères et fils présents (N_p et N_f) dans le système selon la formule suivante :

$$t = \frac{1}{\lambda} \ln \left[\frac{N_f}{N_p} + 1 \right]$$

Le concept de température de fermeture (T_c), tel que développé par Dodson (1973), est basé sur la diffusion en dehors du cristal étudié des isotopes fils de la décroissance radioactive naturelle ou du recuit partiel des traces de fission dans les apatites et les zircons. Ce concept postule qu'au dessus d'une température donnée (la température de fermeture), le système est ouvert c'est à dire que tous les isotopes fils diffusent hors du cristal étudié ou que les traces de fission s'effacent (recuisent) instantanément. Au contraire, sous cette température tous les isotopes fils sont retenus dans le cristal (ou bien les traces s'accumulent) et le système est considéré comme fermé. La température de fermeture est différente pour chaque système et dépend en majeure partie du taux de refroidissement (plus le refroidissement est rapide plus la température de fermeture est élevée et vice-versa). Cependant, ce concept est simplificateur car il existe en fait une gamme de température pour lesquelles la diffusion (ou le recuit des traces) est partielle, on obtient donc toujours un âge apparent.

Chaque thermochronomètre possédant une température de fermeture différente, le choix de la méthode utilisée dépend du problème géologique à résoudre. Ainsi, les systèmes avec une température de fermeture élevée sont utilisés pour dater par exemple la cristallisation du système étudié. Ces méthodes sont dites géochronologiques. Tandis que les systèmes avec des températures de fermetures plus faibles (les méthodes thermochronologiques) seront utilisées pour dater les processus affectant la croûte supérieure.

Uranium-Plomb sur zircon

Cette méthode est communément utilisée dans les études géologiques en particulier pour dater l'âge de cristallisation des roches. En effet, dans les zircons, la diffusion de l'uranium et du plomb est quasiment nulle et la température de fermeture de ce système est donc très élevée (~800 ± 50°C ; Lee et al., 1997). Cette méthode de datation (abrégée ensuite U-Pb sur zircon) est basée sur les deux chaines de décroissance des deux isotopes radioactif de l'uranium naturel (^{238}U et ^{235}U) vers les deux isotopes stables du plomb (^{206}Pb et ^{207}Pb) (Košler and Sylvester, 2003; Jackson et al., 2004). En mesurant respectivement les rapports $^{206}Pb/^{238}U$ et $^{207}Pb/^{235}U$, on obtient donc deux âges indépendants pour le même grain. On peut reporter les rapports obtenus dans le « diagramme Concordia » (Wetherill, 1956). Dans cet espace, la courbe Concordia correspond aux points pour lesquels chacune des deux méthodes U-Pb donnent des âges identiques. Tout zircon analysé pour lequel on obtient des rapports tombant sur la Concordia (c'est à dire des âges concordants) donne l'âge de cristallisation de ce zircon.

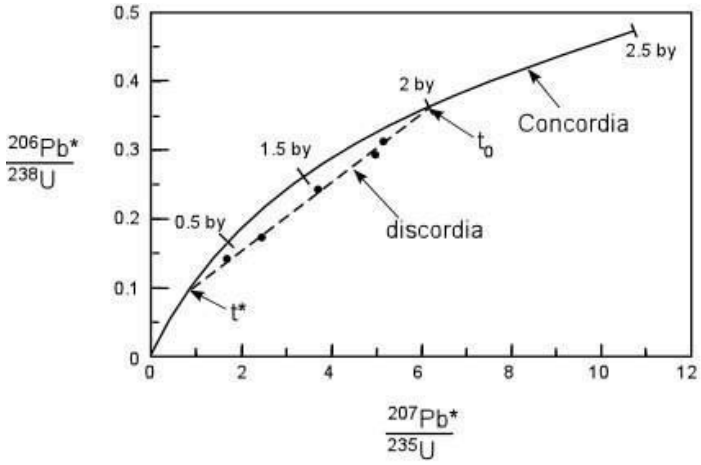

Figure II.5: Digramme Concordia. La courbe noire correspond à la ligne Concordia (Wetherill, 1956), l'âge de n'importe quel zircon analysé et tombant sur cette ligne est indiqué par les tirets. La ligne en pointillés correspond à la Discordia trace pour les zircons analysés dans cet exemple (points noirs). L'intersection haute entre la Discordia et la Concordia corresponds a l'âge de crystallization t0 des zircons analysés tandis que l'intercept bas donne l'â t* de la perte de Pb (par exemple lors d'un évènement métamorphique

Traces de fission sur apatites et zircons

La fission spontanée de l'^{238}U produit deux atomes chargés qui se repoussent mutuellement au moment de la fission. Ces charges parcourent à elles deux une distance totale d'environ 16 µm dans les apatites et 11µm dans les zircons, causant un défaut dans le réseau cristallin. Ces zones endommagées sont appelées traces de fission (Price and Walker, 1963; Fleischer et al., 1975). Les traces de fission sont visibles au microscope optique uniquement après une attaque chimique qui permet de les élargir. Les défauts cristallins occasionnés par la fission spontanée « cicatrisent » à haute température (les traces « recuisent ») mais s'accumulent au cours du temps sous la température de recuit partiel (~100°C pour les apatites, ~220°C pour les zircons). Ainsi, en contant les traces de fission, on est capable d'estimer le nombre de fissions spontanées qui ont eu lieu autour de la surface interne du minéral analysé depuis que ce dernier a refroidit sous la température de recuit partiel. Cependant, la concentration en 238U présent dans le grain reste inconnue. Pour la déterminer et pouvoir dater l'âge de refroidissement, on a ici utilisé la méthode du détecteur externe. Cette technique utilise le fait que le rapport ^{238}U/^{235}U est constant dans la nature (Steiger and Jäger, 1975) et que la fission de l'^{235}U peut être induite par la capture d'un neutron. Il est donc possible d'estimer la concentration en ^{238}U dans le grain analysé indirectement en déterminant la densité des traces de fission de l'^{235}U induites par des neutrons thermiques lors d'une irradiation. Pour ce faire, on attache au montage contenant les grains polis (et attaqués chimiquement) à analyser un détecteur en mica, ne contenant pas d'uranium. On irradie ensemble ces montages, la capture d'un neutron par un 235U proche de la surface du grain poli va entrainer sa fission et la formation d'une trace « induite », visible dans le détecteur après attaque chimique. L'âge traces de fission d'un grain est alors donné par la formule suivante :

$$FTage = \frac{1}{\lambda_d} \ln[1 + g\lambda_d \xi \rho_d \frac{N_s}{N_i}]$$

Ou $FTage$ est l'âge trace de fission de l'apatite ou du zircon analysé, λ_d est la constant de désintégration radioactive de l'^{238}U, g un facteur géométrique, ξ le facteur de calibration personnelle de l'analyste, ρ_d la densité de traces induites (elle dépend du flux de neutrons lors de l'irradiation), N_s le nombre de traces spontanées (comptées dans le grain) et N_i le nombre de traces induites (comptées dans le détecteur externe en micas).

APPENDIX A:
^{40}AR/^{39}AR DATING

Fresh crystals of biotite and muscovite were handpicked from the 500-1000 μm diameter fraction of crushed bedrock samples. Crystals were ultrasonically cleaned in high-purity water and ethanol, ground in a mortal and pestal to remove altered grain edges, and ultrasonically cleaned a second time prior to packaging in Al foil packets. All samples were encapsulated in quartz vials for irradiation. Samples were irradiated at the McMaster University reactor along with flux monitor Fish Canyon Tuff sanidine (28.02 Ma; Renne et al., 1998) and synthetic salts to permit corrections for interfering nuclear reactions. Vertical monitoring of the neutron flux resulted in J values known to better than 0.2 to 0.3%.

Gas was liberated from crystals after incremental heating of the packet in a vacuum furnace in 18 to 20 steps. Plateau dates were calculated using three or more consecutive steps with overlapping uncertainty comprising at least 50% of the total $^{39}Ar_K$ released.

The evolved gas was purified with a series of metal alloy getters and analyzed on the Massachusetts Institute of Technology MAP 215-50 mass spectrometer with an electron multiplier. Total system blanks were measured at the beginning of each analytical session, between sets of two to six incremental heating analyses depending on blank reproducibility. Mass fractionation was monitored by routine analysis of laboratory air over the duration of the analytical campaign. Isotopic measurements were reduced using the ArArCALC routines of Koppers (2002) and corrected for system blanks, mass fractionation, and neutron-induced interferences. Apparent $^{40}Ar/^{39}Ar$ ages were calculated using decay constants recommended by Steiger and Jaeger (1977) and assuming an initial $^{40}Ar/^{36}Ar$ ratio of 295.5. Age uncertainties throughout this study include errors associated with blank and sample isotopic measurements, fractionation, interfering reactions, and J. For samples with weighted mean dates characterized by a MSWD (mean square weighted deviate) > 1, scatter is assumed to be greater than the contribution from analytical errors, and errors were multiplied by the square root of the MSWD (York, 1969).

References

Koppers, A.A.P, 2002, AeArCALC–Software dor 40Ar/39Ar age calculations: Computers and Geosciences, 28, p. 605-619.

Renne, P. R., Swisher, C. C., Deino, A. L., Karner, D. B., Owens, T., and DePaolo, D. J., 1998, Intercalibration of standards, absolute ages and uncertainties in 40Ar/39Ar dating: Chemical Geology, 145, p. 117-152.

Steiger, R. H., and Jaeger, E., 1977, Subcommission on geochronology: Convention on the use of decay constants in geo-and cosmochronology: Earth and Planetary Science Letters, 36, p. 359-362.

York, D., 1969, Least squares fitting of a straight line with correlated errors: Earth and Planetary Science Letters, 5, p. 320-324.

Appendix B:
Zircon (U-Th)/He dating

Estimated closure temperatures for the zircon (U-Th)/He system vary slightly depending on grain size and rate of cooling. Diffusion parameters have been experimentally determined for zircon by Reiners et al. (2004) and yield a nominal closure temperature ranging from ~170 to 190 °C, and a helium partial retention zone spanning a temperature range of 120 – 180 °C (Tagami et al., 2003). The zircon (U-Th)/He thermochronometer has a closure temperature that bridges the gap between the ^{40}Ar-^{39}Ar and apatite fission-track thermochronometers (Reiners, 2005).

Mineral separation was performed following standard crushing, sieving, magnetic and density separation procedures. Grains were hand-picked in the 80 to 200 mm fraction to select idiomorphic and inclusion-free specimens. (U-Th)/He analyses were performed by Thibaud Simon-Labric at the University of Arizona, following the method described by Reiners et al. (2004). The abundance of He in each crystal was measured by laser mass spectrometry. The concentrations of U and Th were measured by isotope dilution. An α-ejection correction (F_t) was applied to each crystal to derive a corrected (U-Th)/He age (Reiners, 2005).

References

Reiners, P.W., Spell, T. L., Nicolescu, S., and Zanetti, K. A., 2004, Zircon (U-Th)/He thermochronology: He diffusion and comparisons with 40Ar/39Ar dating, Geochim. Cosmochim. Acta, 68, 1857 – 1887, doi:10.1016/j.gca.2003.10. 021.

Reiners, P. W., 2005, Zircon (U-Th)/He thermochronometry, Rev Mineral Geochem, 58:151, 179, doi: 10.2138/ rmg.2005.

Tagami, T., Farley, K. A., and Stockli, D. F., 2003, Thermal sensitivities of zircon (U-Th)/He and fission-track systems, Geochim. Cosmochim. Acta, 67(18), 466

Appendix C:
Apatite and zircon fission-track sample preparation

After rock crushing, all samples were sieved and the 100–200 μ m fraction was conserved. Apatite and zircon grains were separated using standard shaking, and magnetic and heavy liquid separation techniques.

Apatites and zircons were mounted in epoxy resin and Teflon® sheets respectively and polished to expose an internal surface for each grain. Apatites were then etched with a 5.5 mol HNO_3 for 20 s at 21°C. Zircons were etched in a NaOH-KOH melt between 19 and 56 hours at 228°C.

In the present study, we used the external detector method for fission-track analysis. Apatite and zircon grain mounts were thus covered with uranium-poor muscovite sheets as external detectors and irradiated at the FRM II reactor at Garching, Germany. Apatite samples were irradiated with a nominal fluence of 4.5×10^{15} neutrons/cm^2 together with Fish Canyon and Durango Tuffs age standards and with IRMM540R (15 ppm) dosimeter glasses. Zircon samples were irradiated with a nominal fluence of 0.5×10^{15} n/cm^2 together with Fish Canyon Tuff and Buluk Tuff age standards and CN1 (39.8 ppm) dosimeter glasses. After irradiation, the muscovite detectors of all mounts were etched for 18 minutes in 48% HF at 21°C to reveal induced tracks. Spontaneous and induced fission tracks were counted at the ISTerre fission-track laboratory, Grenoble University, France, at 1250× magnification using a dry objective and an Olympus BX51 microscope and the FTStage 4.04 system (Dumitru, 1993).

Only crystals with polished surfaces parallel to the crystallographic c-axis were considered. The individual grain ages as well as the pooled and mean ages were calculated as recommended by (Galbraith, 2005). To compute central ages we used the RadialPlotter software (Vermeesch, 2012, 2009).

Due to the low uranium content in apatite, not sufficient horizontally confined tracks were observed to carry out a track length distribution analysis. However, D_{par} values (the etch pit size parallel to the crystallographic c-axis, a kinematic parameter for track annealing) were

measured on at least four etch pits per grain in order to verify if there is a correlation or not between apatite fission-track ages and D_{par} values.

References

Dumitru, T.A., 1993, A new computer-automated microscope stage system for fission-track analysis: Nuclear Tracks and Radiation Measurements, v. 21, p. 575–580, doi: 10.1016/1359-0189(93)90198-I.

Galbraith, R.F., 2005, Statistics for Fission Track Analysis: CRC Press, 248 p.

Vermeesch, P., 2012, On the visualisation of detrital age distributions: Chemical Geology, v. 312–313, p. 190–194, doi: 10.1016/j.chemgeo.2012.04.021.

Vermeesch, P., 2009, Radialplotter: a java application for fission track, luminescence and other radial plots: Radiation Measurments, v. 44, p. 409–410.

Appendix D:
Zircon U-Pb Analyses (In-Situ)

These analyses were performed at UNIL (Université de Lausanne, Switzerland) in collaboration with A. Ulianov and U. Schaltegger.

1M33

					206Pb/238U		207Pb/235U		207Pb/206Pb	
	Pb206/U238	**Rho**	**Pb207/U235**	**Rho**	**AGE (Ma)**	**+/- 2 S.D.**	**AGE (Ma)**	**+/- 2 S.D.**	**AGE (Ma)**	**+/- 2 S.D.**
fe25l05	0.0106	0.0102	0.0753	0.0361	1.4	73.7	5.1	254	164	0
fe25l06	0.0108	0.0079	0.0672	0.0306	1.1	66	3.9	0	26	0
fe25l07	0.0112	0.0056	0.0763	0.0223	0.8	74.7	3.2	156	100	0
fe25l08	0.0109	0.0095	0.0733	0.0403	1.3	71.8	5.6	112	194	0
fe25l09	0.0105	0.0085	0.0721	0.0325	1.1	70.7	4.4	186	154	0
fe25l10	0.0107	0.0085	0.0743	0.0403	1.2	72.7	5.7	206	196	0
fe25l11	0.0106	0.008	0.0692	0.0465	1.1	68	6.1	100	202	0
fe25l12	0.0107	0.005	0.0716	0.0115	0.7	70.2	1.6	114	52	0
fe25l13	0.0111	0.0124	0.0735	0.0844	1.8	72	11.7	104	280	0
fe25m05	0.011	0.82%	0.0726	2.26%	70.2	1.1	71.1	3.1	132	108
fe25m06	0.011	1.63%	0.0761	3.77%	70.3	2.3	74.5	5.4	232	158
fe25m07	0.0108	0.92%	0.0743	3.65%	69.5	1.3	72.8	5.1	188	176

1M37

					206Pb/238U		207Pb/235U		207Pb/206Pb	
	Pb206/U238	**Rho**	**Pb207/U235**	**Rho**	**AGE (Ma)**	**+/- 2 S.D.**	**AGE (Ma)**	**+/- 2 S.D.**	**AGE (Ma)**	**+/- 2 S.D.**
fe24a05	1.14%	0.52%	7.56%	1.77%	73.1	0.8	74	2.5	136	82
fe24a06	1.14%	0.89%	7.65%	3.76%	73	1.3	74.9	5.4	134	170
fe24a07	1.17%	0.75%	7.46%	2.28%	75	1.1	73	3.2	52	100
fe24a08	1.17%	0.84%	7.46%	2.98%	75	1.3	73.1	4.2	58	126
fe24a09	1.14%	0.52%	7.57%	1.71%	72.8	0.8	74.1	2.4	112	76
fe24a10	1.15%	0.59%	7.67%	1.95%	73.7	0.9	75.1	2.8	132	90
fe24a11	1.12%	0.69%	7.40%	2.34%	72.1	1	72.5	3.3	92	110
fe24a12	1.14%	0.60%	7.81%	2.43%	73.3	0.9	76.3	3.6	166	108
fe24a13	1.12%	1.21%	7.39%	6.40%	71.8	1.7	72.4	8.9	70	220
fe24b05	1.15%	0.75%	7.48%	3.16%	73.6	1.1	73.3	4.5	62	138
fe24b06	1.15%	0.74%	7.52%	2.99%	73.8	1.1	73.7	4.3	90	146
fe24b07	1.12%	0.67%	7.03%	2.30%	71.6	0.9	69	3.1	10	66
fe24b08	1.13%	0.93%	7.29%	3.66%	72.4	1.3	71.4	5	42	128
fe24b09	1.14%	0.69%	7.27%	2.60%	72.8	1	71.3	3.6	56	114
fe24b10	1.18%	0.94%	7.54%	3.65%	75.6	1.4	73.8	5.2	24	108
fe24b11	0.0114	0.54%	0.0755	1.75%	72.9	0.8	73.9	2.5	128	88
fe24b12	0.0118	0.74%	0.0812	2.64%	75.7	1.1	79.2	4	188	128

1M38

					206Pb/238U		207Pb/235U		207Pb/206Pb	
	Pb206/U238	**Rho**	**Pb207/U235**	**Rho**	**AGE (Ma)**	**+/- 2 S.D.**	**AGE (Ma)**	**+/- 2 S.D.**	**AGE (Ma)**	**+/- 2 S.D.**
fe25a5	0.0112	0.71%	0.0792	2.67%	72.1	1	77.4	4	280	112
fe25a7	0.0116	0.69%	0.0867	2.79%	74.2	1	84.4	4.5	404	122
fe25a8	0.0111	0.74%	0.0729	2.36%	71.2	1	71.5	3.3	76	120
fe25a10	0.0115	0.57%	0.0891	3.03%	74	0.8	86.7	5	448	130
fe25a11	0.0113	1.08%	0.086	2.61%	72.6	1.6	83.8	4.2	376	112
fe25a12	0.0116	1.85%	0.0787	2.56%	74.1	2.7	76.9	3.8	166	110
fe25a13	0.0113	1.79%	0.0752	2.71%	72.1	2.6	73.7	3.9	140	116
fe25b5	0.0111	0.59%	0.0699	1.69%	71.4	0.8	68.6	2.2	0	38
fe25b7	0.0113	0.72%	0.0772	2.73%	72.2	1	75.5	4	172	126
fe25b8	0.0112	0.66%	0.0724	2.73%	72	0.9	71	3.7	42	110
fe25b9	0.0112	0.65%	0.0731	2.29%	71.9	0.9	71.7	3.2	78	114
fe25b10	0.0119	1.20%	0.0772	1.97%	76.3	1.8	75.5	2.9	68	90
fe25b11	0.0114	0.53%	0.0748	1.95%	73.3	0.8	73.3	2.8	102	86

1M68

					206Pb/238U		207Pb/235U		207Pb/206Pb	
	Pb206/U238	**Rho**	**Pb207/U235**	**Rho**	**AGE (Ma)**	**+/- 2 S.D.**	**AGE (Ma)**	**+/- 2 S.D.**	**AGE (Ma)**	**+/- 2 S.D.**
fe25n05	0.1776	0.75%	1.962	1.22%	1053.9	14.6	1102.6	16.4	1218	32
fe25n06	0.1722	0.56%	1.817	1.32%	1024.3	10.6	1051.6	17.2	1112	38
fe25n08	0.0415	0.61%	0.3083	2.18%	262	3.2	272.9	10.4	384	86
fe25n09	0.0347	0.52%	0.2464	0.99%	220.2	2.2	223.6	4	264	44
fe25n11	0.0397	0.69%	0.2986	1.54%	250.7	3.4	265.3	7.2	386	66

1M73

					206Pb/238U		207Pb/235U		207Pb/206Pb	
	Pb206/U238	**Rho**	**Pb207/U235**	**Rho**	**AGE (Ma)**	**+/- 2 S.D.**	**AGE (Ma)**	**+/- 2 S.D.**	**AGE (Ma)**	**+/- 2 S.D.**
fe25h05	0.0025	1.11%	0.017	4.75%	16.4	0.4	17.1	1.6	134	234
fe25h06	0.0027	1.67%	0.0199	7.73%	17.1	0.6	20	3.1	412	356
fe25h07	0.0027	1.36%	0.0158	8.88%	17.4	0.5	15.9	2.8	0	14
fe25h08	0.0027	2.75%	0.0189	14.31%	17.4	1	19.1	5.4	216	596
fe25h09	0.0025	2.08%	0.0147	10.86%	16.3	0.7	14.9	3.2	0	78
fe25h11	0.0026	1.05%	0.0165	5.33%	16.8	0.4	16.7	1.8	2	132
fe25h12	0.0025	1.20%	0.0178	5.20%	16.1	0.4	18	1.9	282	254
fe25h13	0.0025	0.71%	0.0165	3.17%	16.3	0.2	16.7	1	72	150
fe25i06	0.0025	0.87%	0.0164	3.99%	16.4	0.3	16.5	1.3	54	146
fe25i07	0.0025	1.69%	0.0149	9.00%	15.9	0.5	15	2.7	0	44
fe25i08	0.0027	1.48%	0.0161	7.73%	17.4	0.5	16.2	2.5	0	2

1M74

					206Pb/238U		207Pb/235U		207Pb/206Pb	
	Pb206/U238	**Rho**	**Pb207/U235**	**Rho**	**AGE (Ma)**	**+/- 2 S.D.**	**AGE (Ma)**	**+/- 2 S.D.**	**AGE (Ma)**	**+/- 2 S.D.**
fe25f08	0.026	1.89%	0.1792	3.34%	165.5	6.2	167.4	10.3	202	130
fe25f09	0.0263	0.97%	0.168	3.41%	167.6	3.2	157.7	10	72	146
fe25f10	0.0261	1.12%	0.1781	2.42%	166	3.7	166.4	7.4	174	98
fe25f11	0.0259	0.80%	0.1753	3.56%	165.1	2.6	164	10.8	136	164
fe25f12	0.0261	0.70%	0.1848	3.13%	166.1	2.3	172.2	9.9	208	134
fe25f13	0.0261	0.86%	0.1773	3.17%	165.9	2.8	165.7	9.7	174	142
fe25g05	0.0268	0.74%	0.1674	3.38%	170.4	2.5	157.1	9.9	0	32
fe25g06	0.0268	1.44%	0.1734	2.61%	170.6	4.8	162.3	7.8	56	112
fe25g07	0.026	0.83%	0.1808	3.66%	165.3	2.7	168.8	11.4	232	164
fe25g08	0.0261	0.68%	0.1669	3.25%	165.8	2.2	156.7	9.4	34	106
fe25g09	0.0257	0.69%	0.1729	3.07%	163.7	2.2	161.9	9.2	136	132
fe25g10	0.0268	0.88%	0.1756	3.30%	170.2	3	164.3	10	38	110
fe25g11	0.0263	1.03%	0.1704	3.58%	167.2	3.4	159.8	10.6	84	148
fe25g12	0.026	0.67%	0.1777	2.94%	165.3	2.2	166.1	9	196	120

1M80

					206Pb/238U		207Pb/235U		207Pb/206Pb	
	Pb206/U238	**Rho**	**Pb207/U235**	**Rho**	**AGE (Ma)**	**+/- 2 S.D.**	**AGE (Ma)**	**+/- 2 S.D.**	**AGE (Ma)**	**+/- 2 S.D.**
fe25j05	0.0251	0.38%	0.1701	1.37%	159.9	1.2	159.5	4	168	62
fe25j06	0.0255	0.33%	0.1737	0.92%	162.1	1	162.6	2.8	194	40
fe25j07	0.0255	0.49%	0.1709	0.86%	162.5	1.6	160.2	2.6	160	40
fe25j08	0.0252	0.89%	0.1703	0.87%	160.6	2.8	159.7	2.6	160	36
fe25j09	0.0251	1.41%	0.1723	1.77%	160	4.5	161.4	5.3	198	70
fe25j10	0.0253	0.41%	0.17	0.98%	161.1	1.3	159.4	2.9	154	48
fe25j11	0.0253	0.35%	0.1738	0.93%	161	1.1	162.7	2.8	214	40
fe25j12	0.0257	0.32%	0.1768	0.66%	163.3	1	165.3	2	178	30
fe25k05	0.0252	0.43%	0.1724	0.89%	160.6	1.4	161.5	2.6	184	42
fe25k06	0.0251	0.56%	0.1705	0.83%	159.7	1.8	159.9	2.5	190	36
fe25k07	0.025	2.25%	0.1692	1.96%	159.3	7.1	158.8	5.8	154	74
fe25k08	0.0254	2.39%	0.1712	2.06%	161.7	7.6	160.5	6.1	136	86
fe25k09	0.0259	0.45%	0.178	1.04%	165	1.5	166.3	3.2	198	46
fe25k10	0.0261	0.40%	0.1756	0.69%	166.3	1.3	164.2	2.1	158	28
fe25k11	0.026	0.69%	0.1747	0.77%	165.7	2.3	163.5	2.3	148	38
fe25k13	0.0252	1.00%	0.1714	1.15%	160.5	3.2	160.6	3.4	172	50

3M3

					206Pb/238U		207Pb/235U		207Pb/206Pb	
	Pb206/U238	**Rho**	**Pb207/U235**	**Rho**	**AGE (Ma)**	**+/- 2 S.D.**	**AGE (Ma)**	**+/- 2 S.D.**	**AGE (Ma)**	**+/- 2 S.D.**
fe25c5	0.0014	2.38%	0.0097	10.96%	9	0.4	9.8	2.1	246	492
fe25c6	0.0015	4.28%	0.0102	23.61%	9.7	0.8	10.3	4.9	170	870
fe25c8	0.0014	2.74%	0.0086	14.35%	8.7	0.5	8.7	2.5	38	394
fe25c10	0.0015	1.27%	0.0098	5.96%	9.6	0.2	9.9	1.2	96	238
fe25c11	0.0014	3.95%	0.0092	19.69%	9.2	0.7	9.3	3.7	22	548
fe25c12	0.0015	1.23%	0.0094	5.21%	9.5	0.2	9.5	1	32	152
fe25d05	0.0015	2.14%	0.01	9.53%	9.4	0.4	10.1	1.9	198	438
fe25d07	0.0014	3.25%	0.0096	18.20%	9.3	0.6	9.7	3.5	138	496
fe25d08	0.0015	3.56%	0.0085	22.65%	9.9	0.7	8.6	3.9	0	346
fe25d09	0.0014	3.18%	0.0087	14.00%	9	0.6	8.8	2.5	0	278
fe25d10	0.0014	3.39%	0.0096	18.39%	9.1	0.6	9.7	3.5	150	558
fe25d11	0.0015	2.08%	0.0106	10.35%	9.7	0.4	10.7	2.2	258	466
fe25d12	0.0014	3.37%	0.0118	16.27%	9.2	0.6	11.9	3.9	594	874
fe25e06	0.0016	3.26%	0.0116	16.30%	10.1	0.7	11.7	3.8	380	798
fe25e08	0.0015	2.80%	0.0102	15.10%	9.7	0.5	10.3	3.1	160	498

Appendix E:
Zircon U-Pb analyses (Detrital)

These analyses were performed at LMV (Université de Clermont-Ferrand, France) by J.-L. Paquette.

1M20

Sample 1M20: Conglomerate						2 sigma error		2 sigma error		Age (Ma)	2 sigma error
Analysis_#	Pb ppm	Th ppm	U ppm	Th/U	Pb207/U235	Pb207/U235	Pb206/U238	Pb206/U238	Rho	Pb206/U238	Pb206/U238
29190213a	12	24	897	0.03	0.0974	0.0040	0.01455	0.00054	0.91	93.1	3.4
30190213a	19	23	100	0.23	1.9681	0.0790	0.18737	0.00681	0.91	1107	37
31190213a	19	33	94	0.36	2.0887	0.0799	0.19437	0.00702	0.94	1145	38
32190213a	7.2	65	104	0.63	0.4782	0.0212	0.06288	0.00228	0.82	393	14
35190213a	54	188	544	0.35	0.7962	0.0295	0.09666	0.00348	0.97	595	20
36190213a	46	54	231	0.23	2.1458	0.0795	0.19826	0.00714	0.97	1166	38
37190213a	5.8	361	381	0.95	0.0825	0.0041	0.01244	0.00045	0.73	79.7	2.9
38190213a	69	199	772	0.26	0.7154	0.0264	0.08932	0.00321	0.97	552	19
39190213a	6.7	137	139	0.98	0.2840	0.0136	0.03912	0.00144	0.77	247	9
40190213a	2.6	46	68	0.67	0.2571	0.0145	0.03323	0.00123	0.66	211	8
41190213a	19	115	539	0.21	0.2606	0.0103	0.03313	0.00120	0.92	210	7
42190213a	15	30	83	0.36	1.7839	0.0698	0.17625	0.00636	0.92	1047	35
45190213a	19	192	172	1.11	0.7089	0.0282	0.08819	0.00318	0.91	545	19
46190213a	20	97	186	0.52	0.8297	0.0323	0.09974	0.00360	0.93	613	21
47190213a	143	251	608	0.41	3.0794	0.1128	0.21706	0.00777	0.98	1266	41
48190213a	5.1	320	301	1.07	0.1013	0.0073	0.01326	0.00051	0.54	84.9	3.2
49190213a	6.3	50	62	0.81	0.6872	0.0315	0.08593	0.00312	0.79	531	19
50190213a	18	39	93	0.42	1.8320	0.0773	0.17746	0.00645	0.86	1053	35
51190213a	38	269	895	0.30	0.3031	0.0115	0.04241	0.00153	0.95	268	9
52190213a	5.7	349	364	0.96	0.0827	0.0041	0.01267	0.00045	0.71	81.2	2.9
55190213a	7.6	118	44	2.71	0.8117	0.0402	0.09698	0.00357	0.74	597	21
57190213a	12	41	95	0.43	1.0754	0.0434	0.12276	0.00441	0.89	746	25
58190213a	8.4	27	48	0.57	1.5303	0.0656	0.15708	0.00570	0.85	941	32
59190213a	47	334	3645	0.09	0.0949	0.0039	0.01383	0.00051	0.89	88.5	3.2
60190213a	27	219	247	0.89	0.7548	0.0293	0.09209	0.00330	0.92	568	19

Sample 1M20: Conglomerate						2 sigma error		2 sigma error		Age (Ma)	2 sigma error
Analysis_#	Pb ppm	Th ppm	U ppm	Th/U	Pb207/U235	Pb207/U235	Pb206/U238	Pb206/U238	Rho	Pb206/U238	Pb206/U238
61190213a	4.9	291	323	0.90	0.0813	0.0043	0.01253	0.00045	0.68	80.3	2.9
62190213a	13	71	112	0.63	0.8748	0.0358	0.10272	0.00369	0.88	630	22
05200213a	4.2	336	278	1.21	0.0831	0.0042	0.01240	0.00045	0.71	79.4	2.9
06200213a	10	76	91	0.83	0.8389	0.0338	0.09972	0.00354	0.88	613	21
07200213a	2.5	158	176	0.89	0.0820	0.0047	0.01249	0.00045	0.62	80.0	2.9
08200213a	197	388	652	0.59	4.0027	0.1418	0.27551	0.00969	0.99	1569	49
09200213a	27	80	1985	0.04	0.0987	0.0037	0.01487	0.00051	0.91	95.2	3.3
10200213a	19	43	107	0.40	1.6844	0.0636	0.16770	0.00591	0.93	999	33
11200213a	4.2	254	275	0.92	0.0827	0.0045	0.01250	0.00045	0.67	80.1	2.9
12200213a	5.9	22	67	0.32	0.6961	0.0311	0.08320	0.00297	0.80	515	18
15200213a	44	119	502	0.24	0.7177	0.0260	0.08817	0.00309	0.97	545	18
16200213a	13	45	126	0.35	0.8638	0.0340	0.10309	0.00363	0.90	633	21
17200213a	12	43	135	0.32	0.7351	0.0291	0.08950	0.00315	0.89	553	19
18200213a	53	74	115	0.65	7.2603	0.2581	0.39438	0.01383	0.99	2143	64
19200213a	3.0	168	209	0.80	0.0779	0.0059	0.01237	0.00048	0.51	79.2	3.0
20200213a	20	232	252	0.92	0.5029	0.0196	0.06465	0.00228	0.90	404	14
21200213a	58	79	208	0.38	3.4595	0.1236	0.26369	0.00921	0.98	1509	47
22200213a	13	71	148	0.48	0.6742	0.0266	0.08439	0.00297	0.89	522	18
25200213a	16	76	183	0.41	0.6807	0.0263	0.08573	0.00300	0.91	530	18
26200213a	14	65	141	0.46	0.7735	0.0302	0.09323	0.00327	0.90	575	19
27200213a	82	69	163	0.43	9.9089	0.3492	0.44842	0.01563	0.99	2388	70
28200213a	20	68	171	0.40	0.9376	0.0357	0.11141	0.00390	0.92	681	23
29200213a	20	52	1500	0.03	0.0992	0.0038	0.01486	0.00051	0.90	95.1	3.3
30200213a	16	373	310	1.20	0.2875	0.0112	0.04027	0.00141	0.90	255	9
31200213a	3.2	153	232	0.66	0.0797	0.0044	0.01239	0.00045	0.66	79.4	2.8
32200213a	50	47	198	0.24	3.0820	0.1106	0.24862	0.00864	0.97	1431	45
35200213a	20	57	190	0.30	0.8748	0.0329	0.10426	0.00363	0.93	639	21

Sample 1M20: Conglomerate						2 sigma error		2 sigma error		Age (Ma)	2 sigma error
Analysis_#	Pb ppm	Th ppm	U ppm	Th/U	Pb207/U235	Pb207/U235	Pb206/U238	Pb206/U238	Rho	Pb206/U238	Pb206/U238
36200213a	1.7	5	16	0.30	0.7369	0.0506	0.08810	0.00333	0.55	544	20
37200213a	2.9	147	191	0.77	0.0807	0.0057	0.01265	0.00048	0.54	81.0	3.0
38200213a	16	27	88	0.30	1.7424	0.0677	0.17225	0.00600	0.90	1025	33
39200213a	107	99	282	0.35	5.9896	0.2105	0.35594	0.01230	0.98	1963	59
40200213a	13	21	70	0.30	1.8788	0.0726	0.18160	0.00633	0.90	1076	35
41200213a	12	70	137	0.51	0.6403	0.0258	0.08066	0.00282	0.87	500	17
42200213a	50	54	254	0.21	2.1188	0.0769	0.19700	0.00681	0.95	1159	37
45200213a	14	1097	807	1.36	0.0839	0.0035	0.01272	0.00045	0.85	81.5	2.8
46200213a	41	524	860	0.61	0.3129	0.0115	0.04373	0.00150	0.93	276	9
47200213a	3.2	11	30	0.37	0.8509	0.0452	0.10241	0.00366	0.67	629	21
48200213a	2.0	79	45	1.75	0.2221	0.0154	0.03097	0.00114	0.53	197	7
49200213a	35	63	200	0.31	1.7396	0.0632	0.17163	0.00591	0.95	1021	33
50200213a	8.3	52	78	0.67	0.8148	0.0346	0.09786	0.00342	0.82	602	20
51200213a	4.5	10	24	0.42	1.7102	0.0818	0.16870	0.00600	0.74	1005	33
52200213a	108	162	533	0.30	2.1582	0.0770	0.20004	0.00687	0.96	1176	37
55200213a	102	262	1547	0.17	0.5639	0.0201	0.06785	0.00234	0.97	423	14
56200213a	23	112	265	0.42	0.6676	0.0252	0.08296	0.00285	0.91	514	17
57200213a	25	114	239	0.48	0.8405	0.0314	0.10059	0.00345	0.92	618	20
58200213a	13	38	43	0.88	3.3650	0.1297	0.26100	0.00903	0.90	1495	46
59200213a	25	90	238	0.38	0.8637	0.0323	0.10269	0.00354	0.92	630	21
60200213a	4.5	20	110	0.18	0.3133	0.0152	0.04274	0.00150	0.72	270	9
61200213a	44	58	190	0.31	2.6896	0.0975	0.22508	0.00771	0.95	1309	41
62200213a	38	298	159	1.87	1.6749	0.0617	0.16562	0.00567	0.93	988	31
65200213a	45	93	263	0.35	1.7188	0.0622	0.16884	0.00576	0.94	1006	32
66200213a	14	290	217	1.33	0.3789	0.0158	0.05169	0.00177	0.82	325	11
67200213a	55	63	592	0.11	0.8100	0.0292	0.09733	0.00333	0.95	599	20
68200213a	45	49	106	0.46	6.7058	0.2400	0.37391	0.01275	0.95	2048	60

Sample 1M20: Conglomerate						2 sigma error		2 sigma error		Age (Ma)	2 sigma error
Analysis_#	Pb ppm	Th ppm	U ppm	Th/U	Pb207/U235	Pb207/U235	Pb206/U238	Pb206/U238	Rho	Pb206/U238	Pb206/U238
05200213b	47	66	144	0.46	4.1666	0.1580	0.29468	0.01107	0.99	1665	55
06200213b	8.0	66	67	0.97	0.7899	0.0363	0.09607	0.00366	0.83	591	22
07200213b	38	67	312	0.21	1.0791	0.0414	0.12139	0.00456	0.98	739	26
08200213b	43	78	174	0.45	2.9626	0.1182	0.22633	0.00855	0.95	1315	45
09200213b	41	76	101	0.75	5.5617	0.2121	0.33799	0.01272	0.99	1877	61
10200213b	58	33	391	0.08	1.4929	0.0569	0.15483	0.00582	0.99	928	32
11200213b	19	186	59	3.17	1.7998	0.0737	0.17549	0.00663	0.92	1042	36
15200213b	13	265	250	1.06	0.2959	0.0125	0.04099	0.00156	0.90	259	10
16200213b	18	43	71	0.60	2.6954	0.1065	0.22837	0.00864	0.96	1326	45
17200213b	16	29	144	0.20	0.9650	0.0397	0.11278	0.00426	0.92	689	25
18200213b	48	56	126	0.45	5.5720	0.2145	0.34415	0.01299	0.98	1907	62
19200213b	3.9	13	24	0.55	1.4810	0.0751	0.14994	0.00582	0.77	901	33
20200213b	12	49	62	0.79	1.6847	0.0717	0.16915	0.00645	0.90	1007	35
21200213b	8.0	25	55	0.45	1.2169	0.0529	0.13391	0.00510	0.88	810	29
22200213b	8.2	21	190	0.11	0.3428	0.0153	0.04522	0.00171	0.85	285	11
25200213b	8.6	145	46	3.16	0.8230	0.0390	0.09833	0.00378	0.81	605	22
26200213b	6.7	12	51	0.24	1.2147	0.0556	0.13158	0.00504	0.84	797	29
27200213b	15	19	86	0.22	1.7410	0.0851	0.17170	0.00666	0.79	1022	37
28200213b	28	185	252	0.74	0.8277	0.0332	0.09851	0.00372	0.94	606	22
29200213b	24	87	172	0.51	1.1353	0.0451	0.12709	0.00480	0.95	771	28
30200213b	14	35	61	0.57	2.2999	0.0951	0.20760	0.00792	0.92	1216	42
31200213b	18	39	99	0.40	1.7072	0.0685	0.16917	0.00642	0.95	1008	35
32200213b	24	37	145	0.25	1.5633	0.0619	0.15911	0.00603	0.96	952	34
35200213b	18	100	84	1.19	1.6061	0.0701	0.16135	0.00618	0.88	964	34
36200213b	39	51	115	0.45	4.4992	0.1749	0.30719	0.01164	0.97	1727	57
37200213b	11	44	56	0.79	1.5872	0.0668	0.16101	0.00615	0.91	962	34
38200213b	107	95	465	0.21	2.7851	0.1071	0.22511	0.00852	0.98	1309	45

Sample 1M20: Conglomerate						2 sigma error		2 sigma error		Age (Ma)	2 sigma error
Analysis_#	**Pb ppm**	**Th ppm**	**U ppm**	**Th/U**	**Pb207/U235**	**Pb207/U235**	**Pb206/U238**	**Pb206/U238**	**Rho**	**Pb206/U238**	**Pb206/U238**
39200213b	84	394	659	0.60	1.0099	0.0391	0.11645	0.00441	0.98	710	26
40200213b	62	70	147	0.48	6.7531	0.2606	0.38109	0.01446	0.98	2081	68
41200213b	15	329	304	1.08	0.2760	0.0116	0.03854	0.00147	0.90	244	9
42200213b	60	93	304	0.31	2.1605	0.0840	0.19251	0.00732	0.98	1135	40
45200213b	2.8	168	190	0.88	0.0792	0.0048	0.01240	0.00048	0.63	79.4	3.1
46200213b	64	152	130	1.17	6.7161	0.2611	0.38025	0.01446	0.98	2077	68
47200213b	107	394	1082	0.36	0.8990	0.0358	0.09624	0.00366	0.96	592	22
48200213b	68	117.89	943.04	0.13	0.6200	0.0255	0.07599	0.00291	0.93	472	17
49200213b	45	60.15	105.95	0.57	6.5955	0.2580	0.37322	0.01422	0.97	2045	67
50200213b	185	606.58	626.22	0.97	3.0912	0.1201	0.23855	0.00906	0.98	1379	47

1M28

Sample 1M28 Analysis_#	Pb ppm	Th ppm	U ppm	Th/U	Pb207/U235	2 sigma error Pb207/U235	Pb206/U238	2 sigma error Pb206/U238	Rho	Age (Ma) Pb206/U238	2 sigma error Pb206/U238
05050413d	23	4	149	0.03	1.7269	0.0662	0.16710	0.00612	0.96	996.1	33.7
06050413d	8.0	126	412	0.31	0.1321	0.0062	0.01949	0.00072	0.79	124.4	4.6
07050413d	73	110	197	0.56	5.2588	0.1959	0.33399	0.01221	0.98	1857.7	59.0
08050413d	5.7	93	384	0.24	0.1003	0.0062	0.01519	0.00057	0.61	97.2	3.7
09050413d	12	227	538	0.42	0.1460	0.0065	0.02192	0.00081	0.83	139.8	5.1
10050413d	6.4	81	344	0.24	0.1294	0.0064	0.01914	0.00072	0.76	122.2	4.5
11050413d	14	294	667	0.44	0.1405	0.0060	0.02074	0.00078	0.88	132.3	4.8
12050413d	7.1	214	418	0.51	0.1047	0.0054	0.01590	0.00060	0.73	101.7	3.8
15050413d	19	317	1269	0.25	0.1133	0.0047	0.01506	0.00057	0.92	96.3	3.5
16050413d	269	140	390	0.36	19.7664	0.7355	0.59303	0.02187	0.99	3001.7	88.5
17050413d	9.3	135	371	0.36	0.1712	0.0078	0.02478	0.00093	0.82	157.8	5.8
18050413d	8.2	285	473	0.60	0.1230	0.0063	0.01566	0.00060	0.74	100.1	3.8
19050413d	14	287	711	0.40	0.1310	0.0057	0.01910	0.00072	0.87	122.0	4.5
20050413d	115	114	530	0.21	2.5593	0.0969	0.21649	0.00801	0.98	1263.3	42.5
21050413d	10	360	579	0.62	0.1028	0.0048	0.01549	0.00057	0.79	99.1	3.7
22050413d	23	789	1284	0.61	0.1072	0.0045	0.01597	0.00060	0.90	102.1	3.8
25050413d	11	63	41	1.56	2.2075	0.1053	0.20099	0.00768	0.80	1180.6	41.3
26050413d	4.0	65	276	0.24	0.1057	0.0058	0.01475	0.00057	0.71	94.4	3.6
27050413d	10	319	594	0.54	0.1067	0.0050	0.01610	0.00060	0.79	103.0	3.9
28050413d	0.9	22	48	0.46	0.1190	0.0140	0.01695	0.00072	0.36	108.3	4.6
29050413d	6.0	81	315	0.26	0.1316	0.0070	0.01928	0.00075	0.74	123.1	4.7
30050413d	5.3	202	289	0.70	0.1101	0.0062	0.01628	0.00063	0.68	104.1	4.0
31050413d	2.7	99	143	0.69	0.1258	0.0089	0.01672	0.00066	0.56	106.9	4.2
32050413d	13	268	899	0.30	0.1005	0.0046	0.01482	0.00057	0.84	94.8	3.6
05080413a	27	456	1243	0.37	0.1424	0.0056	0.02109	0.00078	0.93	134.5	4.9

Sample 1M28						2 sigma error		2 sigma error		Age (Ma)	2 sigma error
Analysis_#	Pb ppm	Th ppm	U ppm	Th/U	Pb207/U235	Pb207/U235	Pb206/U238	Pb206/U238	Rho	Pb206/U238	Pb206/U238
06080413a	4.9	67	247	0.27	0.1413	0.0074	0.02020	0.00075	0.71	128.9	4.7
07080413a	11.2	353	637	0.56	0.1137	0.0060	0.01626	0.00060	0.70	104.0	3.9
09080413a	5.3	57	275	0.21	0.1350	0.0069	0.01993	0.00075	0.74	127.2	4.7
10080413a	2.4	43	47	0.92	0.3404	0.0244	0.04314	0.00165	0.53	272.3	10.3
11080413a	8.1	284	305	0.93	0.1505	0.0072	0.02200	0.00081	0.77	140.3	5.1
12080413a	30	1995	1308	1.53	0.1106	0.0044	0.01642	0.00060	0.92	105.0	3.8
15080413a	14	32	157	0.21	0.7432	0.0301	0.09127	0.00333	0.90	563.1	19.7
16080413a	14	701	665	1.05	0.1143	0.0050	0.01694	0.00063	0.85	108.3	3.9
17080413a	54	23	181	0.13	4.4448	0.1653	0.29658	0.01083	0.98	1674.3	53.8
18080413a	41	88	104	0.85	5.1524	0.1981	0.33042	0.01212	0.95	1840.4	58.7
19080413a	8.6	164	426	0.38	0.1361	0.0063	0.01948	0.00072	0.80	124.4	4.5
20080413a	27	979	1474	0.66	0.1100	0.0044	0.01646	0.00060	0.92	105.2	3.8
21080413a	4.9	179	274	0.65	0.1097	0.0060	0.01581	0.00060	0.69	101.1	3.8
22080413a	16	620	859	0.72	0.1167	0.0049	0.01614	0.00060	0.89	103.2	3.8
25080413a	12	146	497	0.29	0.1632	0.0090	0.02340	0.00087	0.67	149.1	5.5
26080413a	4.2	104	241	0.43	0.1136	0.0079	0.01668	0.00063	0.54	106.7	4.1
27080413a	3.4	0	26	0.00	0.7410	0.0516	0.08734	0.00339	0.56	539.8	20.0
29080413a	5.2	186	299	0.62	0.1054	0.0059	0.01594	0.00060	0.68	101.9	3.8
30080413a	6.7	93	333	0.28	0.1359	0.0065	0.02016	0.00075	0.78	128.7	4.7
31080413a	2.7	66	157	0.42	0.1151	0.0077	0.01624	0.00060	0.55	103.8	3.9
32080413a	4.9	57	252	0.23	0.1369	0.0072	0.02004	0.00075	0.71	127.9	4.7
35080413a	4.3	98	255	0.39	0.1148	0.0063	0.01643	0.00060	0.67	105.1	3.9
36080413a	16	36	62	0.58	2.8361	0.1208	0.23465	0.00867	0.87	1358.8	45.2
37080413a	13	332	631	0.53	0.1349	0.0058	0.02010	0.00072	0.84	128.3	4.7
38080413a	13	499	691	0.72	0.1113	0.0048	0.01641	0.00060	0.84	105.0	3.8
39080413a	5.0	214	250	0.86	0.1115	0.0063	0.01699	0.00063	0.66	108.6	4.0
40080413a	13	236	597	0.40	0.1451	0.0062	0.02161	0.00078	0.84	137.8	5.0

Sample 1M28						2 sigma error		2 sigma error		Age (Ma)	2 sigma error
Analysis_#	Pb ppm	Th ppm	U ppm	Th/U	Pb207/U235	Pb207/U235	Pb206/U238	Pb206/U238	Rho	Pb206/U238	Pb206/U238
41080413a	10	391	560	0.70	0.1062	0.0048	0.01577	0.00057	0.80	100.9	3.7
42080413a	12	256	554	0.46	0.1390	0.0060	0.02015	0.00075	0.86	128.6	4.7
45080413a	24	1193	1175	1.01	0.1112	0.0045	0.01644	0.00060	0.90	105.1	3.8
46080413a	4.6	128	268	0.48	0.1010	0.0063	0.01629	0.00060	0.59	104.2	3.8
47080413a	13	631	687	0.92	0.1100	0.0049	0.01625	0.00060	0.84	103.9	3.8
48080413a	11	167	524	0.32	0.1441	0.0063	0.02138	0.00078	0.84	136.4	4.9
49080413a	20	206	475	0.43	0.2821	0.0116	0.03986	0.00144	0.88	251.9	9.0
50080413a	3.2	38	169	0.22	0.1403	0.0116	0.01886	0.00075	0.48	120.5	4.7
52080413a	9.4	163	452	0.36	0.1431	0.0066	0.01997	0.00072	0.79	127.4	4.6
55080413a	7.8	223	248	0.90	0.2100	0.0103	0.02568	0.00096	0.76	163.5	6.0
56080413a	51	89	140	0.64	4.8858	0.1846	0.31922	0.01158	0.96	1785.9	56.6
57080413a	88	59	218	0.27	6.8773	0.2563	0.38408	0.01392	0.97	2095.3	64.8
59080413a	8.4	112	428	0.26	0.1311	0.0062	0.01984	0.00072	0.77	126.7	4.6
60080413a	8.1	71	416	0.17	0.1358	0.0064	0.02023	0.00075	0.79	129.1	4.7
61080413a	7.9	130	394	0.33	0.1324	0.0063	0.01981	0.00072	0.76	126.5	4.6
62080413a	14	288	694	0.41	0.1342	0.0058	0.01937	0.00072	0.86	123.6	4.5
65080413a	87	35	322	0.11	3.8152	0.1442	0.27613	0.00999	0.96	1571.8	50.5
66080413a	7.5	113	379	0.30	0.1339	0.0065	0.01978	0.00072	0.76	126.3	4.6
67080413a	14	482	756	0.64	0.1257	0.0079	0.01595	0.00060	0.60	102.0	3.8
68080413a	19	144	940	0.15	0.1417	0.0059	0.02085	0.00075	0.87	133.0	4.8
69080413a	7.5	117	381	0.31	0.1332	0.0065	0.01981	0.00072	0.75	126.5	4.6
70080413a	9.9	168	477	0.35	0.1388	0.0064	0.02022	0.00075	0.81	129.0	4.7
71080413a	9.2	161	453	0.36	0.1344	0.0062	0.02007	0.00072	0.77	128.1	4.7
72080413a	4.2	148	238	0.62	0.1103	0.0065	0.01637	0.00060	0.63	104.7	3.9
75080413a	78	5219	3686	1.42	0.1165	0.0046	0.01598	0.00057	0.91	102.2	3.7
76080413a	7.3	351	401	0.88	0.1054	0.0053	0.01567	0.00057	0.72	100.2	3.7

1M29

Sample 1M29 Analysis_#	Pb ppm	Th ppm	U ppm	Th/U	Pb207/U235	2 sigma error Pb207/U235	Pb206/U238	2 sigma error Pb206/U238	Rho	Age (Ma) Pb206/U238	2 sigma error Pb206/U238
05080413b	35	123	244	0.50	1.315	0.053	0.1336	0.0049	0.91	808.6	28.0
06080413b	29	108	67	1.61	4.706	0.180	0.3141	0.0116	0.96	1760.8	56.6
07080413b	34	53	62	0.85	10.020	0.377	0.4469	0.0164	0.98	2381.6	73.2
08080413b	6.6	130	312	0.42	0.140	0.007	0.0206	0.0008	0.75	131.2	4.8
09080413b	8.7	99	538	0.18	0.134	0.006	0.0163	0.0006	0.81	104.4	3.8
10080413b	23	91	226	0.40	0.822	0.032	0.0992	0.0036	0.95	609.8	21.3
11080413b	6.5	222	392	0.57	0.107	0.005	0.0157	0.0006	0.76	100.3	3.7
12080413b	160	323	749	0.43	2.304	0.085	0.2039	0.0074	0.99	1196.1	39.9
15080413b	8.8	406	460	0.88	0.136	0.006	0.0162	0.0006	0.81	103.9	3.8
16080413b	3.7	73	219	0.33	0.112	0.007	0.0168	0.0006	0.64	107.6	4.0
17080413b	5.1	49	38	1.31	0.974	0.050	0.1088	0.0041	0.72	665.7	23.8
18080413b	4.9	153	280	0.55	0.109	0.006	0.0166	0.0006	0.72	106.3	3.9
19080413b	47	102	494	0.21	0.803	0.030	0.0976	0.0036	0.98	600.5	20.9
20080413b	9.4	367	543	0.68	0.104	0.005	0.0157	0.0006	0.81	100.5	3.7
21080413b	194	661	467	1.42	4.795	0.174	0.3130	0.0114	0.99	1755.4	56.1
22080413b	8.7	73	89	0.81	0.685	0.031	0.0847	0.0032	0.83	524.4	18.7
25080413b	57	46	309	0.15	2.055	0.076	0.1906	0.0070	0.99	1124.4	37.7
26080413b	24	70	273	0.26	0.722	0.029	0.0896	0.0033	0.91	553.2	19.5
27080413b	27	39	139	0.28	2.037	0.078	0.1917	0.0070	0.95	1130.8	38.0
28080413b	6.6	40	58	0.69	0.861	0.044	0.1030	0.0039	0.73	631.9	22.6
29080413b	5.9	276	338	0.82	0.104	0.005	0.0157	0.0006	0.72	100.1	3.7
30080413b	5.2	106	311	0.34	0.113	0.006	0.0168	0.0006	0.71	107.4	4.0
31080413b	46	67	131	0.51	4.958	0.190	0.3238	0.0119	0.96	1808.4	58.0

Sample 1M29 Analysis_#	Pb ppm	Th ppm	U ppm	Th/U	Pb207/U235	2 sigma error Pb207/U235	Pb206/U238	2 sigma error Pb206/U238	Rho	Age (Ma) Pb206/U238	2 sigma error Pb206/U238
32080413b	70	21	181	0.12	6.971	0.258	0.3856	0.0141	0.99	2102.6	65.7
35080413b	25	52	72	0.72	4.518	0.177	0.3070	0.0113	0.94	1726.0	55.8
36080413b	11	479	541	0.89	0.209	0.009	0.0165	0.0006	0.87	105.3	3.9
37080413b	23	121	269	0.45	0.688	0.028	0.0803	0.0029	0.92	497.9	17.6
38080413b	19	39	70	0.56	3.161	0.125	0.2513	0.0093	0.94	1445.3	47.7
39080413b	78	93	191	0.48	6.395	0.240	0.3717	0.0137	0.98	2037.5	64.1
40080413b	15	106	160	0.66	0.667	0.030	0.0840	0.0031	0.82	519.9	18.5
41080413b	4.1	184	202	0.91	0.112	0.007	0.0168	0.0006	0.63	107.3	4.0
42080413b	22	46	101	0.46	2.376	0.093	0.2057	0.0076	0.94	1205.9	40.4
45080413b	53	2657	2779	0.96	0.106	0.004	0.0160	0.0006	0.97	102.2	3.7
46080413b	42	120	286	0.42	1.336	0.051	0.1387	0.0051	0.96	837.3	28.8
47080413b	11	434	625	0.69	0.110	0.005	0.0157	0.0006	0.80	100.6	3.7
48080413b	20	49	110	0.45	1.764	0.070	0.1730	0.0064	0.93	1028.5	35.0
49080413b	84	89	203	0.44	6.557	0.242	0.3756	0.0137	0.99	2055.6	64.4
50080413b	72	115	342	0.34	2.255	0.084	0.2028	0.0074	0.98	1190.2	39.8
51080413b	5.5	61	340	0.18	0.113	0.006	0.0167	0.0006	0.74	107.0	4.0
52080413b	5.5	54	353	0.15	0.108	0.006	0.0163	0.0006	0.66	104.4	3.9
55080413b	14	249	898	0.28	0.106	0.005	0.0157	0.0006	0.85	100.7	3.7
56080413b	7.8	40	78	0.51	0.754	0.036	0.0929	0.0035	0.78	572.9	20.4
57080413b	7.9	45	67	0.67	0.893	0.041	0.1044	0.0039	0.80	640.1	22.7
58080413b	14	40	98	0.41	1.207	0.051	0.1322	0.0049	0.88	800.5	27.8
59080413b	3.7	0.2	48	0.004	0.631	0.046	0.0834	0.0033	0.54	516.3	19.6
60080413b	9.5	428	510	0.84	0.104	0.005	0.0159	0.0006	0.78	101.5	3.8
61080413b	48	89	144	0.62	4.532	0.174	0.2982	0.0110	0.96	1682.2	54.5
62080413b	29	35	138	0.25	2.351	0.093	0.2090	0.0077	0.93	1223.4	41.1
65080413b	141	133	241	0.55	12.154	0.451	0.4971	0.0182	0.99	2601.1	78.4
66080413b	82	89	83	1.08	28.199	1.049	0.7003	0.0257	0.99	3421.6	97.4

Sample 1M29 Analysis_#	Pb ppm	Th ppm	U ppm	Th/U	Pb207/U235	2 sigma error Pb207/U235	Pb206/U238	2 sigma error Pb206/U238	Rho	Age (Ma) Pb206/U238	2 sigma error Pb206/U238
67080413b	68	89	167	0.53	6.060	0.230	0.3601	0.0132	0.97	1982.5	62.7
68080413b	68	72	251	0.29	3.374	0.127	0.2621	0.0096	0.97	1500.6	49.1
69080413b	3.6	67	211	0.32	0.116	0.007	0.0165	0.0006	0.64	105.3	4.0
70080413b	6.6	182	389	0.47	0.106	0.006	0.0160	0.0006	0.69	102.3	3.8
71080413b	1.8	23	75	0.30	0.172	0.017	0.0239	0.0010	0.42	152.2	6.3
72080413b	41	100	142	0.70	3.982	0.154	0.2397	0.0088	0.95	1385.0	45.9
75080413b	1.6	10	35	0.28	0.345	0.028	0.0467	0.0018	0.48	294.3	11.4
76080413b	6.2	77	311	0.25	0.132	0.007	0.0201	0.0008	0.74	128.0	4.7
77080413b	13	52	148	0.35	0.724	0.031	0.0881	0.0033	0.87	544.6	19.3
78080413b	9.4	50	557	0.09	0.130	0.006	0.0178	0.0007	0.83	113.5	4.2
79080413b	16	30	90	0.33	1.826	0.074	0.1759	0.0065	0.91	1044.6	35.6
80080413b	5.3	126	309	0.41	0.112	0.006	0.0165	0.0006	0.73	105.4	3.9
81080413b	5.3	208	286	0.73	0.109	0.006	0.0160	0.0006	0.68	102.2	3.8
82080413b	62	225	166	1.36	3.642	0.139	0.2719	0.0100	0.96	1550.4	50.6
85080413b	6.3	73	366	0.20	0.117	0.006	0.0177	0.0007	0.74	113.2	4.2
86080413b	206	117	304	0.39	17.638	0.664	0.5837	0.0214	0.98	2963.7	87.2
87080413b	173	118	250	0.47	18.667	0.708	0.5888	0.0217	0.97	2984.6	87.9
88080413b	47	47	198	0.24	2.804	0.109	0.2338	0.0086	0.95	1354.5	44.9
89080413b	83	61	145	0.42	12.213	0.463	0.5010	0.0184	0.97	2617.9	79.1
90080413b	48	94	102	0.92	6.444	0.253	0.3706	0.0137	0.94	2032.1	64.4
91080413b	8.8	40	40	0.99	1.807	0.086	0.1772	0.0067	0.79	1051.6	36.5
92080413b	18	35	68	0.51	2.984	0.128	0.2430	0.0091	0.87	1402.4	47.0
95080413b	4.7	184	246	0.75	0.109	0.006	0.0165	0.0006	0.67	105.4	4.0
96080413b	18	47	67	0.71	2.697	0.126	0.2266	0.0086	0.81	1316.5	44.9
97080413b	3.9	70	242	0.29	0.113	0.007	0.0163	0.0006	0.66	104.5	3.9
98080413b	55	309	568	0.54	0.721	0.029	0.0883	0.0033	0.91	545.6	19.3
05090413a	58	103	129	0.80	6.494	0.231	0.3731	0.0132	0.99	2044.1	62.1

Sample 1M29 Analysis_#	Pb ppm	Th ppm	U ppm	Th/U	Pb207/U235	2 sigma error Pb207/U235	Pb206/U238	2 sigma error Pb206/U238	Rho	Age (Ma) Pb206/U238	2 sigma error Pb206/U238
06090413a	19	448	1135	0.39	0.116	0.005	0.0159	0.0006	0.91	101.5	3.6
07090413a	10	138	472	0.29	0.145	0.007	0.0210	0.0008	0.79	134.1	4.8
08090413a	36	121	326	0.37	0.899	0.033	0.1062	0.0038	0.97	650.7	22.0
09090413a	38	267	144	1.86	1.794	0.067	0.1751	0.0062	0.96	1039.9	34.1
10090413a	79	114	381	0.30	2.269	0.082	0.2012	0.0071	0.99	1181.9	38.3
11090413a	26	64	142	0.45	1.774	0.066	0.1742	0.0062	0.96	1035.1	34.0
12090413a	37	92	195	0.47	1.823	0.067	0.1766	0.0063	0.97	1048.5	34.4
15090413a	30	76	133	0.57	2.211	0.082	0.2018	0.0072	0.96	1185.1	38.5
16090413a	8.6	44	38	1.16	1.831	0.079	0.1784	0.0065	0.84	1058.2	35.2
17090413a	14	128	137	0.93	0.684	0.028	0.0853	0.0031	0.88	527.8	18.1
18090413a	5.2	69	266	0.26	0.136	0.007	0.0194	0.0007	0.70	124.1	4.5
20090413a	7.3	106	381	0.28	0.128	0.006	0.0192	0.0007	0.76	122.6	4.4
21090413a	97	72	154	0.47	14.555	0.517	0.5363	0.0191	1.00	2768.1	79.9
22090413a	6.1	32	387	0.08	0.114	0.005	0.0170	0.0006	0.76	108.5	3.9
25090413a	33	165	220	0.75	1.277	0.052	0.1310	0.0047	0.88	793.4	26.8
26090413a	3.7	40	228	0.18	0.112	0.009	0.0168	0.0007	0.47	107.2	4.1

1M30

Sample 1M30 Analysis_#	Pb ppm	Th ppm	U ppm	Th/U	Pb207/U235	2 sigma error Pb207/U235	Pb206/U238	2 sigma error Pb206/U238	Rho	Age (Ma) Pb206/U238	2 sigma error Pb206/U238
45090413a	35	69	79	0.87	6.0512	0.2245	0.3605	0.0129	0.96	1985	61
46090413a	28	115	137	0.84	1.7806	0.0689	0.1747	0.0063	0.93	1038	34
47090413a	16	57	65	0.87	2.2648	0.0924	0.2053	0.0074	0.88	1204	40
48090413a	25	48	121	0.40	2.1014	0.0806	0.1957	0.0070	0.94	1152	38
49090413a	4.8	7	49	0.15	0.8734	0.0438	0.1014	0.0037	0.73	623	22
50090413a	29	36	133	0.27	2.3826	0.0908	0.2117	0.0076	0.94	1238	40
51090413a	57	16	577	0.03	0.8988	0.0335	0.1066	0.0038	0.96	653	22
52090413a	16	30	69	0.44	2.3743	0.0949	0.2104	0.0076	0.90	1231	40
55090413a	21	144	124	1.17	1.1764	0.0525	0.1303	0.0047	0.82	789	27
56090413a	17	38	78	0.50	2.2715	0.0938	0.2048	0.0074	0.88	1201	40
57090413a	30	27	184	0.15	1.6493	0.0632	0.1656	0.0059	0.94	988	33
58090413a	48	300	457	0.66	0.7527	0.0287	0.0925	0.0033	0.94	570	20
59090413a	232	62	460	0.14	11.1041	0.4048	0.4811	0.0172	0.98	2532	75
60090413a	205	12	1422	0.01	1.6070	0.0591	0.1538	0.0055	0.97	922	31
61090413a	21	47	81	0.58	2.9123	0.1136	0.2391	0.0086	0.92	1382	45
62090413a	45	95	89	1.08	7.0923	0.2651	0.3996	0.0143	0.96	2167	66
65090413a	124	60	414	0.15	4.6583	0.1722	0.2996	0.0107	0.97	1690	53
66090413a	13	99	142	0.70	0.6319	0.0290	0.0800	0.0029	0.79	496	17
67090413a	5.8	28	65	0.44	0.6781	0.0332	0.0849	0.0031	0.75	526	18
68090413a	30	212	263	0.81	0.8300	0.0326	0.0999	0.0036	0.92	614	21
69090413a	8.2	19	30	0.64	2.9894	0.1280	0.2416	0.0088	0.85	1395	46
70090413a	113	274	415	0.66	3.2496	0.1273	0.2383	0.0086	0.92	1378	45
71090413a	15	137	128	1.07	0.7549	0.0321	0.0927	0.0034	0.85	571	20
72090413a	63	144	331	0.43	1.8424	0.0696	0.1794	0.0065	0.95	1064	35
06090413c	17	119	167	0.72	0.7265	0.0299	0.0897	0.0033	0.90	554	20

Sample 1M30 Analysis_#	Pb ppm	Th ppm	U ppm	Th/U	Pb207/U235	2 sigma error Pb207/U235	Pb206/U238	2 sigma error Pb206/U238	Rho	Age (Ma) Pb206/U238	2 sigma error Pb206/U238
07090413c	15	43	141	0.31	0.8956	0.0365	0.1064	0.0039	0.91	652	23
08090413c	35	55	174	0.32	2.1659	0.0907	0.1947	0.0073	0.89	1147	39
09090413c	37	53	211	0.25	1.7976	0.0692	0.1759	0.0065	0.96	1045	36
10090413c	15	42	58	0.72	2.6525	0.1076	0.2220	0.0083	0.92	1292	43
11090413c	35	49	174	0.28	2.1724	0.0831	0.1999	0.0074	0.96	1175	40
12090413c	52	42	194	0.22	3.5410	0.1323	0.2634	0.0097	0.98	1507	49
15090413c	48	60	170	0.35	3.5084	0.1319	0.2678	0.0098	0.98	1530	50
16090413c	13	38	44	0.87	0.7080	0.0608	0.0860	0.0035	0.48	532	21
17090413c	30	83	128	0.65	2.3100	0.0946	0.2055	0.0076	0.91	1205	41
18090413c	3.1	32	132	0.25	0.1574	0.0102	0.0235	0.0009	0.59	150	6
19090413c	35	95	115	0.82	3.3374	0.1270	0.2551	0.0094	0.97	1465	48
20090413c	182	302	398	0.76	6.6902	0.2468	0.3786	0.0139	0.99	2070	65
21090413c	15	27	53	0.50	3.3448	0.1325	0.2597	0.0096	0.93	1489	49
22090413c	3.1	17	28	0.60	0.8569	0.0567	0.1022	0.0040	0.59	627	23
25090413c	25	38	114	0.34	2.3439	0.0912	0.2087	0.0077	0.95	1222	41
26090413c	46	80	495	0.16	0.7809	0.0296	0.0946	0.0035	0.97	583	20
27090413c	26	34	104	0.33	2.8702	0.1111	0.2350	0.0086	0.95	1360	45
28090413c	22	74	121	0.61	1.6301	0.0637	0.1625	0.0060	0.94	971	33
29090413c	6.8	79	49	1.60	0.8006	0.0403	0.0960	0.0036	0.74	591	21
30090413c	50	113	218	0.52	2.3480	0.0892	0.2096	0.0077	0.96	1227	41
31090413c	173	45	284	0.16	15.8509	0.5887	0.5606	0.0205	0.99	2869	85
32090413c	39	43	186	0.23	2.3667	0.0909	0.2108	0.0077	0.96	1233	41
37090413c	47	28	75	0.37	16.3310	0.6166	0.5389	0.0198	0.97	2779	83
38090413c	12	23	62	0.37	1.7417	0.0743	0.1696	0.0063	0.87	1010	35
39090413c	143	137	271	0.50	10.9993	0.4127	0.4550	0.0167	0.98	2417	74
40090413c	104	152	693	0.22	1.4401	0.0547	0.1506	0.0055	0.97	904	31
42090413c	29	231	223	1.03	0.8828	0.0359	0.1053	0.0039	0.90	645	23

Sample 1M30 Analysis_#	Pb ppm	Th ppm	U ppm	Th/U	Pb207/U235	2 sigma error Pb207/U235	Pb206/U238	2 sigma error Pb206/U238	Rho	Age (Ma) Pb206/U238	2 sigma error Pb206/U238
05120413b	79	115	268	0.43	3.6600	0.1323	0.2720	0.0098	0.99	1551	50
06120413b	10	65	106	0.62	0.6906	0.0298	0.0860	0.0031	0.84	532	19
07120413b	6.1	28	54	0.53	0.8595	0.0401	0.1019	0.0037	0.78	626	22
08120413b	33	80	122	0.66	2.8650	0.1063	0.2369	0.0085	0.97	1371	44
09120413b	140	266	336	0.79	6.1382	0.2203	0.3411	0.0122	0.95	1892	59
10120413b	78	67	194	0.35	6.5204	0.2367	0.3723	0.0134	0.99	2040	63
11120413b	18	52	193	0.27	0.7345	0.0287	0.0907	0.0033	0.92	560	19
12120413b	165	208	284	0.73	10.7211	0.3833	0.4736	0.0170	0.95	2499	74
15120413b	10	60	49	1.24	1.5111	0.0659	0.1558	0.0057	0.84	933	32
16120413b	15	30	74	0.41	2.2070	0.0897	0.1987	0.0072	0.90	1168	39
17120413b	4.9	42	105	0.40	0.3176	0.0168	0.0448	0.0017	0.70	283	10
18120413b	91	69	207	0.34	7.6336	0.2751	0.4032	0.0145	0.95	2184	67
19120413b	29	50	148	0.34	2.0307	0.0765	0.1888	0.0068	0.96	1115	37
20120413b	8.4	98	350	0.28	0.1645	0.0077	0.0239	0.0009	0.77	152	5
21120413b	80	157	506	0.31	1.5445	0.0563	0.1535	0.0055	0.99	920	31
22120413b	7.9	0.1	103	0.001	0.6544	0.0290	0.0839	0.0031	0.82	520	18
25120413b	5.0	52	47	1.11	0.7007	0.0365	0.0841	0.0031	0.71	521	19
26120413b	26	44	115	0.38	2.3805	0.0901	0.2106	0.0076	0.95	1232	40
27120413b	19	1	235	0.01	0.7132	0.0275	0.0883	0.0032	0.94	545	19
28120413b	52	80	629	0.13	0.6907	0.0255	0.0864	0.0031	0.97	534	18
29120413b	134	192	222	0.86	11.0003	0.3963	0.4781	0.0172	0.95	2519	75
30120413b	18	45	106	0.43	1.6626	0.0699	0.1618	0.0059	0.86	967	33
31120413b	44	166	460	0.36	0.7566	0.0286	0.0922	0.0033	0.96	569	20
32120413b	442	424	2452	0.17	2.5506	0.0918	0.1815	0.0065	0.95	1075	35
35120413b	38	62	189	0.33	2.1215	0.0796	0.1950	0.0070	0.96	1148	38
36120413b	70	43	691	0.06	0.9201	0.0338	0.1073	0.0038	0.98	657	22
37120413b	134	220	286	0.77	7.0889	0.2569	0.3888	0.0140	0.99	2117	65

Sample 1M30 Analysis_#	Pb ppm	Th ppm	U ppm	Th/U	Pb207/U235	2 sigma error Pb207/U235	Pb206/U238	2 sigma error Pb206/U238	Rho	Age (Ma) Pb206/U238	2 sigma error Pb206/U238
38120413b	9.5	124	226	0.55	0.2869	0.0130	0.0387	0.0014	0.81	245	9
39120413b	13	46	46	0.98	2.5982	0.1084	0.2178	0.0080	0.88	1270	42
40120413b	85	78	122	0.64	16.5056	0.6005	0.5673	0.0204	0.99	2897	84
41120413b	15	23	51	0.46	3.5112	0.1378	0.2646	0.0096	0.92	1514	49
42120413b	74	103	111	0.93	13.2581	0.4842	0.5182	0.0186	0.98	2692	79
45120413b	49	65	122	0.53	6.0156	0.2256	0.3586	0.0129	0.96	1976	61
46120413b	3.5	65	138	0.47	0.1652	0.0100	0.0240	0.0009	0.62	153	6
47120413b	17	150	190	0.79	0.5877	0.0238	0.0748	0.0027	0.89	465	16
48120413b	43	69	374	0.19	1.0427	0.0391	0.1191	0.0043	0.96	725	25
49120413b	7.9	39	54	0.73	1.1602	0.0514	0.1291	0.0047	0.82	783	27
50120413b	53	66	203	0.33	3.1608	0.1183	0.2513	0.0090	0.96	1445	47
51120413b	52	75	431	0.17	1.1036	0.0413	0.1238	0.0044	0.96	752	26
52120413b	32	45	65	0.69	9.6128	0.3616	0.3902	0.0141	0.96	2124	65
55120413b	49	81	229	0.35	2.3090	0.0872	0.2074	0.0075	0.95	1215	40
56120413b	9.3	126	65	1.94	0.7784	0.0376	0.0945	0.0035	0.76	582	20
57120413b	40	124	271	0.46	1.3104	0.0509	0.1404	0.0051	0.93	847	29
58120413b	16	70	173	0.41	0.7124	0.0292	0.0880	0.0032	0.88	544	19
59120413b	15	87	99	0.88	1.1769	0.0495	0.1300	0.0047	0.86	788	27
60120413b	11	97	87	1.12	0.8276	0.0371	0.0988	0.0036	0.81	607	21
61120413b	21	182	153	1.19	0.8933	0.0421	0.1058	0.0039	0.78	648	23
62120413b	1.1	20	42	0.47	0.1772	0.0173	0.0250	0.0010	0.42	159	6
65120413b	49	76	230	0.33	2.2524	0.0861	0.2034	0.0073	0.94	1194	39
66120413b	213	39	373	0.11	14.9151	0.5576	0.5088	0.0183	0.96	2652	78
67120413b	1.3	46	90	0.51	0.0885	0.0089	0.0134	0.0005	0.40	86	3
68120413b	25	7	96	0.08	3.6027	0.1572	0.2705	0.0099	0.84	1543	50

1M31

Sample 1M31 Analysis_#	Pb ppm	Th ppm	U ppm	Th/U	Pb207/U235	2 sigma error Pb207/U235	Pb206/U238	2 sigma error Pb206/U238	Rho	Age (Ma) Pb206/U238	2 sigma error Pb206/U238
32300413a	34	78	124	0.63	2.9782	0.1110	0.24147	0.00840	0.93	1394	44
35300413a	39	57	181	0.31	2.2870	0.0847	0.20709	0.00720	0.94	1213	38
36300413a	93	138	443	0.31	2.2370	0.0805	0.20404	0.00705	0.96	1197	38
37300413a	130	110	224	0.49	12.0997	0.4275	0.49914	0.01728	0.98	2610	74
38300413a	74	92	169	0.55	6.8003	0.2443	0.38201	0.01323	0.96	2086	62
39300413a	206	253	333	0.76	12.1831	0.4311	0.49944	0.01728	0.98	2611	74
40300413a	100	83	590	0.14	1.7688	0.0634	0.17439	0.00603	0.96	1036	33
41300413a	34	61	92	0.66	4.7219	0.1764	0.31555	0.01098	0.93	1768	54
42300413a	190	157	519	0.30	5.7655	0.2040	0.34561	0.01191	0.97	1914	57
45300413a	62	84	96	0.87	12.7924	0.4605	0.50961	0.01764	0.96	2655	75
46300413a	33	159	86	1.85	3.2113	0.1244	0.25422	0.00885	0.90	1460	46
47300413a	42	144	427	0.34	0.7836	0.0295	0.09525	0.00330	0.92	587	19
48300413a	19	22	57	0.38	4.5273	0.1808	0.30735	0.01077	0.88	1728	53
49300413a	12	31	118	0.26	0.8657	0.0373	0.10265	0.00357	0.81	630	21
50300413a	33	25	79	0.31	7.0502	0.2619	0.38742	0.01344	0.93	2111	62
51300413a	7.5	48	61	0.79	0.8473	0.0525	0.10190	0.00372	0.59	626	22
52300413a	11.8	71	110	0.65	0.7662	0.0349	0.09338	0.00327	0.77	576	19
55300413a	37	43	176	0.24	2.3463	0.0884	0.20532	0.00708	0.92	1204	38
56300413a	19	86	148	0.59	0.9867	0.0410	0.11325	0.00393	0.83	692	23
57300413a	67	41	88	0.46	20.6047	0.7454	0.62260	0.02145	0.95	3120	85
58300413a	41	63	172	0.37	2.6236	0.0987	0.22257	0.00768	0.92	1295	41
59300413a	34	75	304	0.25	0.9452	0.0361	0.11036	0.00381	0.90	675	22
60300413a	12	94	108	0.87	0.7128	0.0325	0.08760	0.00306	0.77	541	18
61300413a	13	168	308	0.55	0.2830	0.0127	0.03928	0.00138	0.78	248	8
62300413a	24	116	110	1.06	1.7319	0.0698	0.17205	0.00597	0.86	1023	33

Sample 1M31 Analysis_#	Pb ppm	Th ppm	U ppm	Th/U	Pb207/U235	2 sigma error Pb207/U235	Pb206/U238	2 sigma error Pb206/U238	Rho	Age (Ma) Pb206/U238	2 sigma error Pb206/U238
05300413b	116	151	302	0.50	5.9732	0.2143	0.3434	0.0122	0.99	1903	59
06300413b	12	21	68	0.31	1.7730	0.0848	0.1742	0.0064	0.77	1035	35
07300413b	12	64	132	0.48	0.6930	0.0297	0.0861	0.0031	0.84	532	18
08300413b	18	186	151	1.24	0.7382	0.0307	0.0900	0.0032	0.87	556	19
09300413b	134	7.3	901	0.01	1.5980	0.0574	0.1618	0.0058	0.99	967	32
10300413b	40	58	158	0.36	3.0543	0.1127	0.2422	0.0086	0.97	1398	45
11300413b	34	36	85	0.42	6.2905	0.2312	0.3637	0.0130	0.97	2000	61
12300413b	40	40	267	0.15	1.4957	0.0554	0.1533	0.0055	0.96	919	30
15300413b	92	86	234	0.37	6.7164	0.2406	0.3673	0.0131	0.99	2017	61
16300413b	5.7	9.4	51	0.19	1.0115	0.0491	0.1157	0.0042	0.75	706	24
17300413b	160	253	267	0.95	10.6777	0.3802	0.4688	0.0166	0.97	2478	73
18300413b	35	77	64	1.20	7.9257	0.2909	0.4084	0.0146	0.97	2207	67
19300413b	58	26	311	0.08	2.0917	0.0761	0.1939	0.0069	0.97	1143	37
20300413b	31	147	271	0.54	0.8851	0.0337	0.1048	0.0037	0.93	642	22
21300413b	111	79	183	0.43	14.0660	0.5012	0.5191	0.0184	0.99	2695	78
22300413b	12	28	109	0.25	0.9502	0.0392	0.1108	0.0040	0.87	677	23
25300413b	10	30	99	0.30	0.8711	0.0383	0.1031	0.0037	0.81	633	22
26300413b	11	58	89	0.65	0.9325	0.0400	0.1093	0.0039	0.83	669	23
27300413b	5.4	15	30	0.49	1.6759	0.0839	0.1671	0.0061	0.73	996	34
28300413b	12	114	101	1.13	0.7546	0.0327	0.0922	0.0033	0.83	569	19
29300413b	26	57	105	0.54	2.5836	0.1009	0.2224	0.0079	0.91	1294	42
30300413b	40	62	112	0.55	4.6898	0.1725	0.3154	0.0112	0.96	1767	55
31300413b	176	515	542	0.95	3.3021	0.1184	0.2559	0.0090	0.98	1469	46
32300413b	53	70	163	0.43	4.2300	0.1548	0.2916	0.0103	0.97	1649	52
35300413b	4.2	28	43	0.64	0.7306	0.0686	0.0843	0.0035	0.44	522	21
36300413b	26	87	101	0.86	2.3374	0.0895	0.2079	0.0074	0.93	1218	39
37300413b	25	72	146	0.49	1.5768	0.0644	0.1601	0.0057	0.87	958	32

Sample 1M31 Analysis_#	Pb ppm	Th ppm	U ppm	Th/U	Pb207/U235	2 sigma error Pb207/U235	Pb206/U238	2 sigma error Pb206/U238	Rho	Age (Ma) Pb206/U238	2 sigma error Pb206/U238
38300413b	27	68	321	0.21	0.6832	0.0268	0.0861	0.0031	0.91	532	18
39300413b	3.8	65	145	0.45	0.1796	0.0128	0.0248	0.0009	0.53	158	6
40300413b	3.2	39	66	0.60	0.2986	0.0237	0.0439	0.0017	0.47	277	10
41300413b	5.4	22	59	0.37	0.7159	0.0370	0.0888	0.0032	0.70	548	19
42300413b	27	47	151	0.31	1.7350	0.0668	0.1720	0.0061	0.92	1023	33
45300413b	13	54	124	0.43	0.8065	0.0350	0.0976	0.0035	0.82	601	20
46300413b	11	16	67	0.24	1.6008	0.0863	0.1609	0.0059	0.68	962	33
47300413b	9.0	26	46	0.56	1.7984	0.0811	0.1769	0.0064	0.80	1050	35
48300413b	3.7	18	86	0.21	0.3367	0.0209	0.0444	0.0016	0.59	280	10
49300413b	13	25	79	0.31	1.5272	0.0651	0.1569	0.0056	0.83	940	31
50300413b	38	119	183	0.65	2.0232	0.0767	0.1769	0.0062	0.93	1050	34
51300413b	8	30	48	0.63	1.4070	0.0642	0.1486	0.0053	0.78	893	30
52300413b	22	120	232	0.52	0.7003	0.0286	0.0878	0.0031	0.86	543	18
55300413b	47	413	372	1.11	0.8326	0.0315	0.0997	0.0035	0.93	613	21
56300413b	5.1	14	26	0.52	1.7818	0.1054	0.1747	0.0065	0.63	1038	36
57300413b	4.7	24	16	1.44	2.3157	0.1292	0.2070	0.0076	0.66	1213	41
58300413b	3.3	22	10	2.19	2.3149	0.1601	0.2046	0.0078	0.55	1200	42
59300413b	7.9	52	30	1.72	1.8338	0.0890	0.1768	0.0064	0.74	1050	35
60300413b	20	41	59	0.71	3.9586	0.1544	0.2872	0.0101	0.91	1628	51
61300413b	3.8	14	22	0.65	1.4588	0.0906	0.1532	0.0057	0.60	919	32
62300413b	15	21	76	0.28	2.1413	0.0972	0.1914	0.0069	0.79	1129	37
65300413b	5.7	23	58	0.40	0.7794	0.0397	0.0941	0.0034	0.71	580	20
66300413b	18	144	140	1.03	0.8807	0.0370	0.1046	0.0037	0.84	641	22
67300413b	9	58	68	0.86	0.8821	0.0522	0.1045	0.0038	0.62	641	22
68300413b	49	75	289	0.26	1.7033	0.0633	0.1683	0.0059	0.94	1003	32
69300413b	24	127	222	0.57	0.8071	0.0335	0.0984	0.0035	0.85	605	20
70300413b	22	187	427	0.44	0.3604	0.0147	0.0489	0.0017	0.86	308	11

Sample 1M31 Analysis_#	Pb ppm	Th ppm	U ppm	Th/U	Pb207/U235	2 sigma error Pb207/U235	Pb206/U238	2 sigma error Pb206/U238	Rho	Age (Ma) Pb206/U238	2 sigma error Pb206/U238
71300413b	18	41	74	0.55	2.5690	0.1015	0.2195	0.0077	0.89	1279	41
72300413b	132	235	270	0.87	7.1771	0.2594	0.3915	0.0137	0.96	2130	63
75300413b	30	42	186	0.23	1.6480	0.0678	0.1622	0.0057	0.86	969	32
76300413b	18	43	68	0.63	2.8288	0.1149	0.2304	0.0081	0.87	1337	43
77300413b	22	31	64	0.49	4.5364	0.1744	0.3069	0.0108	0.91	1725	53
78300413b	21	171	177	0.97	0.7976	0.0325	0.0962	0.0034	0.86	592	20
79300413b	13	68	154	0.45	0.6578	0.0282	0.0819	0.0029	0.82	507	17
80300413b	22	83	200	0.42	0.8629	0.0346	0.1029	0.0036	0.87	632	21
81300413b	111	195	360	0.54	3.8043	0.1405	0.2690	0.0094	0.94	1536	48
82300413b	49	135	250	0.54	1.8612	0.0709	0.1775	0.0062	0.91	1053	34
85300413b	30	41	147	0.28	2.2317	0.0855	0.2035	0.0071	0.91	1194	38
86300413b	36	75	194	0.39	1.8340	0.0698	0.1767	0.0062	0.91	1049	34
87300413b	36	176	163	1.08	1.7692	0.0683	0.1751	0.0061	0.90	1040	33
88300413b	184	276	255	1.08	14.5598	0.5293	0.5375	0.0187	0.95	2773	78
89300413b	64	233	678	0.34	0.7480	0.0281	0.0920	0.0032	0.92	567	19
90300413b	8.3	60	88	0.68	0.6567	0.0336	0.0825	0.0029	0.70	511	17
91300413b	23	40	94	0.42	2.7627	0.1110	0.2307	0.0081	0.87	1338	42
92300413b	56	37	70	0.53	23.3447	0.8517	0.6508	0.0226	0.95	3231	88
95300413b	3.4	28	84	0.34	0.2988	0.0305	0.0391	0.0016	0.40	247	10
96300413b	12	27	40	0.67	3.3127	0.1382	0.2557	0.0090	0.84	1468	46
97300413b	119	399	223	1.79	6.9882	0.2568	0.3696	0.0128	0.94	2028	60
98300413b	42	20	164	0.12	3.3974	0.1282	0.2619	0.0091	0.92	1500	46

Appendix F:
Zircon Fission-track analyses
(Plutonic and Metamorphic rocks)

These analyses were performed at Université de Grenoble fission-track laboratory with ζ = 128 ± 9 for glass dosimeter CN1.

1M04

Migmatite
NW of Mollendo
Lat. / Long. : -16.87171 ; -72.02515
Alt. = 1180 m.

	Age	2σ se(t)	Min (2σ)	Max (2σ)	P(X2) (%)	Dispersion (%)
Pooled	148.99	39.18	109.81	188.17	93.32	0.00
Mean	166.30	31.50	134.80	197.80		
Central	149.00	39.20	109.80	188.20		

Single grain data :

n	Nd	ρd	rse(ρd)	Mean Length
19	7335	1.83E+05	1.21	-

Ns	Ni	Counted squares	Age (Ma)	2σ se(t)	U (ppm)	Uerr (%)	Mean Dpar
75	7	24	124.90	100.26	99.10	72.41	-
46	2	25	265.20	384.91	27.18	34.39	-
60	2	25	343.80	496.58	27.18	34.39	-
67	7	20	111.69	90.10	118.92	86.89	-
57	6	21	110.87	96.42	97.07	76.19	-
56	6	20	108.94	94.82	101.93	80.00	-
49	4	20	142.61	149.65	67.95	64.09	-
64	7	21	106.73	86.28	113.25	82.75	-
41	3	15	158.90	191.37	67.95	72.66	-
58	5	15	135.12	127.37	113.25	96.62	-
64	3	28	246.35	293.08	36.40	38.93	-
55	7	15	91.83	74.81	158.55	115.85	-
59	4	18	171.33	178.65	75.50	71.21	-
111	5	25	256.16	236.95	67.95	57.97	-
48	3	16	185.64	222.48	63.70	68.12	-
72	4	14	208.47	216.16	97.07	91.55	-
60	5	20	139.73	131.54	84.94	72.47	-
36	4	15	105.08	111.73	90.60	85.45	-
36	3	18	139.73	169.07	56.63	60.55	-

1M05

Pink leucosomes of a migmatite
NW of Mollendo
Lat. / Long. : -16.91787 ; -72.04906
Alt. = 863 m.

	Age	2σ se(t)	Min (2σ)	Max (2σ)	P(X2) (%)	Dispersion (%)
Pooled	194.16	41.11	153.05	235.26	88.49	0.00
Mean	220.95	48.18	172.77	269.13		
Central	194.20	41.20	153.00	235.40		

Single grain data :

n	Nd	ρd	rse(ρd)	Mean Length
20	9115	2.14E+05	1.40	-

Ns	Ni	Counted squares	Age (Ma)	2σ se(t)	U (ppm)	Uerr (%)	Mean Dpar
55	4	18	186.49	193.62	64.58	60.92	-
180	14	35	174.54	97.67	116.25	61.14	-
41	6	8	93.35	81.89	217.97	171.10	-
16	1	5	216.50	446.60	58.13	94.93	-
68	5	16	184.48	171.48	90.82	77.49	-
96	6	16	216.50	182.88	108.99	85.55	-
57	6	16	129.42	111.49	108.99	85.55	-
90	2	20	591.28	846.50	29.06	36.77	-
117	8	21	198.18	145.55	110.72	76.01	-
59	3	15	265.10	314.38	58.13	62.16	-
63	5	12	171.10	159.47	121.10	103.33	-
55	2	12	367.73	530.09	48.44	61.28	-
116	6	16	260.70	219.10	108.99	85.55	-
53	3	6	238.64	283.77	145.31	155.40	-
80	8	25	136.16	101.46	93.00	63.85	-
61	5	12	165.73	154.66	121.10	103.33	-
103	5	20	277.42	254.87	72.66	62.00	-
95	9	30	143.64	100.73	87.19	56.63	-
53	5	20	144.24	135.36	72.66	62.00	-
89	5	16	240.41	221.66	90.82	77.49	-

1M06

Migmatite
NW of Mollendo
Lat. / Long. : -16.95583 ; -72.0559
Alt. = 565 m.

	Age	2σ se(t)	Min (2σ)	Max (2σ)	P(X2) (%)	Dispersion (%)
Pooled	147.07	36.72	110.35	183.79	42.86	17.00
Mean	152.88	31.99	120.89	184.87		
Central	144.90	38.00	106.90	182.90		

Single grain data :

n	Nd	ρd	rse(ρd)	Mean Length
20	9115	2.15E+05	1.38	-

Ns	Ni	Counted squares	Age (Ma)	2σ se(t)	U (ppm)	Uerr (%)	Mean Dpar
88	7	12	170.97	136.38	169.28	123.71	-
52	9	9	79.14	58.20	290.19	188.47	-
50	11	17	62.34	42.42	187.77	110.86	-
32	2	8	216.82	317.51	72.55	91.79	-
58	6	8	131.86	114.59	217.64	170.84	-
45	2	7	302.86	439.76	82.91	104.90	-
39	4	10	132.99	140.87	116.08	109.48	-
32	3	7	145.35	176.70	124.37	133.00	-
59	6	11	134.11	116.45	158.29	124.25	-
32	5	12	87.60	85.14	120.91	103.17	-
22	2	12	149.84	222.32	48.37	61.19	-
33	3	4	149.84	181.92	217.64	232.75	-
35	5	9	95.76	92.53	161.22	137.56	-
51	5	10	139.06	131.77	145.10	123.80	-
104	4	18	348.72	358.68	64.49	60.82	-
146	8	21	246.73	182.46	110.55	75.90	-
39	4	6	132.99	140.87	193.46	182.47	-
72	6	11	163.29	140.63	158.29	124.25	-
58	5	12	157.92	148.85	120.91	103.17	-
54	5	6	147.15	139.10	241.83	206.34	-

1M08

Weathered migmatite
Islay
Lat. / Long. : -16.99694 ; -72.10288
Alt. = 5 m.

	Age	2σ se(t)	Min (2σ)	Max (2σ)	P(X2) (%)	Dispersion (%)
Pooled	226.78	61.33	165.45	288.11	31.36	19.00
Mean	319.62	92.90	226.72	412.52		
Central	226.80	64.60	162.20	291.40		

Single grain data :

n	Nd	ρd	rse(ρd)	Mean Length
20	9115.00	2.15E+05	1.33	-

Ns	Ni	Counted squares	Age (Ma)	2σ se(t)	U (ppm)	Uerr (%)	Mean Dpar
75	9	15	114.19	82.12	173.58	112.73	-
60	4	20	204.10	212.71	57.86	54.57	-
45	4	12	153.68	161.79	96.43	90.95	-
47	4	18	160.42	168.60	64.29	60.64	-
87	2	15	574.94	826.29	38.57	48.80	-
57	4	12	194.05	202.56	96.43	90.95	-
83	4	12	280.66	290.00	96.43	90.95	-
96	10	20	131.37	89.21	144.65	89.36	-
30	1	12	401.94	819.08	24.11	39.37	-
51	7	13	99.94	81.77	155.77	113.84	-
72	3	16	323.53	383.95	54.24	58.01	-
75	1	15	961.43	1940.28	19.29	31.50	-
89	5	12	241.49	224.53	120.54	102.85	-
88	3	16	393.27	465.04	54.24	58.01	-
71	5	16	193.38	180.97	90.40	77.13	-
36	1	14	479.40	974.33	20.66	33.75	-
75	5	14	204.10	190.68	103.32	88.15	-
42	1	8	555.95	1127.72	36.16	59.06	-
56	2	14	375.91	543.56	41.33	52.29	-
84	4	18	283.96	293.34	64.29	60.64	-

1M14

Leucocratic pegmatite in a greenish precambrian gneiss
Cerro Verde
Lat. / Long. : -16.513310 ; -71.63135
Alt. = 2514 m.

	Age	2σ se(t)	Min (2σ)	Max (2σ)	P(X2) (%)	Dispersion (%)
Pooled	52.78	9.28	43.51	62.06	0.84	23.00
Mean	61.94	14.48	47.46	76.42		
Central	52.50	10.40	42.10	62.90		

Single grain data :

n	Nd	ρd	rse(ρd)	Mean Length
29	9115.00	2.16E+05	1.31	-

Ns	Ni	Counted squares	Age (Ma)	2σ se(t)	U (ppm)	Uerr (%)	Mean Dpar
105	28	25	51.71	23.15	323.52	121.50	-
78	19	20	56.59	30.01	274.42	124.49	-
48	10	13	66.12	46.88	222.20	137.27	-
107	26	36	56.73	26.04	208.62	81.24	-
28	8	9	48.28	39.29	256.77	176.27	-
35	22	25	21.99	12.35	254.20	107.39	-
39	9	20	59.72	44.95	129.99	84.42	-
28	6	10	64.29	58.53	173.32	136.04	-
43	19	16	31.26	17.77	343.02	155.62	-
37	18	18	28.40	16.80	288.86	134.53	-
77	20	20	53.08	27.66	288.86	127.82	-
44	10	12	60.63	43.32	240.72	148.71	-
41	11	15	51.40	35.64	211.83	125.05	-
123	29	36	58.46	25.48	232.69	85.90	-
52	10	15	71.60	50.44	192.57	118.97	-
46	11	16	57.64	39.52	198.59	117.24	-
19	10	8	26.25	20.84	361.08	223.06	-
42	7	12	82.54	68.37	168.50	123.14	-
60	16	25	51.71	29.98	184.87	91.15	-
65	17	15	52.72	29.65	327.38	156.75	-
83	16	24	71.42	40.26	192.57	94.95	-
52	17	24	42.21	24.31	204.61	97.97	-
44	3	12	199.93	240.22	72.22	77.22	-

Ns	Ni	Counted squares	Age (Ma)	2σ se(t)	U (ppm)	Uerr (%)	Mean Dpar
71	18	18	54.38	29.69	288.86	134.53	-
82	6	21	186.49	159.88	82.53	64.78	-
44	12	12	50.57	33.68	288.86	163.58	-
65	22	20	40.78	20.91	317.75	134.23	-
61	14	16	60.04	36.56	252.75	132.92	-
73	28	30	36.00	16.77	269.60	101.25	-

1M21

Foliated diorite
NE of Palca
Lat. / Long. : -16.36188 ; -71.78576
Alt. = 1646 m.

	Age	2σ se(t)	Min (2σ)	Max (2σ)	P(X2) (%)	Dispersion (%)
Pooled	52.88	9.19	43.69	62.06	94.17	0.00
Mean	54.60	4.67	49.93	59.27		
Central	52.90	9.20	43.70	62.10		

Single grain data :

n	Nd	ρd	rse(ρd)	Mean Length
21	9115.00	2.18E+05	1.17	-

Ns	Ni	Counted squares	Age (Ma)	2σ se(t)	U (ppm)	Uerr (%)	Mean Dpar
59	11	10	74.62	50.11	314.40	185.57	-
83	19	16	60.84	32.09	339.40	153.92	-
118	34	16	48.38	20.01	607.35	207.29	-
89	19	15	65.21	34.20	362.03	164.19	-
92	23	16	55.73	27.12	410.86	169.78	-
62	15	9	57.58	34.10	476.36	242.25	-
53	15	12	49.25	29.62	357.27	181.68	-
87	33	18	36.78	15.89	523.99	181.48	-
46	14	10	45.81	28.69	400.14	210.37	-
39	13	9	41.84	27.43	412.84	224.93	-
87	22	25	55.10	27.40	251.52	106.21	-
101	18	20	78.04	41.39	257.23	119.76	-
40	8	9	69.59	54.77	254.06	174.38	-
35	8	6	60.93	48.51	381.09	261.57	-
94	26	25	50.39	23.41	297.25	115.69	-
88	29	19	42.32	19.06	436.24	160.96	-
228	57	50	55.73	18.25	325.83	86.28	-
191	51	35	52.19	17.99	416.47	116.48	-
72	21	20	47.80	24.63	300.10	129.63	-
69	19	20	50.62	27.16	271.52	123.14	-
58	17	12	47.56	27.06	404.90	193.81	-

1M47

Granitoïd with centimetric orthoses
N of Ilo
Lat. / Long. : -17.4656 ; -71.37315
Alt. = 0 m.

	Age	2σ se(t)	Min (2σ)	Max (2σ)	P(X2) (%)	Dispersion (%)
Pooled	61.11	12.30	48.81	73.41	11.52	9.00
Mean	66.77	21.35	45.42	88.12		
Central	60.70	12.60	48.10	73.30		

Single grain data :

n	Nd	ρd	rse(ρd)	Mean Length
20	7335.00	1.88E+05	1.17	-

Ns	Ni	Counted squares	Age (Ma)	2σ se(t)	U (ppm)	Uerr (%)	Mean Dpar
90	19	30	56.97	29.85	209.68	95.09	-
110	17	18	77.69	41.93	312.68	149.67	-
35	5	7	84.01	81.18	236.48	201.75	-
38	13	11	35.21	23.16	391.27	213.18	-
40	10	14	48.14	34.70	236.48	146.06	-
62	8	9	92.95	71.04	294.29	202.00	-
104	19	16	65.78	34.09	393.15	178.30	-
16	6	6	32.13	31.09	331.07	259.83	-
22	10	8	26.52	20.57	413.84	255.61	-
101	18	16	67.43	35.77	372.46	173.41	-
25	7	7	43.00	37.26	331.07	241.90	-
42	2	6	248.81	361.84	110.36	139.62	-
67	7	16	114.60	92.44	144.84	105.83	-
58	14	12	49.85	30.50	386.25	203.07	-
23	8	8	34.64	28.84	331.07	227.25	-
80	14	18	68.66	40.93	257.50	135.38	-
43	11	21	47.05	32.47	173.42	102.36	-
93	14	18	79.75	47.07	257.50	135.38	-
68	14	12	58.41	35.25	386.25	203.07	-
47	13	9	43.53	27.95	478.21	260.55	-

1M66

Granite
Atico
Lat. / Long. : -16.93881 ; -71.593492
Alt. = 39 m.

	Age	2σ se(t)	Min (2σ)	Max (2σ)	P(X2) (%)	Dispersion (%)
Pooled	108.04	25.32	82.72	133.36	18.53	22.00
Mean	158.83	56.42	102.41	215.25		
Central	110.20	28.20	82.00	138.40		

Single grain data :

n	Nd	ρd	rse(ρd)	Mean Length
20	7335.00	1.92E+05	1.19	-

Ns	Ni	Counted squares	Age (Ma)	2σ se(t)	U (ppm)	Uerr (%)	Mean Dpar
75	11	36	83.33	55.06	99.34	58.64	-
55	3	12	221.66	264.66	81.28	86.91	-
51	4	12	154.96	162.37	108.37	102.21	-
103	15	49	83.92	47.85	99.53	50.62	-
41	6	18	83.51	73.94	108.37	85.06	-
38	2	11	229.58	334.65	59.11	74.79	-
47	3	12	189.89	227.71	81.28	86.91	-
76	8	52	115.81	87.61	50.02	34.33	-
42	2	28	253.28	368.33	23.22	29.38	-
87	16	40	66.54	37.38	130.05	64.11	-
41	3	20	165.96	199.87	48.77	52.15	-
77	13	28	72.45	44.62	150.95	82.25	-
56	4	27	169.95	177.52	48.17	45.43	-
33	8	40	50.54	40.46	65.02	44.63	-
54	1	28	632.21	1279.13	11.61	18.96	-
32	4	18	97.66	104.49	72.25	68.14	-
33	3	12	133.91	162.58	81.28	86.91	-
32	3	12	129.89	157.91	81.28	86.91	-
60	10	20	73.39	51.17	162.56	100.41	-
83	7	30	144.23	115.31	75.86	55.43	-

1M72

Granite with plurimetric orthoses
NE of Camana
Lat. / Long. : -16.57268 ; -72.62976
Alt. = 600 m.

	Age	2σ se(t)	Min (2σ)	Max (2σ)	P(X2) (%)	Dispersion (%)
Pooled	244.12	61.77	182.35	305.89	65.66	3.00
Mean	331.48	127.87	203.61	459.35		
Central	243.70	61.80	181.90	305.50		

Single grain data :

n	Nd	ρd	rse(ρd)	Mean Length
16	9115.00	2.24E+05	1.07	-

Ns	Ni	Counted squares	Age (Ma)	2σ se(t)	U (ppm)	Uerr (%)	Mean Dpar
16	1	4	226.57	468.15	69.37	113.29	-
115	7	26	232.53	183.93	74.71	54.58	-
46	3	6	217.29	260.72	138.75	148.35	-
161	6	21	375.58	316.69	79.28	62.22	-
75	5	12	212.64	198.66	115.62	98.63	-
122	10	12	173.48	116.66	231.24	142.81	-
120	6	20	281.99	239.19	83.25	65.33	-
93	1	15	1217.74	2454.43	18.50	30.21	-
32	1	5	445.45	906.84	55.50	90.64	-
111	6	18	261.26	222.02	92.50	72.59	-
71	3	15	332.38	394.55	55.50	59.34	-
218	15	36	206.13	113.74	115.62	58.79	-
195	14	30	197.68	112.82	129.50	68.07	-
97	10	18	138.31	93.88	154.16	95.21	-
66	4	10	233.52	242.69	111.00	104.68	-
102	3	15	472.29	557.23	55.50	59.34	-

Appendix G:
Apatite Fission-track analyses
(Plutonic and Metamorphic rocks)

These analyses were performed at Université de Grenoble fission-track laboratory with ζ = 254 ± 12 for glass dosimeter IRMM540.

1M06

Migmatite
NW of Mollendo
Lat. / Long. : -16.95583 ; -72.0559
Alt. = 565 m.

	Age	2σ se(t)	Min (2σ)	Max (2σ)	P(X2) (%)	Dispersion (%)
Pooled	54.64	9.74	44.89	64.38	24.69	13.00
Mean	60.14	10.12	50.02	70.26		
Central	54.90	10.40	44.50	65.30		

Single grain data :

n	Nd	ρd	rse(ρd)	Mean Length
19	8323.00	6.01E+05	1.13	-

Ns	Ni	Counted squares	Age (Ma)	2σ se(t)	U (ppm)	Uerr (%)	Mean Dpar
14	21	28	50.68	35.31	29.30	12.65	-
15	13	24	87.46	66.82	21.16	11.53	-
22	29	20	57.64	33.07	56.64	20.90	-
23	40	48	43.73	23.28	32.55	10.26	-
21	33	25	48.38	27.42	51.57	17.86	-
13	21	16	47.07	33.54	51.27	22.15	-
16	12	15	100.96	77.73	31.25	17.69	-
29	27	35	81.45	44.28	30.14	11.51	-
12	9	9	100.96	89.57	39.06	25.36	-
15	19	15	59.97	41.83	49.48	22.44	-
8	8	18	75.87	76.22	17.36	11.92	-
18	19	27	71.90	47.81	27.49	12.47	-
14	19	20	55.99	39.81	37.11	16.83	-
18	28	30	48.87	29.91	36.46	13.68	-
11	21	20	39.85	29.92	41.02	17.72	-
23	24	28	72.72	43.02	33.48	13.55	-
14	24	21	44.36	30.15	44.65	18.07	-
7	19	14	28.05	24.96	53.02	24.04	-
14	41	30	26.01	16.30	53.39	16.62	-

1M08

Wheathered migmatite, with very few white zones
Mollendo
Lat. / Long. : -16.99694 ; -71.10288
Alt. = 5 m.

	Age	2σ se(t)	Min (2σ)	Max (2σ)	P(X2) (%)	Dispersion (%)
Pooled	81.57	18.08	63.49	99.65	28.70	21.00
Mean	101.55	23.45	78.10	125.00		
Central	83.20	20.20	63.00	103.40		

Single grain data :

n	Nd	ρd	rse(ρd)	Mean Length
20	7814.00	5.91E+05	1.44	-

Ns	Ni	Counted squares	Age (Ma)	2σ se(t)	U (ppm)	Uerr (%)	Mean Dpar
6	7	40	64.04	71.53	6.95	5.08	-
14	9	72	115.76	99.55	4.96	3.22	-
18	15	39	89.48	63.17	15.27	7.77	-
17	31	100	41.05	25.09	12.31	4.40	-
8	12	42	49.87	45.78	11.34	6.43	-
5	3	15	123.95	181.44	7.94	8.49	-
12	13	80	68.94	55.60	6.45	3.52	-
14	6	50	172.87	169.54	4.76	3.74	-
5	10	48	37.44	41.17	8.27	5.11	-
12	13	32	68.94	55.60	16.13	8.79	-
11	8	66	102.43	95.71	4.81	3.30	-
6	5	28	89.48	108.72	7.09	6.05	-
8	8	28	74.66	75.01	11.34	7.79	-
9	3	12	221.42	296.01	9.93	10.61	-
13	14	72	69.35	53.85	7.72	4.06	-
10	10	80	74.66	67.17	4.96	3.07	-
9	4	25	166.77	201.09	6.35	5.99	-
16	6	50	197.19	189.77	4.76	3.74	-
7	4	16	130.08	163.56	9.93	9.36	-
11	12	65	68.47	57.55	7.33	4.15	-

1M09

Quarte-diorite at the base of the Linga laccolith, U-Pb(zr) = 89.8 ± 0.7 Ma
Cerro Verde
Lat. / Long. : -16.55688 ; -71.44484
Alt. = 2480 m.

	Age	2σ se(t)	Min (2σ)	Max (2σ)	P(X2) (%)	Dispersion (%)
Pooled	88.37	20.45	67.92	108.82	35.00	22.00
Mean	122.23	30.11	92.12	152.34		
Central	91.80	23.60	68.20	115.40		

Single grain data :

n	Nd	ρd	rse(ρd)	Mean Length
20	7814.00	5.97E+05	1.29	-

Ns	Ni	Counted squares	Age (Ma)	2σ se(t)	U (ppm)	Uerr (%)	Mean Dpar
4	4	32	75.43	106.93	4.91	4.63	-
5	7	36	53.97	63.42	7.64	5.58	-
16	18	40	67.10	46.57	17.68	8.23	-
3	3	25	75.43	123.40	4.71	5.04	-
4	1	25	296.58	663.80	1.57	2.57	-
7	6	30	87.92	98.20	7.86	6.17	-
7	2	40	260.24	418.08	1.96	2.49	-
29	38	42	57.65	28.98	35.55	11.49	-
8	4	18	149.99	184.28	8.73	8.23	-
6	3	28	149.99	212.62	4.21	4.50	-
9	5	60	135.15	151.34	3.27	2.79	-
21	12	42	131.44	95.98	11.23	6.36	-
8	4	20	149.99	184.28	7.86	7.41	-
12	7	40	128.78	123.13	6.88	5.02	-
11	5	60	164.80	178.50	3.27	2.79	-
9	7	25	96.83	98.04	11.00	8.04	-
9	8	85	84.80	82.82	3.70	2.54	-
9	4	50	168.50	203.17	3.14	2.96	-
7	16	25	33.11	30.18	25.15	12.40	-
13	14	60	70.07	54.41	9.17	4.82	-

1M14

Leucocratic pegmatite in a greenish precambrian gneiss
Cerro Verde
Lat. / Long. : -16.51331 ; -71.63135
Alt. = 2514 m.

	Age	2σ se(t)	Min (2σ)	Max (2σ)	P(X2) (%)	Dispersion (%)
Pooled	36.79	9.25	27.54	46.04	38.68	8.00
Mean	39.18	9.52	29.66	48.70		
Central	36.80	9.40	27.40	46.20		

Single grain data :

n	Nd	ρd	rse(ρd)	Mean Length
16	8323.00	6.43E+05	1.14	-

Ns	Ni	Counted squares	Age (Ma)	2σ se(t)	U (ppm)	Uerr (%)	Mean Dpar
4	13	70	25.07	28.78	6.78	3.69	-
10	11	100	73.81	64.89	4.02	2.37	-
6	10	80	48.81	50.63	4.56	2.82	-
2	14	70	11.65	17.66	7.30	3.84	-
8	12	100	54.21	49.76	4.38	2.48	-
6	22	100	22.23	20.59	8.03	3.39	-
2	12	100	13.59	20.81	4.38	2.48	-
7	13	100	43.82	41.30	4.75	2.59	-
13	22	100	48.07	33.95	8.03	3.39	-
10	14	100	58.06	48.41	5.11	2.69	-
6	19	80	25.73	24.23	8.67	3.93	-
13	22	70	48.07	33.95	11.47	4.85	-
6	11	100	44.38	45.26	4.02	2.37	-
3	13	48	18.82	24.17	9.89	5.39	-
4	5	25	64.99	87.43	7.30	6.23	-
8	26	100	25.07	20.42	9.49	3.69	-

1M15

Gabbro, U-Pb(zr) = 200.0 ± 1.1 Ma
Cerro Verde
Lat. / Long. : -16.47991 ; -71.61873
Alt. = 2370 m.

	Age	2σ se(t)	Min (2σ)	Max (2σ)	P(X2) (%)	Dispersion (%)
Pooled	47.15	7.76	39.39	54.90	54.40	4.00
Mean	49.33	6.90	42.43	56.23		
Central	47.10	7.80	39.30	54.90		

Single grain data :

n	Nd	ρd	rse(ρd)	Mean Length
20	8323.00	5.97E+05	1.11	-

Ns	Ni	Counted squares	Age (Ma)	2σ se(t)	U (ppm)	Uerr (%)	Mean Dpar
13	22	12	44.67	31.55	72.05	30.42	-
9	8	36	84.79	82.81	8.73	5.99	-
18	37	15	36.80	21.45	96.93	31.73	-
3	17	20	13.37	16.80	33.40	15.99	-
21	29	24	54.70	31.79	47.48	17.52	-
22	36	21	46.19	25.40	67.37	22.35	-
15	16	15	70.73	51.30	41.92	20.66	-
16	18	20	67.08	46.56	35.37	16.46	-
17	34	50	37.82	22.77	26.72	9.12	-
8	13	16	46.52	42.05	31.93	17.39	-
11	19	20	43.77	33.44	37.33	16.93	-
20	56	36	27.04	14.33	61.13	16.32	-
19	33	24	43.53	25.43	54.03	18.71	-
51	66	50	58.36	22.48	51.87	12.77	-
15	19	18	59.62	41.59	41.48	18.81	-
48	67	64	54.12	21.13	41.14	10.06	-
9	13	20	52.31	45.65	25.54	13.92	-
28	50	30	42.34	20.41	65.50	18.49	-
13	20	24	49.12	35.32	32.75	14.48	-
12	17	20	53.33	40.55	33.40	15.99	-

1M16

Tiabaya Granite, U-Pb(zr) = 82.3 ± 0.4 Ma
S of Arequipa, N of Cerro Verde
Lat. / Long. : -16.46333 ; -71.62493
Alt. = 2274 m.

	Age	2σ se(t)	Min (2σ)	Max (2σ)	P(X2) (%)	Dispersion (%)
Pooled	68.75	14.99	53.76	83.74	0.57	35.00
Mean	94.63	37.54	57.09	132.17		
Central	72.60	23.20	49.40	95.80		

Single grain data :

n	Nd	ρd	rse(ρd)	Mean Length
10	8442.00	6.34E+05	1.09	-

Ns	Ni	Counted squares	Age (Ma)	2σ se(t)	U (ppm)	Uerr (%)	Mean Dpar
7	18	40	31.21	27.97	16.67	7.76	-
22	15	50	116.94	79.13	11.12	5.65	-
25	32	100	62.56	33.94	11.86	4.17	-
6	4	24	119.58	154.81	6.18	5.82	-
29	23	80	100.66	57.05	10.65	4.40	-
25	32	100	62.56	33.94	11.86	4.17	-
26	26	50	79.96	45.03	19.27	7.50	-
6	2	30	236.97	387.66	2.47	3.12	-
21	53	100	31.80	16.69	19.64	5.39	-
28	22	100	101.60	58.72	8.15	3.44	-

1M17

Pegmatitic dykes in a microgabbro
Mollebaya
Lat. / Long. : -16.48177 ; -71.46170
Alt. = 2549 m.

	Age	2σ se(t)	Min (2σ)	Max (2σ)	P(X2) (%)	Dispersion (%)
Pooled	58.13	12.92	45.21	71.05	81.00	0.00
Mean	68.00	15.17	52.83	83.17		
Central	58.10	13.00	45.10	71.10		

Single grain data :

n	Nd	ρd	rse(ρd)	Mean Length
19	7814.00	5.97E+05	1.29	-

Ns	Ni	Counted squares	Age (Ma)	2σ se(t)	U (ppm)	Uerr (%)	Mean Dpar
11	18	24	46.20	35.65	29.47	13.72	1.55
4	6	25	50.39	65.23	9.43	7.40	1.84
4	5	12	60.42	81.27	16.37	13.97	1.54
8	16	20	37.83	32.96	31.43	15.50	1.88
8	9	20	67.10	65.53	17.68	11.48	1.87
14	12	28	87.92	69.70	16.84	9.54	2.07
15	28	40	40.52	26.23	27.50	10.33	2.01
17	20	29	64.17	42.80	27.10	11.99	1.92
9	10	40	67.93	62.77	9.82	6.07	1.72
7	3	15	174.66	241.65	7.86	8.40	2.32
8	13	21	46.53	42.06	24.32	13.25	1.83
4	5	9	60.42	81.27	21.83	18.62	2.04
6	7	12	64.71	72.28	22.92	16.75	2.07
7	5	20	105.36	123.81	9.82	8.38	2.05
7	5	9	105.36	123.81	21.83	18.62	2.24
7	13	25	40.73	38.39	20.43	11.13	1.77
11	12	32	69.18	58.15	14.73	8.34	1.91
22	24	40	69.18	41.39	23.57	9.54	1.99
8	19	18	31.87	27.04	41.47	18.81	2.03

1M22

Aplitic subvertical dykes in the 1M21 foliated granitoïd
NE of Palca
Lat. / Long. : -16.36188 ; -71.78576
Alt. = 1707 m.

	Age	2σ se(t)	Min (2σ)	Max (2σ)	P(X2) (%)	Dispersion (%)
Pooled	58.60	12.31	46.29	70.91	28.79	13.00
Mean	73.75	17.69	56.06	91.44		
Central	59.30	13.00	46.30	72.30		

Single grain data :

n	Nd	ρd	rse(ρd)	Mean Length
18	8442.00	6.15E+05	1.15	-

Ns	Ni	Counted squares	Age (Ma)	2σ se(t)	U (ppm)	Uerr (%)	Mean Dpar
9	10	36	69.91	64.60	10.60	6.55	-
8	6	18	103.30	112.03	12.72	9.99	-
15	30	60	38.93	24.91	19.09	6.93	-
9	4	50	173.37	209.05	3.05	2.88	-
8	13	48	47.88	43.28	10.34	5.63	-
9	5	20	139.07	155.72	9.54	8.14	-
12	30	50	31.16	21.50	22.90	8.31	-
21	26	100	62.77	37.34	9.92	3.86	-
15	14	100	83.14	62.32	5.34	2.81	-
11	21	40	40.78	30.61	20.04	8.66	-
14	13	50	83.56	64.88	9.92	5.41	-
11	9	20	94.76	85.67	17.18	11.15	-
6	7	20	66.60	74.38	13.36	9.76	-
20	31	50	50.19	29.20	23.67	8.45	-
9	16	30	43.78	36.73	20.36	10.03	-
10	8	35	96.89	92.40	8.72	5.99	-
9	17	36	41.22	34.21	18.03	8.63	-
6	8	28	58.31	63.24	10.91	7.49	-

1M23

Dyke of dacite in a Chocolate conglomerate
South of Socosani
Lat. / Long. : -16.28733 ; -71.73173
Alt. = 2830 m.

	Age	2σ se(t)	Min (2σ)	Max (2σ)	P(X2) (%)	Dispersion (%)
Pooled	42.60	10.21	32.39	52.81	65.86	5.00
Mean	52.90	12.97	39.93	65.87		
Central	42.16	10.20	31.96	52.36		

Single grain data :

n	Nd	ρd	rse(ρd)	Mean Length
20	7814.00	6.01E+05	1.23	-

Ns	Ni	Counted squares	Age (Ma)	2σ se(t)	U (ppm)	Uerr (%)	Mean Dpar
8	11	40	55.23	51.61	10.75	6.34	-
5	7	30	54.25	63.75	9.12	6.66	2.09
4	5	30	60.73	81.69	6.51	5.56	-
8	13	60	46.77	42.28	8.47	4.61	-
8	24	100	25.37	20.86	9.38	3.80	1.78
3	9	50	25.37	33.92	7.04	4.57	2.47
6	6	60	75.83	87.87	3.91	3.07	-
10	29	76	26.25	19.42	14.91	5.50	1.75
2	4	30	38.02	65.96	5.21	4.92	1.98
8	10	40	60.73	57.92	9.77	6.04	2.32
7	9	40	59.05	59.80	8.79	5.71	2.41
4	2	40	150.77	261.55	1.95	2.47	-
6	9	50	50.65	53.62	7.04	4.57	2.58
7	6	24	88.38	98.71	9.77	7.67	2.53
8	18	100	33.81	28.92	7.04	3.28	1.84
4	20	91	15.24	16.76	8.59	3.80	-
12	17	100	53.62	40.77	6.64	3.18	2.39
6	10	70	45.60	47.31	5.58	3.45	2.66
5	9	36	42.24	47.29	9.77	6.35	2.22
9	14	9	48.85	42.01	60.80	31.97	2.92

1M24

Biotite rich granitoïd (U-Pb = 76.7 ± 0.4 Ma)
S of Uchumayo
Lat. / Long. : -16.547026 ; -71.70082
Alt. = 2126 m.

	Age	2σ se(t)	Min (2σ)	Max (2σ)	P(X2) (%)	Dispersion (%)
Pooled	67.05	10.17	56.88	77.21	87.90	1.00
Mean	68.40	5.91	62.49	74.31		
Central	67.10	10.20	56.90	77.30		

Single grain data :

n	Nd	ρd	rse(ρd)	Mean Length
20	8442.00	6.06E+05	1.24	-

Ns	Ni	Counted squares	Age (Ma)	2σ se(t)	U (ppm)	Uerr (%)	Mean Dpar
18	19	36	72.46	48.18	20.46	9.28	-
28	31	70	69.10	36.65	17.16	6.13	-
64	62	70	78.92	29.15	34.33	8.73	-
35	35	50	76.47	37.30	27.13	9.13	-
16	26	36	47.16	30.32	27.99	10.90	-
31	30	40	79.00	41.18	29.07	10.55	-
40	40	100	76.47	34.99	15.50	4.89	-
26	25	50	79.50	45.20	19.38	7.69	-
37	66	60	42.98	18.14	42.63	10.51	-
40	52	100	58.90	25.42	20.15	5.59	-
37	47	100	60.27	27.13	18.22	5.31	-
12	16	50	57.43	44.22	12.40	6.11	-
20	19	80	80.46	52.14	9.20	4.18	-
20	22	36	69.55	43.50	23.68	10.00	-
17	20	80	65.05	43.38	9.69	4.29	-
18	22	80	62.63	40.27	10.66	4.50	-
29	22	100	100.61	57.72	8.53	3.60	-
30	34	100	67.52	34.45	13.18	4.50	-
14	20	60	53.62	37.73	12.92	5.72	-
20	22	100	69.55	43.50	8.53	3.60	-

1M25

Granitoïd
SW of La Reparticion
Lat. / Long. : -16.54084 ; -71.79558
Alt. = 1707 m.

	Age	2σ se(t)	Min (2σ)	Max (2σ)	P(X2) (%)	Dispersion (%)
Pooled	55.69	9.61	46.08	65.30	2.21	27.00
Mean	64.25	13.25	51.00	77.50		
Central	57.10	12.20	44.90	69.30		

Single grain data :

n	Nd	ρd	rse(ρd)	Mean Length
20	8442.00	6.01E+05	1.31	-

Ns	Ni	Counted squares	Age (Ma)	2σ se(t)	U (ppm)	Uerr (%)	Mean Dpar
7	14	36	38.05	35.42	15.19	7.99	1.83
12	37	70	24.71	16.59	20.65	6.76	1.47
14	7	30	150.87	140.44	9.11	6.66	1.35
11	15	49	55.73	44.57	11.96	6.08	1.63
25	42	100	45.27	23.29	16.41	5.05	1.93
28	25	100	84.92	47.45	9.76	3.88	1.34
25	27	80	70.29	39.61	13.18	5.04	1.58
25	24	100	79.02	45.81	9.37	3.80	2.1
19	13	48	110.60	80.34	10.58	5.76	1.64
7	8	24	66.44	69.07	13.02	8.94	1.98
12	10	30	90.95	78.38	13.02	8.04	2.12
12	13	60	70.07	56.51	8.46	4.61	2.01
7	12	48	44.37	42.42	9.76	5.53	1.77
18	22	100	62.15	39.96	8.59	3.63	1.92
14	28	70	38.05	25.18	15.62	5.87	1.56
18	52	100	26.37	14.65	20.31	5.63	1.75
18	26	80	52.62	32.67	12.69	4.94	1.49
21	26	70	61.35	36.49	14.51	5.65	1.75
29	35	100	62.93	32.19	13.67	4.60	2.08
18	28	100	48.88	29.91	10.94	4.11	2.12

1M27

Quartz-diorite, U-Pb(zr) = 160.5 ± 0.8 Ma
NW of Chapi
Lat. / Long. : -16.67595 ; -71.34001
Alt. = 2975 m.

	Age	2σ se(t)	Min (2σ)	Max (2σ)	P(X2) (%)	Dispersion (%)
Pooled	48.85	24.67	24.18	73.53	70.03	0.00
Mean	52.63	17.35	35.28	69.98		
Central	48.80	24.60	24.20	73.40		

Single grain data :

n	Nd	ρd	rse(ρd)	Mean Length
4	8323.00	5.86E+05	1.11	-

Ns	Ni	Counted squares	Age (Ma)	2σ se(t)	U (ppm)	Uerr (%)	Mean Dpar
4	5	60	59.30	79.76	3.34	2.85	-
9	9	100	74.04	70.17	3.60	2.34	-
7	14	100	37.13	34.56	5.60	2.95	-
7	13	100	39.97	37.68	5.20	2.84	-

1M50

Granite
Mejía
Lat. / Long. : -16.89878. ; -71.84192
Alt. = 1230 m.

	Age	2σ se(t)	Min (2σ)	Max (2σ)	P(X2) (%)	Dispersion (%)
Pooled	63.54	9.84	53.70	73.38	36.83	9.00
Mean	65.47	8.45	57.02	73.92		
Central	63.40	10.20	53.20	73.60		

Single grain data :

n	Nd	ρd	rse(ρd)	Mean Length
24	7814.00	6.10E+05	1.13	-

Ns	Ni	Counted squares	Age (Ma)	2σ se(t)	U (ppm)	Uerr (%)	Mean Dpar
8	24	70	25.77	21.19	13.19	5.34	-
11	14	40	60.58	49.17	13.47	7.08	-
36	42	100	66.06	30.69	16.16	4.97	-
12	13	45	71.11	57.35	11.12	6.06	-
10	15	50	51.44	42.30	11.55	5.87	-
39	29	100	103.34	51.67	11.16	4.12	-
21	20	70	80.83	51.12	11.00	4.86	-
34	27	100	96.82	50.79	10.39	3.97	-
19	32	70	45.83	26.92	17.59	6.18	-
24	20	60	92.29	56.60	12.83	5.67	-
12	16	40	57.84	44.53	15.39	7.59	-
16	20	60	61.68	41.81	12.83	5.67	-
24	41	100	45.19	23.64	15.78	4.91	-
20	30	100	51.44	30.12	11.55	4.19	-
18	26	80	53.41	33.16	12.51	4.87	-
19	31	100	47.30	27.95	11.93	4.26	-
19	25	56	58.61	36.13	17.18	6.82	-
29	23	70	96.94	54.95	12.64	5.22	-
18	27	70	51.44	31.70	14.84	5.67	-
30	33	100	70.04	35.99	12.70	4.40	-
19	25	60	58.61	36.13	16.04	6.36	-
33	38	100	66.92	32.51	14.62	4.73	-
11	8	30	105.64	98.71	10.26	7.04	-
20	30	60	51.44	30.12	19.24	6.98	-

1M51

Granite, U-Pb(zr) = 163.8 ± 0.9 Ma
Cocachacra
Lat. / Long. : -16.57268 ; -72.62976
Alt. = 156 m.

	Age	2σ se(t)	Min (2σ)	Max (2σ)	P(X2) (%)	Dispersion (%)
Pooled	93.23	27.88	65.36	121.11	42.02	5.00
Mean	123.69	62.77	60.92	186.46		
Central	93.20	28.00	65.20	121.20		

Single grain data :

n	Nd	ρd	rse(ρd)	Mean Length
12	8965.00	7.10E+05	1.07	-

Ns	Ni	Counted squares	Age (Ma)	2σ se(t)	U (ppm)	Uerr (%)	Mean Dpar
8	8	40	89.60	90.02	6.61	4.54	-
5	5	16	89.60	113.67	10.33	8.81	-
2	4	14	44.96	77.99	9.44	8.90	-
14	6	36	207.17	203.17	5.51	4.32	-
3	5	20	53.91	78.92	8.26	7.05	-
14	9	49	138.85	119.41	6.07	3.94	-
3	3	12	89.60	146.58	8.26	8.83	-
19	19	36	89.60	58.79	17.44	7.91	-
5	1	20	436.06	956.29	1.65	2.70	-
4	3	6	119.20	182.44	16.52	17.66	-
20	23	97	77.99	48.28	7.83	3.24	-
5	12	14	37.49	40.07	28.32	16.03	-

1M61

Granitoïd, U-Pb(zr) = 161.9 ± 0.9 Ma
Pampa La Joya
Lat. / Long. : -16.89878. ; -71.84192
Alt. = 1230 m.

	Age	2σ se(t)	Min (2σ)	Max (2σ)	P(X2) (%)	Dispersion (%)
Pooled	64.84	10.71	54.13	75.55	32.00	9.00
Mean	71.90	12.89	59.01	84.79		
Central	65.20	11.20	54.00	76.40		

Single grain data :

n	Nd	ρd	rse(ρd)	Mean Length
20	8323.00	6.13E+05	1.13	-

Ns	Ni	Counted squares	Age (Ma)	2σ se(t)	U (ppm)	Uerr (%)	Mean Dpar
24	12	8	153.86	109.81	57.44	32.52	-
24	16	80	115.74	75.55	7.66	3.77	-
20	26	64	59.61	35.93	15.56	6.05	-
10	16	50	48.48	39.37	12.25	6.04	-
23	30	88	59.41	33.43	13.05	4.74	-
18	25	100	55.81	34.93	9.57	3.80	-
6	10	36	46.54	48.28	10.64	6.57	-
22	27	100	63.13	36.78	10.34	3.95	-
12	20	100	46.54	34.29	7.66	3.39	-
44	72	40	47.40	18.72	68.92	16.26	-
17	17	79	77.39	53.62	8.24	3.94	-
20	31	70	50.03	29.11	16.96	6.05	-
18	19	80	73.34	48.77	9.09	4.12	-
26	22	100	91.36	53.67	8.42	3.56	-
5	4	21	96.59	129.93	7.29	6.88	-
13	9	50	111.49	97.29	6.89	4.48	-
18	23	50	60.64	38.62	17.61	7.28	-
31	38	90	63.20	31.20	16.17	5.22	-
14	25	100	43.45	29.31	9.57	3.80	-
46	49	84	72.68	30.66	22.34	6.37	-

1M66

Granite
Atico
Lat. / Long. : -16.938801 ; -71.593492
Alt. = 0 m.

	Age	2σ se(t)	Min (2σ)	Max (2σ)	P(X2) (%)	Dispersion (%)
Pooled	73.81	9.73	64.08	83.55	10.80	12.00
Mean	77.14	9.27	67.87	86.41		
Central	74.20	10.60	63.60	84.80		

Single grain data :

n	Nd	ρd	rse(ρd)	Mean Length
19	7814.00	6.16E+05	1.15	-

Ns	Ni	Counted squares	Age (Ma)	2σ se(t)	U (ppm)	Uerr (%)	Mean Dpar
69	55	35	97.43	36.47	59.87	16.13	-
86	85	50	78.69	25.26	64.77	14.09	-
64	39	70	127.15	53.12	21.23	6.77	-
97	108	80	69.90	20.70	51.43	9.95	-
47	57	80	64.20	26.06	27.14	7.19	-
34	35	90	75.57	37.13	14.82	4.98	-
32	37	35	67.33	33.16	40.27	13.19	-
87	116	49	58.42	17.52	90.19	16.84	-
30	22	36	105.83	60.30	23.28	9.83	-
56	64	60	68.11	25.79	40.64	10.16	-
29	44	48	51.37	25.08	34.92	10.50	-
39	50	30	60.75	26.62	63.50	17.93	-
37	33	36	87.15	42.58	34.92	12.09	-
39	48	42	63.27	27.96	43.54	12.54	-
67	80	54	65.21	22.51	56.44	12.65	-
34	38	70	69.64	33.57	20.68	6.68	-
31	42	50	57.50	27.80	32.00	9.85	-
56	41	90	106.01	44.78	17.36	5.40	-
46	39	44	91.64	40.88	33.77	10.77	-

1M68

Coarse grained granite
Pescadores
Lat. / Long. : -16.41116 ; -73.23413
Alt. = 0 m.

	Age	2σ se(t)	Min (2σ)	Max (2σ)	P(X2) (%)	Dispersion (%)
Pooled	67.70	11.37	56.33	79.07	71.30	1.00
Mean	70.77	11.37	59.40	82.14		
Central	67.70	11.40	56.30	79.10		

Single grain data :

n	Nd	ρd	rse(ρd)	Mean Length
20	8323.00	5.64E+05	1.38	-

Ns	Ni	Counted squares	Age (Ma)	2σ se(t)	U (ppm)	Uerr (%)	Mean Dpar
3	5	28	42.86	62.74	7.43	6.34	-
4	6	24	47.60	61.63	10.40	8.16	-
13	16	35	57.97	43.65	19.02	9.38	-
7	6	16	83.08	92.79	15.60	12.24	-
13	15	8	61.81	47.23	78.00	39.68	-
47	43	60	77.86	33.72	29.81	9.08	-
47	38	56	88.04	39.35	28.23	9.13	-
61	65	60	66.91	24.72	45.06	11.21	-
36	48	42	53.53	24.17	47.54	13.72	-
25	35	42	50.99	27.16	34.66	11.68	-
10	14	60	50.99	42.51	9.71	5.10	-
8	20	36	28.60	24.09	23.11	10.23	-
17	12	40	100.74	76.59	12.48	7.07	-
32	30	48	76.00	39.32	26.00	9.44	-
13	9	100	102.70	89.62	3.74	2.43	-
14	17	27	58.75	42.79	26.19	12.54	-
10	5	50	141.77	155.90	4.16	3.55	-
29	28	54	73.80	39.76	21.57	8.10	-
13	11	98	84.15	69.43	4.67	2.76	-
13	14	100	66.21	51.40	5.82	3.06	-

1M72

Ordovician granite with pluricentimetric orthoses
NE of Camana
Lat. / Long. : -16.57268 ; -72.62976
Alt. = 600 m.

	Age	2σ se(t)	Min (2σ)	Max (2σ)	P(X2) (%)	Dispersion (%)
Pooled	64.13	13.47	50.67	77.60	28.51	13.00
Mean	41.76	22.19	19.57	63.95		
Central	64.60	14.20	50.40	78.80		

Single grain data :

n	Nd	ρd	rse(ρd)	Mean Length
19	8965.00	6.82E+05	1.27	-

Ns	Ni	Counted squares	Age (Ma)	2σ se(t)	U (ppm)	Uerr (%)	Mean Dpar
17	32	100	45.83	27.87	11.02	3.88	-
11	13	20	72.85	60.10	22.38	12.20	-
17	17	36	86.00	59.58	16.26	7.78	-
12	13	45	79.43	64.06	9.95	5.42	-
8	16	50	43.15	37.60	11.02	5.43	-
4	13	20	26.59	30.51	22.38	12.20	-
12	11	15	93.77	78.81	25.25	14.91	-
8	6	15	114.42	124.08	13.77	10.81	-
6	10	18	51.74	53.67	19.13	11.82	-
11	13	28	72.85	60.10	15.99	8.71	-
6	14	50	37.00	36.29	9.64	5.07	-
11	14	36	67.67	54.92	13.39	7.04	-
9	27	100	28.80	22.34	9.30	3.55	-
12	8	30	128.58	118.04	9.18	6.30	-
16	18	76	76.50	53.09	8.16	3.80	-
11	13	30	72.85	60.10	14.92	8.13	-
14	22	42	54.86	37.89	18.04	7.62	-
6	4	18	128.58	166.46	7.65	7.22	-
10	6	20	142.71	148.04	10.33	8.11	-

Appendix H:
Zircon Fission-track analyses (Huanca basin)

These analyses were performed at Université de Grenoble fission-track laboratory with ζ = 128 ± 9 for glass dosimeter CN1.

1M19

Plutonic weathered pluricentimetric clasts of a conglomerate (U-Pb = 80.6 ± 0.4 Ma)
Huanca
Lat. / Long. : -16.12189 ; -71.81254
Alt. = 2992 m.

	Age	2σ se(t)	Min (2σ)	Max (2σ)	P(X2) (%)	Dispersion (%)
Pooled	49.71	8.16	41.54	57.87	35.20	3.00
Mean	52.66	5.61	47.05	58.27		
Central	49.60	8.20	41.40	57.80		

Single grain data :

n	Nd	ρd	rse(ρd)	Mean Length
33	9115.00	2.17E+05	1.20	-

Ns	Ni	Counted squares	Age (Ma)	2σ se(t)	U (ppm)	Uerr (%)	Mean Dpar
39	17	14	31.92	19.08	348.12	166.64	-
55	9	15	84.69	62.04	172.01	111.69	-
24	5	9	66.61	66.15	159.27	135.88	-
52	12	10	60.17	39.44	344.03	194.79	-
101	26	32	53.96	24.90	232.93	90.67	-
103	27	20	53.00	24.08	387.03	147.90	-
172	47	49	50.85	18.18	274.99	80.07	-
68	27	20	35.04	16.67	387.03	147.90	-
59	12	11	68.23	44.25	312.75	177.08	-
87	17	20	71.00	38.94	243.69	116.65	-
56	13	9	59.81	37.76	414.11	225.63	-
68	15	16	62.93	36.96	268.77	136.69	-
359	101	70	49.39	13.09	413.65	82.71	-
47	10	16	65.23	46.34	179.18	110.68	-
36	16	15	31.31	19.32	305.80	150.74	-
28	11	12	35.41	25.68	262.80	155.12	-
41	17	12	33.56	19.92	406.14	194.42	-
55	15	16	50.95	30.52	268.77	136.69	-
13	3	6	60.17	77.53	143.34	153.28	-
131	43	100	42.36	16.02	123.28	37.50	-
44	8	12	76.27	59.59	191.13	131.19	-
51	19	15	37.34	20.74	363.14	164.70	-
15	4	4	52.10	59.09	286.69	270.38	-

Ns	Ni	Counted squares	Age (Ma)	2σ se(t)	U (ppm)	Uerr (%)	Mean Dpar
116	22	28	73.14	35.51	225.26	95.13	-
114	29	35	54.61	23.96	237.54	87.66	-
125	38	30	45.73	18.10	363.14	117.37	-
32	8	20	55.56	44.60	114.68	78.71	-
97	28	21	48.15	21.72	382.25	143.50	-
68	23	18	41.11	20.65	366.32	151.39	-
18	8	4	31.31	26.97	573.38	393.57	-
76	30	20	35.24	15.97	430.03	156.08	-
65	10	14	90.04	62.45	204.78	126.49	-
28	13	12	29.98	20.55	310.58	169.22	-

1M20

Fined grained matrix of a red-conglomerate
Huanca
Lat. / Long. : -16.12189 ; -71.81254
Alt. = 2992 m.

	Age	2σ se(t)	Min (2σ)	Max (2σ)	P(X2) (%)	Dispersion (%)
Pooled	95.47	16.24	79.23	111.71	0.00	54.00
Mean	128.60	26.01	102.59	154.61		
Central	91.40	20.00	71.40	111.40		

Single grain data :

n	Nd	ρd	rse(ρd)	Mean Length
69	9115.00	2.18E+05	1.18	-

Ns	Ni	Counted squares	Age (Ma)	2σ se(t)	U (ppm)	Uerr (%)	Mean Dpar
27	5	4	75.00	73.78	357.83	305.27	-
28	14	8	27.88	18.66	500.96	263.38	-
36	6	6	83.28	74.36	286.26	224.66	-
29	3	4	133.66	163.19	214.70	229.58	-
35	5	6	97.06	93.79	238.55	203.52	-
10	2	3	69.48	108.07	190.84	241.44	-
35	8	6	60.83	48.43	381.68	261.99	-
37	6	10	85.58	76.27	171.76	134.80	-
11	6	9	25.56	26.19	190.84	149.78	-
53	11	10	66.96	45.35	314.89	185.86	-
30	4	15	103.94	111.60	76.34	71.99	-
24	5	6	66.71	66.25	238.55	203.52	-
19	5	4	52.87	53.66	357.83	305.27	-
63	13	10	67.35	42.10	372.14	202.76	-
18	3	4	83.28	104.52	214.70	229.58	-
62	39	14	22.17	9.58	797.45	254.46	-
90	23	17	54.44	26.55	387.30	160.05	-
17	2	6	117.67	176.69	95.42	120.72	-
125	10	25	172.31	115.78	114.51	70.73	-
55	1	12	725.94	1468.52	23.86	38.96	-
33	3	4	151.88	184.39	214.70	229.58	-
13	2	4	90.18	137.56	143.13	181.08	-
20	6	4	46.40	43.68	429.39	337.00	-
39	6	6	90.18	80.08	286.26	224.66	-
39	8	26	67.75	53.43	88.08	60.46	-

Ns	Ni	Counted squares	Age (Ma)	2σ se(t)	U (ppm)	Uerr (%)	Mean Dpar
18	3	6	83.28	104.52	143.13	153.05	-
72	4	12	246.69	255.78	95.42	89.99	-
21	1	4	286.91	588.68	71.57	116.88	-
15	3	4	69.48	88.42	214.70	229.58	-
41	5	4	113.55	108.74	357.83	305.27	-
3	4	6	10.47	16.06	190.84	179.98	-
30	3	4	138.22	168.49	214.70	229.58	-
37	4	10	127.95	135.87	114.51	107.99	-
25	4	4	86.73	94.19	286.26	269.98	-
105	8	20	180.81	135.01	114.51	78.60	-
69	3	9	313.58	372.45	95.42	102.03	-
52	7	9	102.96	84.14	222.65	162.68	-
37	4	6	127.95	135.87	190.84	179.98	-
95	7	15	186.87	148.68	133.59	97.61	-
148	7	20	288.81	227.03	100.19	73.21	-
41	5	9	113.55	108.74	159.04	135.68	-
46	6	9	106.23	93.40	190.84	149.78	-
93	7	12	182.99	145.69	166.99	122.01	-
62	5	6	170.95	160.73	238.55	203.52	-
32	3	4	147.32	179.10	214.70	229.58	-
29	4	4	100.50	108.12	286.26	269.98	-
20	4	4	69.48	76.72	286.26	269.98	-
40	6	6	92.47	81.99	286.26	224.66	-
58	3	8	264.60	315.50	107.35	114.79	-
34	4	6	117.67	125.48	190.84	179.98	-
7	2	6	48.71	78.41	95.42	120.72	-
25	4	4	86.73	94.19	286.26	269.98	-
125	42	30	41.45	15.88	400.77	123.31	-
159	6	20	359.98	303.61	85.88	67.40	-
108	29	18	51.82	22.85	461.20	170.18	-
27	4	4	93.62	101.16	286.26	269.98	-
78	4	18	266.83	276.11	63.61	59.99	-
27	1	4	366.59	748.38	71.57	116.88	-
10	5	6	27.88	30.79	238.55	203.52	-
18	2	4	124.53	186.44	143.13	181.08	-
22	4	12	76.38	83.72	95.42	89.99	-
66	11	15	83.28	55.48	209.93	123.91	-
26	3	4	119.96	147.24	214.70	229.58	-
61	12	8	70.63	45.69	429.39	243.11	-
50	7	12	99.03	81.11	166.99	122.01	-
55	3	6	251.17	299.89	143.13	153.05	-
168	13	32	178.06	105.49	116.29	63.36	-
68	10	16	94.31	65.22	178.91	110.51	-
61	12	12	70.63	45.69	286.26	162.08	-

1M28

Mid to fine-grained red sandstone at the base of the "red beds" serie
Querque
Lat. / Long. : -15.88321 ; -72.09644
Alt. = 4055 m.

	Age	2σ se(t)	Min (2σ)	Max (2σ)	P(X2) (%)	Dispersion (%)
Pooled	45.05	7.64	37.42	52.69	0.04	33.00
Mean	59.17	10.53	48.64	69.70		
Central	44.70	8.60	36.10	53.30		

Single grain data :

n	Nd	ρd	rse(ρd)	Mean Length
70	7335.00	1.86E+05	1.17	-

Ns	Ni	Counted squares	Age (Ma)	2σ se(t)	U (ppm)	Uerr (%)	Mean Dpar
35	7	9	59.46	49.94	260.37	190.24	-
27	11	6	29.26	21.33	613.72	362.24	-
40	9	4	52.88	39.71	753.21	489.06	-
25	5	7	59.46	58.85	239.11	203.99	-
35	9	6	46.29	35.20	502.14	326.04	-
65	16	21	48.35	27.82	255.05	125.72	-
20	6	8	39.70	37.37	251.07	197.04	-
33	3	8	130.09	157.95	125.53	134.23	-
84	19	15	52.60	27.72	424.03	192.30	-
44	19	10	27.61	15.64	636.04	288.45	-
52	13	12	47.61	30.27	362.65	197.59	-
24	12	6	23.85	17.19	669.52	379.06	-
28	11	8	30.34	22.01	460.29	271.68	-
67	7	15	113.35	91.43	156.22	114.15	-
19	8	4	28.31	24.19	669.52	459.55	-
17	2	4	100.76	151.30	167.38	211.76	-
40	9	18	52.88	39.71	167.38	108.68	-
52	17	15	36.44	20.99	379.39	181.60	-
37	7	8	62.84	52.54	292.91	214.02	-
6	5	15	14.32	17.46	111.59	95.20	-
51	3	12	199.96	239.23	83.69	89.49	-
27	27	24	11.94	6.71	376.60	143.90	-
40	4	9	118.37	125.25	148.78	140.32	-

Ns	Ni	Counted squares	Age (Ma)	2σ se(t)	U (ppm)	Uerr (%)	Mean Dpar
21	2	4	124.24	184.69	167.38	211.76	-
22	5	6	52.35	52.39	278.97	237.99	-
16	4	5	47.61	53.65	267.81	252.57	-
27	13	6	24.77	17.08	725.31	395.17	-
14	5	4	33.36	35.08	418.45	356.99	-
20	11	8	21.69	16.56	460.29	271.68	-
18	3	8	71.29	89.47	125.53	134.23	-
21	5	6	49.98	50.23	278.97	237.99	-
66	9	20	87.02	63.03	150.64	97.81	-
13	7	10	22.15	21.00	234.33	171.22	-
78	18	25	51.56	27.91	241.03	112.22	-
37	4	9	109.57	116.36	148.78	140.32	-
18	5	4	42.87	43.75	418.45	356.99	-
6	3	4	23.85	33.89	251.07	268.47	-
26	7	8	44.22	38.17	292.91	214.02	-
33	5	12	78.37	76.02	139.48	119.00	-
19	3	15	75.22	94.06	66.95	71.59	-
22	1	10	257.61	528.04	33.48	54.67	-
10	3	9	39.70	52.56	111.59	119.32	-
22	10	6	26.23	20.34	557.93	344.61	-
20	4	8	59.46	65.66	167.38	157.86	-
10	4	20	29.80	35.50	66.95	63.14	-
46	16	12	34.26	20.45	446.34	220.01	-
21	5	6	49.98	50.23	278.97	237.99	-
18	3	9	71.29	89.47	111.59	119.32	-
16	4	4	47.61	53.65	334.76	315.71	-
30	6	6	59.46	53.83	334.76	262.72	-
54	14	9	45.92	28.28	520.74	273.77	-
67	20	20	39.90	21.09	334.76	148.08	-
34	9	8	44.98	34.30	376.60	244.53	-
13	4	4	38.71	44.60	334.76	315.71	-
7	1	4	83.09	178.03	83.69	136.68	-
20	2	4	118.37	176.36	167.38	211.76	-
6	5	3	14.32	17.46	557.93	475.98	-
20	4	4	59.46	65.66	334.76	315.71	-
10	3	9	39.70	52.56	111.59	119.32	-
25	13	9	22.93	16.01	483.54	263.45	-
17	1	6	199.96	412.47	55.79	91.12	-
24	11	9	26.01	19.29	409.15	241.49	-
14	2	4	83.09	126.16	167.38	211.76	-
49	13	15	44.87	28.70	290.12	158.07	-
29	8	6	43.16	35.00	446.34	306.37	-
22	7	6	37.44	32.91	390.55	285.36	-
51	14	12	43.37	26.87	390.55	205.33	-

Ns	Ni	Counted squares	Age (Ma)	2σ se(t)	U (ppm)	Uerr (%)	Mean Dpar
16	4	4	47.61	53.65	334.76	315.71	-
23	7	4	39.13	34.23	585.83	428.05	-
50	16	25	37.23	22.01	214.25	105.61	-

1M30

Red sandstones with few conglomeratic beds
Huanca
Lat. / Long. : -15.90835 ; -72.13488
Alt. = 4144 m.

	Age	2σ se(t)	Min (2σ)	Max (2σ)	P(X2) (%)	Dispersion (%)
Pooled	150.06	25.25	124.81	175.32	0.00	50.00
Mean	198.75	31.74	167.01	230.49		
Central	137.50	27.40	110.10	164.90		

Single grain data :

n	Nd	ρd	rse(ρd)	Mean Length
100	9115.00	2.18E+05	1.15	-

Ns	Ni	Counted squares	Age (Ma)	2σ se(t)	U (ppm)	Uerr (%)	Mean Dpar
91	3	16	411.65	486.50	53.51	57.22	-
63	3	9	287.76	342.46	95.13	101.72	-
50	3	8	229.43	274.62	107.02	114.44	-
35	2	9	240.69	351.58	63.42	80.23	-
92	5	16	252.82	234.86	89.18	76.08	-
79	9	10	121.85	87.40	256.85	166.77	-
6	2	4	41.90	68.68	142.70	180.53	-
17	3	6	78.92	99.46	142.70	152.58	-
16	5	4	44.69	46.21	356.74	304.34	-
66	7	12	130.79	105.57	166.48	121.64	-
27	3	4	124.90	153.02	214.04	228.87	-
27	1	4	367.68	750.60	71.35	116.52	-
22	2	6	152.33	226.01	95.13	120.35	-
52	3	8	238.44	285.10	107.02	114.44	-
25	3	5	115.73	142.35	171.23	183.10	-
24	2	9	166.01	245.45	63.42	80.23	-
36	2	4	247.43	361.17	142.70	180.53	-
64	7	10	126.87	102.55	199.77	145.97	-
95	1	20	1210.22	2439.00	14.27	23.30	-
118	7	18	232.00	183.38	110.99	81.09	-
31	2	4	213.63	313.13	142.70	180.53	-
74	4	15	254.17	263.35	76.10	71.77	-
29	2	4	200.06	293.85	142.70	180.53	-

Ns	Ni	Counted squares	Age (Ma)	2σ se(t)	U (ppm)	Uerr (%)	Mean Dpar
84	10	32	116.65	79.72	89.18	55.08	-
97	18	18	75.08	39.94	285.39	132.87	-
24	1	4	327.84	670.77	71.35	116.52	-
48	4	12	166.01	174.33	95.13	89.72	-
46	15	19	42.83	26.16	225.31	114.57	-
48	7	6	95.38	78.32	332.96	243.28	-
38	9	8	58.90	44.44	321.06	208.47	-
11	5	4	30.76	33.45	356.74	304.34	-
89	7	16	175.75	140.15	124.86	91.23	-
83	6	15	191.00	163.67	114.16	89.59	-
11	2	8	76.62	118.28	71.35	90.26	-
68	3	10	310.06	368.39	85.62	91.55	-
37	1	6	498.70	1013.18	47.57	77.68	-
49	2	10	334.50	484.86	57.08	72.21	-
33	2	5	227.17	332.38	114.16	144.42	-
19	5	4	53.03	53.82	356.74	304.34	-
31	4	8	107.70	115.42	142.70	134.57	-
36	3	10	166.01	200.85	85.62	91.55	-
105	8	30	181.35	135.42	76.10	52.24	-
16	4	4	55.81	62.88	285.39	269.15	-
20	4	6	69.69	76.96	190.26	179.43	-
40	6	9	92.75	82.24	190.26	149.32	-
83	4	18	284.41	293.88	63.42	59.81	-
66	6	12	152.33	131.64	142.70	111.99	-
29	5	5	80.77	79.03	285.39	243.47	-
49	5	8	135.89	129.00	178.37	152.17	-
80	8	12	138.63	104.62	190.26	130.59	-
12	1	4	166.01	346.34	71.35	116.52	-
36	4	8	124.90	132.81	142.70	134.57	-
113	7	22	222.34	175.96	90.81	66.35	-
40	2	6	274.35	399.41	95.13	120.35	-
63	7	12	124.90	101.04	166.48	121.64	-
67	10	13	93.21	64.52	219.53	135.59	-
34	4	8	118.03	125.86	142.70	134.57	-
41	5	8	113.90	109.07	178.37	152.17	-
25	3	3	115.73	142.35	285.39	305.17	-
118	7	20	232.00	183.38	99.89	72.98	-
10	1	4	138.63	291.44	71.35	116.52	-
18	1	9	247.43	509.60	31.71	51.79	-
225	11	40	280.45	177.57	78.48	46.32	-
21	2	4	145.49	216.28	142.70	180.53	-
46	4	15	159.17	167.43	76.10	71.77	-
123	4	32	417.12	427.83	35.67	33.64	-
83	7	23	164.05	131.15	86.86	63.46	-

Ns	Ni	Counted squares	Age (Ma)	2σ se(t)	U (ppm)	Uerr (%)	Mean Dpar
28	5	6	78.00	76.52	237.83	202.89	-
41	11	18	52.02	36.07	174.41	102.94	-
70	3	12	318.96	378.74	71.35	76.29	-
21	2	4	145.49	216.28	142.70	180.53	-
25	3	4	115.73	142.35	214.04	228.87	-
73	3	10	332.28	394.23	85.62	91.55	-
19	2	6	131.77	196.78	95.13	120.35	-
28	1	6	380.90	777.10	47.57	77.68	-
146	21	40	96.70	47.11	149.83	64.72	-
35	3	6	161.45	195.56	142.70	152.58	-
140	3	30	622.88	732.08	28.54	30.52	-
32	1	4	433.52	882.56	71.35	116.52	-
20	5	4	55.81	56.35	356.74	304.34	-
46	3	6	211.37	253.62	142.70	152.58	-
28	4	10	97.36	104.96	114.16	107.66	-
13	3	6	60.44	77.88	142.70	152.58	-
59	4	16	203.45	212.15	71.35	67.29	-
52	2	10	354.43	513.17	57.08	72.21	-
77	15	25	71.54	41.60	171.23	87.08	-
63	2	10	426.97	616.22	57.08	72.21	-
24	9	6	37.26	29.59	428.09	277.95	-
90	7	15	177.70	141.64	133.18	97.31	-
26	1	4	354.43	724.05	71.35	116.52	-
40	3	12	184.19	222.01	71.35	76.29	-
30	1	6	407.26	829.94	47.57	77.68	-
199	5	36	534.92	490.13	39.64	33.82	-
47	13	20	50.47	32.40	185.50	101.07	-
27	2	4	186.46	274.52	142.70	180.53	-
49	5	10	135.89	129.00	142.70	121.74	-
20	3	30	92.75	115.58	28.54	30.52	-
24	6	6	55.81	51.54	285.39	223.98	-
53	17	15	43.54	25.02	323.44	154.81	-
153	11	40	192.03	122.85	78.48	46.32	-

1M31

Matrix of a conglomerate. Clasts = weathered andesites, quartzites, very few limestones, no basement, no granitoïd

Querque

Lat. / Long. : -16.90835 ; -72.14540

Alt. = 4234 m.

	Age	2σ se(t)	Min (2σ)	Max (2σ)	P(X2) (%)	Dispersion (%)
Pooled	108.67	17.96	90.71	126.62	0.00	54.00
Mean	147.60	16.85	130.75	164.45		
Central	105.40	21.00	84.40	126.40		

Single grain data :

n	Nd	ρd	rse(ρd)	Mean Length
100	9115.00	2.19E+05	1.12	-

Ns	Ni	Counted squares	Age (Ma)	2σ se(t)	U (ppm)	Uerr (%)	Mean Dpar
36	5	4	100.41	96.86	355.69	303.43	-
35	3	6	161.92	196.13	142.27	152.13	-
44	3	10	202.91	243.81	85.36	91.28	-
53	2	36	362.09	524.09	15.81	20.00	-
24	7	14	48.01	41.79	142.27	103.95	-
47	3	8	216.52	259.63	106.71	114.10	-
40	3	6	184.73	222.66	142.27	152.13	-
17	3	4	79.16	99.75	213.41	228.20	-
30	3	4	139.04	169.50	213.41	228.20	-
91	4	24	312.07	321.82	47.42	44.73	-
28	6	8	65.26	59.42	213.41	167.48	-
94	5	17	258.96	240.43	83.69	71.40	-
41	4	6	142.48	150.58	189.70	178.90	-
56	25	30	31.41	15.73	237.12	94.07	-
15	1	4	207.45	429.48	71.14	116.18	-
21	1	4	288.60	592.15	71.14	116.18	-
12	2	4	83.78	128.51	142.27	179.99	-
40	6	10	93.03	82.48	170.73	133.99	-
25	5	6	69.89	69.17	237.12	202.29	-
26	12	18	30.38	21.62	189.70	107.39	-
39	2	10	268.41	390.99	56.91	72.00	-
37	10	10	51.79	37.62	284.55	175.74	-

Ns	Ni	Counted squares	Age (Ma)	2σ se(t)	U (ppm)	Uerr (%)	Mean Dpar
38	3	6	175.62	212.06	142.27	152.13	-
89	3	18	404.03	477.67	47.42	50.71	-
50	6	8	116.07	101.60	213.41	167.48	-
22	2	5	152.78	226.68	113.82	143.99	-
61	3	35	279.63	333.03	24.39	26.08	-
33	2	6	227.83	333.34	94.85	119.99	-
43	5	12	119.75	114.39	118.56	101.14	-
17	3	4	79.16	99.75	213.41	228.20	-
106	9	15	163.45	115.77	170.73	110.85	-
41	3	6	189.28	227.95	142.27	152.13	-
49	9	9	76.07	56.19	284.55	184.75	-
54	7	20	107.52	87.68	99.59	72.77	-
72	8	16	125.27	94.99	142.27	97.65	-
87	5	12	240.03	223.30	118.56	101.14	-
69	4	14	238.00	247.04	81.30	76.67	-
16	1	6	221.05	456.74	47.42	77.45	-
109	10	24	151.41	102.26	118.56	73.23	-
25	2	4	173.34	255.90	142.27	179.99	-
18	4	6	62.94	70.13	189.70	178.90	-
25	3	6	116.07	142.77	142.27	152.13	-
165	8	36	283.55	209.09	63.23	43.40	-
62	10	20	86.56	60.22	142.27	87.87	-
22	7	15	44.02	38.70	132.79	97.02	-
20	5	6	55.98	56.52	237.12	202.29	-
56	3	12	257.16	306.90	71.14	76.07	-
20	7	9	40.03	35.60	221.32	161.70	-
74	8	24	128.71	97.48	94.85	65.10	-
27	3	8	125.27	153.47	106.71	114.10	-
21	3	4	97.64	121.30	213.41	228.20	-
46	7	9	91.71	75.50	221.32	161.70	-
38	7	8	75.85	63.29	248.98	181.91	-
53	7	12	105.55	86.16	165.99	121.28	-
25	2	4	173.34	255.90	142.27	179.99	-
18	1	4	248.15	511.08	71.14	116.18	-
67	7	12	133.14	107.39	165.99	121.28	-
26	2	4	180.17	265.61	142.27	179.99	-
39	3	12	180.17	217.36	71.14	76.07	-
21	5	12	58.76	59.05	118.56	101.14	-
40	2	12	275.14	400.56	47.42	60.00	-
31	2	6	214.25	314.05	94.85	119.99	-
38	9	9	59.07	44.57	284.55	184.75	-
18	1	4	248.15	511.08	71.14	116.18	-
16	4	6	55.98	63.07	189.70	178.90	-
73	13	30	78.44	48.48	123.30	67.18	-

Ns	Ni	Counted squares	Age (Ma)	2σ se(t)	U (ppm)	Uerr (%)	Mean Dpar
27	4	9	94.18	101.77	126.47	119.27	-
32	2	9	221.05	323.70	63.23	80.00	-
30	1	9	408.43	832.32	31.62	51.63	-
21	4	5	73.37	80.70	227.64	214.68	-
37	6	20	86.09	76.73	85.36	66.99	-
16	2	4	111.47	167.93	142.27	179.99	-
51	7	12	101.60	83.12	165.99	121.28	-
45	5	24	125.27	119.39	59.28	50.57	-
130	12	60	150.49	93.21	56.91	32.22	-
33	5	10	92.10	89.33	142.27	121.37	-
34	21	20	22.72	13.00	298.78	129.05	-
29	3	12	134.45	164.16	71.14	76.07	-
65	4	15	224.44	233.35	75.88	71.56	-
30	12	14	35.04	24.43	243.90	138.08	-
32	3	15	148.20	180.16	56.91	60.85	-
60	14	40	59.96	36.56	99.59	52.36	-
46	6	12	106.86	93.96	142.27	111.65	-
31	3	9	143.62	174.83	94.85	101.42	-
33	10	10	46.22	33.98	284.55	175.74	-
78	9	70	120.67	86.62	36.58	23.75	-
14	2	5	97.64	148.25	113.82	143.99	-
51	4	16	176.75	185.21	71.14	67.09	-
54	5	20	150.03	141.82	71.14	60.69	-
35	5	9	97.64	94.35	158.08	134.86	-
37	19	18	27.31	15.88	300.36	136.20	-
74	6	24	171.05	147.17	71.14	55.83	-
25	5	8	69.89	69.17	177.84	151.72	-
50	13	25	53.83	34.35	147.97	80.61	-
22	2	10	152.78	226.68	56.91	72.00	-
42	4	15	145.91	154.06	75.88	71.56	-
23	2	12	159.64	236.43	47.42	60.00	-
20	1	8	275.14	565.18	35.57	58.09	-
112	14	100	111.47	65.08	39.84	20.94	-
42	4	12	145.91	154.06	94.85	89.45	-
40	3	10	184.73	222.66	85.36	91.28	-
107	22	70	68.00	33.22	89.43	37.76	-

Appendix I:
Apatite Fission-track analyses (Huanca basin)

These analyses were performed at Université de Grenoble fission-track laboratory with ζ = 254 ± 12 for glass dosimeter IRMM540.

1M19

Fine grained matrix of a red conglomerate
East of Huasamayo
Lat. / Long. : -16.12189 ; -71.81254
Alt. = 2992 m.

	Age	2σ se(t)	Min (2σ)	Max (2σ)	P(X2) (%)	Dispersion (%)
Pooled	72.9	12.3	60.6	85.1	0.08	33.00
Mean	96.6	23.4	73.2	120.0		
Central	80.5	18.0	62.5	98.5		

Single grain data :

n	Nd	ρd	rse(ρd)	Mean Length
24	8323.00	5.94E+05	1.10	-

Ns	Ni	Counted squares	Age (Ma)	2σ se(t)	U (ppm)	Uerr (%)	Mean Dpar
6	9	16	50.07	53.00	22.24	14.44	3.36
22	22	50	74.96	45.78	17.40	7.35	3.47
18	14	49	96.21	69.20	11.30	5.94	1.65
38	35	25	81.34	38.92	55.36	18.62	1.4
3	10	42	22.58	29.81	9.41	5.81	2.77
17	4	16	312.71	348.88	9.89	9.32	2.06
43	39	100	82.60	37.40	15.42	4.92	3.11
16	10	25	119.52	97.05	15.82	9.77	3.33
18	9	25	149.05	122.56	14.24	9.24	3.73
9	9	35	74.96	71.04	10.17	6.60	3.01
11	8	40	102.84	96.09	7.91	5.43	4.1
6	3	18	149.05	211.29	6.59	7.05	3.66
20	12	24	124.45	91.68	19.77	11.19	3.3
21	32	60	49.29	28.09	21.09	7.41	4.01
24	24	36	74.96	43.88	26.36	10.67	3.92
17	9	12	140.86	116.94	29.66	19.25	-
12	8	28	112.11	102.92	11.30	7.75	3.57
41	96	68	32.12	12.38	55.82	11.43	4.07
12	11	25	81.73	68.69	17.40	10.27	3.12
18	23	30	58.74	37.40	30.32	12.52	3.31
15	10	40	112.11	92.18	9.89	6.11	2.68
8	10	24	60.03	57.25	16.48	10.18	3.67
14	14	42	74.96	57.13	13.18	6.93	2.91
9	9	30	74.96	71.04	11.86	7.70	-

1M20

Fine grained matrix of a red conglomerate
East of Huasamayo
Lat. / Long. : -16.12189 ; -71.81254
Alt. = 2992 m.

	Age	2σ se(t)	Min (2σ)	Max (2σ)	P(X2) (%)	Dispersion (%)
Pooled	59.7	8.6	51.1	68.3	0.02	33.00
Mean	77.7	16.0	61.7	93.6		
Central	63.2	11.8	51.4	75.0		

Single grain data :

n	Nd	ρd	rse(ρd)	Mean Length
39	8323.00	5.90E+05	1.10	-

Ns	Ni	Counted squares	Age (Ma)	2σ se(t)	U (ppm)	Uerr (%)	Mean Dpar
41	42	100	72.74	32.71	16.71	5.14	3.7
17	20	100	63.38	42.27	7.96	3.52	3.79
24	25	100	71.54	41.47	9.95	3.95	3.73
26	24	70	80.67	46.34	13.64	5.52	3.86
20	27	100	55.27	33.05	10.74	4.10	3.8
26	46	28	42.22	21.12	65.36	19.22	3.64
5	7	30	53.30	62.64	9.28	6.78	2.47
2	1	16	148.15	363.18	2.49	4.06	2.47
3	3	40	74.50	121.88	2.98	3.19	4.23
30	15	100	148.15	94.80	5.97	3.03	3.5
4	10	28	29.90	35.50	14.21	8.78	2.7
22	25	70	65.61	38.88	14.21	5.64	4.16
15	14	70	79.79	59.81	7.96	4.18	2.81
11	3	100	269.06	351.47	1.19	1.28	3.58
6	12	50	37.36	37.53	9.55	5.41	1.66
13	12	28	80.67	65.06	17.05	9.65	3.59
19	38	100	37.36	21.30	15.12	4.88	3.39
5	10	32	37.36	41.08	12.43	7.68	-
31	80	50	28.97	12.58	63.66	14.26	2.94
12	9	40	99.15	87.97	8.95	5.81	3.02
20	14	40	106.17	74.71	13.92	7.32	3.29
7	5	48	104.06	122.28	4.14	3.54	3.84
7	8	40	65.24	67.82	7.96	5.46	1.83

Ns	Ni	Counted squares	Age (Ma)	2σ se(t)	U (ppm)	Uerr (%)	Mean Dpar
3	11	30	20.40	26.65	14.59	8.61	2.59
25	58	20	32.22	15.73	115.38	30.28	3.17
20	24	36	62.14	38.11	26.52	10.73	2.94
12	12	80	74.50	61.26	5.97	3.38	3.92
7	12	80	43.56	41.65	5.97	3.38	4.36
8	16	28	37.36	32.56	22.73	11.20	4.06
6	6	70	74.50	86.33	3.41	2.68	4.57
15	15	100	74.50	54.89	5.97	3.03	2.17
20	23	91	64.83	40.14	10.06	4.15	3.73
51	37	100	102.47	45.36	14.72	4.82	4.02
6	8	100	55.96	60.68	3.18	2.18	4.01
15	14	80	79.79	59.81	6.96	3.66	3.82
11	18	50	45.63	35.21	14.32	6.67	4.14
38	68	40	41.74	17.39	67.63	16.41	2.63
10	4	16	184.67	219.23	9.95	9.38	2.22
12	5	100	177.38	189.62	1.99	1.70	3.65

1M28

Mid to fine grained sandstone at the bottom of the red beds serie
East of Huasamayo
Lat. / Long. : -15.88321 ; 72.09644
Alt. = 4055 m.

	Age	2σ se(t)	Min (2σ)	Max (2σ)	P(X2) (%)	Dispersion (%)
Pooled	82.66	9.96	72.70	92.62	35.10	12.00
Mean	96.12	9.13	86.99	105.25		
Central	83.00	10.20	72.80	93.20		

Single grain data :

n	Nd	ρd	rse(ρd)	Mean Length
100	8323.00	5.83E+05	1.13	-

Ns	Ni	Counted squares	Age (Ma)	2σ se(t)	U (ppm)	Uerr (%)	Mean Dpar
7	3	12	170.38	235.73	10.07	10.77	2.39
11	4	24	200.34	234.75	6.71	6.33	1.87
6	4	12	110.05	142.47	13.43	12.67	2.19
5	3	20	122.16	178.82	6.04	6.46	3.04
5	4	16	91.84	123.53	10.07	9.50	2.46
8	11	49	53.59	50.07	9.04	5.34	2.49
12	6	100	146.32	147.00	2.42	1.90	1.82
24	15	16	117.32	78.06	37.77	19.21	2.69
13	15	32	63.81	48.76	18.89	9.60	2.37
14	17	56	60.65	44.17	12.23	5.85	2.45
20	10	28	146.32	114.22	14.39	8.89	2.36
24	21	90	84.02	50.87	9.40	4.06	2.39
37	39	100	69.82	32.76	15.71	5.01	2.65
10	12	34	61.37	52.89	14.22	8.05	2.56
15	11	40	100.12	80.08	11.08	6.54	2.9
7	3	28	170.38	235.73	4.32	4.62	2.32
40	45	100	65.44	29.14	18.13	5.39	2.44
12	16	42	55.26	42.54	15.35	7.56	2.77
9	10	50	66.25	61.22	8.06	4.98	3.13
6	4	18	110.05	142.47	8.95	8.44	2.45
61	36	90	124.18	53.57	16.12	5.35	2.71
5	4	21	91.84	123.53	7.67	7.24	2.2
13	9	40	106.01	92.51	9.07	5.89	2.43

Ns	Ni	Counted squares	Age (Ma)	2σ se(t)	U (ppm)	Uerr (%)	Mean Dpar
11	9	35	89.81	81.20	10.36	6.73	3.21
20	11	16	133.15	100.80	27.70	16.35	2.62
18	17	60	77.88	53.21	11.42	5.46	2.44
4	4	10	73.57	104.29	16.12	15.20	2.73
21	17	60	90.76	59.88	11.42	5.46	2.38
16	9	48	130.22	109.25	7.55	4.90	1.95
52	46	20	83.11	34.60	92.67	27.26	2.76
7	8	15	64.42	66.98	21.49	14.75	2.3
36	13	49	201.72	132.00	10.69	5.82	2.57
28	30	64	68.70	36.71	18.89	6.85	1.72
4	8	35	36.89	45.32	9.21	6.32	2.36
30	40	80	55.26	27.23	20.14	6.35	2.48
16	16	42	73.57	52.51	15.35	7.56	3.01
10	10	32	73.57	66.19	12.59	7.78	2.74
18	22	72	60.26	38.75	12.31	5.20	2.56
19	16	30	87.28	59.83	21.49	10.59	2.34
17	12	42	103.98	79.06	11.51	6.52	2.86
13	17	100	56.34	41.87	6.85	3.28	2.31
14	24	35	43.02	29.23	27.63	11.18	2.68
8	8	28	73.57	73.92	11.51	7.90	2.18
9	8	20	82.71	80.78	16.12	11.06	2.36
21	5	20	303.52	303.50	10.07	8.59	1.88
35	33	60	78.01	38.60	22.16	7.67	2.78
22	24	100	67.47	40.37	9.67	3.91	2.74
16	12	60	97.91	75.38	8.06	4.56	2.46
14	13	80	79.20	61.49	6.55	3.57	2.41
8	12	25	49.14	45.11	19.34	10.95	2.24
11	5	48	160.77	174.12	4.20	3.58	2.46
11	4	8	200.34	234.75	20.14	19.00	2.79
9	5	28	131.83	147.62	7.19	6.14	2.65
13	11	36	86.86	71.67	12.31	7.27	2.26
30	25	49	88.19	48.52	20.56	8.15	2.46
20	6	40	242.05	226.56	6.04	4.74	2.66
14	17	40	60.65	44.17	17.12	8.20	2.38
10	6	44	122.16	126.72	5.49	4.31	2.19
12	15	30	58.93	46.00	20.14	10.24	2.38
7	6	36	85.76	95.78	6.71	5.27	2.38
32	19	70	123.43	72.49	10.94	4.96	2.4
14	12	24	85.76	67.98	20.14	11.40	1.98
10	18	64	40.98	32.57	11.33	5.28	2.43
26	18	35	106.01	65.82	20.72	9.65	2.03
5	2	32	182.38	305.70	2.52	3.19	2.33
37	27	62	100.61	51.86	17.55	6.70	2.15
24	30	70	58.93	32.78	17.27	6.27	2.39

Ns	Ni	Counted squares	Age (Ma)	2σ se(t)	U (ppm)	Uerr (%)	Mean Dpar
11	9	28	89.81	81.20	12.95	8.41	2.43
16	8	24	146.32	127.51	13.43	9.22	3.03
15	10	45	110.05	90.49	8.95	5.53	2.8
19	14	80	99.65	70.86	7.05	3.71	2
14	7	80	146.32	136.21	3.53	2.58	2.52
11	11	35	73.57	63.15	12.66	7.47	2.39
6	6	30	73.57	85.26	8.06	6.32	1.75
26	27	54	70.86	39.54	20.14	7.70	2.74
11	6	30	134.25	136.89	8.06	6.32	2.51
24	25	100	70.65	40.96	10.07	4.00	2.43
8	11	50	53.59	50.07	8.86	5.23	2.31
10	18	70	40.98	32.57	10.36	4.82	1.72
15	15	70	73.57	54.20	8.63	4.39	2.27
14	18	59	57.30	41.21	12.29	5.72	2.21
16	11	42	106.74	84.25	10.55	6.23	2.54
16	19	85	62.01	42.51	9.01	4.08	2.2
5	3	12	122.16	178.82	10.07	10.77	2.29
10	10	36	73.57	66.19	11.19	6.91	2.16
20	23	28	64.02	39.64	33.09	13.67	2.52
10	9	24	81.70	75.49	15.11	9.81	2.74
13	15	35	63.81	48.76	17.27	8.78	2.24
21	19	30	81.27	52.06	25.52	11.57	2.51
8	11	49	53.59	50.07	9.04	5.34	2.2
13	11	50	86.86	71.67	8.86	5.23	2.69
26	37	100	51.79	26.98	14.91	4.88	2.64
12	6	20	146.32	147.00	12.09	9.49	2.93
14	10	40	102.77	85.68	10.07	6.22	2.3
17	19	40	65.87	44.44	19.14	8.68	2.28
23	10	72	167.98	128.30	5.60	3.46	2.2
18	23	35	57.65	36.71	26.48	10.94	2.28
47	41	59	84.27	36.93	28.00	8.72	2.28
18	23	100	57.65	36.71	9.27	3.83	2.27
21	23	72	67.21	41.09	12.87	5.32	2.62

1M29

Matrix of a conglomerate with subrounded clasts
East of Huasamayo
Lat. / Long. : -15.89284 ; -72.12676
Alt. = 4086 m.

	Age	2σ se(t)	Min (2σ)	Max (2σ)	P(X2) (%)	Dispersion (%)
Pooled	82.14	9.08	73.06	91.23	0.10	20.00
Mean	90.33	7.34	82.99	97.67		
Central	83.20	9.80	73.40	93.00		

Single grain data :

n	Nd	ρd	rse(ρd)	Mean Length
100	8323.00	5.79E+05	1.16	-

Ns	Ni	Counted squares	Age (Ma)	2σ se(t)	U (ppm)	Uerr (%)	Mean Dpar
9	9	80	73.12	69.30	4.56	2.96	2.84
18	11	40	119.22	91.98	11.15	6.58	2.46
16	14	40	83.50	61.65	14.19	7.46	2.49
18	20	50	65.84	43.26	16.22	7.17	2.69
47	55	40	62.54	25.57	55.74	15.02	2.12
28	22	60	92.92	53.71	14.87	6.28	2.74
23	24	80	70.09	41.46	12.16	4.92	2.84
34	22	40	112.66	62.61	22.30	9.42	2.54
74	69	100	78.39	27.32	27.97	6.74	2.28
19	18	21	77.16	51.31	34.75	16.18	2.62
32	30	60	77.96	40.34	20.27	7.36	2.7
31	23	42	98.36	54.97	22.20	9.17	3.07
13	10	42	94.89	80.36	9.65	5.96	2.73
35	25	70	102.14	54.40	14.48	5.74	2.45
15	18	42	60.99	43.05	17.37	8.09	2.12
27	33	50	59.89	31.62	26.76	9.27	2.62
47	21	70	162.51	86.76	12.16	5.25	2.28
21	9	60	169.34	135.93	6.08	3.95	2.37
48	62	45	56.68	22.48	55.86	14.19	2.5
45	36	100	91.27	41.77	14.59	4.84	2.85
51	62	16	60.21	23.50	157.10	39.91	2.32
42	30	90	102.14	49.83	13.51	4.90	2.48
25	10	25	181.27	136.78	16.22	10.02	2.35

Ns	Ni	Counted squares	Age (Ma)	2σ se(t)	U (ppm)	Uerr (%)	Mean Dpar
50	51	84	71.69	29.37	24.61	6.88	1.96
42	40	100	76.75	34.72	16.22	5.11	2.83
29	13	40	161.99	109.27	13.18	7.18	2.57
51	33	70	112.66	51.51	19.11	6.62	2.79
20	16	70	91.27	61.86	9.27	4.57	2.21
52	35	40	108.34	48.52	35.47	11.94	3.14
22	25	36	64.39	38.16	28.15	11.17	-
44	16	50	199.12	117.85	12.97	6.39	2.49
29	33	70	64.30	33.32	19.11	6.62	2.63
29	31	100	68.43	35.97	12.57	4.49	2.48
41	37	64	80.97	37.55	23.44	7.67	2.45
11	15	25	53.70	42.95	24.32	12.37	2.42
17	22	80	56.57	36.95	11.15	4.71	1.76
72	91	80	57.92	19.12	46.12	9.70	2.07
56	53	100	77.23	30.54	21.49	5.90	2.4
7	7	25	73.12	78.49	11.35	8.29	2.71
36	32	100	82.20	40.73	12.97	4.56	2.25
21	21	42	73.12	45.68	20.27	8.76	2.99
67	17	100	283.49	156.41	6.89	3.30	3.02
9	11	20	59.89	54.15	22.30	13.16	2.46
14	15	35	68.27	51.17	17.37	8.84	2.52
21	20	45	76.75	48.54	18.02	7.97	2.44
35	23	90	110.94	60.52	10.36	4.28	2.2
29	22	60	96.21	55.20	14.87	6.28	2.38
18	22	40	59.89	38.51	22.30	9.42	2.51
34	21	90	117.97	66.48	9.46	4.09	2.57
36	39	100	67.52	31.89	15.81	5.04	-
33	39	70	61.92	29.90	22.59	7.21	2.55
40	31	88	94.19	46.00	14.28	5.10	2.28
33	32	80	75.39	38.12	16.22	5.70	2.8
34	14	70	176.16	113.18	8.11	4.26	2.53
16	22	60	53.26	35.38	14.87	6.28	1.93
15	9	35	121.41	103.06	10.42	6.77	2.34
33	54	25	44.78	20.26	87.57	23.81	2.99
31	21	40	107.65	61.74	21.28	9.19	2.5
14	9	40	113.39	97.51	9.12	5.92	2.92
29	47	64	45.21	21.80	29.77	8.67	2.19
12	15	24	58.56	45.72	25.34	12.89	3.25
15	11	50	99.50	79.59	8.92	5.26	2.21
32	15	70	155.00	98.16	8.69	4.42	1.67
74	72	100	75.14	25.92	29.19	6.89	2.54
43	31	80	101.20	48.69	15.71	5.61	1.9
12	11	28	79.73	67.01	15.93	9.40	3.01
28	18	50	113.39	69.39	14.59	6.79	2.18

Ns	Ni	Counted squares	Age (Ma)	2σ se(t)	U (ppm)	Uerr (%)	Mean Dpar
20	18	50	81.19	53.34	14.59	6.79	3.35
44	40	100	80.39	35.98	16.22	5.11	2.63
13	19	50	50.12	36.41	15.41	6.99	2.44
18	18	60	73.12	49.26	12.16	5.66	2.48
15	17	60	64.56	46.17	11.49	5.50	3.36
46	38	100	88.41	39.70	15.41	4.98	2.24
31	32	70	70.85	36.36	18.53	6.52	2.47
21	14	30	109.37	76.21	18.92	9.95	1.77
36	23	60	114.08	61.90	15.54	6.42	2.49
48	55	100	63.86	25.98	22.30	6.01	2.45
32	24	100	97.31	53.39	9.73	3.94	2.54
40	35	100	83.50	39.49	14.19	4.77	2.56
28	29	100	70.61	38.04	11.76	4.34	2.79
17	18	35	69.08	47.20	20.85	9.71	2.42
22	14	30	114.53	79.10	18.92	9.95	2.35
13	9	18	105.35	91.94	20.27	13.16	2.52
19	13	32	106.59	77.42	16.47	8.97	2.5
11	12	32	67.06	56.36	15.20	8.61	2.61
29	38	81	55.88	28.08	19.02	6.15	2.13
31	20	70	112.98	65.73	11.58	5.12	1.73
38	34	91	81.67	39.36	15.15	5.17	2.94
9	5	54	131.02	146.71	3.75	3.20	1.07
9	9	30	73.12	69.30	12.16	7.90	2.39
22	18	32	89.26	57.39	22.80	10.62	2.59
19	10	48	138.23	108.83	8.45	5.22	2.8
15	19	36	57.79	40.32	21.40	9.70	2.44
44	36	80	89.26	41.04	18.24	6.05	2.33
30	26	70	84.30	45.91	15.06	5.86	1.87
14	13	90	78.71	61.11	5.86	3.19	1.54
19	29	100	48.00	28.71	11.76	4.34	2.49
64	53	100	88.19	33.86	21.49	5.90	2.37
38	38	70	73.12	34.29	22.01	7.11	2.36
55	60	100	67.06	25.87	24.32	6.28	1.73

1M30

Red sandstones with few conglomeratic beds
East of Huasamayo
Lat. / Long. : -15.89489 ; -72.13488
Alt. = 4144 m.

	Age	2σ se(t)	Min (2σ)	Max (2σ)	P(X2) (%)	Dispersion (%)
Pooled	81.07	9.83	71.24	90.90	0.33	25.00
Mean	71.54	22.77	48.77	94.31		
Central	84.20	11.40	72.80	95.60		

Single grain data :

n	Nd	ρd	rse(ρd)	Mean Length
93	8323.00	5.75E+05	1.20	-

Ns	Ni	Counted squares	Age (Ma)	2σ se(t)	U (ppm)	Uerr (%)	Mean Dpar
14	19	45	53.61	38.12	17.23	7.81	3.09
15	6	24	180.13	174.89	10.20	8.01	2.45
18	21	70	62.33	40.49	12.24	5.29	2.8
19	10	26	137.35	108.15	15.69	9.69	2.67
5	7	30	51.98	61.08	9.52	6.96	2.43
56	44	90	92.33	38.26	19.95	6.00	1.51
7	2	30	250.79	402.89	2.72	3.44	3.33
11	2	9	389.84	600.53	9.07	11.47	1.26
15	13	42	83.76	64.00	12.63	6.88	2.4
17	13	60	94.85	70.49	8.84	4.82	2.46
39	15	42	187.23	115.21	14.57	7.41	2.17
35	22	100	115.21	63.68	8.98	3.79	3.14
21	14	35	108.68	75.73	16.32	8.58	1.66
23	27	80	61.94	35.66	13.77	5.26	2.7
9	9	16	72.66	68.86	22.95	14.90	1.78
6	3	40	144.50	204.84	3.06	3.27	1.75
6	3	12	144.50	204.84	10.20	10.91	1.82
6	6	37	72.66	84.19	6.62	5.19	3.19
15	10	70	108.68	89.36	5.83	3.60	2.53
16	17	64	68.40	48.11	10.84	5.19	2.38
10	13	40	55.96	47.39	13.26	7.23	2.58
3	1	9	215.55	498.24	4.53	7.40	2.18
10	9	36	80.68	74.55	10.20	6.62	2.62

Ns	Ni	Counted squares	Age (Ma)	2σ se(t)	U (ppm)	Uerr (%)	Mean Dpar
6	4	16	108.68	140.70	10.20	9.62	1.4
5	6	20	60.60	73.63	12.24	9.61	1.35
67	61	100	79.76	29.27	24.89	6.38	2.45
13	11	60	85.78	70.77	7.48	4.42	1.75
8	4	21	144.50	177.53	7.77	7.33	-
5	3	6	120.64	176.60	20.40	21.81	1.5
8	4	50	144.50	177.53	3.26	3.08	-
12	11	60	79.22	66.58	7.48	4.42	-
7	16	64	31.89	29.07	10.20	5.03	2.52
8	6	12	96.69	104.86	20.40	16.01	2.73
101	123	70	59.72	17.05	71.69	13.02	2.54
4	3	15	96.69	148.00	8.16	8.73	3.6
11	2	60	389.84	600.53	1.36	1.72	1.43
27	22	100	89.05	51.88	8.98	3.79	2.85
20	14	100	103.54	72.86	5.71	3.00	2.39
9	19	16	34.52	28.14	48.45	21.98	1.91
5	5	36	72.66	92.17	5.67	4.83	3.29
4	2	8	144.50	250.68	10.20	12.90	1.76
14	17	44	59.89	43.62	15.76	7.55	2.96
31	26	85	86.53	46.78	12.48	4.86	3.21
10	4	24	180.13	213.84	6.80	6.41	-
43	26	100	119.72	60.61	10.61	4.13	2.04
10	6	50	120.64	125.15	4.90	3.84	3.05
7	9	25	56.58	57.29	14.69	9.54	2.34
24	20	100	87.09	53.41	8.16	3.61	2.99
9	12	36	54.57	48.41	13.60	7.70	2
10	12	91	60.60	52.23	5.38	3.05	3.48
10	8	30	90.69	86.49	10.88	7.47	3.36
27	21	80	93.26	55.02	10.71	4.63	2.31
5	3	6	120.64	176.60	20.40	21.81	3.33
12	21	15	41.62	30.39	57.12	24.68	-
41	26	80	114.20	58.32	13.26	5.16	2.89
50	27	100	133.91	65.27	11.02	4.21	-
11	4	24	197.86	231.85	6.80	6.41	2.85
6	6	36	72.66	84.19	6.80	5.34	3.25
17	9	36	136.56	113.36	10.20	6.62	3.25
12	9	70	96.69	85.79	5.25	3.41	2.19
5	2	9	180.13	301.91	9.07	11.47	1.58
14	17	100	59.89	43.62	6.94	3.32	1.82
40	22	24	131.50	70.96	37.40	15.80	2.44
7	5	25	101.49	119.26	8.16	6.96	1.96
31	30	70	75.06	39.13	17.49	6.35	1.76
28	31	80	65.66	34.82	15.81	5.65	2.69
30	49	41	44.58	21.12	48.76	13.91	1.45

Ns	Ni	Counted squares	Age (Ma)	2σ se(t)	U (ppm)	Uerr (%)	Mean Dpar
13	1	12	886.08	1841.06	3.40	5.55	1.89
17	15	20	82.28	58.84	30.60	15.56	1.72
10	8	50	90.69	86.49	6.53	4.48	1.68
8	11	32	52.92	49.45	14.03	8.28	2.92
24	20	100	87.09	53.41	8.16	3.61	2.53
6	5	15	87.09	105.81	13.60	11.60	2.27
11	8	20	99.69	93.15	16.32	11.20	2.27
18	21	60	62.33	40.49	14.28	6.17	2.82
16	12	20	96.69	74.44	24.48	13.86	1.58
11	12	32	66.63	56.00	15.30	8.66	1.68
26	24	12	78.67	45.19	81.60	33.03	2.16
10	11	82	66.08	58.10	5.47	3.23	4.47
6	5	36	87.09	105.81	5.67	4.83	3.13
7	6	9	84.69	94.59	27.20	21.35	2.39
10	15	35	48.53	39.90	17.49	8.89	2.76
6	9	32	48.53	51.37	11.48	7.45	2.14
26	26	89	72.66	40.91	11.92	4.64	2.3
13	4	35	233.20	267.63	4.66	4.40	2.08
33	62	100	38.77	17.13	25.30	6.43	1.82
36	32	28	81.68	40.47	46.63	16.40	2.65
17	13	24	94.85	70.49	22.10	12.04	2.25
20	16	70	90.69	61.47	9.33	4.60	2.63
7	9	30	56.58	57.29	12.24	7.95	2
34	57	80	43.44	19.29	29.07	7.70	2.05
8	3	15	191.96	260.58	8.16	8.73	2.63
7	4	42	126.61	159.19	3.89	3.66	3.98

1M31

Matrix of a conglomerate. Clasts = weathered andesites, quartzites, very few limestones no basement, no granitoïde

East of Huasamayo
Lat. / Long. : -15.90835 ; -72.14540
Alt. = 4234 m.

	Age	2σ se(t)	Min (2σ)	Max (2σ)	P(X2) (%)	Dispersion (%)
Pooled	100.55	15.89	84.65	116.44	55.90	18.00
Mean	143.44	31.17	112.27	174.61		
Central	100.90	17.00	83.90	117.90		

Single grain data :

n	Nd	ρd	rse(ρd)	Mean Length
59	8323.00	5.75E+05	1.20	-

Ns	Ni	Counted squares	Age (Ma)	2σ se(t)	U (ppm)	Uerr (%)	Mean Dpar
6	5	20	87.09	105.81	10.20	8.70	3.37
7	1	30	492.19	1053.42	1.36	2.22	2.88
6	3	6	144.50	204.84	20.40	21.81	3.14
7	1	12	492.19	1053.42	3.40	5.55	2.68
8	10	12	58.19	55.49	34.00	21.00	2.82
7	7	20	72.66	77.99	14.28	10.43	3.52
5	3	12	120.64	176.60	10.20	10.91	2.47
24	14	85	124.06	84.30	6.72	3.53	3.02
10	6	40	120.64	125.15	6.12	4.80	3.16
6	6	35	72.66	84.19	6.99	5.49	2.97
3	1	15	215.55	498.24	2.72	4.44	3.29
6	1	9	424.13	917.16	4.53	7.40	3.62
9	1	10	626.18	1321.49	4.08	6.66	1.65
22	15	46	106.28	71.92	13.30	6.77	2.75
24	20	92	87.09	53.41	8.87	3.92	3.21
9	9	6	72.66	68.86	61.20	39.74	2.27
14	9	50	112.67	96.89	7.34	4.77	2.9
2	3	11	48.53	88.72	11.13	11.90	3.06
4	2	12	144.50	250.68	6.80	8.60	-
7	4	16	126.61	159.19	10.20	9.62	3.3
14	20	80	50.94	35.85	10.20	4.51	2.6

Ns	Ni	Counted squares	Age (Ma)	2σ se(t)	U (ppm)	Uerr (%)	Mean Dpar
8	4	16	144.50	177.53	10.20	9.62	2.78
8	8	31	72.66	73.00	10.53	7.23	2.73
7	3	10	168.27	232.81	12.24	13.09	3.24
5	2	16	180.13	301.91	5.10	6.45	2.83
4	1	6	285.83	639.75	6.80	11.11	2.83
6	3	28	144.50	204.84	4.37	4.67	2.86
4	6	12	48.53	62.83	20.40	16.01	2.86
6	6	20	72.66	84.19	12.24	9.61	2.9
14	5	25	201.41	210.77	8.16	6.96	2.78
7	8	20	63.62	66.14	16.32	11.20	2.95
26	21	84	89.83	53.43	10.20	4.41	-
62	49	50	91.79	36.20	39.99	11.41	-
13	12	35	78.67	63.45	13.99	7.92	3.32
5	5	15	72.66	92.17	13.60	11.60	2.89
4	4	12	72.66	102.99	13.60	12.83	2.67
6	3	12	144.50	204.84	10.20	10.91	2.94
7	9	16	56.58	57.29	22.95	14.90	2.94
36	6	48	424.13	376.31	5.10	4.00	-
2	1	16	144.50	354.23	2.55	4.16	3.04
1	1	8	72.66	205.62	5.10	8.33	4.45
4	2	6	144.50	250.68	13.60	17.21	2.78
15	16	80	68.14	49.42	8.16	4.02	3.26
9	5	20	130.20	145.79	10.20	8.70	2.81
5	5	12	72.66	92.17	17.00	14.50	3.44
11	10	40	79.88	70.23	10.20	6.30	2.8
5	6	30	60.60	73.63	8.16	6.40	2.79
32	28	60	82.97	43.69	19.04	7.15	-
4	3	15	96.69	148.00	8.16	8.73	2.46
12	6	24	144.50	145.18	10.20	8.01	-
5	4	28	90.69	121.99	5.83	5.50	3.08
8	3	12	191.96	260.58	10.20	10.91	3.17
11	17	100	47.11	36.74	6.94	3.32	3.55
6	2	24	215.55	352.62	3.40	4.30	3.16
7	3	15	168.27	232.81	8.16	8.73	2.95
31	21	90	106.97	61.35	9.52	4.11	1.6
5	4	35	90.69	121.99	4.66	4.40	2.34
10	7	64	103.54	102.55	4.46	3.26	3.16
2	2	16	72.66	145.48	5.10	6.45	-

Appendix J:
Zircon Fission-track analyses
(Modern river sediments)

These analyses were performed at Université de Grenoble fission-track laboratory by E. Hardwick with $\zeta = 174 \pm 3$ for glass dosimeter CN1.

1M36

Placer sand of Rio Tambo. Clasts = andesites, basalts with bt and sedimentary rocks
Quinistanillas
Lat. / Long. : -16.7744 ; -70.912240
Alt. = 1496 m.

	Age	2σ se(t)	Min (2σ)	Max (2σ)	P(X2) (%)	Dispersion (%)
Pooled	37.39	2.45	34.94	39.83	0.00	0.00
Mean	141.56	38.02	103.53	179.58		
Central	0.00	0.00	0.00	0.00		

Single grain data :

n	Nd	ρd	rse(ρd)	Mean Length
56	9392.00	2.32E+05	1.03	-

Ns	Ni	Counted squares	Age (Ma)	2σ se(t)	U (ppm)	Uerr (%)	Mean Dpar
14	24	24	11.76	7.92	268.93	108.81	-
14	19	12	14.85	10.48	425.81	193.05	-
17	25	20	13.70	8.63	336.17	133.32	-
17	11	12	31.10	24.10	246.52	145.48	-
18	49	50	7.41	4.09	263.55	75.12	-
20	15	8	26.84	18.37	504.25	256.37	-
20	5	4	80.19	80.26	336.17	286.77	-
24	59	20	8.20	3.99	793.35	206.35	-
31	2	3	305.33	445.68	179.29	226.81	-
33	3	4	218.16	263.27	201.70	215.67	-
38	25	32	30.59	15.81	210.10	83.33	-
42	42	12	20.14	8.83	941.26	289.42	-
43	146	50	5.94	2.08	785.28	130.76	-
46	86	23	10.78	3.96	1005.57	217.23	-
50	83	32	12.14	4.38	697.54	153.35	-
53	139	35	7.69	2.50	1068.05	182.19	-
59	2	4	569.20	818.84	134.47	170.11	-
61	75	50	16.39	5.69	403.40	93.22	-
61	3	8	397.65	470.61	100.85	107.83	-
63	17	15	74.33	40.74	304.79	145.85	-
65	70	50	18.70	6.49	376.51	90.02	-
67	86	20	15.70	5.16	1156.41	249.81	-
73	11	9	132.50	85.88	328.70	193.97	-

Ns	Ni	Counted squares	Age (Ma)	2σ se(t)	U (ppm)	Uerr (%)	Mean Dpar
74	68	70	21.91	7.42	261.25	63.36	-
83	15	8	110.67	62.26	504.25	256.37	-
91	3	8	584.57	686.46	100.85	107.83	-
99	3	10	633.51	742.98	80.68	86.27	-
106	2	9	989.20	1412.67	59.76	75.60	-
107	13	16	163.93	96.54	218.51	119.03	-
109	107	48	20.52	5.65	599.50	116.30	-
121	4	16	583.03	593.08	67.23	63.40	-
127	10	25	251.23	165.35	107.57	66.43	-
131	7	12	366.87	285.04	156.88	114.61	-
157	90	80	35.09	9.39	302.55	63.91	-
181	6	28	581.50	483.19	57.63	45.22	-
204	10	50	398.91	258.93	53.79	33.22	-
247	46	70	107.42	34.78	176.73	51.96	-
344	22	50	307.95	136.04	118.33	49.95	-
13	31	20	8.44	5.59	417.39	148.98	-
17	38	30	9.01	5.27	341.09	110.17	-
19	8	12	47.67	40.23	179.52	123.21	-
19	19	18	20.11	13.08	284.24	128.87	-
23	30	35	15.43	8.57	230.81	83.72	-
25	18	24	27.96	17.32	201.70	93.88	-
41	20	28	41.22	22.55	192.09	84.95	-
50	73	51	13.80	5.10	384.94	90.15	-
57	102	60	11.26	3.75	457.19	90.80	-
59	24	49	49.40	24.01	131.72	53.29	-
63	3	18	410.28	485.20	44.82	47.93	-
77	148	50	10.49	2.98	796.04	131.67	-
84	122	60	13.87	3.98	546.83	99.45	-
89	122	22	14.70	4.14	1491.35	271.24	-
124	96	44	26.00	7.15	586.76	120.07	-
125	6	15	407.13	340.72	107.57	84.42	-
189	9	21	410.28	280.47	115.26	74.83	-
237	105	60	45.37	10.80	470.63	92.15	-

1M49

Placer deposits, outlet of rio Tambo.
Clasts = volcanic and plutonic rocks, few sedimentary rocks

Punta de Bonbon
Lat. / Long. : -17.13322 ; -71.77887
Alt. = 0 m.

	Age	2σ se(t)	Min (2σ)	Max (2σ)	P(X2) (%)	Dispersion (%)
Pooled	34.37	2.29	32.08	36.67	0.00	0.00
Mean	98.08	65.53	32.55	163.60		
Central	0.00	0.00	0.00	0.00		

Single grain data :

n	Nd	ρd	rse(ρd)	Mean Length
57	9392.00	2.31E+05	1.03	-

Ns	Ni	Counted squares	Age (Ma)	2σ se(t)	U (ppm)	Uerr (%)	Mean Dpar
17	20	21	17.06	11.28	257.01	113.65	-
22	8	3	55.05	45.51	719.64	493.89	-
28	47	10	11.96	5.73	1268.37	368.99	-
29	68	29	8.57	3.82	632.79	153.47	-
32	70	24	9.18	3.94	787.11	188.19	-
32	37	20	17.36	8.41	499.25	163.38	-
38	37	20	20.61	9.56	499.25	163.38	-
40	40	10	20.07	9.01	1079.46	339.97	-
43	90	42	9.60	3.58	578.28	122.16	-
43	34	16	25.37	11.69	573.46	195.62	-
45	90	35	10.04	3.69	693.94	146.59	-
49	47	18	20.92	8.59	704.65	205.00	-
53	2	8	511.85	737.70	67.47	85.35	-
57	84	12	13.63	4.71	1889.05	412.84	-
68	88	32	15.52	5.05	742.13	158.51	-
73	62	16	23.63	8.22	1045.73	265.43	-
74	15	24	98.42	55.88	168.67	85.75	-
75	92	60	16.37	5.14	413.79	86.47	-
77	9	10	169.74	119.79	242.88	157.68	-
78	51	60	30.67	11.12	229.39	64.10	-
79	19	49	83.05	42.58	104.64	47.44	-

Ns	Ni	Counted squares	Age (Ma)	2σ se(t)	U (ppm)	Uerr (%)	Mean Dpar
96	226	50	8.53	2.11	1219.79	164.04	-
96	40	24	48.07	18.20	449.77	141.65	-
100	28	26	71.40	30.67	290.62	109.04	-
102	78	40	26.23	7.97	526.24	119.28	-
126	4	12	604.03	614.05	89.95	84.83	-
133	10	16	261.97	172.14	168.67	104.16	-
135	4	20	645.08	655.11	53.97	50.90	-
147	19	20	153.68	75.20	256.37	116.23	-
149	48	35	62.10	20.77	370.10	106.56	-
150	20	15	149.03	71.22	359.82	159.11	-
152	65	31	46.84	14.02	565.85	140.32	-
157	12	35	257.79	154.78	92.53	52.37	-
162	30	40	107.65	43.02	202.40	73.42	-
252	74	50	68.10	18.23	399.40	92.91	-
341	14	70	471.94	258.12	53.97	28.37	-
5	27	50	3.28	3.20	165.28	63.12	-
6	3	6	35.35	50.02	153.03	163.63	-
13	21	12	10.96	7.75	535.62	231.29	-
13	5	12	45.92	48.37	127.53	108.79	-
14	1	4	243.49	504.17	76.52	124.96	-
15	9	5	33.42	28.21	485.76	315.36	-
16	18	30	17.84	12.28	161.92	75.36	-
17	15	8	22.74	16.14	506.00	257.26	-
19	11	36	34.63	26.28	82.46	48.66	-
23	11	24	41.90	30.77	123.69	72.99	-
26	64	32	8.16	3.81	539.73	134.87	-
28	41	5	13.71	6.75	2212.89	688.53	-
31	2	4	304.30	444.18	134.93	170.70	-
31	26	36	23.92	12.76	194.90	75.83	-
36	26	40	27.77	14.34	175.41	68.25	-
37	1	4	703.93	1427.05	67.47	110.18	-
45	102	27	8.86	3.19	1019.49	202.49	-
45	33	42	27.35	12.59	212.04	73.40	-
47	80	55	11.80	4.36	392.53	87.87	-
71	30	39	47.40	20.74	207.59	75.30	-
210	41	67	102.15	35.14	165.14	51.38	-

1M52

Rio Camana. Panned sand with lots of magnetite. Inside Puno group
Laguna Lagunilla
Lat. / Long. : -15.69121 ; -70.81274
Alt. = 4208 m.

	Age	2σ se(t)	Min (2σ)	Max (2σ)	P(X2) (%)	Dispersion (%)
Pooled	40.85	2.53	38.33	43.38	0.00	0.00
Mean	125.87	65.22	60.64	191.09		
Central	0.00	0.00	0.00	0.00		

Single grain data :

n	Nd	ρd	rse(ρd)	Mean Length
88	10126.00	2.04E+05	1.00	-

Ns	Ni	Counted squares	Age (Ma)	2σ se(t)	U (ppm)	Uerr (%)	Mean Dpar
8	7	12	20.30	21.03	177.84	129.93	-
15	9	16	29.59	24.98	171.49	111.33	-
15	15	20	17.77	13.00	228.65	116.25	-
21	29	9	12.87	7.40	982.36	362.27	-
22	3	5	129.19	159.11	182.92	195.59	-
23	6	3	67.85	62.27	609.74	478.47	-
25	51	12	8.72	4.27	1295.69	362.03	-
26	10	12	46.10	34.36	254.06	156.89	-
34	32	12	18.88	9.33	812.99	285.68	-
35	35	20	17.77	8.53	533.52	179.41	-
35	14	32	44.33	28.10	133.38	70.11	-
37	3	30	215.81	259.25	30.49	32.60	-
38	5	24	133.84	127.46	63.51	54.18	-
39	13	20	53.16	34.12	198.17	107.94	-
40	29	50	24.50	11.99	176.82	65.21	-
43	36	44	21.22	9.63	249.44	82.73	-
52	42	10	21.99	9.17	1280.45	393.66	-
52	4	6	227.27	236.04	203.25	191.67	-
56	53	15	18.77	7.24	1077.21	295.33	-
59	33	30	31.74	13.86	335.36	116.08	-
62	24	14	45.81	22.10	522.63	211.43	-
66	62	28	18.91	6.74	675.07	171.31	-
66	57	42	20.57	7.49	413.75	109.44	-

Ns	Ni	Counted squares	Age (Ma)	2σ se(t)	U (ppm)	Uerr (%)	Mean Dpar
69	17	18	71.82	39.01	287.93	137.78	-
69	9	20	135.00	95.85	137.19	89.06	-
85	95	18	15.90	4.79	1609.03	330.87	-
85	20	40	75.19	37.50	152.43	67.40	-
86	3	14	490.93	577.03	65.33	69.85	-
90	28	35	56.94	24.75	243.90	91.50	-
91	35	21	46.10	18.44	508.12	170.86	-
96	28	40	60.72	26.20	213.41	80.06	-
97	54	28	31.89	10.91	587.96	159.72	-
99	75	30	23.45	7.24	762.17	176.09	-
111	54	15	36.47	12.19	1097.53	298.15	-
112	72	24	27.62	8.42	914.61	215.61	-
115	39	35	52.26	19.48	339.71	108.32	-
132	5	20	453.45	413.60	76.22	65.02	-
140	7	24	346.41	268.70	88.92	64.96	-
153	107	36	25.39	6.48	906.14	175.73	-
11	14	2	15.76	12.71	1891.51	994.24	-
15	1	9	294.33	608.08	30.02	49.03	-
15	18	8	16.71	11.70	607.99	282.99	-
17	16	8	21.30	14.86	540.43	266.32	-
18	4	2	89.72	99.26	540.43	509.65	-
19	20	15	19.04	12.23	360.29	159.32	-
24	23	9	20.92	12.24	690.55	285.26	-
27	18	32	30.04	18.33	152.00	70.75	-
28	39	24	14.40	7.16	439.10	140.02	-
32	16	4	40.03	24.57	1080.86	532.65	-
33	10	20	65.91	47.66	135.11	83.44	-
36	7	19	102.43	84.73	99.55	72.73	-
39	40	35	19.54	8.83	308.82	97.26	-
42	38	36	22.15	9.96	285.23	92.12	-
45	2	4	436.60	631.27	135.11	170.92	-
45	38	10	23.73	10.50	1026.82	331.65	-
46	2	4	445.97	644.53	135.11	170.92	-
46	31	24	29.72	13.87	349.03	124.58	-
46	46	50	20.05	8.40	248.60	73.09	-
47	35	20	26.90	12.06	472.88	159.03	-
53	37	11	28.69	12.35	908.91	297.44	-
54	10	12	107.51	74.16	225.18	139.06	-
56	26	38	43.10	20.53	184.88	71.93	-
60	1	9	1104.36	2227.51	30.02	49.03	-
64	3	15	414.67	490.21	54.04	57.79	-
66	78	15	16.97	5.72	1405.12	318.50	-
68	1	6	1238.28	2495.23	45.04	73.55	-
71	57	30	24.96	8.94	513.41	135.83	-

Ns	Ni	Counted squares	Age (Ma)	2σ se(t)	U (ppm)	Uerr (%)	Mean Dpar
71	34	60	41.79	17.52	153.12	52.23	-
79	18	33	87.52	45.86	147.39	68.60	-
81	41	60	39.54	15.25	184.65	57.45	-
82	20	20	81.79	40.94	270.22	119.49	-
82	48	25	34.21	12.51	518.81	149.38	-
84	2	8	792.45	1134.43	67.55	85.46	-
89	24	9	74.02	34.19	720.58	291.53	-
91	50	40	36.44	12.92	337.77	95.32	-
92	37	24	49.73	19.47	416.58	136.33	-
92	115	50	16.04	4.54	621.50	116.37	-
96	4	9	464.68	474.65	120.10	113.25	-
98	3	9	624.58	732.61	90.07	96.31	-
98	103	48	19.07	5.44	579.84	114.61	-
99	53	90	37.39	12.82	159.13	43.63	-
112	15	16	148.19	81.72	253.33	128.80	-
116	31	25	74.69	30.36	335.07	119.60	-
128	9	15	279.39	193.04	162.13	105.26	-
138	14	24	194.92	109.64	157.63	82.85	-
161	73	60	44.13	12.59	328.76	76.99	-
173	44	36	78.46	26.69	330.26	99.25	-
175	118	30	29.71	7.18	1062.85	196.50	-

1M58

Lake Titicaca. Placer deposits on red sands (on the lower red beds of the Puno Group)
Tililaca
Lat. / Long. : -15.91089 ; -69.72815
Alt. = 3847 m.

	Age	2σ se(t)	Min (2σ)	Max (2σ)	P(X2) (%)	Dispersion (%)
Pooled	151.65	11.80	139.85	163.46	0.00	0.00
Mean	242.11	101.00	141.11	343.10		
Central	0.00	0.00	0.00	0.00		

Single grain data :

n	Nd	ρd	rse(ρd)	Mean Length
91	10126.00	2.05E+05	1.00	-

Ns	Ni	Counted squares	Age (Ma)	2σ se(t)	U (ppm)	Uerr (%)	Mean Dpar
24	10	8	42.73	32.21	379.60	234.42	-
24	2	2	210.88	310.53	303.68	384.18	-
32	13	30	43.82	28.88	131.59	71.68	-
35	2	6	305.28	444.07	101.23	128.06	-
37	5	16	130.86	124.82	94.90	80.95	-
37	7	6	93.74	77.37	354.29	258.84	-
37	13	6	50.64	32.72	657.97	358.40	-
43	12	11	63.70	41.67	331.29	187.52	-
54	12	9	79.89	51.10	404.91	229.19	-
54	22	9	43.70	22.18	742.33	313.35	-
64	6	24	187.79	160.54	75.92	59.58	-
67	18	9	66.15	35.23	607.36	282.68	-
68	19	13	63.62	33.12	443.84	201.22	-
77	8	8	169.69	126.26	303.68	208.41	-
81	27	28	53.37	23.82	292.83	111.84	-
89	11	11	142.94	91.55	303.68	179.20	-
92	15	15	108.65	60.67	303.68	154.39	-
119	10	12	209.15	137.99	253.07	156.28	-
120	4	11	514.81	523.74	110.43	104.14	-
122	12	40	179.11	108.62	91.10	51.57	-
126	3	15	709.75	829.76	60.74	64.94	-
182	9	20	351.49	240.48	136.66	88.72	-
428	10	45	722.54	463.22	67.48	41.67	-

Ns	Ni	Counted squares	Age (Ma)	2σ se(t)	U (ppm)	Uerr (%)	Mean Dpar
15	8	4	33.41	29.28	607.36	416.82	-
18	5	4	63.99	64.75	379.60	323.81	-
24	6	4	71.06	64.94	455.52	357.46	-
29	8	3	64.43	51.53	809.81	555.76	-
37	7	4	93.74	77.37	531.44	388.25	-
40	6	40	118.01	103.44	45.55	35.75	-
41	16	11	45.62	26.96	441.72	217.67	-
43	13	16	58.82	37.31	246.74	134.40	-
43	14	30	54.64	33.70	141.72	74.49	-
44	20	5	39.18	21.19	1214.72	537.12	-
46	1	4	773.44	1563.93	75.92	123.99	-
46	8	20	101.91	78.19	121.47	83.36	-
46	3	4	268.26	319.89	227.76	243.53	-
48	6	9	141.35	122.55	202.45	158.87	-
50	2	7	431.81	623.02	86.77	109.76	-
50	1	4	836.51	1690.01	75.92	123.99	-
51	9	12	100.44	72.75	227.76	147.86	-
52	7	8	131.36	105.91	265.72	194.13	-
53	1	5	883.41	1783.78	60.74	99.19	-
54	8	12	119.47	90.65	202.45	138.94	-
58	2	9	498.30	717.04	67.48	85.37	-
58	1	6	960.83	1938.54	50.61	82.66	-
58	16	9	64.43	36.49	539.88	266.04	-
60	3	7	347.73	411.69	130.15	139.16	-
61	16	15	67.75	38.16	323.93	159.62	-
61	10	13	108.06	73.87	233.60	144.26	-
61	3	6	353.37	418.20	151.84	162.35	-
65	17	14	67.95	37.12	368.75	176.45	-
66	13	23	90.06	54.78	171.65	93.49	-
70	20	30	62.22	31.66	202.45	89.52	-
73	15	25	86.36	49.09	182.21	92.63	-
86	1	12	1377.97	2772.48	25.31	41.33	-
88	6	8	256.82	216.98	227.76	178.73	-
93	3	8	531.28	623.67	113.88	121.76	-
93	2	6	781.36	1117.28	101.23	128.06	-
95	12	12	139.90	85.91	303.68	171.89	-
96	18	35	94.58	48.74	156.18	72.69	-
97	8	7	213.04	156.98	347.06	238.18	-
98	20	50	86.95	42.81	121.47	53.71	-
100	12	19	147.18	90.13	191.80	108.57	-
104	21	12	87.87	42.20	531.44	229.47	-
107	28	15	67.91	28.96	566.87	212.67	-
110	2	9	914.49	1305.52	67.48	85.37	-
113	22	30	91.11	42.63	222.70	94.00	-

Ns	Ni	Counted squares	Age (Ma)	2σ se(t)	U (ppm)	Uerr (%)	Mean Dpar
115	4	12	494.16	503.09	101.23	95.46	-
116	7	24	289.44	225.61	88.57	64.71	-
116	13	28	157.46	92.33	140.99	76.80	-
119	8	21	260.40	190.52	115.69	79.39	-
120	4	18	514.81	523.74	67.48	63.64	-
122	34	12	63.78	24.88	860.43	293.48	-
125	7	20	311.36	242.20	106.29	77.65	-
128	6	24	370.26	309.69	75.92	59.58	-
132	7	15	328.36	255.07	141.72	103.53	-
141	6	12	406.71	339.47	151.84	119.15	-
147	22	25	118.27	54.29	267.24	112.80	-
150	46	42	57.99	19.69	332.60	97.78	-
152	44	15	61.42	21.18	890.80	267.67	-
157	10	20	274.54	179.43	151.84	93.77	-
165	26	49	112.38	47.65	161.14	62.69	-
165	9	20	319.46	219.10	136.66	88.72	-
172	18	20	168.48	83.76	273.31	127.21	-
194	11	20	307.60	191.09	167.02	98.56	-
201	7	24	493.57	380.08	88.57	64.71	-
204	12	30	296.76	176.72	121.47	68.76	-
205	11	40	324.61	201.37	83.51	49.28	-
225	15	42	262.54	140.43	108.46	55.14	-
265	12	30	382.90	226.56	121.47	68.76	-
287	9	30	545.89	370.26	91.10	59.14	-

1M64

Rio Camana Panned sand clasts = precambrian basement, volcanic rocks, quartz arenites and some granite

Camana

Lat. / Long. : -16.55228 ; -72.718

Alt. = 78 m.

	Age	2σ se(t)	Min (2σ)	Max (2σ)	P(X2) (%)	Dispersion (%)
Pooled	61.81	3.76	58.06	65.57	0.00	0.00
Mean	138.41	44.50	93.90	182.91		
Central	0.00	0.00	0.00	0.00		

Single grain data :

n	Nd	ρd	rse(ρd)	Mean Length
99	10126.00	2.06E+05	0.99	-

Ns	Ni	Counted squares	Age (Ma)	2σ se(t)	U (ppm)	Uerr (%)	Mean Dpar
19	7	10	48.49	42.93	211.75	154.70	-
21	1	9	366.02	749.42	33.61	54.89	-
26	17	20	27.37	17.11	257.13	123.03	-
27	3	7	159.42	194.15	129.64	138.62	-
29	11	16	47.11	33.42	207.97	122.72	-
36	20	12	32.20	18.01	504.17	222.93	-
36	15	15	42.90	26.43	302.50	153.79	-
36	10	4	64.24	46.00	756.25	467.01	-
37	6	12	109.65	96.62	151.25	118.69	-
37	25	21	26.49	13.76	360.12	142.81	-
40	34	12	21.06	9.86	857.08	292.33	-
41	12	25	60.98	40.11	145.20	82.19	-
42	47	27	16.01	6.83	526.57	153.16	-
43	3	30	252.06	301.21	30.25	32.34	-
44	33	14	23.87	11.04	713.04	246.79	-
49	58	12	15.13	5.91	1462.08	383.41	-
51	11	50	82.62	55.03	66.55	39.27	-
52	16	22	58.02	33.26	220.00	108.41	-
53	16	25	59.13	33.82	193.60	95.40	-
54	19	34	50.77	27.16	169.04	76.64	-
54	18	26	53.58	29.25	209.42	97.47	-
54	2	10	466.89	672.67	60.50	76.54	-

Ns	Ni	Counted squares	Age (Ma)	2σ se(t)	U (ppm)	Uerr (%)	Mean Dpar
55	4	21	241.99	250.83	57.62	54.34	-
55	8	25	122.13	92.56	96.80	66.43	-
57	9	12	112.59	80.90	226.88	147.28	-
59	12	5	87.58	55.58	726.00	410.94	-
62	9	24	122.38	87.45	113.44	73.64	-
62	94	72	11.82	3.90	394.93	81.63	-
65	40	27	29.08	11.75	448.15	141.12	-
65	28	28	41.50	18.84	302.50	113.49	-
72	8	24	159.42	119.00	100.83	69.20	-
73	2	8	623.44	894.04	75.63	95.67	-
76	13	60	104.00	62.57	65.54	35.70	-
76	99	24	13.75	4.23	1247.81	251.41	-
78	14	56	99.15	57.70	75.63	39.75	-
79	91	49	15.55	4.82	561.79	117.99	-
81	45	28	32.20	12.05	486.16	144.47	-
83	7	28	209.21	164.91	75.63	55.25	-
88	21	48	74.72	36.42	132.34	57.14	-
88	3	12	505.70	594.16	75.63	80.86	-
91	15	26	107.89	60.29	174.52	88.72	-
92	16	18	102.30	55.58	268.89	132.50	-
93	8	24	205.18	151.43	100.83	69.20	-
95	16	50	105.61	57.24	96.80	47.70	-
104	5	12	362.63	332.38	126.04	107.52	-
110	36	30	54.57	21.07	363.00	120.38	-
113	56	35	36.09	11.89	484.00	129.14	-
121	22	20	97.89	45.55	332.75	140.45	-
123	23	41	95.20	43.43	169.70	70.09	-
124	35	42	70.57	27.17	225.47	75.83	-
124	35	40	70.57	27.17	236.75	79.62	-
124	35	42	70.57	27.17	225.47	75.83	-
135	84	40	32.11	9.02	568.19	124.19	-
136	6	14	438.68	366.45	115.96	91.00	-
141	144	22	19.58	4.71	1770.99	296.95	-
146	11	30	260.48	163.24	99.21	58.55	-
175	40	60	87.03	30.72	180.38	56.81	-
208	7	35	569.21	438.09	54.11	39.54	-
14	19	8	13.20	9.31	718.44	325.70	-
19	3	24	112.59	139.97	37.81	40.43	-
24	4	12	106.72	115.35	100.83	95.09	-
28	3	9	165.25	200.89	100.83	107.81	-
33	39	29	15.16	7.20	406.81	129.71	-
35	17	30	36.82	21.82	171.42	82.02	-
37	32	25	20.70	10.03	387.20	136.06	-
38	42	32	16.21	7.29	397.03	122.06	-

Ns	Ni	Counted squares	Age (Ma)	2σ se(t)	U (ppm)	Uerr (%)	Mean Dpar
48	13	29	65.88	41.28	135.60	73.86	-
50	16	60	55.80	32.14	80.67	39.75	-
50	54	30	16.58	6.54	544.50	147.91	-
56	19	20	52.64	28.04	287.38	130.28	-
56	62	40	16.18	6.00	468.88	118.98	-
58	9	20	114.55	82.21	136.13	88.37	-
60	1	9	995.12	2007.16	33.61	54.89	-
60	13	40	82.24	50.43	98.31	53.55	-
64	18	34	63.45	33.96	160.15	74.53	-
64	10	24	113.77	77.51	126.04	77.83	-
66	21	14	56.12	28.21	453.75	195.92	-
74	16	9	82.42	45.57	537.78	265.00	-
74	12	12	109.65	68.40	302.50	171.22	-
75	15	12	89.05	50.51	378.13	192.23	-
77	32	25	43.01	18.18	387.20	136.06	-
79	17	41	82.81	44.41	125.43	60.02	-
79	5	20	277.30	256.01	75.63	64.51	-
80	19	15	75.07	38.44	383.17	173.71	-
81	15	38	96.12	54.18	119.41	60.71	-
82	20	25	73.11	36.59	242.00	107.01	-
88	64	60	24.61	8.15	322.67	80.61	-
88	18	16	87.09	45.20	340.31	158.39	-
92	27	21	60.82	26.74	388.93	148.53	-
94	6	12	275.01	231.88	151.25	118.69	-
99	11	17	159.42	101.54	195.74	115.50	-
101	5	12	352.45	323.27	126.04	107.52	-
102	45	47	40.52	14.60	289.63	86.07	-
105	23	56	81.36	37.61	124.24	51.32	-
110	33	48	59.50	23.75	207.97	71.98	-
114	13	30	155.38	91.19	131.08	71.40	-
121	66	32	32.80	10.13	623.91	153.51	-
127	28	28	80.83	33.91	302.50	113.49	-
142	86	100	29.54	8.16	260.15	56.18	-

1M65

Rio Majes. Clasts = Mostly volcanic rocks, basement, granitoids and a few quartzites
Ongoro
Lat. / Long. : -15.92971 ; -72.46313
Alt. = 816 m.

	Age	2σ se(t)	Min (2σ)	Max (2σ)	P(X2) (%)	Dispersion (%)
Pooled	48.68	5.52	43.16	54.21	0.00	0.00
Mean	180.99	118.97	62.01	299.96		
Central	0.00	0.00	0.00	0.00		

Single grain data :

n	Nd	ρd	rse(ρd)	Mean Length
22	10126.00	2.07E+05	1.00	-

Ns	Ni	Counted squares	Age (Ma)	2σ se(t)	U (ppm)	Uerr (%)	Mean Dpar
18	15	19	21.58	15.11	237.89	120.94	-
27	36	24	13.50	6.89	451.99	149.90	-
30	37	18	14.59	7.19	619.40	202.67	-
42	95	45	7.96	2.97	636.14	130.81	-
50	46	30	19.55	8.03	462.04	135.83	-
55	60	18	16.49	6.19	1004.43	259.05	-
56	29	24	34.69	15.94	364.11	134.27	-
64	3	8	373.28	441.27	113.00	120.82	-
65	11	30	105.58	68.98	110.49	65.20	-
68	7	25	172.66	137.25	84.37	61.64	-
68	5	9	240.45	223.05	167.41	142.80	-
75	12	57	111.62	69.55	63.44	35.91	-
116	8	56	256.05	187.48	43.05	29.54	-
14	1	4	274.57	568.53	67.73	110.61	-
19	4	2	94.47	104.02	541.84	510.98	-
19	5	9	75.69	76.15	150.51	128.40	-
25	6	12	82.95	75.49	135.46	106.30	-
25	2	9	245.70	361.25	60.20	76.16	-
57	2	10	547.13	787.54	54.18	68.55	-
72	2	16	683.71	980.66	33.87	42.84	-
99	92	58	21.52	6.30	429.74	89.81	-
210	18	62	229.61	113.18	78.65	36.61	-

Appendix K:
Apatite Fission-track analyses

(Modern river sediments)

These analyses were performed at Université de Grenoble fission-track laboratory by Mélanie Noury with ζ = 254 ± 12 for glass dosimeter IRMM540.

1M36

Rio Tambo, clasts = andesites, basalts, quartzites

Quinistaquillas

Lat. / Long. : -16.77440 ; -70.91224

Alt. = 1496 m.

	Age	2σ se(t)	Min (2σ)	Max (2σ)	P(X2) (%)	Dispersion (%)
Pooled	31.09	9.77	21.32	40.86	0.00	139.00
Mean	89.26	74.90	14.36	164.16		
Central	27.20	19.00	8.20	46.20		

Single grain data :

n	Nd	ρd	rse(ρd)	Mean Length
21	7814.00	6.04E+05	1.18	-

Ns	Ni	Counted squares	Age (Ma)	2σ se(t)	U (ppm)	Uerr (%)	Mean Dpar
9	1	48	655.55	1383.48	0.81	1.32	1.88
0	8	49	4.79	13.97	6.35	4.36	-
0	1	9	38.22	132.46	4.32	7.06	-
0	2	28	19.14	60.55	2.78	3.51	-
0	6	21	6.39	18.81	11.11	8.72	-
0	7	35	5.47	16.04	7.78	5.68	-
14	32	80	33.46	21.69	15.55	5.47	2.49
2	3	6	50.91	93.08	19.44	20.79	-
0	9	60	4.26	12.38	5.83	3.79	-
1	1	20	76.22	215.71	1.94	3.18	-
2	6	40	25.51	41.73	5.83	4.58	-
0	12	100	3.19	9.23	4.67	2.64	-
1	16	60	4.79	9.89	10.37	5.11	-
7	1	15	515.52	1103.37	2.59	4.23	2.43
0	6	80	6.39	18.81	2.92	2.29	-
0	5	25	7.66	22.74	7.78	6.63	-
7	8	30	66.74	69.39	10.37	7.12	1.9
10	7	40	108.61	107.57	6.80	4.97	2.21
0	3	16	12.77	39.02	7.29	7.80	-
8	20	42	30.60	25.77	18.52	8.19	1.91
2	1	60	151.55	371.50	0.65	1.06	-

1M49

Outlet of the Rio Tambo, clasts = volcanic rocks, plutons, few sedimentary rocks
Punta de Bonbon
Lat. / Long. : -17.13322 ; -71.77887
Alt. = 5 m.

	Age	2σ se(t)	Min (2σ)	Max (2σ)	P(X2) (%)	Dispersion (%)
Pooled	22.51	3.47	19.04	25.98	0.00	86.00
Mean	32.46	7.57	24.89	40.03		
Central	21.30	5.20	16.10	26.50		

Single grain data :

n	Nd	ρd	rse(ρd)	Mean Length
99	7814.00	6.07E+05	1.15	-

Ns	Ni	Counted squares	Age (Ma)	2σ se(t)	U (ppm)	Uerr (%)	Mean Dpar
13	39	100	25.64	16.61	15.09	4.81	2.8
24	73	100	25.29	12.15	28.24	6.62	3.7
4	4	21	76.61	108.60	7.37	6.95	2.67
1	20	20	3.85	7.90	38.68	17.11	2.26
6	12	20	38.42	38.60	23.21	13.14	4.66
0	12	60	3.21	9.27	7.74	4.38	-
0	10	50	3.85	11.17	7.74	4.78	-
2	4	12	38.42	66.65	12.89	12.16	2.84
2	1	12	152.32	373.41	3.22	5.26	3.71
1	2	24	38.42	94.18	3.22	4.08	-
3	6	70	38.42	54.46	3.32	2.60	2.43
11	13	36	64.88	53.53	13.97	7.61	3.43
8	12	25	51.18	46.98	18.57	10.51	2.21
0	10	100	3.85	11.17	3.87	2.39	-
0	6	50	6.42	18.91	4.64	3.64	-
0	9	60	4.28	12.44	5.80	3.77	-
10	5	35	152.32	167.52	5.53	4.71	-
2	1	12	152.32	373.41	3.22	5.26	-
2	4	40	38.42	66.65	3.87	3.65	2.5
0	13	60	2.96	8.55	8.38	4.57	-
1	15	16	5.14	10.62	36.27	18.44	-

0	4	35	9.63	28.89	4.42	4.17	-
Ns	Ni	Counted squares	Age (Ma)	2σ se(t)	U (ppm)	Uerr (%)	Mean Dpar
2	2	16	76.61	153.40	4.84	6.12	-
1	35	70	2.20	4.47	19.34	6.51	-
0	9	50	4.28	12.44	6.96	4.52	-
4	9	24	34.16	41.19	14.51	9.42	-
0	5	40	7.70	22.86	4.84	4.13	-
22	41	60	41.22	22.15	26.43	8.23	4.01
1	6	30	12.83	27.75	7.74	6.07	2.34
0	5	25	7.70	22.86	7.74	6.60	-
0	11	60	3.50	10.13	7.09	4.19	-
0	11	50	3.50	10.13	8.51	5.02	-
18	50	80	27.69	15.46	24.18	6.83	4.01
1	8	40	9.63	20.44	7.74	5.31	-
4	6	70	51.18	66.25	3.32	2.60	-
0	10	100	3.85	11.17	3.87	2.39	-
2	8	40	19.24	30.48	7.74	5.31	2.35
1	8	49	9.63	20.44	6.32	4.33	-
5	7	28	54.81	64.41	9.67	7.07	3
3	13	100	17.76	22.82	5.03	2.74	-
9	30	25	23.08	17.69	46.42	16.84	-
2	7	70	21.98	35.31	3.87	2.83	-
9	7	100	98.33	99.57	2.71	1.98	3.28
4	6	45	51.18	66.25	5.16	4.05	-
2	6	70	25.64	41.94	3.32	2.60	2.39
1	4	10	19.24	43.06	15.47	14.59	-
0	16	100	2.41	6.92	6.19	3.05	-
4	3	49	101.95	156.04	2.37	2.53	-
1	4	49	19.24	43.06	3.16	2.98	-
3	21	80	11.00	13.62	10.15	4.39	3.36
4	20	64	15.40	16.93	12.09	5.35	2.75
4	4	70	76.61	108.60	2.21	2.08	-
1	1	9	76.61	216.82	4.30	7.02	-
12	63	40	14.66	9.35	60.93	15.36	-
0	3	40	12.83	39.22	2.90	3.10	-
0	9	28	4.28	12.44	12.43	8.07	-
5	3	8	127.18	186.17	14.51	15.51	2.7
3	23	100	10.04	12.37	8.90	3.68	-
1	5	20	15.40	33.76	9.67	8.25	-
10	12	70	63.91	55.08	6.63	3.75	1.94
0	16	100	2.41	6.92	6.19	3.05	-
1	2	15	38.42	94.18	5.16	6.53	2.8
3	11	14	20.98	27.41	30.39	17.94	1.96
3	17	100	13.59	17.07	6.58	3.15	-
0	8	49	4.81	14.05	6.32	4.33	-

0	7	50	5.50	16.12	5.42	3.96	-
Ns	Ni	Counted squares	Age (Ma)	2σ se(t)	U (ppm)	Uerr (%)	Mean Dpar
2	12	100	12.83	19.64	4.64	2.63	-
1	3	25	25.64	59.26	4.64	4.96	-
0	2	36	19.24	60.87	2.15	2.72	-
13	24	54	41.61	28.94	17.19	6.96	3.76
3	4	27	57.54	88.08	5.73	5.40	-
8	19	48	32.37	27.46	15.31	6.94	-
4	2	20	152.32	264.25	3.87	4.89	-
2	9	80	17.10	26.79	4.35	2.83	-
15	9	40	127.18	107.96	8.70	5.65	-
0	4	25	9.63	28.89	6.19	5.84	-
15	67	100	17.23	9.99	25.92	6.34	-
4	11	36	27.96	32.77	11.82	6.98	-
7	23	100	23.41	20.34	8.90	3.68	3
1	8	18	9.63	20.44	17.19	11.80	-
7	14	80	38.42	35.76	6.77	3.56	-
0	6	60	6.42	18.91	3.87	3.04	8
0	8	42	4.81	14.05	7.37	5.06	-
7	4	42	133.48	167.83	3.68	3.47	-
0	11	80	3.50	10.13	5.32	3.14	-
2	7	16	21.98	35.31	16.92	12.37	-
3	6	30	38.42	54.46	7.74	6.07	-
0	2	42	19.24	60.87	1.84	2.33	-
0	5	100	7.70	22.86	1.93	1.65	-
0	19	100	2.03	5.81	7.35	3.33	-
0	12	100	3.21	9.27	4.64	2.63	-
4	16	36	19.24	21.59	17.19	8.47	-
1	5	40	15.40	33.76	4.84	4.13	-
0	9	100	4.28	12.44	3.48	2.26	-
9	22	100	31.45	25.08	8.51	3.59	-
0	15	100	2.57	7.39	5.80	2.95	-
14	34	50	31.66	20.34	26.30	8.98	3.3
2	4	50	38.42	66.65	3.09	2.92	-
1	11	100	7.00	14.64	4.26	2.51	-

1M52

Rio Camana, inside Puno group
East of Laguna Lagunilla
Lat. / Long. : -15.69121 ; -70.81274
Alt. = 4208 m.

	Age	2σ se(t)	Min (2σ)	Max (2σ)	P(X2) (%)	Dispersion (%)
Pooled	41.84	13.56	28.28	55.40	1.62	75.00
Mean	77.13	61.44	15.69	138.57		
Central	39.70	18.60	21.10	58.30		

Single grain data :

n	Nd	ρd	rse(ρd)	Mean Length
26	8502.00	5.71E+05	1.21	-

Ns	Ni	Counted squares	Age (Ma)	2σ se(t)	U (ppm)	Uerr (%)	Mean Dpar
1	2	30	36.15	88.62	2.74	3.47	2.97
2	2	48	72.10	144.37	1.71	2.17	2.22
1	3	30	24.12	55.76	4.11	4.40	2.87
8	27	50	21.45	17.39	22.20	8.49	1.93
2	5	48	28.94	48.50	4.28	3.65	1.41
7	15	38	33.75	31.07	16.23	8.25	2.08
3	3	16	72.10	117.94	7.71	8.24	2.87
0	1	20	36.15	125.28	2.06	3.36	-
0	3	36	12.07	36.90	3.43	3.66	-
1	1	25	72.10	204.04	1.64	2.69	-
12	1	90	816.12	1700.74	0.46	0.75	2.62
3	4	17	54.15	82.88	9.67	9.12	1.88
0	1	16	36.15	125.28	2.57	4.20	-
1	3	100	24.12	55.76	1.23	1.32	1.93
2	2	60	72.10	144.37	1.37	1.73	-
1	3	12	24.12	55.76	10.28	10.99	-
0	2	15	18.10	57.27	5.48	6.94	-
5	2	21	178.76	299.62	3.92	4.95	2.78
0	2	25	18.10	57.27	3.29	4.16	-
1	8	12	9.06	19.23	27.41	18.82	1.26
0	2	20	18.10	57.27	4.11	5.20	-
0	1	50	36.15	125.28	0.82	1.34	-
1	3	20	24.12	55.76	6.17	6.60	2.57
1	3	60	24.12	55.76	2.06	2.20	2.1
9	4	8	161.10	194.25	20.56	19.39	2.61
5	11	40	32.87	35.60	11.31	6.67	-

1M58

Lake Titicaca, red sands beach (in the lower red beds of Puno group)
Playa Charcas, east of Chicuito
Lat. / Long. : -15.91089 ; -69.72815
Alt. = 3847 m.

	Age	2σ se(t)	Min (2σ)	Max (2σ)	P(X2) (%)	Dispersion (%)
Pooled	58.72	7.63	51.10	66.35	3.34	25.00
Mean	80.59	13.60	66.99	94.19		
Central	60.50	8.60	51.90	69.10		

Single grain data :

n	Nd	ρd	rse(ρd)	Mean Length
100	8502.00	5.75E+05	1.26	-

Ns	Ni	Counted squares	Age (Ma)	2σ se(t)	U (ppm)	Uerr (%)	Mean Dpar
13	10	42	94.20	79.77	9.72	6.01	-
24	27	100	64.56	36.76	11.03	4.22	2.43
6	4	40	108.57	140.55	4.08	3.85	-
19	40	40	34.58	19.56	40.84	12.88	-
7	4	16	126.48	159.03	10.21	9.63	-
6	3	42	144.35	204.62	2.92	3.12	2.14
7	8	25	63.55	66.07	13.07	8.97	-
4	3	15	96.59	147.84	8.17	8.74	2.26
10	18	100	40.42	32.13	7.35	3.42	-
11	11	44	72.58	62.30	10.21	6.03	-
15	18	48	60.54	42.73	15.32	7.13	1.95
11	10	54	79.79	70.16	7.56	4.67	-
22	12	25	132.45	95.92	19.61	11.10	-
10	11	40	66.02	58.04	11.23	6.63	-
3	5	70	43.65	63.89	2.92	2.49	2.74
10	16	100	45.46	36.91	6.54	3.22	2.14
8	14	60	41.57	37.07	9.53	5.01	2.32
10	8	40	90.60	86.40	8.17	5.61	-
39	53	30	53.49	23.16	72.16	19.81	1.55
7	5	32	101.38	119.14	6.38	5.44	1.89
9	16	50	40.93	34.34	13.07	6.44	-
11	8	49	99.59	93.05	6.67	4.58	-

Ns	Ni	Counted squares	Age (Ma)	2σ se(t)	U (ppm)	Uerr (%)	Mean Dpar
3	3	24	72.58	118.73	5.11	5.46	3.3
8	4	18	144.35	177.35	9.08	8.56	-
7	13	49	39.18	36.93	10.84	5.90	1.42
16	19	40	61.17	41.94	19.40	8.80	1.21
10	11	60	66.02	58.04	7.49	4.42	1.4
3	8	17	27.31	37.08	19.22	13.19	-
6	17	40	25.71	24.54	17.36	8.31	-
2	1	21	144.35	353.87	1.94	3.18	-
6	16	60	27.31	26.28	10.89	5.37	-
8	8	36	72.58	72.92	9.08	6.23	1.83
4	4	14	72.58	102.88	11.67	11.01	2.41
7	11	16	46.28	44.98	28.08	16.58	-
19	15	33	91.80	64.03	18.57	9.44	1.58
2	3	35	48.48	88.63	3.50	3.74	1.61
9	8	60	81.60	79.69	5.45	3.74	2.21
5	5	20	72.58	92.08	10.21	8.71	-
7	1	30	491.69	1052.36	1.36	2.22	-
5	11	36	33.09	35.84	12.48	7.37	1.94
8	6	60	96.59	104.75	4.08	3.21	2.59
10	24	100	30.34	23.03	9.80	3.97	1.84
7	6	40	84.60	94.49	6.13	4.81	-
10	11	100	66.02	58.04	4.49	2.65	2.34
16	21	32	55.37	37.14	26.80	11.58	1.49
28	34	40	59.83	31.08	34.72	11.85	1.26
20	28	50	51.93	30.82	22.87	8.59	-
12	13	15	67.03	54.06	35.40	19.29	-
19	14	30	98.30	69.90	19.06	10.02	-
7	8	40	63.55	66.07	8.17	5.61	1.72
24	53	42	32.97	16.53	51.54	14.15	-
6	3	18	144.35	204.62	6.81	7.28	-
6	12	21	36.39	36.56	23.34	13.22	-
5	5	16	72.58	92.08	12.76	10.89	-
1	3	10	24.28	56.13	12.25	13.10	-
3	3	9	72.58	118.73	13.61	14.56	-
17	27	100	45.79	28.70	11.03	4.22	1.66
10	8	100	90.60	86.40	3.27	2.24	1.99
4	3	20	96.59	147.84	6.13	6.55	1.5
1	2	14	36.39	89.21	5.83	7.38	-
4	9	80	32.36	39.02	4.59	2.98	1.89
11	33	50	24.28	17.07	26.96	9.34	-
4	7	12	41.57	52.27	23.83	17.41	-
2	6	18	24.28	39.73	13.61	10.69	-
6	12	42	36.39	36.56	11.67	6.61	2.05
9	20	28	32.76	26.49	29.17	12.91	-

Ns	Ni	Counted squares	Age (Ma)	2σ se(t)	U (ppm)	Uerr (%)	Mean Dpar
10	17	21	42.79	34.36	33.06	15.83	1.66
6	2	30	215.33	352.26	2.72	3.44	-
4	2	16	144.35	250.42	5.11	6.46	2.1
15	15	63	72.58	53.47	9.72	4.95	1.79
4	6	60	48.48	62.76	4.08	3.21	2.02
2	3	6	48.48	88.63	20.42	21.84	-
18	13	100	100.28	73.64	5.31	2.89	2.03
1	3	30	24.28	56.13	4.08	4.37	-
4	11	50	26.49	31.04	8.99	5.30	-
18	19	30	68.78	45.73	25.87	11.73	-
8	5	36	115.74	132.44	5.67	4.84	2.01
16	32	50	36.39	22.56	26.14	9.19	-
9	10	9	65.36	60.39	45.38	28.03	1.86
15	6	49	179.94	174.71	5.00	3.93	2.04
2	2	15	72.58	145.33	5.45	6.89	-
4	1	12	285.54	639.09	3.40	5.56	-
8	19	60	30.66	26.01	12.93	5.87	2.94
2	4	30	36.39	63.13	5.45	5.14	1.96
1	4	12	18.22	40.78	13.61	12.84	1.18
20	19	35	76.38	49.49	22.17	10.06	1.49
17	32	24	38.66	23.51	54.46	19.15	-
22	15	100	106.17	71.84	6.13	3.12	1.42
17	5	18	243.51	248.89	11.35	9.68	1.77
18	25	42	52.34	32.75	24.31	9.65	1.36
4	5	24	58.13	78.19	8.51	7.26	-
15	23	15	47.43	31.81	62.63	25.89	-
4	4	15	72.58	102.88	10.89	10.27	-
10	16	48	45.46	36.91	13.61	6.71	-
10	10	40	72.58	65.30	10.21	6.31	1.95
14	9	42	112.55	96.79	8.75	5.68	1.35
5	1	12	354.99	778.51	3.40	5.56	1.27
15	20	100	54.51	37.61	8.17	3.61	2.53
3	2	30	108.57	198.49	2.72	3.44	2.74
9	6	17	108.57	114.92	14.42	11.31	-

1M64

Rio Camana. Clasts = basement, volcanic rocks, quartz-arenites, some granites
North of Camana
Lat. / Long. : -16.55228 ; -72.71800
Alt. = 78 m.

	Age	2σ se(t)	Min (2σ)	Max (2σ)	P(X2) (%)	Dispersion (%)
Pooled	45.81	8.63	37.17	54.44	0.00	64.00
Mean	63.51	17.34	46.17	80.85		
Central	48.50	15.20	33.30	63.70		

Single grain data :

n	Nd	ρd	rse(ρd)	Mean Length
31	8502.00	5.79E+05	1.33	-

Ns	Ni	Counted squares	Age (Ma)	2σ se(t)	U (ppm)	Uerr (%)	Mean Dpar
2	1	42	145.30	356.20	0.97	1.58	1.4
5	3	16	121.31	177.58	7.61	8.14	-
12	6	28	145.30	145.99	8.69	6.82	1.49
6	9	12	48.80	51.66	30.43	19.76	1.42
4	4	30	73.06	103.57	5.41	5.10	2.66
22	17	30	94.39	61.65	22.99	11.01	1.77
0	1	8	36.63	126.95	5.07	8.28	-
9	11	40	59.84	54.10	11.16	6.59	1.84
26	30	80	63.37	34.51	15.22	5.52	1.73
18	15	35	87.57	61.82	17.39	8.85	1.5
7	24	60	21.40	18.50	16.23	6.57	2.18
6	10	16	43.94	45.58	25.36	15.67	1.78
5	5	12	73.06	92.69	16.91	14.42	1.53
12	13	20	67.47	54.41	26.37	14.37	-
18	7	49	186.23	166.88	5.80	4.24	2.11
3	33	15	6.68	8.08	89.26	30.94	1.28
15	17	36	64.51	46.13	19.16	9.17	1.67
12	60	100	14.68	9.39	24.34	6.29	2.55
0	7	15	5.25	15.37	18.93	13.84	-
7	5	25	102.06	119.92	8.11	6.92	1.63
0	2	15	18.34	58.03	5.41	6.84	-
1	4	9	18.34	41.06	18.03	17.01	-

Ns	Ni	Counted squares	Age (Ma)	2σ se(t)	U (ppm)	Uerr (%)	Mean Dpar
2	17	15	8.64	12.94	45.98	22.02	1.91
3	13	50	16.93	21.75	10.55	5.75	1.96
1	1	12	73.06	206.77	3.38	5.52	-
9	4	10	163.24	196.83	16.23	15.31	1.35
2	7	20	20.96	33.67	14.20	10.38	2.16
8	15	21	39.07	34.42	28.98	14.74	-
16	19	18	61.58	42.21	42.83	19.43	1.8
16	35	9	33.50	20.48	157.79	53.13	-
2	3	15	48.80	89.22	8.11	8.68	2.32

1M65

Rio Majes. Clasts = mostly volcanic rocks, basement, granitoïdes and a few quartzites
North of Corrire
Lat. / Long. : -16.92971 ; -72.46313
Alt. = 816 m.

	Age	2σ se(t)	Min (2σ)	Max (2σ)	P(X2) (%)	Dispersion (%)
Pooled	18.81	3.05	15.76	21.86	0.00	107.00
Mean	31.28	10.26	21.02	41.54		
Central	18.70	6.00	12.70	24.70		

Single grain data :

n	Nd	ρd	rse(ρd)	Mean Length
67	8502.00	5.82E+05	1.40	-

Ns	Ni	Counted squares	Age (Ma)	2σ se(t)	U (ppm)	Uerr (%)	Mean Dpar
2	2	16	73.53	147.24	5.04	6.38	1.38
2	52	100	2.84	4.11	20.96	5.82	-
8	30	80	19.69	15.79	15.12	5.49	-
1	3	25	24.60	56.87	4.84	5.17	1.55
2	6	50	24.60	40.25	4.84	3.80	-
12	18	70	49.12	36.92	10.37	4.83	-
10	22	100	33.53	25.78	8.87	3.75	2.92
25	14	70	130.73	88.19	8.06	4.24	-
2	1	12	146.24	358.49	3.36	5.49	-
3	1	14	218.14	504.21	2.88	4.70	-
7	23	60	22.47	19.52	15.45	6.39	2.13
0	33	30	1.12	3.19	44.34	15.37	-
2	6	36	24.60	40.25	6.72	5.27	-
3	22	48	10.08	12.44	18.48	7.81	-
7	7	40	73.53	78.93	7.05	5.16	-
2	12	42	12.31	18.85	11.52	6.52	-
6	19	96	23.31	21.95	7.98	3.62	2.69
0	29	100	1.27	3.64	11.69	4.32	-
13	21	50	45.62	32.50	16.93	7.32	2.8
0	1	36	36.87	127.78	1.12	1.83	-
13	21	100	45.62	32.50	8.47	3.66	2.64
6	23	100	19.26	17.76	9.27	3.83	2.42
0	4	8	9.24	27.73	20.16	19.01	-

Ns	Ni	Counted squares	Age (Ma)	2σ se(t)	U (ppm)	Uerr (%)	Mean Dpar
0	9	40	4.11	11.94	9.07	5.89	-
0	12	100	3.08	8.90	4.84	2.74	-
0	25	100	1.48	4.23	10.08	4.00	-
1	3	64	24.60	56.87	1.89	2.02	-
1	12	100	6.16	12.84	4.84	2.74	-
0	2	25	18.46	58.41	3.22	4.08	-
5	22	100	16.79	16.71	8.87	3.75	-
0	15	36	2.46	7.09	16.80	8.55	-
0	4	48	9.24	27.73	3.36	3.17	-
6	4	16	109.99	142.40	10.08	9.51	2.15
2	7	50	21.10	33.89	5.64	4.12	1.96
12	28	100	31.62	22.03	11.29	4.24	4.02
1	15	60	4.93	10.19	10.08	5.13	-
0	21	60	1.76	5.04	14.11	6.10	-
5	23	100	16.06	15.92	9.27	3.83	1.87
15	22	100	50.23	33.99	8.87	3.75	2.18
0	31	42	1.19	3.40	29.75	10.64	-
0	17	35	2.17	6.24	19.58	9.38	-
37	19	80	142.43	81.58	9.57	4.34	-
3	10	40	22.15	29.24	10.08	6.23	-
1	36	49	2.05	4.17	29.62	9.84	-
9	6	18	109.99	116.43	13.44	10.55	-
0	20	28	1.85	5.30	28.79	12.74	-
1	9	24	8.21	17.33	15.12	9.82	-
2	26	28	5.69	8.36	37.43	14.58	-
4	4	12	73.53	104.24	13.44	12.67	3.18
1	19	100	3.89	7.99	7.66	3.48	-
3	16	60	13.85	17.48	10.75	5.30	-
0	10	28	3.70	10.72	14.40	8.89	-
0	41	70	0.90	2.57	23.61	7.36	-
9	20	100	33.19	26.84	8.06	3.57	1.95
7	10	60	51.56	51.07	6.72	4.15	2.69
9	49	94	13.57	9.93	21.01	6.00	2.72
3	20	10	11.08	13.77	80.62	35.68	-
9	10	48	66.22	61.19	8.40	5.19	2.62
0	6	30	6.16	18.14	8.06	6.33	-
2	16	42	9.24	13.89	15.36	7.57	-
6	16	60	27.67	26.63	10.75	5.30	2.58
1	33	40	2.24	4.55	33.26	11.53	-
0	15	50	2.46	7.09	12.09	6.15	-
3	52	48	4.27	5.08	43.67	12.12	-
1	1	12	73.53	208.11	3.36	5.49	-
1	17	100	4.35	8.96	6.85	3.28	-
11	43	100	18.89	12.90	17.33	5.28	2.92